All-optical frequency division with self-phase-locked parametric oscillators

The research presented in this thesis is supported financially by the Deutsche Forschungsgesellschaft (DFG)
and by the Stichting Fundamenteel Onderzoek der Materie (FOM).

The work was carried out at the Laser Physics and Non-Linear Optics Group at the Faculty of Applied Physics, University of Twente, P.O. Box 217, 7500 AE Enschede, The Netherlands.

ISBN 90-365-1936-5

ALL-OPTICAL FREQUENCY DIVISION WITH SELF-PHASE-LOCKED PARAMETRIC OSCILLATORS

PROEFSCHRIFT

ter verkrijging van
de graad van doctor aan de Universiteit Twente,
op gezag van de rector magnificus,
prof. dr. F. A. van Vught,
volgens het besluit van het College voor Promoties
in het openbaar te verdedigen
op woensdag 17 september 2003 te 13.15 uur.

door

Petra Groß
geboren op 30 december 1972
te Landstuhl, Duitsland

Dit proefschrift is goedgekeurd door
de promotor prof. dr. K.-J. Boller

Abstract

Time and, equivalently, frequency are physical quantities that can be measured with the highest relative accuracy, to an extent such that other fundamental measurements are reduced to time measurements, wherever possible. The precision measurement of time and frequency has become of fundamental importance for scientific and technical applications, such as fundamental research in geophysics or astrophysics, telecommunication technology, and modern navigation systems.

The goal of the current work is to considerably expand the range accessible for high precision metrology. A new method is investigated both theoretically and experimentally, in order to enable the measurement of unknown frequencies in a spectral range, which is currently not yet easy approachable.

To determine any unknown frequency, this frequency has to be measured, directly or indirectly, with respect to an existing frequency standard. Such a high precision measurement is usually realized using harmonic frequency chains or difference-frequency synthesis chains. However, up to now these standards only cover the visible and the near infrared spectral range, and there are only few standards at specific frequencies available further in the infrared. In order to expand the range accessible for high precision frequency measurements to the mid or far infrared, subsequent steps of phase-coherent frequency division are required. A promising candidate for this task is the all-optical division by the integer numbers 2 or 3. The process of transferring the frequency to another spectral region should provide a high power efficiency and high frequency stability. Furthermore, for practical reasons such a divider stage should be designed to warrant full wavelength flexibility to serve future applications.

In the present work, the first wavelength flexible phase-coherent division of an optical frequency by 2 is realized using a self-phase-locked continuous-wave (cw) optical parametric oscillator (OPO). The OPO converts a pump frequency into two subharmonic waves with approximately half the pump frequency and with different polarizations. Using an intracavity quarter-wave plate, a part of each of the orthogonally polarized subharmonic waves is rotated to the other polarization state, thereby enabling mutual injection-locking of the two waves. If the frequency difference between the two waves is tuned sufficiently close to zero, self-injection locking of the OPO waves occurs. As a result, and contrary to standard OPOs, the pump wave and the subharmonic waves are mutually phase-locked, oscillating phase-coherently with the exact frequency ratio of 2:1:1, respectively.

The all-optical by-2-divider is designed to warrant the full wavelength flexibility required for future applications. This is achieved by carefully choosing the components of the OPO. Firstly, as the pump source we have chosen a wavelength tunable laser, which in our case is an AlGaAs diode master-oscillator power-amplifier (MOPA) system, operating around a wavelength of 802 nm. Such and other types of diode lasers are now available over a wide spectral range from the ultraviolet to the far infrared. Secondly, the nonlinear conversion process in the OPO crystal

is also chosen to be wavelength tunable. This is achieved by the method of quasi-phase matching (QPM), which can enable any three-wave mixing process within the transparency range of the crystal. The present experiments rely on QPM in periodically poled lithium niobate (PPLN), which is transparent between 400 nm and 5 μm.

In the theoretical part, the coupled field equations of the OPO divider are first solved analytically in the steady-state regime. From this, the properties of the self-phase-locked field eigenstates and their dependence on experimentally controllable parameters such as the adjustable locking strength are calculated. In the self-phase-locked state, one obtains two different values for the pump power at threshold. However, by using a stability analysis, it is proven that, unlike previously expected, only the lower threshold state is stable and thus observable in the experiment, while the higher threshold solution is unstable. The investigation of the output waves' phases reveals a two-fold symmetry in phase space. Considering phase fluctuations based on temporal instabilities of the experimental setup for the first time an expression for the divider's frequency stability is derived analytically.

In order to gain insight also in the dynamical properties of self-phase locking in by-2-divider OPOs, which is not possible with the analytical steady state models, we completed the theoretical considerations by a numerical analysis. The analysis is based on the integration of the envelopes of three OPO fields, i.e on the integration of their temporal changes versus time using a Runge-Kutta algorithm. The numerical model confirms the solutions found in the analytical calculations, regarding the locking range, the steady-state solutions and the instability of the high-threshold solution as well as the two possible eigenvalues of the subharmonic waves' phase states. A rich scenario of theoretical phase dynamics is discovered and presented. However, this field is still open to experiments.

In our experiments, all-optical self-injection locking is demonstrated by measuring the suppression of the beat note of the two subharmonic waves within the locking range around a zero beat frequency. Typically, the OPO operates stably in this self-locked state for 15 minutes. The locking range, which is measured as a function of the quarter-wave plate rotation angle, is as wide as 160 MHz for a rotation angle of 6 deg. This is far beyond what could be achieved with conventional phase locking based on electronics, electro-optics, and piezo-control. By measuring the bandwidth of the beat signal, the fractional frequency instability of all-optical frequency division by 2 is determined for the first time. The fractional frequency stability is as low as $1.5 \cdot 10^{-14}$ for measurement times between 200 ms and 14 s, which is still limited by the resolution of the used equipment. To achieve a much higher precision of the divider phase stability, a direct measurement of the phase difference of the two subharmonic waves is carried out. This measurement yields a residual fluctuation of the relative phase of the two subharmonic waves of 0.7 rad in 40 s, which corresponds to an extremely low residual fractional frequency instability of by-2 division of $8 \cdot 10^{-18}$. We found that there is a good agreement

with the measured fractional frequency instability of the divider.

By measuring the subharmonic phase difference and the power ratio of the self-phase-locked divider OPO as a function of the cavity detunings, the validity of the derived theory is affirmed. In addition, the possibility to monitor and to fully control the cavity mode detunings with respect to the exactly divided pump frequency is demonstrated for the first time. This forms a valuable tool to steer the divider, such that the OPO can be kept in the self-phase-locked operation state, basically for an unlimited time.

In conclusion, we realized the first fully wavelength flexible phase-coherent frequency division by 2, which is based on an optically self-phase-locked cw OPO. The experimental results prove the successful and stable operation of the divider. The measured properties of all-optical frequency division are in good agreement with the theory derived from the coupled field equations. The observed reliability and excellent stability together with the wavelength flexibility of the design clearly demonstrate the high potential of self-phase-locked OPOs to serve as frequency dividers in future precision frequency metrology.

Samenvatting

Tijd, en equivalent frequentie, zijn fysische grootheden die gemeten kunnen worden met de hoogste relatieve nauwkeurigheid, zodat, bij voorkeur, andere fundamentele metingen gereduceerd worden tot tijdsmetingen. Precieze metingen van tijd en frequentie zijn van fundamenteel belang voor wetenschappelijke en technische toepassingen, zoals fundamenteel onderzoek in geofysica, astrofysica, telecommunicatie en moderne navigatie systemen.

Het doel van het huidige werk is om het gebied, waarin zeer nauwkeurige frequentie metingen mogelijk zijn, duidelijk uit te breiden. Om dit te bereiken, wordt experimenteel en theoretisch een nieuwe methode bestudeerd, waarmee het mogelijk is om onbekende frequenties te meten in een tot op heden moeilijk toegangelijkke spektraal gebied.

Onbekende frequenties worden direct of indirect ten opzichte van bestaande frequentiestandaarden gemeten. Voor deze nauwkeurige relative metingen maakt men gebruik van "harmonic frequency chains" of van "difference-frequency synthesis chains". Tot nu toe omvatten deze standaarden echter alleen het zichtbare en nabije infrarode spectrale gebied. In het midden infrarood zijn nog slechts een beperkt aantal frequentiestandaarden beschikbaar. Om frequenties in het midden en zelfs verre infrarood te correleren aan de frequentiestandaarden is het noodzakelijk om fase-coherente frequentiedeling toe te passen in één of merdere stappen. Een veelbelovende kandidaat voor deze taak is de volledig optische deling door de gehele getallen 2 of 3. Het proces van frequentie overbrenging naar een ander gebied in het spectrum zal vanzelfsprekend met een goede frequentiestabiliteit en een hoog vermogensrendement moeten plaatsvinden. Bovendien moet het ontwerp van deze delingsstap flexibel zijn in de keuze van de golflengte om toekomstige toepassingen mogelijk te maken.

In het huidige werk is voor het eerst een golflengte flexibele fase-coherente door-2-deling van een optische frequentie gerealiseerd door het gebruik van een "self-phase-locked" continue golf (cw) optische parametrische oscillator (OPO). De fase-coherente deler wordt als volgt gerealiseerd. De OPO zet een pompfrequentie om in twee sub-harmonische golven met ongeveer de halve pompfrequentie en met verschillende polarisatie. Met een kwart-golf plaat in de resonator wordt een deel van elk van de orthogonaal gepolariseerde subharmonische golven geroteerd naar de andere polarisatie toestand, zodat onderlinge "injection-locking" van de twee golven mogelijk wordt. Als het frequentieverschil tussen de twee golven voldoende dicht naar nul geregeld is, treedt "injection-locking" van de OPO golven op. In tegenstelling tot een standaard OPO resulteert dit in een onderlinge fase-koppeling tussen de pompgolf en de subharmonische golven, en oscilleren deze fase-coherent met de exacte frequentieverhouding van respectievelijk 2:1:1.

De volledig optische door-2-deler is ontworpen om de volledige golflengte flexibiliteit te garanderen die noodzakelijk is voor toekomstige toepassingen. Dit is bereikt door een zorgvuldige keuze van de OPO componenten. Ten eerste, als

pompbron hebben we een in golflengte verstelbare laser gekozen, in ons geval een AlGaAs diode "master-oscillator power-amplifier" (MOPA) systeem, die werkt rond een golflengte van 802 nm. Deze en andere typen diodelasers zijn beschikbaar in een breed spectraal gebied vanaf het ultraviolet tot in het verre infrarood. Ten tweede hebben we gekozen voor OPO kristallen gebaseerd op quasi-phase matching (QPM), waardoor elke drie-golf mengproces mogelijk is binnen het transparante gebied van het kristal. Hierdoor bereiken we de gewenste flexibiliteit in de keuze van de frequentie die we willen locken aan de frequentiestandaard. De huidige experimenten zijn gebaseerd op QPM in periodiek gepoold lithium niobaat (PPLN), dat transparant is tussen 400 nm en 5 μm.

In het theoretische deel worden eerst de gekoppelde veldvergelijkingen van de OPO door-2-deler analytisch opgelost voor de stationaire toestand. Hiermee worden de eigenschappen van eigentoestanden van het "self-phase-locked" veld bepaald en hun afhankelijkheid van experimenteel regelbare parameters zoals de verstelbare "locking" sterkte onderzocht. In de "self-phase-locked" toestand, verkrijgt men twee verschillende waarden voor de drempel van het pompvermogen. Een stabiliteitsanalyse wijst uit dat, anders dan verwacht, alleen de toestand bij de lagere drempel stabiel is, en dus meetbaar in het experiment, terwijl de oplossing bij de hogere drempel instabiel is. Onderzoek van de fase van de uitgaande golven laat een twee-voudige symmetrie in de faseruimte zien. Voor het eerst is een analytische uitdrukking afgeleid voor de stabiliteit van de frequentie van de deler door het beschouwen van faseveranderingen ten gevolge van tijdsafhankelijke instabiliteiten van de experimentele opstelling.

Om ook inzicht te verkrijgen in de dynamische eigenschappen van de "self-phase locking" in door 2 delende OPO's, wat niet kan met de analytische stationaire modellen, hebben we de theoretische beschouwingen uitgebreidt met een numerieke analyse. De analyse is gebaseerd op numerieke integratie van de gekoppelde tijdsafhankelijke differentiaal vergelijkingen van de omhullenden van de drie OPO velden. Het numerieke model bevestigd de oplossingen gevonden in de analytische berekeningen, zowel wat betreft het "locking" gebied, de steady-state oplossingen, de instabiliteit van de hoog-drempelige oplossing als de twee mogelijke eigenwaarden van de fasetoestand van de subharmonische golven. De numerieke analyse laat een grote verscheidenheid aan dynamisch gedrag in de faseruimte zien en biedt interessante mogelijkheden voor toekomstige experimenten op dit terrein.

In onze experimenten is volledig optische "self-injection-locking" gedemonstreerd door het meten van de onderdrukking van de resulteerende zweving van de twee subharmonische golven in het "locking" gebied rond een zwevende frequentie van nul. Karakteristiek voor de OPO is een stabiele werking in deze "self-locked" toestand gedurende 15 minuten. Het "locking" gebied is gemeten als een functie van de rotatie hoek van de kwart-golf plaat en is 160 MHz breed bij een hoek van 6 graden. Dit is veel meer dan haalbaar met gebruikelijke "phase-locking" gebaseerd op elektronica, elektro-optica en piëzo-regeling. Door het meten van

de bandbreedte van de zweving is de instabiliteit van de volledig optische door-2-frequentiedeler voor het eerst bepaald. De gemeten frequentie instabiliteit is met $1.5 \cdot 10^{-14}$ voor meettijden tussen 200 ms en 14 s zeer laag. De meting wordt beperkt door de resolutie van de gebruikte apparatuur. Om de resolutie van de instabiliteitsmeting te verhogen wordt het faseverschil tussen de twee subharmonische golven direct gemeten. Deze meting laat zien dat de resulteerde fluctuatie in het faseverschil 0.7 rad is over een periode van 40 s. Dit correspondeert met een uiterst kleine frequentieinstabiliteit van de optische frequentiedeler van $8 \cdot 10^{-18}$. Deze waarde stemt goed overeen met de verwachtingen op grond van onze theoretische analyse.

De geldigheid van de theoretisch afgeleide stationaire oplossingen wordt experimenteel bevestigd door de metingen van het faseverschil en de vermogensverhouding van de "self-phase-locked" subharmonische golven van de OPO als een functie van de bedrijfsparameters. Bovendien word voor het eerst een meetmethode gedemonstreerd die het mogelijk maakt de positie van de resonator modi te meten relatief ten opzichte van de door 2 gedeelde pompfrequentie. Deze methode heeft als grote voordeel dat de meting gebruikt kan worden voor het stabiliseren van de OPO zodat deze in principe tot in het oneinige haar "self-phase-locked" toestand kan vasthouden.

Concluderend, hebben we de eerste volledig golflengte flexibele fase-coherente frequentie door-2-deler gerealiseerd, gebaseerd op een optische "self-phase-locked" cw OPO. De experimentele resultaten bewijzen de succesvolle en stabiele werking van de deler. De gemeten eigenschappen van volledig optische frequentiedeling komen goed overeen met de theorie afgeleid van de gekoppelde veldvergelijkingen. De waargenomen betrouwbaarheid en de excellente stabiliteit samen met de golflengte flexibiliteit van het ontwerp laten duidelijk de uitstekende mogelijkheden zien van "self-phase-locked" OPO's als frequentiedelers in toekomstige precisie frequentie-metrologie.

Zusammenfassung

Zeit und Frequenz können von allen physikalischen Größen mit der bei weitem höchsten Präzision gemessen werden. Daher werden die Messungen anderer fundamentaler Größen auf Zeitmessungen zurückgeführt, wo immer dieses möglich ist. In den letzten Jahrzehnten haben viele Bereiche von Wissenschaft und Technik enorm von der stets höheren Genauigkeit profitiert, mit der Zeit- und Frequenzmessungen durch die Entwicklung von präzisen, hochstabilen optischen Frequenzstandards ("Atomuhren") möglich wurden. Heute sind solche Präzisionsmessungen von zentraler Bedeutung für Anwendungen in der Grundlagenforschung, wie zum Beispiel auf den Gebieten der Geophysik und Astrophysik, ebenso wie für die Telekommunikationstechnik und für moderne Navigationssysteme.

Die vorliegende Arbeit zielt darauf ab, den Einsatzbereich von Frequenzmessungen höchster Präzision deutlich zu erweitern. Hierfür untersucht sie experimentell und theoretisch eine neue Methode, mit der unbekannte Frequenzen in einem bisher schwer zugänglichen optischen Spektralbereich vermessen werden können.

Jede Messung einer unbekannten Frequenz muss sich notwendigerweise direkt oder indirekt auf einen existierende Frequenzstandard beziehen. Für eine solche Relativmessung von Frequenzen mit höchster Genauigkeit werden sogenannte harmonische Frequenzketten oder Differenzfrequenzketten eingesetzt. Bisher decken diese Frequenzstandards jedoch lediglich den sichtbaren und nahen infraroten Spektralbereich ab, wohingegen im ferneren Infrarot bisher nur einzelne Standards bei bestimmten Frequenzen zur Verfügung stehen. Um den für präzise Frequenzmessungen zugänglichen Wellenlängenbereich weiter ins mittlere oder ferne Infarot auszudehnen, sind mehrere aufeinanderfolgende phasenkohärente Frequenzteilungsstufen erforderlich. Hierfür sollte die rein optische Frequenzteilung durch die ganzen Zahlen 2 oder 3 besonders gut geeignet sein. Ein solcher Transfer der Frequenz eines Standards in eine andere Spektralregion soll selbstverständlich mit höchster Stabilität und Effizienz erfolgen. Aus praktischen Gründen muss außerdem gefordert werden, dass eine solche Frequenzteilerstufe nicht nur für eine bestimmte Messaufgabe (Frequenz) tauglich ist, sondern sie muss konzeptionell möglichst flexibel in der Wellenlänge sein.

In der vorliegenden Arbeit wird die erstmalige Realisierung einer wellenlängenflexiblen und phasenkohärenten, optischen Frequenzzweiteilung mit Hilfe eines selbstphasenstabilisierten kontinuierlichen (cw) optisch parametrischen Oszillators (OPOs) vorgestellt. Der OPO konvertiert die sogenannte Pumpwelle in zwei subharmonische Lichtwellen mit ungefähr der halben Frequenz der Pumpwelle und mit unterschiedlichen Polarisationen. Mittels einer resonatorinternen Viertelwellenplatte wird jeweils ein Teil der beiden senkrecht zueinander polarisierten subharmonischen Wellen rotiert und dadurch in den jeweils anderen Polarisationszustand übergeführt. Dadurch wird eine gegenseitige Injektion der beiden Wellen ermöglicht. Für einen hinreichend kleinen Frequenzunterschied zwischen den bei-

den OPO-Wellen bewirkt dies eine gegenseitige Selbstinjektionsstabilisierung der Frequenzen und Phasen. Die beiden subharmonischen Wellen nehmen damit, im Gegensatz zu herkömmlichen OPOs, die exakt gleiche Frequenz und eine feste Phasenbeziehung untereinander und relativ zur Pumpwelle an, so dass alle drei Wellen phasenkohärent oszillieren mit dem exakten Frequenzverhältnis von 2:1:1.

Das Designkonzept des hier vorgestellten rein optischen Zweiteilers zeichnet sich durch eine hohe Wellenlängenflexibilität aus, welche garantiert, dass es zukünftig problemlos auf die verschiedensten Frequenzmessaufgaben übertragen werden kann. Dies wurde möglich durch eine passende Wahl der Hauptkomponenten des Frequenzteilers, nämlich der Pumpquelle und des nichtlinearen OPO-Kristalls. Als Pumquelle wurde ein wellenlängenabstimmbarer Lasertyp ausgewählt. In der konkreten Realisierung wurde hierfür ein auf AlGaAs-Diodenlasern basierendes Oszillator-Leistungsverstärker-System (MOPA) mit einer Emissionswellenlänge von 802 nm verwendet. Solche und ähnliche Diodenlasersysteme sind über einen großen Spektralbereich von ultraviolett bis hin ins ferne Infrarot verfügbar. Des weiteren wurde für den nichtlinearen Konversionsprozess im OPO ein spezieller Kristalltyp verwendet, der ebenfalls prinzipiell für einem weiten Wellenlängenbereich geeignet ist. Bei dem verwendeten Kristalltyp basiert die Frequenzkonversion auf der Technik der Quasiphasenanpassung (QPM), welche jeden Dreiwellenmischprozess innerhalb des Transparenzbereich des Kristalls mit hoher Effizienz möglich macht. Die hier vorgestellten Experimente beruhen auf QPM in dem Material periodisch gepoltes Lithiumniobat (PPLN), dessen Transparenzbereich sich von 400 nm bis 5 μm erstreckt.

Im theoretischen Teil der Arbeit werden zunächst die gekoppelten Amplitudengleichungen, welche die Wechselwirkung der Lichtfelder im OPO beschreiben, im stationären Zustand analytisch gelöst. Daraus können dann die Eigenschaften der selbstphasenstabilisierten Eigenzustände der Felder und deren Abhängigkeit von experimentell kontrollierbaren Parametern, wie z. B. die einstellbare Stärke der Selbstinjektionsstabilisierung, berechnet werden. Im selbstphasenstabilisierten Zustand erhält man zwei unterschiedliche Werte für die Schwellenpumpleistung. Durch die Anwendung einer Stabilitätsanalyse kann jedoch nachgewiesen werden, dass nur die Lösung mit dem niedrigeren Schwellenwert stabil und somit auch experimentell beobachtbar ist. Dahingegen ist die Lösung mit dem höheren Schwellenzustand nicht stabil, was allen bisherigen Erwartungen widerspricht. Die Untersuchung der Phasen der erzeugten subharmonischen Lichtwellen ergibt eine zweifache Symmetrie des Phasenraumes. Durch die Einbeziehung von Phasenschwankungen, die durch zeitliche Instabilitäten des experimentellen Aufbaus hervorgerufen werden, wird zum ersten Mal ein Ausdruck für die Frequenzstabilität des Frequenzteilers analytisch hergeleitet.

Um auch Erkenntnisse über die dynamischen Eigenschaften der Selbstphasenstabilisierung von Frequenzzweiteiler-OPOs zu gewinnen, was mit der analytischen Untersuchung des stationären Zustandes nicht möglich ist, werden die theore-

tischen Arbeiten durch eine numerische Analyse vervollständigt. Die numerischen Berechnungen beruhen auf der Integration der Einhüllenden der drei OPO Lichtfelder, d. h . auf der Integration der zeitlichen Änderungen dieser Felder mit Hilfe eines Runge-Kutta-Algorithmus. Das numerische Modell bestätigt die Ergebnisse der analytischen Rechnungen bezüglich des Fangbereichs, der stationären Zustände, der Instabilität der Lösung mit der höheren Pumpschwelle, sowie der beiden Eigenwerte, die die Phasen der subharmonischen Wellen annehmen können. Das theoretisch berechnete und hier vorgestellte dynamische Verhalten der Phasen bietet ein reichhaltiges Szenario, das durch zukünftige Experimente noch erforscht werden kann.

Der experimentelle Nachweis der rein optischen Selbstinjektionsstabilisierung, und damit der phasenkohärenten Frequenzzweiteilung, erfolgt durch Vermessung der Unterdrückung des Schwebungssignals zwischen den beiden subharmonischen Wellen innerhalb des Fangbereiches um die Schwebungsfrequenz null. Der OPO verharrt typischerweise für Zeitspannen von ca. 15 Minuten in diesem selbststabilisierten Zustand. Der Fangbereich der optischen Frequenzstabilisierung wurde als Funktion des Rotationswinkels der Viertelwellenplatte gemessen. Mit 160 MHz ist er deutlich größer als Fangbereiche, welche mit Hilfe von Standardverfahren zur Phasenstabilisierung realisierbar sind und auf elektronischen, elektro-optischen oder piezo-basierenden Techniken beruhen. Erstmalig wurde die relative Frequenzinstabilität der rein optischen Teilung einer Frequenz durch 2 gemessen. Für Messzeiten zwischen 200 ms und 14 s wird durch die Bestimmung der Bandbreite des Schwebungssignals eine relative Frequenzinstabilität von kleiner als $1.5 \cdot 10^{-14}$ ermittelt. Dieser Wert ist durch die Auflösungsgrenze der benutzten Messapparatur begrenzt. Um eine weitaus höhere Präzision für die Phasenstabilität des Teilers zu erzielen, wird eine direkte Messung der Phasendifferenz der beiden subharmonischen Wellen vorgenommen. Diese Messung ergibt eine Schwankung der relativen Phase der beiden Wellen von 0.7 rad in 40 s, was einer extrem niedrigen relativen Frequenzinstabilität der Frequenzzweiteilung von $8 \cdot 10^{-18}$ entspricht. Die Frequenzinstbilität ist in guter Übereinstimmung mit der theoretisch hergeleiteten relativen Frequenzinstabilität des Teilers.

Durch die Messung des Phasenunterschieds der subharmonischen Wellen des selbstphasenstabilisierten OPOs und durch die gleichzeitige Messung des Verhältnisses der Leistungen der beiden Wellen als Funktion der Arbeitsparameter des OPOs wird die Gültigkeit der theoretisch abgeleiteten Gleichgewichtslösungen bestätigt. Des Weiteren wird die Möglichkeit demonstriert, die Lage der Resonatormoden relativ zur genau durch zwei geteilten Pumpfrequenz zu beobachten und vollständig zu kontrollieren. Dies stellt eine mächtige Methode dar, mit deren Hilfe es möglich sein sollte, den OPO für grundsätzlich unbegrenzte Zeit im selbstphasengelockten Zustand zu halten.

Zusammenfassend wird in der vorliegenden Arbeit erstmalig die Realisierung einer vollständig wellenlängenflexiblen, phasenkohärenten Teilung einer optischen

Frequenz durch 2 mit einem optisch selbstphasenstabilisierten cw OPO beschrieben. Die experimentellen Ergebnisse belegen den erfolgreichen und stabilen Betrieb des Frequenzteilers. Die gemessenen Eigenschaften der rein optischen Frequenzteilung sind in guter Übereinstimmung mit denen, die theoretisch unter Verwendung von gekoppelten Amplitudengleichungen hergeleitet wurden. Die beobachtete Verlässlichkeit und die exzellente Stabilität des vorgestellten Frequenzteilers und sein wellenlängenflexibles Design machen das enorme Potenzial deutlich, welches selbstphasenstabilisierte OPOs als Frequenzteiler für zukünftige Anwendungen in der Präzisionsmetrologie besitzen.

Publications

International journals

1. M. E. Klein, P. Adel, M. Auerbach, C. Fallnich, P. Groß, and K.-J. Boller, *Microsecond pulsed optical parametric oscillator pumped by a Q-switched fiber laser*, accepted for publication by Opt. Lett.

2. M. E. Klein, P. Groß, K.-J. Boller, M. Auerbach, P. Weßels, and C. Fallnich, *Rapidly tunable continuous-wave optical parametric oscillator*, Opt. Lett. **28**, 920-922 (2003).

3. D.-H. Lee, M. E. Klein, J.-P. Meyn, R. Wallenstein, P. Groß, and K.-J. Boller *Phase-coherent all-optical frequency division by three*, Phys. Rev. A **67**, 013808 (2003).

4. P. Groß, M. E. Klein, H. Ridderbusch, D.-H. Lee, J.-P Meyn, R. Wallenstein, and K.-J. Boller, *Wide wavelength tuning of an optical parametric oscillator through electro-optic shaping of the gain spectrum*, Opt. Lett. **27**, 1433-1435 (2002).

5. P. Groß, M. E. Klein, T. Walde, K.-J. Boller, M. Auerbach, P. Weßels, and C. Fallnich, *Fiber-laser-pumped continuous-wave singly resonant optical parametric oscillator*, Opt. Lett. **27**, 418-420 (2002).

6. H. Ridderbusch, M. E. Klein, P. Groß, D.-H. Lee, J.-P. Meyn, R. Wallenstein, and K.-J. Boller, *Electro-optic modification of second-harmonic phase-matching spectra in segmented periodically poled $LiNbO_3$*, J. Opt. Soc. Am. B **19**, 280-288 (2002)

7. D.-H. Lee, M. E. Klein, J.-P. Meyn, P. Groß, S. Marzenell, R. Wallenstein, and K.-J. Boller, *All-optical frequency-by-three division with a diode laser pumped CW-OPO using PPLN*, Proc. SPIE Vol. **3928**, 25-28 (2000)

8. D.-H. Lee, M. E. Klein, J.-P. Meyn, P. Groß, R. Wallenstein, and K.-J. Boller, *Self-injection-locking of a cw OPO by intracavity frequency-doubling the idler wave*, Opt. Expr. **5**, 114-119 (1999)

International conferences

1. P. Groß, K.-J. Boller, M. E. Klein, and D.-H. Lee, *Frequency stability of a self-phase-locked degenerate continuous-wave optical parametric oscillator*,

Conference on Lasers and Electro-Optics 2003, Baltimore, Maryland, USA, Postdeadline Papers Book (Optical society of America, Washington, D.C. 2003), postdeadline paper CPDB1

2. M. E. Klein, P. Groß, K.-J. Boller, M. Auerbach, P. Weßels, and C. Fallnich, *Rapidly tunable fiber laser pumped continuous-wave optical parametric oscillator*, Conference on Lasers and Electro-Optics 2003, Baltimore, Maryland, USA, Technical Digest (Optical society of America, Washington, D.C. 2003), paper no. CThG3

3. M. E. Klein, P. Groß, T. Walde, K.-J. Boller, M. Auerbach, P. Weßels, and C. Fallnich, *Fiber Laser Pumped Continuous-wave Singly-resonant Optical Parametric Oscillator*, Conference on Lasers and Electro-Optics 2002, Long Beach, California, USA, Technical Digest p. 149 (Optical society of America, Washington, D.C. 2002), paper no. CTuC7

4. P. Groß, H. Ridderbusch, M. E. Klein, D.-H. Lee, J.-P. Meyn, R. Wallenstein, and K.-J. Boller, and *In situ shaping of phase-matching profiles using the electro-optic effect in segmented QPM crystals*, Conference on Lasers and Electro-Optics 2001, Baltimore, Maryland, USA, Technical Digest p. 573 (Optical society of America, Washington, D.C. 2001), paper no. CFF6

5. K.-J. Boller, M. E. Klein, D.-H. Lee, P. Groß, H. Ridderbusch, M. A. Tremont, A. Robertson, J.-P. Meyn, and R. Wallenstein, *Diode-pumped optical parametric oscillators*, Conference on Lasers and Electro-Optics Europe'00, Nice, France, conference digest p. 13, paper no. CMD1, 2000

6. J.-P. Meyn, D.-H. Lee, S. Zelt, P. Groß, H. Ridderbusch, C. Laue, M. E. Klein, R. Wallenstein, and K.-J. Boller, *Quasi phase matched oxide crystals for SHG and OPO*, IEEE Lasers and Electro-Optics Society LEOS 2000 Annual Meeting (IEEE, Piscataway, NJ, USA, 2000), vol. 2 p. 452-453

7. D.-H. Lee, P. Groß, M. E. Klein, J.-P. Meyn, R. Wallenstein, and K.-J. Boller, *Observation of phase-locking in an all-optical frequency-by-three divider*, Conference on Lasers and Electro-Optics 2000, San Francisco, California, USA, Technical Digest p. 523 (Optical society of America, Washington, D.C. 2000), paper CThQ6

8. D.-H. Lee, M. E. Klein, J.-P. Meyn, P. Groß, S. Marzenell, R. Wallenstein, and K.-J. Boller, *All-optical frequency-by-three division with a diode laser pumped cw-OPO using PPLN*, Photonics West 2000 / Laser 2000, 3928-04, Adv. Tech. Prog. p. 47

National conferences

1. P. Groß, M. E. Klein, D.-H. Lee and K.-J. Boller, *Phase locking dynamics of a degenerate optical parametric oscillator*, 27e Najaarsvergadering van de Sectie Atoom- Molecuul- en Optische Fysica, Nederlandse Natuurkundige Vereniging, abstract no. B 32 (2002)

2. P. Groß, M. E. Klein, T. Walde, K.-J. Boller, M. Auerbach, P. Weßels, and C. Fallnich, *Fiber laser pumped continuous-wave singly-resonant optical parametric oscillator*, 26e Najaarsvergadering van de Sectie Atoom- Molecuul- en Optische Fysica, Nederlandse Natuurkundige Vereniging, abstract no. A 20 (2001)

3. T. Walde, P. Groß, M. E. Klein, K.-J. Boller, and F. J. M. Harren *Yb^{3+}-doped fiber amplifier as a tunable pump source for an optical parametric oscillator*, 26e Najaarsvergadering van de Sectie Atoom- Molecuul- en Optische Fysica, Nederlandse Natuurkundige Vereniging, abstract no. B 35 (2001)

4. H. L. Offerhaus, P. Groß, F. A. van Goor, and K.-J. Boller, *A parametric amplifier for a laser wakefield accelerator*, 26e Najaarsvergadering van de Sectie Atoom- Molecuul- en Optische Fysica, Nederlandse Natuurkundige Vereniging, abstract no. B 8. (2001)

5. D.-H. Lee, M. E. Klein, P. Groß, J.-P. Meyn, R. Wallenstein, and K.-J. Boller, *Diode-pumped CW optical parametric oscillator based on quasi-phase-matching*, Optical Society of Korea Summer Meeting, invited talk, conference proceeding p. 260, (2001)

6. H. Ridderbusch, M. E. Klein, D.-H. Lee, P. Groß, J.-P. Meyn, K.-J. Boller and R. Wallenstein, *Neue elektro-optische Effekte in Kristallen mit Quasiphasenanpassung*, 64. Physikertagung Bonn 2000, Verhandl. DPG (VI) 35, p. 1052, paper no. Q 6.4 (2000)

7. P. Groß, D.-H. Lee, M. E. Klein, H. Ridderbusch, J.-P. Meyn, R. Wallenstein and K.-J. Boller, *Optische Frequenzteilung durch Zwei und Drei in kontinuierlichen parametrischen Oszillatoren mit Quasiphasenanpassung*, 64. Physikertagung Bonn 2000, Verhandl. DPG (VI) 35, p. 1051, paper no. Q 6.2 (2000)

Contents

Chapter 1

Introduction

Time and frequency are the physical quantities that can be measured with, by far, the highest accuracy. Time can now be measured so accurately that, wherever possible, other fundamental measurements are reduced to time measurements. Therefore today frequency measurements are not only used to define the basic units of time and length [1], but also, for example, the unit of voltage is maintained via the Josephson tunneling effect in superconductivity, which involves the precision measurement of a microwave frequency [2].

Precision measurements of time and frequency have become of fundamental importance in science and engineering. Some of the most direct and important applications of high-precision metrology are in spectroscopy. In fact, many of the technical advances for improving time measurements have been directly applied to the improvement of spectroscopic techniques and vice versa.

Modern telecommunication techniques and navigation systems depend on a precise measurement of time and the accurate control of frequencies. For example, navigation in outer space benefited from improved time measurements during the Voyager mission to Neptune, when the Voyager's position was determined by three radar telescopes, each equipped with two hydrogen masers for precise time measurements. Navigation here on earth was greatly improved by the entirely new global positioning system (GPS) [3]. 24 satellites containing highly accurate clocks transmit synchronized signals, which enable one to determine one's position anywhere on the globe to within 20 m using an inexpensive receiver, or even within 3 m when using a better receiver that exploits the correction technique of differential GPS (DGPS) [4].

Knowledge in geophysics is obtained by means of time and distance measurements. For example, the movement of the earth's surface has been studied by measuring the distances between the radio telescopes used for Very Long Baseline Interferometry (VLBI). Recently, in 1999, GPS has been used for a very valuable study of earth's crustal dynamics during an earthquake in Turkey [5]. By comparing a careful survey from shortly before and after the earthquake, the movement of the earth surface could be determined. Today GPS is routinely used to observe deformations of important geographic marks and large engineering structures such as dams [6], and to calculate the strain rates of certain parts of the earth's crust [7], which is of high importance especially in densely populated areas.

Research in astrophysics relies on precise time and distance measurements as well. With higher precision time measurements, the variability of quantities can be determined, that once have been taken as constant, like e.g. the rotation period of the earth, or the change of the periods of pulsars. Millisecond pulsars have been found to have remarkably constant periods [8]. In fact, one of these pulsars is so stable that, in future, it may be used as a long-term time standard [9].

Other applications can be found within basic research, like the measurement of fundamental constants as for example the Rydberg constant R_∞, the Sommerfeld constant α or the Planck constant h [10]. Important tests of both the Special and the General Theory of Relativity were made possible by using high-precision clocks to measure the change of the periodic rate of a hydrogen maser with speed and altitude [11], [12] or by measuring the modulation of the rate of a millisecond pulsar through the Doppler shift when approaching and receding from the earth [9], [13]. As measurement stability and accuracy improve, scientists will find themselves able to view the physical world with an even finer grid. Of particular interest will be the improved determination of fundamental constants, the observation of physical constants evolving in time [2], the search for variations in the isotropy of space [14], [15] and charge-parity-time (CPT) violations [16].

For the precise measurement of any unknown frequency, highly accurate and stable frequency standards are required, which cover the entire range from microwaves up to the far ultraviolet spectral range [17]. The unknown frequencies can be measured by phase-coherent comparison with a reference frequency from secondary standards, which again are all calibrated with respect to one single standard, the primary standard. The latter should, ideally, be the most stable of all standards.

Over the last 50 years, advances in laser manipulation and atom and ion handling have enabled the establishment of atomic clocks with ever increasing accuracy and stability. A thorough survey on this topic can be found for example in Refs. [18], [19] and [20]. Atomic clocks complete the two basic components of normal clocks, i.e. an oscillator and a cycle counter, by an additional third component, namely the ultra-stable resonance of a well-isolated atomic or ionic transition. This transition, or quantum oscillator, is used as the reference with respect to which the oscillator frequency is controlled. Atomic clocks in the microwave as well as in the optical frequency domain have been developed, operated and mutually compared. Principially, optical atomic clocks are advantageous compared to microwave atomic clocks like, for example, the present primary frequency standard, the Cs atomic clock at 9.2 GHz, because with all other factors being equal, a $\approx$100000 times higher transition frequency can provide a finer division of time and thus potentially a higher precision.

Today, highly stable and accurate optical clocks covering the visible and near infrared spectral region based on transitions in cesium, rubidium and hydrogen atoms and mercury ions are in operation [19], with an ultimate fractional frequency uncertainty close to 10^{-18} due to systematic effects [21]. At the National Institute of Standards and Technology (NIST) in Boulder, an optical (visible) clock is operated, which is based on a transition at 1064 THz in a trapped single mercury ion [22]. A second (UV) optical standard at NIST is based on a collection of $\approx 10^7$ laser-cooled ^{40}Ca atoms held in a magneto-optical trap [23]. The absolute frequencies of both standards have recently been measured with respect to the SI second, adding to the practical use of these optical standards [24]. A similar experiment has been performed to measure the absolute frequency of a 435.5-nm optical clock based on a single trapped $^{171}Yb^+$ ion operated at the Physikalisch-Technische Bundesanstalt (PTB) in Germany [25]. The measurements of the $^{171}Yb^+$ and the Hg^+ clock frequencies have been achieved with a relative uncertainty as low as 10^{-14}, which demonstrates the potential of the two standards as ultraprecise optical frequency references. Another promising candidate is a single trapped indium ion, which reveals very low systematic uncertainties in the order of 10^{-18} [21] in the UV.

To apply the new UV, visible and near infrared frequency standards to the original problem, namely the measurement of time and frequency, one has to be able to compare an unknown frequency to a known one, and one also has to be

able to perform comparisons to the primary standard and inter-standard-reliability tests. Two techniques have been developed during the last 20 years to enable the required frequency comparisons.

The first technique is the technique of harmonic frequency chains [26]. In 1996, Schnatz and colleagues presented the determination of a ^{40}Ca transition at 456 THz or 658 nm with respect to the Cs atomic clock [27]. For this first phase-coherent measurement of visible radiation, a frequency gap of a ratio of ≈50000 had to be bridged with about 20 different laser oscillators with their frequencies distributed throughout the gap and phase-locked with respect to each other, mostly with electronic servo loops. Most unsatisfactory aspects of harmonic chains are their enormous complexity, high susceptibility to failure, and their lack of generality. The latter means, that they address only a set of frequencies, where laser oscillators can be built or suitable intermediate references are available, such that harmonic chains cannot be readily applied to different tasks.

This disadvantage can be overcome by the second, more flexible technique of difference-frequency synthesis chains [28], which can be realized with tunable light sources in the visible and near infrared spectral range, where they are readily available. Based on this technique, one can consider converter stages like e.g. a by-6 divider based on optical parametric oscillators, as was proposed by Wong in 1992 [29]. The key building blocks of difference-frequency synthesis chains are optical frequency-interval dividers, which phase-coherently divide the interval between two optical signals by an integer. This integer may be a small number like 2 or 3 in the case of nonlinear processes at a few discrete frequencies [28], or of the order of 10^6 in the case of a frequency comb generated with femtosecond pulses [30]. The development of the latter octave-spanning frequency comb has been made possible by the recent advent of micro-structured fibers, which via nonlinear effects [31] enable broadening of a femtosecond Kerr-lens mode-locked comb [32], [33] in the visible and the near infrared spectral range. The spectral lines of such a frequency comb are equally spaced within a relative uncertainty of $3 \cdot 10^{-17}$ [34], enabling an easy measurement of any frequency within the interval covered by the comb, if that frequency falls into the named range. Using such a comb and locking it to an optical frequency standard based on a single trapped mercury ion operated at NIST, the precision and accuracy of the UV frequency standard was transferred to a carrier frequency of 1 GHz [35]. Ref. [36] gives an overview over recent achievements in frequency metrology with a strong emphasis

on octave-spanning frequency combs.

However, one disadvantage of active optical frequency comb generators is obvious: The method is restricted to frequency regions, where broad-band laser gain media are available. In other spectral regions, i.e. from the near infrared down to the mid infrared, one has to rely on frequency divider stages based on nonlinear processes at discrete frequencies.

Nevertheless, these divider stages should be broadband in the sense that they provide the possibility to tune the involved frequencies to any target frequency. Therefore the concept of the divider's setup has to be such that they can be taken into operation over a wide spectral region. At the same time, they should be highly stable in transferring the frequency of a standard to a different spectral region. Furthermore, a high power efficiency for the frequency transfer is desirable in order to maintain a high signal-to-noise ratio, such that several divider stages can be operated subsequently without any intermediate amplifiers [37].

By far most promising for this task is all-optical frequency division using a continuous-wave (cw) optical parametric oscillator (OPO). CW OPOs are devices, which convert input laser radiation, the so-called pump wave, into two coherent light waves with lower frequencies, via three-wave interaction in a nonlinear medium. Furthermore, OPOs satisfy some of the named fundamental requirements, such as a high efficiency, wavelength tunability, and potential for a narrow bandwidth. The most basic case of an OPO frequency divider is frequency division by 2, as described in this work. It can be realized by a cw OPO with both of the subharmonic waves' frequencies tuned to exactly one-half of the pump frequency and by additionally forcing them to oscillate in phase. In any OPO, the two subharmonic waves are phase-correlated via the three-wave interaction process, i.e., their sum phase follows the pump phase, but their difference phase undergoes a diffusion process [38]. In order to achieve phase-coherent frequency division, this diffusion has to be suppressed, which can be achieved either by an electronic or by an optical phase control of the OPO waves. In the first case, the frequency difference between the two subharmonic waves is measured as an electronic error signal to control the OPO frequencies via an active electronic servo loop. In the second case of an all-optical phase control, the OPO waves are phase-locked by the injection of an optical wave, similar to injection locking of lasers [39]. As compared to an electronic control, an all-optically phase-locked frequency divider is expected to provide a higher precision due to the faster response time. This is

possible, because there are no electronic circuits involved for obtaining an error signal and because there is no external feedback loop. The mechanical picture of an all-optically phase-locked OPO divider stage is a gear transmission, as can be found in mechanical clocks. In such a gear transmission, the oscillations of the balance spring are phase-coherently transferred to the clock face, where the induced rhythmical movement of the pointers indicates the progress in time.

In the current work, an all-optical frequency by-2-divider based on a self-phase-locked OPO is realized, thoroughly characterized and the frequency stability of phase-coherent frequency division by 2 is measured for the first time.

In contrast to previous work, the divider is designed to warrant the full wavelength flexibility required for future applications. This is achieved by carefully choosing the components the divider and its pump source are based on. Firstly, as the pump source we have chosen a wavelength tunable laser, which in our case is a AlGaAs diode master-oscillator power-amplifier (MOPA) system, emitting a wavelength of about 802 nm. Such and other types of diode lasers are now available over a wide spectral range from the ultraviolet to the far infrared. Secondly, the nonlinear conversion process in the OPO crystal is also chosen to be wavelength tunable. This is achieved by quasi-phase matching (QPM), which can enable any three-wave mixing process within the transparency range of the crystal. The present experiments relied on QPM in periodically poled lithium niobate (PPLN), which is transparent between 400 nm and 5 μm.

Division of the pump frequency by two is achieved by tuning the OPO subharmonic wavelengths close to each other, such that the frequency difference between the subharmonic waves is brought close to zero. An intracavity quarter-wave plate is used to introduce an adjustable polarization rotation of the formerly orthogonally polarized subharmonic waves. This results in a mutual phase locking of the two waves and consequently in a phase-coherent oscillation of the subharmonic waves at exactly one-half of the pump frequency.

In this work, phase-coherent division of the pump frequency by 2 is investigated both theoretically and experimentally. The thesis is organized as follows:

The following chapter 2 describes some general properties of OPOs. After that, OPOs are introduced as frequency dividers, giving an overview on former experiments and outlining the basic working principle of self-phase locking of the OPO subharmonic waves.

In chapter 3, a detailed theoretical analysis of the self-phase-locked OPO is

presented, which follows and extends earlier work by Fabre and colleagues [40]. In the self-phase-locked regime, the OPO fields assume certain amplitudes and phases, which are calculated by solving the coupled-field equations in steady-state for comparison with the experimental conditions. For the first time, a stability analysis is applied to the steady-state solutions of a by-2-divider, which obtains as a result that, unlike previously expected, only one threshold state is stable and should be observable in the experiment. An estimate of the locking range is derived for the specific experimental parameters used. Taking into account phase instabilities caused by thermal drift, the fractional frequency stability is derived theoretically for the first time.

However, the analytical calculations only describe the steady-state of the divider. In order to understand the dynamical properties and to gain some insight into the process of self-phase locking, it is essential to consider the temporal evolution of the coupled fields. One possibility to achieve this is to investigate the coupled field equations numerically. Therefore, the theoretical considerations are completed by the first numerical analysis of a by-2-divider's fields presented in chapter 4, which is based on the evolution of the three OPO fields with time, as calculated using a Runge-Kutta algorithm. The numerical evaluation serves as a confirmation of the solutions found during the analytical calculations, but in addition gives one a deeper insight into the study of the dynamical properties of self-phase-locked frequency division and paves the way for a detailed understanding of its process.

Chapter 5 presents the experimental setup used to achieve frequency division by 2, with an emphasis on the wavelength tuning properties on a small scale to identify a tuning strategy which ensures that in the experiment the OPO subharmonic frequencies can be tuned across exact frequency degeneracy.

The experimental results are presented in chapter 6. Self-phase locking of the by-2-divider OPO is achieved and maintained for typically 15 minutes. The locking range is measured as a function of rotation angle of the quarter-wave plate (QWP) which provides different strengths of optical coupling of the subharmonic waves. The locking range is determined to be as large as 160 MHz at a QWP angle of 6 deg. For the first time, the frequency stability of an all-optical by-2 divider is measured, where we found an extremely high stability of better than $8 \cdot 10^{-18}$. Note, that this excelleant stability compares well to the accuracy of modern optical clocks in the UV and visible spectral range.

Also, the first quantitative measurement of the phases of a self-phase-locked OPO and their variation within the locking range is presented, for which we use a phase-sensitive detector setup. The experimental results are compared with the theoretically expected phase variation upon self-phase locking and are found to be in excellent agreement. In addition, these measurements demonstrate the possibility to monitor and to fully control the e- and o-wave cavity mode detunings. With these results, a new, powerful tool is presented to control the divider, such that the OPO can be kept in the self-phase-locked operation state, basically for an unlimited time. This possibility to steer the OPO, together with the excellent frequency stability of $8 \cdot 10^{-18}$ should enable the by-2-divider OPO to open the mid and far-infrared spectral range for high-precision frequency metrology. The possible improvement of measurement stability and accuracy, might enable scientists to view the physical world with a finer grid, for example, for an improved observation of physical constants evolving in time, or for a more meticulous search for variations in the isotropy of space.

In conclusion, this work paves the way to use OPOs as stable, self-phase-locked all-optical frequency divider stages. The first wavelength-flexible by-2-divider is realized, using the specific example of dividing the output frequency of an 800 nm diode laser, to obtain a phase-coherent near infrared wave at a wavelength of 1600 nm. For future applications, this concept can be readily extended by choosing e.g. other visible or near infrared diode lasers and adjusting the QPM in the PPLN OPO crystal accordingly. Already this straightforward modification would enable the frequency division by 2 of light between 400 nm and about 2 μm. A further, significant extension could be obtained with other crystals allowing QPM, such as the recently developed orientation patterned GaAs. This should enable the division by 2 of light between 1 μm and about 8 μm wavelength [41] [42]. In addition, by quasi-phase matching in waveguides [43], the design of on-chip frequency divider stages will be possible. Frequency division by 4, 6 or larger integer numbers can be realized by subsequent divider stages, which is achievable due to the high conversion efficiency of OPOs. Divider stages like the one presented in this work may also be used to transfer one particular, selected mode from a high-precision comb into the MIR. Future experiments might aim for an extension of the by-2 divider's concept to the simultaneous division of a few modes or to divide even the frequencies in an entire comb simultaneously, thereby overcoming the lack of broadband gain media in the MIR. The combination of two promising techniques,

namely frequency combs and frequency dividers might provide the requirements for an easily achievable high precision frequency metrology in the mid infrared.

Chapter 2

Properties of OPOs and frequency divider OPOs

In this chapter, the working principle and general properties of optical parametric oscillators (OPOs) are reviewed, with a focus on continuous-wave (cw) OPOs as phase-coherent frequency dividers and their suitability for precision metrology.

2.1 Working principle of cw OPOs

In 1965, Giordmaine and Miller [44] demonstrated the first optical parametric oscillator (OPO), a device that converts laser radiation into two coherent waves with lower frequencies. A very important characteristic of OPOs is that the frequencies of the two generated waves are not fixed but they can be tuned over wide wavelength ranges. This frequency tunable down-conversion of the pump laser in an OPO is caused by the nonlinear interaction of the three waves (laser and generated waves) via the $\chi^{(2)}$ dielectric susceptibility in a nonlinear optical crystal. The efficiency of the process can be very high, i.e., basically all of the pump laser radiation can be converted into the two lower-frequency beams (see, e.g. Ref. [45]).

Since the first realization of an OPO, many different types of OPOs have been developed as wavelength tunable sources of pulsed and continuous-wave coherent light [46], [47], [48]. OPOs are now available in a wide spectral range from the ultra-violet to the infrared [49], [50], providing average output powers in the range of a few mW to several Watts [51]. The wavelength tuning capabilities and high

power efficiency make OPOs ideal light source for a large number of applications, such as high resolution spectroscopy and trace-gas detection [52], precision frequency metrology, environmental monitoring [53], and light detection and ranging (LIDAR) [54]. Other applications exploit the fact that the amplitudes and phases of the two waves generated in an OPO are quantum-correlated, and thus can be used, e.g. for a reduction of quantum noise in fundamental and applied optical measurements [55] [56] [57] [58].

Before addressing the specific properties of cw OPO as frequency dividers, the basic operation principles of OPOs shall be reviewed briefly.

2.1.1 OPO basics

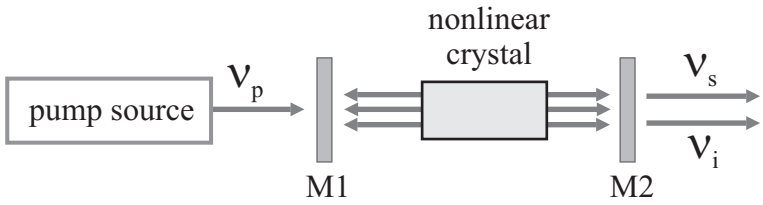

Figure 2.1: Schematic setup of an OPO. An optical wave with frequency ν_p from the pump source is converted into two output waves with frequencies ν_s and ν_i via a three-wave interaction in a nonlinear crystal. M1 and M2 are mirrors of a feedback resonator.

For a qualitative description of the working principle, we want to consider the most basic setup of an OPO, as shown schematically in Fig. 2.1. A powerful laser beam provided by a pump source at an optical frequency ν_p, is send through an optically nonlinear crystal placed in an optical resonator formed by the mirros M1 and M2. The nonlinear crystal is selected for providing significant second order dielectric susceptibility, $\chi^{(2)} \neq 0$, which enables so-called three-wave-mixing processes [59]. As a result, the pump wave traveling through the crystal provides gain for two lower frequencies, ν_s and ν_i, which are named the signal and idler wave. Traditionally, the term signal wave refers to the higher frequency and idler wave to the lower frequency wave. The output frequencies satisfy the following condition, which can be seen as a photon-wise energy conservation law:

$$\nu_p = \nu_s + \nu_i. \tag{2.1}$$

The gain provided by the pump wave for the signal and idler waves means that a weak signal (or idler) wave traveling through the crystal will be amplified while the power of the pump wave is reduced. Simultaneously, some of the pump power is also transferred to the idler (or signal) wave. Due to the existence of vacuum fluctuations, there is always a minute signal and idler wave present in the crystal, even if only the pump laser beam is injected. By placing the nonlinear crystal inside a resonator for the signal wave, the signal wave is fed back into the crystal where it is further amplified through power transfer from the pump wave.

The gain increases with the intensity of the pump wave, and as a consequence, there is a minimum pump intensity at which the amplification of the signal wave in the crystal compensates for the round trip losses in the resonator (due to mirror transmission, absorption and scattering). At this threshold pump intensity, optical parametric oscillation sets in, i.e. a periodically oscillating signal wave is generated from an (initially) random (vacuum) field fluctuation. At the same time, a significant portion of the pump power is converted into signal and idler power. This transfer of power from the pump wave to the generated waves reduces the (spatial average) pump intensity inside the nonlinear crystal and thus the signal gain. In close analogy to the case of laser oscillation, this effect is called "gain saturation". It leads to steady-state operation of the OPO, where the signal power generated inside the crystal exactly balances the resonator losses for the signal wave.

2.1.2 Frequency selection in OPOs

While equation 2.1 states that the sum-frequency of a signal and idler wave pair is equal to the pump frequency, it does not determine which of all possible signal-idler frequency pairs will actually be generated. In steady-state operation, the signal and idler frequency pair is generated which has a minimum threshold pump intensity (in analogy to a laser with spectrally broadened gain). Thus, the generated frequencies, and with them the *ratio* of the signal and idler frequency, are determined by the frequency dependence of the parametric gain in the crystal and by the frequency dependence of the resonator losses. In general, the parametric gain in the crystal provides only a coarse selection of the frequency ranges of the signal and idler wave, whereas the exact frequencies are given by the frequency selectiv-

ity of the OPO resonator. Both will be discussed qualitatively in the following sections.

Frequency selection by the nonlinear crystal - Phase-matching and quasi-phase-matching

At each spot along the path of the pump wave through the crystal, the nonlinear susceptibility results in local polarization oscillations (i.e. periodic motion of crystal electrons) at the signal and idler frequencies. Along the entire crystal length, the superposition of the electromagnetic "wavelets" radiated off these local oscillations forms the signal and idler waves. Thus, the generation of the signal and idler wave is most efficient, if the local electromagnetic "wavelets" are in phase with radiation from other spots, such that they constructively interfere with each other along the direction defined by the pump field.

A rigorous mathematical treatment of parametric amplification (see e.g. [59] or [60]) reveals that the sum of the phases of the local oscillations at the signal and idler frequency is given by the local phase of the pump wave. As the local phases of the three waves are given by the k-vectors, $\vec{k_x}$, in the crystal, strongest interaction of the three waves will occur, if

$$\vec{k_p} = \vec{k_s} + \vec{k_i}. \tag{2.2}$$

Equation 2.2 is known as phase matching condition for optical parametric amplification/oscillation. For the case of collinear interaction of the three beams, where

$$|\vec{k_x}| = \frac{2\pi\nu_x n_x}{c}, \tag{2.3}$$

the phase matching condition can be written as a scalar equation

$$n_p\nu_p = n_s\nu_s + n_i\nu_i, \tag{2.4}$$

where n_p, n_s, n_i denote the refractive indices for the pump, the signal and the idler waves. It is obvious that in the case of normal dispersion, where $n_p > n_s > n_i$, Eqs. 2.1 and 2.4 cannot be fulfilled simultaneously. However, most crystals with non-zero $\chi^{(2)}$ susceptibility are also birefringent [61], and by choosing different polarizations of the three waves (with respect to the crystal axis) and an appropriate propagation direction, the phase-matching condition may be fulfilled

for certain frequency combinations. This type of phase-matching is often referred to as birefrigent phase-matching (BPM).

For signal and idler pairs with small phase-mismatch (i.e. $\Delta k = k_p - k_s - k_i \neq 0$, but small), the constructive interference along the entire crystal length is not perfect. As a result, such signal and idler frequencies have a lower parametric gain of their intensities, as compared to perfect phase matching. The decrease of the gain with increasing Δk is given by

$$\text{gain} \sim \text{sinc}^2(\Delta k L_C) \equiv \frac{\sin^2(\Delta k L_C)}{(\Delta k L_C)^2}, \tag{2.5}$$

where L_C is the length of the nonlinear crystal. For wavelengths with $\Delta k \neq 0$, the threshold pump intensity is higher as compared to a phase-matched frequency pair (assuming identical resonator losses). Therefore, an OPO tends to operate at signal and idler frequencies for which $|\Delta k|$ is minimum. By changing the refractive indices for the three waves, for example, by changing the crystal temperature or the direction of the beams through the crystal, this condition can be fulfilled for different frequency combinations, and it allows, within certain limits, to tune the output frequencies of an OPO.

It is known that a powerful alternative to exploiting the birefringence for achieving phase-matching, is so-called quasi-phase matching (QPM) [62]. Because of the advantages it offers, for all of the experiments described in this thesis we decided to use QPM crystals for optical parametric oscillation. With QPM, a special microstructuring of the crystal results in an effective compensation of the phase-mismatch. In its most basic implementation, the crystal is periodically poled, i.e., it consists of alternating sections with opposite orientation of the crystal axis. While this does not affect the linear refractive indices of the waves (and thus their k-vectors), the phase of the local polarization oscillations induced by the pump wave via the $\chi^{(2)}$ susceptibility is different by π in adjacent crystal sections. By choosing a suitable spatial poling period Λ (often called the grating period) according to

$$\Lambda = \frac{2\pi}{\Delta k} \tag{2.6}$$

(in which $\Delta k \neq 0$ is the remaining mismatch due to the dispersion of the crystal), the periodic phase jumps ensure that the waves generated by the local polarization are *in average* in phase with the waves generated at other locations along the beam

path. Constructive interference of the generated waves along the entire crystal length is thus approximately achieved. For QPM processes, the dependence of the parametric gain on the wavelengths of the interacting waves is expressed by the same formula Eq. 2.5 as for birefringent phase matching, if the phase-mismatch is replaced by an effective phase-mismatch $\Delta k'$, that is given by [63]:

$$\Delta k' = 2\pi \left(n_p \nu_p - n_s \nu_s - n_i \nu_i - 1/\Lambda \right). \tag{2.7}$$

Particularly for OPOs, quasi-phase matching has several important advantages over birefringent phase matching: Firstly, QPM can be achieved basically for any signal and idler wavelength pair, and is not limited by the natural birefringence of suitable nonlinear crystals. Secondly, QPM gives access to the highest nonlinear coefficient (usually found with parallel polarizations of all three waves), which results in highest output powers and conversion efficiencies [51] and in lowest OPO threshold intensities. Note that an OPO with a threshold as low as 60 μW was realized in our former work [64]. Furthermore, QPM allows one to design crystals which provide simultaneous phase matching of several *different* frequency conversion processes on one crystal. This can be exploited for realizing cascaded nonlinear frequency conversion devices based on a single crystal [65]. Finally, using QPM, the shape of the phase-matching curve, i.e., the parametric gain as a function of the phase-mismatch, can be designed. This can be used to influence the temporal [66] and spectral [67], [68] properties of light during frequency conversion.

As with BPM, an OPO based on QPM will tend to operate at a signal/idler frequency combination which provides highest parametric gain in the nonlinear crystal and thus lowest pump threshold intensity, which corresponds to minimum $|\Delta k'|$. With QPM based OPOs, tuning of the generated signal and idler frequencies is often achieved by changing the temperature of the nonlinear crystal (and thus the refractive indices for all waves), or by switching to another grating period which may be fabricated on the same crystal. The bandwidth of the parametric gain, which is defined as the full-width at half-maximum of the sinc^2-function Eq. 2.5 as a function of the signal frequency detuning from the (quasi-)phase-matched center frequency, can vary between a few tens of GHz and several tens of THz for cw OPOs based on BPM or QPM. Within this relatively wide bandwidth, the exact oscillation frequencies of the signal and idler wave are often determined by the frequency selective losses of the OPO resonator elements.

Frequency selection by the OPO resonator

In general, the optical cavity in which the OPO crystal is placed provides resonant feedback for the signal and idler wave. Here, we want to assume the simplest case of a singly-resonant OPO (SRO), where the cavity mirrors are only reflective for one of the generated waves, let's say the signal wave.

Resonant feedback implies that the phase of the resonant wave at any location in the cavity reproduces after one cavity roundtrip. This means that the optical path length L_{opt} corresponding to one cavity roundtrip is identical to an integer multiple N of the wavelength of the resonant signal wave, $\lambda_s = c/\nu_s$, where c is the vacuum speed of light: $L_{opt} = N\lambda_s$.

This resonance condition defines a grid of signal frequencies, corresponding to the well-known longitudinal modes of the OPO cavity. Not taking into account any dispersion in the OPO cavity, the frequencies of the cavity modes are equidistant, and the frequency difference of adjacent modes is called the free spectral range (FSR) of the cavity:

$$FSR = \frac{c}{L_{opt}}. \tag{2.8}$$

For cw OPOs with a cavity length of a few cm, the FSR is typically between several hundred MHz and a few GHz. For an ideal OPO resonator with precisely zero roundtrip losses, the OPO can only oscillate at signal frequencies which are exactly on the grid of the longitudinal modes. In reality, an OPO resonator has always non-zero roundtrip losses due to mirror transmission, absorption and scattering in the crystal, etc. As a consequence, the resonator provides also feedback a signal frequencies that are slightly off the center frequencies defined by the grid. The frequency bandwidth $\Delta\nu_{s,cav}$ of a cavity mode of a real OPO signal resonator is given by [69]

$$\Delta\nu_{s,cav} = \frac{FSR}{F_s}, \tag{2.9}$$

where F_s is the so-called finesse of the OPO resonator for the signal wave. The cavity finesse is given as $F_s = 2\pi/\gamma$, where γ is the power loss per roundtrip [69]. For cw OPOs, this bandwidth is typically between a few and about 100 MHz. The bandwidth of the OPO cavity mode is not to be confused with the actual frequency bandwidth of the OPO signal wave, which is usually much smaller than

the bandwidth of the cavity mode. This is why the latter one is often referred to as the cold-cavity bandwidth.

Assuming that the OPO cavity finesse is constant for a wide range of signal frequencies, the OPO will operate at a signal frequency (and an idler frequency), which lies in the cavity mode closest to the peak of the parametric gain bandwidth. The situation is very similar to the laser oscillation that occurs at the peak of a spectrally broadened laser gain curve.

Note that the frequency selection in a so-called doubly-resonant OPO (DRO), where both the signal and the idler wave are resonated, is much more complicated. This is because signal/idler frequency pairs that fulfill the energy conservation condition Eq. 2.1 do not necessarily correspond simultaneously to a pair of signal and idler cavity modes. A full discussion of the implications e.g. for the stability and tuning of the OPO frequencies is beyond the scope of this introduction, but further details can be found in chapter 5.6.

In summary, this section gave an introduction to the basic operation principles of OPOs, explaining important terms such as parametric gain, (quasi-)phase-matching and cavity modes. Parameters such as the parametric gain bandwidth, and the cavity free spectral range and finesse, which are essential for the frequency selection process in OPOs were defined.

2.2 Phase-coherent frequency dividers based on cw OPOs

Recently, a phase-coherent link between the current primary international time standard, the Cs atomic clock, and optical frequencies in the visible and near infrared range has been realized by using a cw mode-locked laser followed by wide-band optical comb generation in a nonlinear fiber [70]. The comb allows one to measure basically any visible and near-infrared optical frequency with the absolute precision of the international frequency standard. This fulfills one precondition for the future implementation of a new international time and frequency standard that will be several orders of magnitude more accurate than the current Cs standard. The new frequency standard will be based on the much higher absolute frequency of an atomic transition in the optical or ultra-violet wavelength range. Due to the phase-coherent link between the existing standard and the new standard, all measurements based on the existing standard can be transferred to

the new standard with the maximum accuracy possible.

The above cited work bridges a huge frequency gap of about 6 orders of magnitude between the Cs standard and a future standard. However, the method does actually not cover the entire frequency range *in between* the current standard and the new standard in the visible. Even when a new optical frequency standard becomes reality, the entire mid-infrared and far-infrared wavelength range will still remain extremely difficult to access with conventional phase-coherent frequency links. In particular, the mid-infrared wavelength range with frequencies from about $5 \cdot 10^{12}$ to $1.5 \cdot 10^{14}$ Hz is of high practical importance due to the molecular vibrational transitions in this range. Therefore, the development of practical and reliable phase-coherent links is imperative for fundamental research, technical and life-science applications.

In order to measure with the precision of the frequency standard any unknown optical frequency that is further in the infrared than e.g. the above mentioned frequency comb, subsequent steps of phase-coherent frequency division are required.

Phase-coherent frequency dividers are based on division by factors that are either exact (small) integer numbers, such as 2 or 3, or very close to such integer numbers, because this facilitates a control of the phase-coherence.

Continuous-wave optical parametric oscillators are ideal for the realization of phase-coherent frequency dividers with such small divider ratios to link mid-infrared wavelengths to a visible frequency standard. It has been shown that the OPO idler wave can be phase-locked to precisely one-half or one-third of the pump laser frequency, using electronic [71] [72] and all-optical [73] locking techniques. In our previous work we have also demonstrated the first all-optical frequency by-3 divider [65].

In an OPO, the phase sum $\varphi_s + \varphi_i$ of the idler and signal waves adiabatically follows the pump phase, whereas the phase difference $\varphi_s - \varphi_i$ undergoes a diffusion process [38]. In order to achieve phase-coherent frequency division, this diffusion has to be suppressed by some phase locking mechanism. The residual variance of the phase difference then determines the divider's stability. This stability, i.e., the deviation of the idler frequency from the exactly divided pump frequency, characterizes the precision of the frequency division.

CW OPOs offer many advantageous properties, which make them promising candidates for phase-coherent frequency division. One advantage is their potential for a very narrow bandwidth [74], which is one precondition for cw OPOs being

used for the realization of frequency-dividers [37].

The second advantage of OPOs is their high conversion efficiency, which provides orders of magnitude higher powers at the new wavelength than other frequency dividers (typically mW rather than nW). This results in shorter averaging times for any frequency comparison and phase-locking, and thus a higher frequency stability in the corresponding range.

A third advantage of OPOs is their wavelength flexibility: In principle, any optical frequency from a pump laser can be divided phase-coherently. In practice, this becomes possible by the availability of quasi-phase matching crystals that can be designed for this purpose.

There are two ways in how to achieve the required phase coherence of the idler with respect to the pump field oscillation (and thus of the division by an integer number): Either by an electronic or by an optical phase control of the OPO fields. For a comparison, both methods will be reviewed in the following sections.

2.2.1 OPO frequency dividers with electronic phase locking

In the case of an electronic control, the frequency and phase difference between the signal and idler waves needs first to be determined via a beat measurement which generates a RF error signal, if the signal and idler frequencies are sufficiently close to each other. The electronic error signal can then be used to control the OPO frequencies and phases via a tuning element in the OPO setup, such as a piezo electric transducer controlling the OPO cavity length. For a division by 2, based on an OPO tuned close to degeneracy, a RF error signal can readily be achieved by directly beating the two subharmonic waves with each other. Electronically controlled phase locking of the beat frequency between the subharmonic waves of an OPO to a microwave reference frequency source has been demonstrated with a beat-note linewidth at the Hertz-level [71]. Electronically controlled division by 3 is more involved, because the idler wave needs first to be frequency-doubled before a beat with the signal wave can be measured in the RF range. By externally frequency-doubling the idler wave, a frequency division by three has been demonstrated using a doubled Nd:YAG laser and thereby generating four frequencies with the exact ratio 6:4:3:2 [75], as well as by dividing the frequency of a tunable diode laser [72].

A major disadvantage of electronically phase-locked frequency division is a slow response time. This has two main reason: Firstly, the power of the beat signal is

low, such that the RF error signal needs to be averaged over milliseconds to seconds for a sufficiently high signal-to-noise ratio in the feedback loop. And secondly, the piezo-electric transducer used to control the cavity length and thus the divider phase is limited to response times of typically 0.1 to 1 ms. The slow response of electronic locking limits the phase-stability of the divider, because phase-shifting external perturbations on time-scales of milliseconds and shorter, as caused e.g. by acoustic vibrations, cannot be compensated.

An all-optical phase locking does not suffer from these restrictions. It rather offers a response as fast as the inverse bandwidth of the OPO's cold cavity modes, which is in the order of tens of nanoseconds. An overview over the working principle and recent achievements of all-optically phase-locked frequency dividers based on cw OPOs is given in the following section.

2.2.2 OPO frequency dividers with all-optical phase locking

To control the phases of an OPO divider with all-optical methods, one of the output waves is phase-locked by injecting another optical wave, similar to injection locking of lasers [39]. If the injected wave is generated by the OPO itself, the method may be termed self-phase locking. All-optical frequency division by 3 through self-phase locking has been demonstrated in our previous work with a cw OPO. Here the signal wave is injection-locked through the intracavity frequency-doubled idler wave [76], [77]. Measurements of the locking range of the self-phase-locked by-3 divider OPO and of its fractional frequency instability have been presented recently in Ref. [65]. A theoretical model has been developed and numerically evaluated by Zondy and colleagues to analyze the steady-state and dynamics of signal and idler resonant by-3 divider OPO [78] as well as of a signal and pump resonant by-3 divider OPO [79].

The most fundamental example for such self-phase locking is a frequency-degenerate, type-I phase-matched cw OPO. Here, the subharmonic waves' polarizations are parallel, such that the signal wave phase-locks the idler wave and vice versa. Such self-phase locking has been demonstrated qualitatively by Nabors et al. [80]. However, a type-I phase-matched OPO near degeneracy usually reveals an enormously wide bandwidth and other severe tuning difficulties, as observed in Refs. [80] and [71]. A more favorable alternative is frequency division by 2 using a type-II phase-matched cw OPO.

Self-phase locking with a type-II phase-matched cw OPO, i.e. with orthogo-

nally polarized subharmonic waves, can be achieved by introducing a wave plate in the OPO cavity, as shown by Mason and Wong [73]. However, the concept of their OPO and its pump source was not wavelength-tunable, and they did not further specify the frequency stability or phase properties. In the current work, we present the first wavelength-flexible type-II phase-matched frequency-by-2-divider. A first measurement of a by-2-divider's frequency stability has been published in our previous work [81]. In this thesis, we also present the first quantitative measurement of a divider's optical phase and compare it to theory.

The self-phase-locked by-2-divider has been theoretically described by Fabre et al. [40]. In our theoretical investigations presented in the following chapter 3, we follow and extend these calculations to make them applicable for comparison with an experiment. In addition, we present the first stability analysis applied to the steady-state solutions of the divider OPO, which shows that, unlike previously expected, only one single threshold state should be observable in the experiment. We also present the first theoretical derivation of the frequency stability of such a self-phase-locked by-2-divider OPO.

In order to gain insight also in the dynamical properties of self-phase locking in by-2-divider OPOs, which is not possible with the analytical steady-state models, we completed the theoretical considerations by a numerical analysis. In this thesis, the novel results of such a numerical analysis are presented in chapter 4. In contrast to the steady state analysis, a rich scenario of phase dynamics is revealed, which can be expected to provide considerable inspiration for future experimental investigations.

Chapter 3

Theoretical Analysis

For an accurate, all-optical frequency division by 2, the OPO subharmonic frequencies should oscillate at the same frequency and thus at exactly one-half of the pump frequency. An all-optical method of phase locking has to provide a constant phase relation of the three waves. In the following section 3.1, the working principle of self-phase locking in the type-II phase-matched by-2-divider OPO used is briefly described in a phenomenological way. In the next section 3.2, the coupled field equations describing the three wave interaction process in the OPO are introduced and their parameters explained. The coupled field equations are solved analytically in the steady-state regime in the section 3.3. Conditions for self-phase-locked oscillation and corresponding expressions for the phase eigenvalues of the locked fields are derived.

In the self-phase-locked case, one obtains two different values for the pump power at threshold, which is described in section 3.4. Section 3.5 contains a stability analysis applied to the frequency by-2-divider to investigate the stability of these two solutions. A quantitative prediction for the locking-range in section 3.6 takes into account a temperature drift as the major mechanism disturbing the self-phase-locked state.

In section 3.7, the phases of the output waves are derived, and in section 3.8 phase instabilities induced by the experimentally observed temperature drift are taken into account to derive the divider's fractional frequency stability.

3.1 Self-injection locking of cw-OPOs

The basic concept for optical self-phase locking is injection locking of a cw OPO by an optical wave whose frequency is close to one of the subharmonic waves, similar to the injection locking of lasers [39]. In the current work on frequency division by 2, we use a cw OPO where one of the subharmonic waves is directly injection-locked by the other subharmonic wave and vice versa. The schematic setup of the cw-OPO used for exact division of the pump frequency by 2 is shown in the upper part of Fig. 3.1, while the lower part shows a corresponding frequency scheme of the locking process.

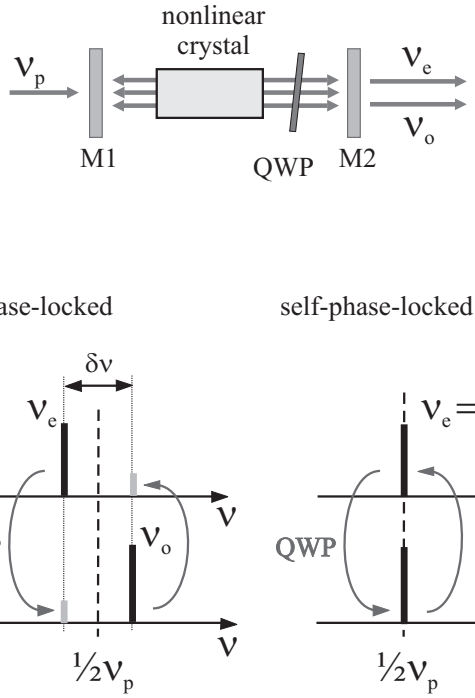

Figure 3.1: Upper part: Schematic setup of an OPO with intracavity quarter-wave plate (QWP) for division of the pump frequency ν_p by 2; M1, M2: cavity mirrors, ν_p, ν_e, ν_o: frequencies of the pump, the e- and the o-wave, respectively. Lower part: Frequency diagram of the self-phase locking process. For details see text.

The OPO consists of a nonlinear crystal in a linear two-mirror cavity. Further details on the crystal will be given in section 5.2. The cavity is assumed to be resonant for the pump wave and for the two OPO subharmonic waves. The nonlinear crystal provides type-II phase matching of the OPO process, so that it converts the ordinary polarized pump wave with frequency ω_p into two subharmonic waves with approximately half the pump frequency, but with orthogonal linear polarizations. The o-wave has its polarization parallel to the pump wave, and the e-wave has its polarization perpendicular to the pump and the o-wave. To enable self-phase locking of the divider OPO, the cavity is equipped with a quarter-wave plate which introduces a polarization rotation and thus mutual injection of the two independent subharmonic waves into each other.

The diagram in the lower part of Fig. 3.1 illustrates the working principle of self-phase locking. Here, the modes of the two subharmonic waves are displayed as a function of frequency. For clarity, the modes of the two independent waves are plotted above each other, the extraordinary polarized wave on the upper axis, the ordinary polarized wave on the lower axis. Via the quarter-wave plate, a small amount of each wave is transferred (rotated and projected) to the other polarization state, which enables mutual injection. We define the difference between the two light frequencies as $\delta\nu = \nu_e - \nu_o$.

If the frequency difference $\delta\nu$ is adjusted by tuning the phase-matching wavelengths and the cavity length of the OPO, such that $\delta\nu$ becomes smaller than a characteristic frequency difference $\delta\nu_{lock}$, i.e. $|\delta\nu| = |\nu_e - \nu_o| \leq \delta\nu_{lock}$, one expects injection locking of the e-wave by the o-wave and vice versa. The full interval, $2\delta\nu_{lock}$, within which injection locking can occur, is called the locking range.

This injection locking of the OPO waves is analogous to the well-known injection locking of lasers [39]. In a laser injection locking occurs if the frequencies of the injected wave and the free running wave of an oscillator lie within the locking range. In this case the free running wave assumes precisely the frequency of the injected wave. The same should occur in an OPO, with the difference that, in the considered OPO-injection locking, both waves are generated by the same process, namely optical parametric oscillation. This situation can thus be termed self-injection locking. In the case that the e-wave is injection-locked by the o-wave and vice versa, the pump, the e- and the o-wave should oscillate with the exact frequency ratio of 2:1:1. This situation is depicted in the right diagram in the lower part of Fig. 3.1, where the e- and the o-wave frequency equal each other and

thus exactly one-half of the pump frequency: $\nu_e = \nu_o = \frac{1}{2}\nu_p$.

If the free running wave of a laser is injection-locked, also its phase is determined with respect to the phase of the injected wave, i.e., both waves oscillate phase-coherently. A similar effect should be observed for a self-injection-locked OPO: Without locking, the phases φ_e and φ_o of the e- and the o-wave are free with respect to each other. Only their sum is determined by the phase of the pump wave [38]. When the OPO waves are self-injection-locked, however, their phase difference $\varphi_e - \varphi_o$ is determined as well. Therefore, the three OPO waves oscillate in phase with each other, and the frequency division of the pump laser can be called phase-coherent.

In the following, we start from the coupled wave equations of an OPO with intracavity quarter-wave plate, to derive analytically the steady-state solutions of the self-phase-locked by-2-divider OPO. Our approach follows an earlier theoretical description of such a system by Fabre and colleagues [40]. However, the theoretical description presented in the following chapter 3 is carried a few steps further in several aspects. The steady-state operation parameters of the self-phase-locked OPO are determined as a function of the actual experimental parameters and, for the first time, a stability analysis is applied to the solutions. A thorough consideration of the tuning properties enables a direct comparison with the experiment. Specifically, an estimate of the measurable locking range as a function of the quarter-wave plate rotation angle is given and compared with the experimental results. For the first time, the divider's frequency stability is determined by considering temporal phase instabilities. The analytical calculations are completed by a numerical evaluation presented in chapter 4. The investigation the three OPO fields' evolution with time serves as a confirmation of the analytical calculations, and in addition allows a deeper insight and understanding into the process of self-phase-locked frequency division.

3.2 Coupled field equations

The nonlinear wave mixing processes in the OPO can be described in the mean-field, plane-wave approximation by three coupled equations for the OPO internal electric field $q(t) = q_p(t)e^{i\Omega_p t} + q_e(t)e^{i\Omega_e t} + q_o(t)e^{i\Omega_o t}$. The carrier frequencies Ω_p, Ω_e and Ω_o are chosen such that $\Omega_e = \Omega_o = \frac{\Omega_p}{2}$. If the OPO frequencies are close to the given carrier frequencies of an exact divider, the amplitudes q_p, q_e and

q_o are slowly varying with time. If, for example, these amplitudes oscillate as a function of time, their oscillation frequencies are the frequency deviations of the OPO fields from the carrier frequencies, i.e., the frequency deviation from exact division by 2. We choose $\Omega_p \equiv 2\pi\nu_p$, such that the carrier frequencies Ω_p, Ω_e and Ω_o are determined by the pump laser frequency ν_p. The coupled equations for the field amplitudes can then be written as follows [82]:

$$\begin{aligned} \frac{d}{dt}q_p &= -\frac{1}{2}\kappa_p q_p + iDq_e q_o + F \\ \frac{d}{dt}q_e &= -\frac{1}{2}\left(\kappa_e - i\Delta_e\right)q_e + iDq_o^* q_p + \gamma q_o \\ \frac{d}{dt}q_o &= -\frac{1}{2}\left(\kappa_o - i\Delta_o\right)q_o + iDq_p q_e^* - \gamma^* q_e. \end{aligned} \tag{3.1}$$

The field amplitudes q_x are normalized such that the squares of their absolute values give the intracavity photon numbers $N_x = |q_x|^2$ [82], where the indices $x = p, e, o$ designate the pump wave, the e- and the o-wave, respectively.

The first terms on the right hand side (RHS) of Eqs. 3.1 describe the decay of the field amplitudes due to resonator losses. The cavity decay rates are given by

$$\kappa_x = FSR_x \cdot |ln\left[\left(1 - T_x1\right)\left(1 - T_x2\right)\left(1 - A_x\right)^2\right]|, \tag{3.2}$$

where T_x1 is the power transmission of the input mirror M1 and where T_x2 is that of the output mirror M2 (see upper part of Fig. 3.1). A_x is the single-pass power loss caused e.g., by scattering and absorption at the mirrors and the crystal.

The free spectral range of the cavity is given by

$$FSR_x = \frac{c_0}{2\left(L_{cav} + L_{cr} \cdot (n_x - 1)\right)} \tag{3.3}$$

where c_0 is the vacuum velocity of light, L_{cav} and L_{cr} are the geometrical length of the cavity and of the nonlinear crystal, respectively, and where n_x are the refractive index of the crystal for each of the three waves. Note that due to dispersion in the crystal, $n_p \neq n_e \neq n_o$, such that the free spectral range (FSR) is different for each of the three waves.

The last term in the first Eq. 3.1, F, describes the pumping of the OPO with the external laser that is to be frequency divided. F is proportional to the square

root of the pump laser power P_p times the pump input transmission of the cavity mirror M1: $F^2 = \frac{c_0}{2L_{cav}} T_p 1 \frac{P_p}{\hbar\omega_p}$.

The terms containing the nonlinear coupling coefficient D give the strength of nonlinear interaction of the pump, the e- and the o-wave. The value of D depends on construction parameters of the OPO and the involved light frequencies. If the crystal provides phase matching, the nonlinear coupling coefficient is given by

$$D = \frac{d_{eff}}{4 n_p n_e n_o} \sqrt{\frac{2\hbar}{\epsilon_0 V_c} \omega_p \omega_e \omega_o} \frac{L_c}{L_{cav}}, \tag{3.4}$$

where d_{eff} is the effective nonlinear coefficient of the crystal, V the volume of the nonlinear interaction in the crystal, and n_x the refractive indices.

The values of Δ_e and Δ_o give the detunings of the OPO's cold cavity modes from exact division by 2. A zero detuning of the pump cavity from the pump frequency, i.e. $\Delta_p = 0$, is assumed. When comparing the theoretical description derived here with the experiment this assumption is well-justified, because the pump cavity length is electronically locked to the pump laser wavelength. The subharmonic waves are assumed to oscillate in the cavity modes which are closest to frequency degeneracy. How this can be achieved in the experiment is described in detail in section 5.6.

To illustrate the definition of the cavity detunings, they are depicted schematically in Fig. 3.2 for the case that the OPO is not phase-locked (Fig. 3.2a) and for the case that the OPO is phase-locked (Fig. 3.2b). The cavity modes are shown as the Lorentzian-like curves as a function of frequency. As the refractive indices of the crystal depend on the polarization of an optical wave, the resonator length and thus also the frequencies of the cavity modes are different for the e-wave and the o-wave. For an easier discussion, these two line-shapes are plotted separately above each other, such that the e-wave frequency increases to the right (upper part), while the o-wave frequency increases to the left (lower part). The two axes are positioned relative to each other such that at any arbitrary vertical line (such as the dashed or the solid lines in Fig. 3.2) the sum of the frequencies at the intersection points gives the pump frequency. Thus, two frequencies (marked as thick lines) belonging to any e-o-wave-pair that is allowed by the energy conservation condition according to Eq. 2.1 lie precisely above each other. Pairs of e-o-frequencies lying not precisely above each other violate this energy conservation condition.

The two cases of not phase-locked and phase-locked operation of the OPO

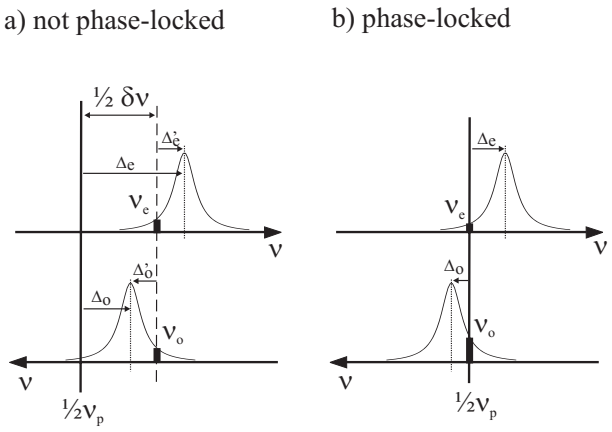

Figure 3.2: Definition of the cavity detunings Δ_e and Δ_o, a) for the case where the OPO is not phase-locked, and b) for the case where the OPO is phase-locked. The line shape of the cavity modes and the light frequencies of the e-wave (upper axis) and of the o-wave (lower axis) are plotted as a function of frequency: from left to right, the e-wave frequency increases, while the o-wave frequency decreases. The cavity detunings Δ_e and Δ_o are given by the distances between half the pump frequency and the nearest cavity modes, whereas the lightfield detunings Δ'_e and Δ'_o are given by the distances between the light frequencies and the cavity modes.

are two completely different modes of oscillation, and one has to clearly distinguish between these two states. Figure 3.2a illustrates the cavity detunings in the not-phase-locked state. In this case, for operation with minimum pump power at threshold, the OPO will adjust its frequencies to minimize the cavity losses. This is achieved, if the *product* of the e- and o-lineshape functions is maximum, corresponding to the product of the lengths of the two thick lines representing the e- and o-frequencies. From Fig. 3.2a it can be seen, that this corresponds to oscillation at light frequencies $\nu_e = \frac{1}{2}\nu_p + \frac{1}{2}\delta\nu$, and $\nu_o = \frac{1}{2}\nu_p - \frac{1}{2}\delta\nu$, where $\delta\nu$ is the frequency difference between the e- and the o-wave. We define the corresponding lightfield detuning of the light frequencies from the cavity modes as Δ'_e and Δ'_o. It can be shown [82], that in steady-state the light fields of a "free-running" OPO, i.e. without injection locking, adjust to specific values of lightfield detunings, given by the relative roundtrip losses, i.e.:

$$\frac{\Delta'_e}{\Delta'_o} = \frac{\kappa_e}{\kappa_o}. \tag{3.5}$$

Note, that this spectral behavior includes the sign of the detunings. For example, in Fig. 3.2a the detunings Δ'_e and Δ'_o are both positive, such that (due to the positive κ_e and κ_o) the sign of the detunings is equal. In contrast, the condition of Eq. 3.5 is not valid any more when the OPO is phase-locked, which is depicted in Fig. 3.2b. Instead, the frequencies of the e-wave and the o-wave are both exactly half of the pump frequency, and the lightfield detunings Δ'_e and Δ'_o are given simply by the cavity detunings Δ_e and Δ_o.

The last terms on the RHS of the second and third Eqs. 3.1 describes the mutual injection of the two OPO subharmonic fields introduced by the intracavity quarter-wave plate. The parameter γ is a measure for the injection (coupling) strength and is proportional to the experimentally adjustable angle of the QWP's fast axis, as will be explained in section 3.3 in more detail.

The coupled field equations can be solved for two very different regimes. First, there is the regime where the frequency difference between the e-wave and the o-wave frequency is larger than the so-called locking range, i.e., $|\delta\nu| > \delta\nu_{lock}$ (for a derivation of $\delta\nu_{lock}$ see section 3.6). In this case, the solutions for the field envelopes in Eqs. 3.1 ($q_e(t), q_o(t)$) will not be constant field amplitudes but, for example, an oscillatory function of time. In this case, the total electric field, $A_{e,o}(t) = q_{e,o}(t) \cdot e^{2\pi i \frac{\nu_p}{2} t}$, contains optical sidebands, which corresponds to Fig. 3.2a, where phase locking is absent.

In the second regime, where the frequency difference $\delta\nu$ between the e- and the o-wave is smaller than the locking range, i.e., $|\delta\nu| \leq \delta\nu_{lock}$, the solutions of Eqs. 3.1 will be time independent, constant field amplitudes. The solutions then attain the form $A_e(t) = A_e^0 \cdot e^{2\pi i \frac{\nu_p}{2} t + \varphi_e^0}$ and $A_o(t) = A_o^0 \cdot e^{2\pi i \frac{\nu_p}{2} t + \varphi_o^0}$. In this case, the e- and the o-waves will be oscillating with constant relative phases (phase-locked) and the OPO works as a phase-coherent frequency divider. To quantify these qualitative considerations, the coupled field equations are solved analytically in the steady-state regime in the following sections. There, conditions for self-phase-locked oscillation and corresponding expressions for the phase eigenvalues of the locked fields are derived.

3.3 Steady-state solution

In this section, the nonlinear coupled equations 3.1 are solved for the case of phase-locked operation. The cavity detunings Δ_e and Δ_o are experimental parameters, which can be continuously varied in the setup. The other construction parameters of the OPO, such as the cavity losses and the crystal's nonlinear coefficient, are fixed and can be derived from the experimental setup in independent measurements. The parameter for the coupling strength between the two OPO subharmonic waves, γ, is also treated as a constant parameter. In a particular locking experiment, it can be set to an arbitrary value, and then remains constant during the experiment.

For the following calculations, we use the last two equations of 3.1 and consider steady-state conditions, i.e., zero time derivatives on the LHS of Eqs. 3.1. One then obtains four linear coupled equations for q_e and q_o, and for their complex conjugates q_e^* and q_o^*:

$$\begin{pmatrix} -\frac{1}{2}(\kappa_e - i\Delta_e) & \gamma & 0 & iDq_p \\ -\gamma^* & -\frac{1}{2}(\kappa_o - i\Delta_o) & iDq_p & 0 \\ 0 & -iDq_p^* & -\frac{1}{2}(\kappa_e + i\Delta_e) & \gamma^* \\ -iDq_p^* & 0 & -\gamma & -\frac{1}{2}(\kappa_o + i\Delta_o) \end{pmatrix} \times \begin{pmatrix} q_e \\ q_o \\ q_e^* \\ q_o^* \end{pmatrix} = \begin{pmatrix} 0 \\ 0 \\ 0 \\ 0 \end{pmatrix} \tag{3.6}$$

This equation has non-zero electric field solutions only if the determinant of the matrix on the LHS is zero. To calculate the determinant, the complex field amplitudes q_x are separated into real positive amplitudes b_x and real phases φ_x by setting $q_x = b_x e^{i\varphi_x}$, and the complex coupling parameter γ is separated into the real amplitude γ_0 and the real phase θ by $\gamma = \gamma_0 e^{i\theta}$. With this separation, we follow the earlier publication of Fabre [40]. The coupling strength is proportional to the part of the e-wave and the o-wave, which is transferred to the other polarization state, and is given by:

$$\gamma_0 = \sin(2\vartheta_{QWP}) \cdot \sqrt{\kappa_e \kappa_o}. \tag{3.7}$$

The projected and injected portion of each beam is proportional to the sine of two times the QWP rotation angle ϑ_{QWP}, because in our setup the QWP is passed twice per round trip. The normalization factor $\sqrt{\kappa_e \kappa_o}$ is chosen in accordance with Ref. [40]. The phase θ takes into account a propagational phase shift that

the waves acquire while traveling through the quarter-wave plate. Calculating the determinant yields the following quartic equation:

$$\begin{aligned} D^4 b_p^4 &- \frac{1}{2} D^2 b_p^2 \left(\kappa_e \kappa_o + \Delta_e \Delta_o + 4\gamma_0^2\right) + \gamma_0^4 \\ &+ \frac{1}{2}\gamma_0^2 \left(\kappa_e \kappa_o - \Delta_e \Delta_o\right) + \frac{1}{16}\left(\Delta_e + \kappa_e\right)\left(\Delta_o + \kappa_o\right) = 0 \end{aligned} \tag{3.8}$$

By taking the square root of this equation, one obtains a quadratic expression, which is a condition for self-phase-locked operation:

$$D^2 b_p^2 = \gamma_0^2 + \frac{1}{4}\kappa_e \kappa_o + \frac{1}{4}\Delta_e \Delta_o \pm \sqrt{\alpha} \tag{3.9}$$

where the abbreviation α is defined as

$$\alpha = 16\gamma_0^2 \Delta_e \Delta_o - \left(\Delta_e \kappa_o - \Delta_o \kappa_e\right)^2 . \tag{3.10}$$

Except for the expression for α, all terms of Eq. 3.9 are real, the term b_p^2 on the LHS of the equation is even a directly measurable quantity, as it is equal to the intracavity pump photon number. Therefore the complete RHS of Eq. 3.9 must be real, which means that $\sqrt{\alpha}$ must be real as well. From $\alpha(\Delta_e, \Delta_o) \geq 0$ one obtains the following condition for an OPO operating in a steady self-injection-locked state:

$$16\gamma_0^2 \Delta_e \Delta_o \geq \left(\Delta_e \kappa_o - \Delta_o \kappa_e\right)^2 . \tag{3.11}$$

Note, that if the QWP is set to a neutral position ($\vartheta_{QWP} = 0$), such that $\gamma_0 = 0$, condition 3.11 reduces to $\Delta_e \kappa_o - \Delta_o \kappa_e = 0$, which is the condition for unlocked, free-running OPO operation given in Eq. 3.5.

Locking can occur for those pairs of cavity detunings Δ_e and Δ_o, for which the condition 3.11 is satisfied. For example, using the specific experimental parameters κ_e and κ_o of the OPO that are present in our experiments, and assuming a QWP angle $\vartheta_{QWP} = 6$ deg, we yield from the condition 3.11, that locking can occur if $0.43 \leq \frac{\Delta_e}{\Delta_o} \leq 2.19$.

This locking condition is depicted schematically in Fig. 3.3, where the parameter plane is spanned by the cavity detunings Δ_e and Δ_o. Locking can occur for detunings Δ_e and Δ_o within the gray area between the two diagonals $\frac{\Delta_e}{\Delta_o} = 0.43$ and $\frac{\Delta_e}{\Delta_o} = 2.19$, which can be called the locking area. The angle between the two diagonals widens with increasing coupling strength γ_0 and thus with increasing quarter-wave plate angle ϑ_{QWP}. Note, however, that the diagonals approach the

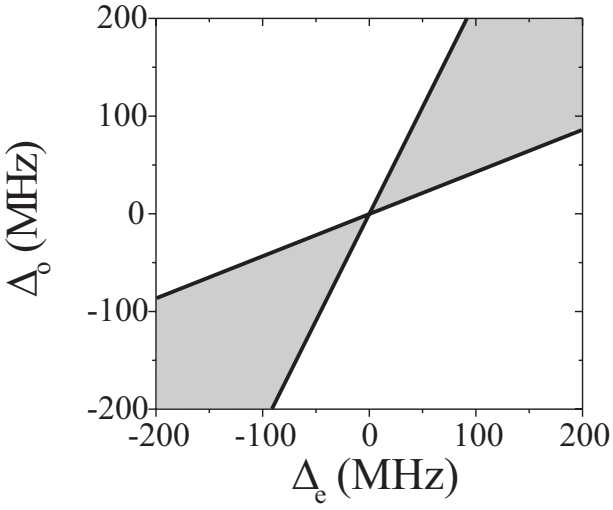

Figure 3.3: Parameter plane spanned by the cavity detunings. The gray area gives the theoretically calculated sets of cavity detunings (Δ_e, Δ_o), for which the OPO is self-phase-locked. The locking area is calculated with the experimental parameters κ_e and κ_o and with a QWP angle of 6 deg.

horizontal or vertical axis only asymptotically and that there is no locking observable for any QWP angle, if the OPO is operated with detunings of opposite sign, $\Delta_e \Delta_o < 0$.

To illustrate the importance of the signs of detunings, the cavity detunings are depicted in Fig. 3.4a for the case of equal sign, and in Fig. 3.4b for the case of opposite sign. Again, the e-wave frequency given by the upper axis increases from left to right, while the o-wave frequency, given by the lower axis, decreases. On the left side, in Fig. 3.4a, the vertical dashed line depicts the e- and o-wave frequencies that the OPO would assume without the effect of self-phase locking. The self-phase locking causes the OPO subharmonic frequencies to be shifted to exactly half of the pump frequency. As one can see in Fig. 3.4a, this means that the resonant enhancement for the e-wave is decreased and that this should therefore be a less favorable point of operation for the e-wave. But, at the same time, the enhancement for the o-wave increases, which makes the situation more favorable for the o-wave. In this situation, the OPO can self-phase-lock by shifting

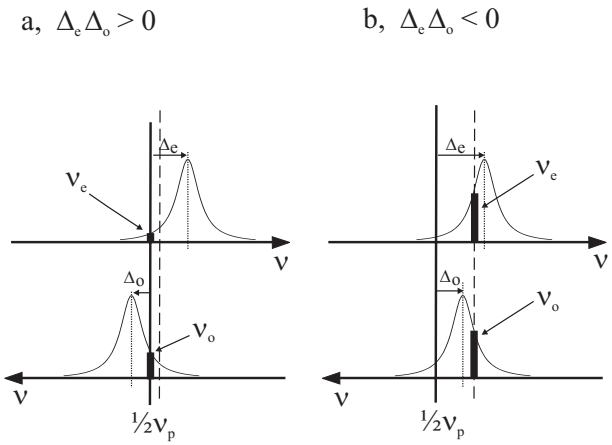

Figure 3.4: Qualitative comparison of locking and non-locking behavior. In a), the cavity detunings Δ_e and Δ_o are of the same sign and the OPO can self-phase-lock by shifting its frequencies from the dashed line (where the frequencies of the free-running OPO would be) to the solid line (which gives $\nu_e = \nu_o = \frac{1}{2}\nu_p$). In b), the detunings are of opposite sign. Such a shift as in a) can not occur, because it would decrease the resonant enhancement of both waves.

its frequencies from the dashed line in Fig. 3.4a, where the frequencies of the free-running OPO would be (see Eq. 3.5), to the solid line, which depicts exact frequency division $\nu_e = \nu_o = \frac{1}{2}\nu_p$. In contrast, if the detunings are of opposite sign, as depicted on the right side in Fig. 3.4b, shifting the OPO frequencies to one-half of the pump wave would mean that the resonant enhancement of both waves decreases. Therefore, the product of the intracavity fields, $E_e \cdot E_o$, would decrease, and the self-phase-locked operation is less favorable with respect to the unlocked case. From this example, it can be understood, that there is no self-phase locking observable, if the detunings are of opposite sign.

3.4 Intracavity pump photon number

Besides the locking condition of Eq. 3.11, the solution of the determinant of Eq. 3.6 also yields the pump photon number inside the OPO cavity for a given pump power and a given set of cavity detunings (see Eqs. 3.9 and 3.10):

$$N_{p,\pm} = b_{p,\pm}^2 = \frac{1}{D^2}\left(\gamma_0^2 + \frac{1}{4}\kappa_e\kappa_o + \frac{1}{4}\Delta_e\Delta_o \pm \sqrt{\alpha}\right). \tag{3.12}$$

Note that, in steady-state, from Eq. 3.12, one finds two different solutions for the intracavity pump field b_p, because of the two possible signs of $\sqrt{\alpha}$. As, above threshold, the pump photon number N_p inside the OPO cavity is clamped to its threshold value [83], these two solutions belong to two different pump powers at threshold $N_{th,\pm} = N_{p,\pm} = b_{p,\pm}$. Note that these two threshold pump powers do not depend on the external pump rate F, unlike it is the case for a self-phase-locked by-3 divider OPO [78]. Here and in Eq. 3.12, the upper of the signs $\pm$ designates the high-threshold solution $b_{p,+}$, and the lower one the low-threshold one, $b_{p,-}$. According to Eq. 3.10, the separation of the two values for the OPO threshold is a function of the detunings Δ_e and Δ_o. Furthermore, the difference between the threshold values increases with increasing γ_0. This means that a stronger optical coupling between the e-wave and the o-wave, corresponding to a further rotation of the intracavity QWP, results in an increased difference in the threshold photon number. Such a splitting was also predicted by Fabre and colleagues [40].

Figure 3.5 shows an example for the two threshold pump power values. The pump photon number inside the cavity is plotted as a function of the e-wave detuning Δ_e, while the o-wave detuning is constant at $\Delta_o = 100$ MHz. The gray straight line shows the pump photon number for the case that there is no self-injection locking of the OPO, i.e., for the QWP at neutral position, $\vartheta_{QWP} = 0$ deg. The pump photon number, and thus the pump power at threshold, rises linearly with the e-wave detuning. If the QWP is rotated out of the neutral position to $\vartheta_{QWP} = 3$ deg, the pump photon number splits into two values, which are displayed by the inner, dark gray curve. On rotating the QWP further, to $\vartheta_{QWP} = 6$ deg, the area in which locking occurs increases as well as the difference between the lower and the higher threshold value, as shown by the outer black curve. The curves for the various QWP positions are calculated assuming the same constant passive losses introduced on the pump wave through the QWP. Note, that the lower threshold value is almost always below the threshold value of the OPO without self-injection locking.

The described energetic separation of the divider's states is a phenomenon, that can be found also in other physical situations. One example is the splitting of the resonance frequencies of two coupled harmonic pendulums. In Mason's experiment [73], two different polarization states have been measured and assigned to the two

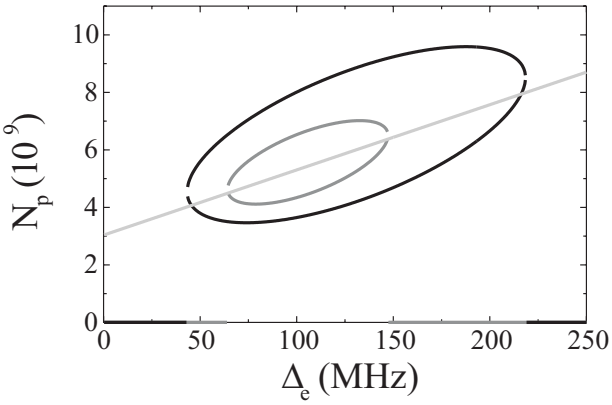

Figure 3.5: Intracavity pump photon number for the two threshold values as a function of the e-wave detuning Δ_e, calculated with a fixed o-wave detuning of $\Delta_o = 100$ MHz. Inner, dark gray circle: pump photon number splitting for a QWP angle of $\vartheta_{QWP} = 3$ deg; outer, black circle: splitting for a larger QWP angle of $\vartheta_{QWP} = 6$ deg; light gray solid line: pump photon number for the case that there is no locking, i.e., $\vartheta_{QWP} = 0$ deg.

threshold states. As one polarization state has been observed more often than the other, this was taken as evidence of the OPO operating preferably in the lower-threshold state. However, we claim that such clear addressing of the two polarization states to the two threshold states is not possible, as there exist two phase states for each threshold state. This will be proven in detail via a stability analysis in the sections 3.5 and 3.7.

The locking area in Fig. 3.3 is not only limited by the two border lines, which are defined by the locking condition 3.11. Instead, the direction left boundless in that figure is limited by the threshold pump power, which increases with increasing cavity detunings, as is the case for any OPO. Figure 3.6 shows the locking area arising from both these considerations for the low-threshold case (3.6a), and for the high-threshold case (3.6b) calculated with an QWP angle of 6 deg. In the figures, the intracavity pump photon number is coded as gray scales within the Δ_e-Δ_o-plane. As an example, only those intracavity pump photon number are displayed in the graphs, which can be realized with an external pump power of 300 mW. For larger cavity detunings, the pump power at threshold of the self-

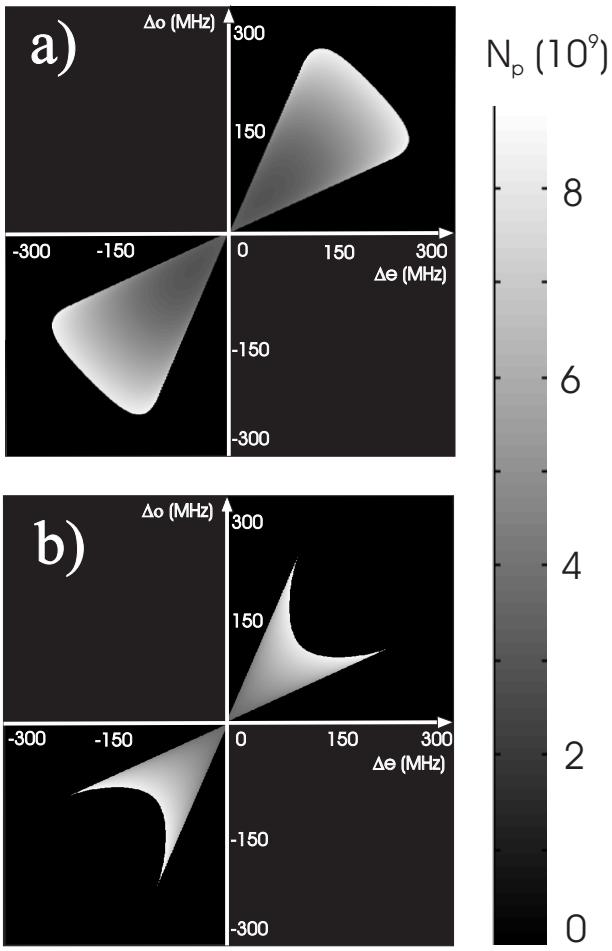

Figure 3.6: Intracavity pump photon number for a) the lower pump power threshold value and b) for the higher value as two-parameter plots of the cavity detunings Δ_e and Δ_o, calculated with a QWP angle of $\vartheta_{QWP} = 6$ deg. The intracavity pump photon numbers are coded using gray-scales.

phase-locked OPO would be higher than the pump power available available in the experiments described in this thesis. Therefore, the areas depicted in the Figs. 3.6a and b are the actual locking areas of the by-two divider OPO with the QWP

set to 6 deg.

From the considerations of this section, the question arises what we can expect to measure in the experiment. Is it possible to measure two distinctly different pump powers at threshold as suggested by Eq. 3.12 and claimed by Mason [73], and are there accordingly different output powers on the OPO's subharmonic waves observable? Would the two threshold states appear with the same probability, or would any external OPO parameter determine, which threshold state would be assumed, leading to a general preference? An answer to these questions is not only important before carrying out an experiment, but it is also useful to know before further investigating the steady-state solutions analytically. Therefore, in the following section a stability analysis of the two solutions is presented.

3.5 Stability analysis of the two threshold states

The system of equations 3.6, which was the starting point for calculating the steady-state intracavity pump photon number, and which leads to the two solutions of the high- and the low-threshold state, is a system of linear equations. Therefore a linear stability analysis can be applied directly to the equations to investigate the stability of the two solutions [84], [85]. A similar stability analysis has been applied by Zondy and colleagues to the steady-state solutions of a by-3 divider OPO, which also reveals two threshold states. In the case of an OPO, where both subharmonic waves are enhanced in a resonator, the low-threshold state was found to be stable, while the high-threshold state was found to be unstable [78]. In the case of a singly resonant by-3 divider OPO, both states have been found to be always stable [79]. For a by-2-divider OPO, however, such a stability analysis has not been performed yet.

The algebraic problem for the stability analysis of a system of nonlinear equations is equivalent to finding the eigenvalues and eigenvectors of the linearized system. Therefore the linear system is expressed in matrix form

$$\dot{\vec{x}}(t) = \mathbf{A}\vec{x}(t), \tag{3.13}$$

where $\mathbf{A}$ is an $n \times n$ matrix. Any vector $\vec{v}$ solving the equation

$$\mathbf{A}\vec{v} = \lambda\vec{v} \tag{3.14}$$

is an eigenvector of the matrix $\mathbf{A}$, and the corresponding value of λ is called an eigenvalue.

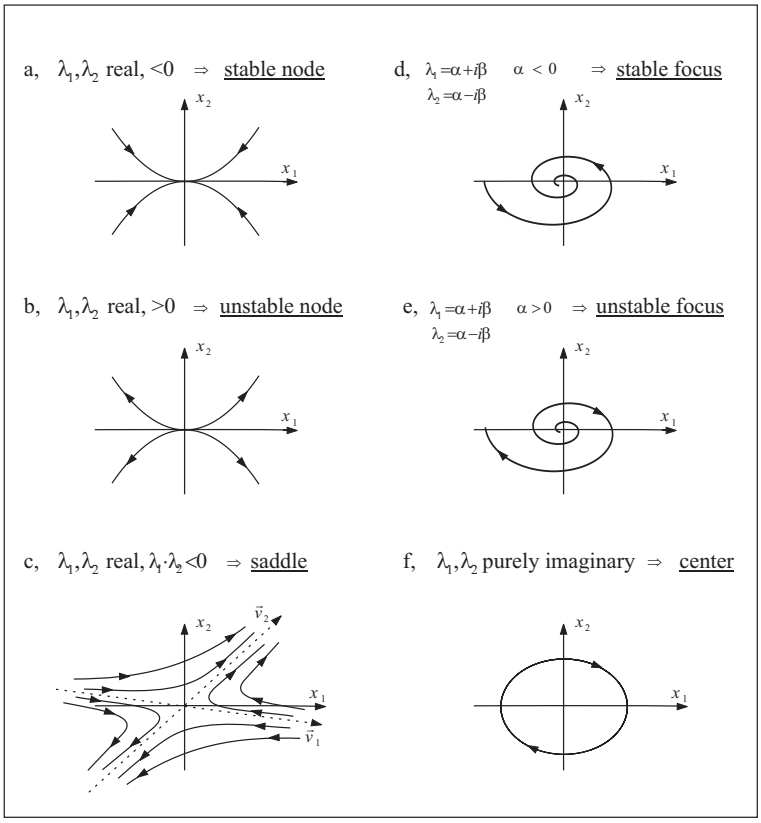

Figure 3.7: Overview over different kind of equilibria of a system of two linear coupled equations. The system is described by a 2×2 matrix $\mathbf{A}$: $\dot{\vec{x}} = \mathbf{A}\vec{x}$. The eigenvalues are solutions of $\det(\mathbf{A}) = 0$. $\Rightarrow$ Let λ_1, λ_2 be the eigenvalues and $\vec{\nu}_1$, $\vec{\nu}_2$ be the corresponding eigenvectors, which solve $\mathbf{A}\vec{\nu}_{1,2} = \lambda_{1,2}\vec{\nu}_{1,2}$.

For a system of n equations, n eigenvalues can be found, some of which may be degenerate. The correlation between the eigenvalues and the behavior of a system in close vicinity of a solution is summarized in Fig. 3.7. The left side shows the possible trajectories in the two-dimensional phase space for a one-dimensional

system like e.g., the position and velocity of a pendulum, if all eigenvalues are real. If all eigenvalues are negative, the equilibrium is referred to as a stable node, if the eigenvalues are positive, as an unstable node. If the real eigenvalues are not of the same sign, the resulting trajectories form a saddle. The equilibrium point is called a focus, if the eigenvalues of $\mathbf{A}$ are complex conjugates, $\alpha \pm i\beta$, $\alpha \neq 0$. If the real parts of the eigenvalues are negative, the solution, which is then also called a fixed-point solution, is oscillatory and stable. If the real parts are positive, the solution is oscillatory and unstable. If the eigenvalues are purely imaginary, the equilibrium is called a center or limit-cycle solution. The phase plane trajectories corresponding to a stable and unstable focus and to a center are displayed on the right side of Fig. 3.7.

To find the eigenvalues that solve Eq. 3.14, this equation can be rewritten:

$$(\mathbf{A} - \lambda \mathbf{I})\, \vec{v} = 0, \tag{3.15}$$

where $\mathbf{I}$ is the unit matrix of appropriate size. We require $\vec{v} \neq 0$, and the condition for a non-trivial solution of Eq. 3.15 is that the determinant of $\mathbf{A} - \lambda \mathbf{I}$ is zero:

$$\det(\mathbf{A} - \lambda \mathbf{I}) = 0. \tag{3.16}$$

Applying the above considerations to the linear system of equations 3.6 yields

$$\begin{vmatrix} -\frac{1}{2}(\kappa_e - i\Delta_e) - \lambda & \gamma & 0 & iD\overline{q_p} \\ -\gamma^* & -\frac{1}{2}(\kappa_o - i\Delta_o) - \lambda & iD\overline{q_p} & 0 \\ 0 & -iD\overline{q_p^*} & -\frac{1}{2}(\kappa_e + i\Delta_e) - \lambda & \gamma^* \\ -iD\overline{q_p^*} & 0 & -\gamma & -\frac{1}{2}(\kappa_o + i\Delta_o) - \lambda \end{vmatrix} = 0. \tag{3.17}$$

The eigenvalues λ are solutions of the quartic characteristic equation

$$\lambda^4 + \xi_3 \lambda^3 + \xi_2 \lambda^2 + \xi_1 \lambda + \xi_0 = 0, \tag{3.18}$$

where the coefficients ξ_i are all real:

$$\xi_3 = \kappa_e + \kappa_o \tag{3.19}$$

$$\xi_2 = \kappa_e\kappa_o + \frac{1}{4}\kappa_e^2 + \frac{1}{4}\kappa_o^2 + \frac{1}{4}\Delta_e^2 + \frac{1}{4}\Delta_o^2 - 2\left(D^2 b_p^2 - \gamma_0^2\right) \tag{3.20}$$

$$\xi_1 = \frac{1}{4}\Delta_e^2\kappa_o + \frac{1}{4}\Delta_o^2\kappa_e + \frac{1}{4}\kappa_e^2\kappa_o + \frac{1}{4}\kappa_o^2\kappa_e - (\kappa_e + \kappa_o)\left(D^2 b_p^2 - \gamma_0^2\right) \tag{3.21}$$

$$\begin{aligned}\xi_0 = {} & \frac{1}{16}\Delta_e^2\Delta_o^2 + \frac{1}{16}\kappa_e^2\kappa_o^2 + \frac{1}{16}\Delta_e^2\kappa_o^2 + \frac{1}{16}\Delta_o^2\kappa_e^2 \\ & + \left(D^2 b_p^2 - \gamma_o^2\right)^2 - \frac{1}{2}\kappa_e\kappa_o\left(D^2 b_p^2 - \gamma^2\right) - \frac{1}{2}\Delta_e\Delta_o\left(D^2 b_p^2 - \gamma^2\right) - \Delta_e\Delta_o\gamma_0^2\end{aligned} \tag{3.22}$$

After inserting the results of the steady-state solution (Eq. 3.12), Eqs. 3.19 to 3.22 read:

$$\xi_3 = \kappa_e + \kappa_o \tag{3.23}$$

$$\xi_2 = \left(\frac{1}{2}\kappa_e + \frac{1}{2}\kappa_o\right)^2 + \left(\frac{1}{2}\Delta_e - \frac{1}{2}\Delta_o\right)^2 \mp 2\sqrt{\alpha} \tag{3.24}$$

$$\xi_1 = (\Delta_e - \Delta_o)\left(\frac{1}{4}\Delta_e\kappa_o - \frac{1}{4}\Delta_o - \kappa_e\right) \mp (\kappa_o + \kappa_e)\sqrt{\alpha} \tag{3.25}$$

$$\xi_0 = 15\gamma_0^2\Delta_e\Delta_o - \frac{15}{16}\left(\Delta_e\kappa_o - \Delta_o\kappa_e\right)^2 \tag{3.26}$$

In the above Eqs. 3.23 to 3.26, the upper sign of $\mp$ belongs to the high-threshold solution, whereas the lower one belongs to the low-threshold solution, with α being defined as in Eq. 3.10. The eigenvalues have been calculated for various detunings Δ_e and Δ_o and coupling coefficients γ_0 for nontrivial solutions of b_p. For example, for the experimental cavity decay rates ($\kappa_e = 114$ MHz, $\kappa_o = 117$ MHz) and for a QWP angle of $\vartheta_{QWP} = 6$ deg, inserting the cavity detunings $\Delta_e = \Delta_o = 75$ MHz, one obtains the following sets of eigenvalues for the high- and for the low-threshold value:

high threshold	low threshold
$\lambda_1 = -168.811 \cdot 10^6$	$\lambda_1 = -57.750 \cdot 10^6 - 45.438 \cdot 10^6 i$
$\lambda_2 = -151.210 \cdot 10^6$	$\lambda_2 = -57.750 \cdot 10^6 + 45.438 \cdot 10^6 i$
$\lambda_3 = +35.710 \cdot 10^6$	$\lambda_3 = -57.750 \cdot 10^6 - 75.263 \cdot 10^6 i$
$\lambda_4 = +53.311 \cdot 10^6$	$\lambda_4 = -57.750 \cdot 10^6 + 75.263 \cdot 10^6 i$
$\rightarrow$ saddle	$\rightarrow$ stable focus

In this case, the eigenvalues of the high-threshold solution are all real, but two of them are positive. This means, that the high-threshold equilibrium is a saddle, and therefore *not stable*. The eigenvalues of the low-threshold solution, on the other hand, are two pairs of complex conjugates. As the real parts of all eigenvalues are negative, this equilibrium is a *stable* focus. Thus, in the experiment we expect to find only one *single* threshold pump power.

Analog calculations have been carried out for various detunings and quarter-wave plate angles. Figure 3.8 shows the different kinds of equlilibria found for a QWP angle of $\vartheta_{QWP} = 6$ deg, for the high-threshold solution in Fig. 3.8a and for the low-threshold solution in Fig. 3.8b. Only the quarter with positive detunings $\Delta_e > 0$ and $\Delta_o > 0$ is plotted, because the quarter with negative detunings is a mirrored image of the one shown. The high-threshold solutions, which were calculated in steps of 0.1 MHz, have all been found to be unstable. However, three regions with different behavior in direct vicinity of the solution can be distinguished: the eigenvalues of solutions with similar detunings, i.e. $\frac{\Delta_e}{\Delta_o} \approx 1$, are two pairs of complex conjugate numbers, where the real parts of one pair is positive. This case of a saddle as unstable equilibrium is indicated in Fig. 3.8a, by dark gray coloring. For more asymmetric detunings, we obtain one pair of real, positive eigenvalues, and one pair of complex conjugates (light gray), for even more asymmetric detunings two pairs of complex conjugate eigenvalues, where the real parts of one pair are positive (indicated by white coloring). All these kinds of equilibria are not stable.

The low-threshold solutions, on the other hand, are all proven to be stable. Here also different kinds of equilibria can be distinguished, which are indicated on the right side in Fig. 3.8b.The solutions for small cavity detunings Δ_e and Δ_o

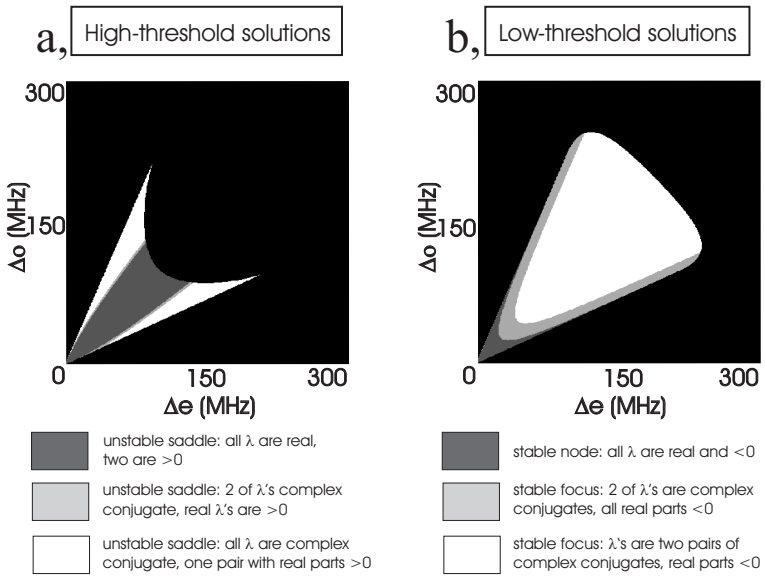

Figure 3.8: Different kinds of equilibria calculated for the cavity decay rates $\kappa_e = 114$ MHz and $\kappa_o = 117$ MHz and for a QWP angle of $\vartheta_{QWP} = 6$ deg. The high-threshold solutions, plotted on the left side, are all found to be unstable, whereas the low-threshold solutions on the right side are all stable.

have four purely real, negative eigenvalues, which corresponds to the equilibrium being a stable node, and which is indicated by dark gray coloring. For slightly larger detunings, one yields two real, negative eigenvalues and one set of complex conjugates, the real parts of which are negative (light gray). For large detunings, two pairs of eigenvalues with negative real parts are obtained (indicated by white coloring in Fig. 3.8b). The last two eigenvalue constellations correspond to the solutions being stable foci.

Summarizing this section, for the first time a linear stability analysis was applied to the two solutions for the intracavity pump photon number of the self-phase-locked by-2-divider OPO. The characteristic equation has been determined and solved for various cavity detunings and quarter-wave plate angles. It has been shown, that the high-threshold solution always is an unstable equilibrium, whereas the low-threshold solution is stable. We therefore expect only one threshold pump power to be observable in the experiments.

3.6 Locking range

Considering the results of the previous section like, for example, the shape of the locking area in the plane spanned by the cavity detunings Δ_e and Δ_o, the question arises what we can expect to measure when tuning the OPO towards degeneracy. The goal of this section is to qualitatively describe the tuning possibilities within the plane spanned by the cavity detunings. Based on these considerations, an estimate for the experimentally observable locking range is derived.

The locking area depends on some experimental parameters that are constant (e.g., the mirror transmissions) and others, that can be adjusted during the experiment. Like it will be explained in detail in section 5.6, the adjustable parameters are the physical length of the crystal, when moved laterally through the OPO cavity, the crystal temperature and the pump frequency. These parameters determine both cavity detunings Δ_e and Δ_o at the same time, such that we do not have an individual control over each of them. Taking into account the shape of the locking area in the two-parameter plane of Δ_e and Δ_o, it is not evident that we should be able to observe locking at all. For example, if we monitored the beat frequency, i.e., the difference frequency between the two subharmonic waves while tuning the OPO towards degeneracy, but the detunings where of opposite sign, we could observe the beat frequency getting smaller and close to zero, but phase locking of the OPO subharmonic waves would simply never occur. Therefore it is necessary to investigate the relation between the externally adjustable parameters and the cavity detunings. Only if these relations are known, the measurements can be interpreted and the expected locking range can be expressed in numbers. The possibilities of tuning the OPO towards degeneracy will be investigated in detail in section 5.6. Here, the tuning is regarded only within the locking area and with respect to the locking range one can expect to measure.

In the next paragraphs, the possibilities of tuning within the parameter plane spanned by the are briefly described.

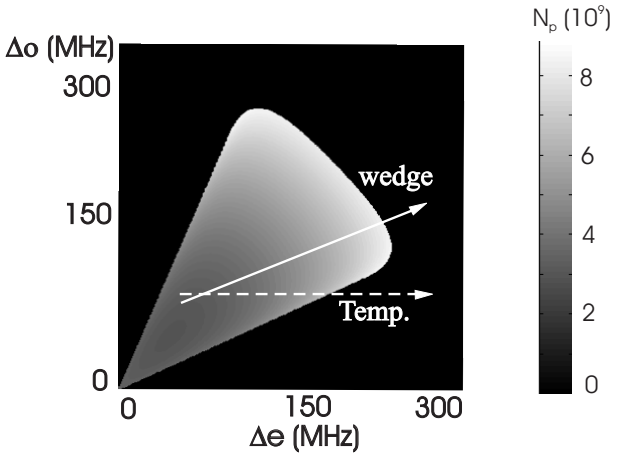

Figure 3.9: Experimental possibilities to change the cavity detunings Δ_e and Δ_o in a two-mirror OPO. The dashed arrow indicates the direction induced by an increasing crystal temperature, the solid arrow the change when laterally adjusting the wedged crystal. The gray scales inside the locking area give the intracavity pump photon number.

Tuning via the crystal's lateral position

On changing the lateral position of the crystal, the optical cavity lengths of the pump, e-wave and o-wave change, because we use a crystal which has wedges on both sides (see details in Fig. 5.10). The geometrical cavity length is controlled by a Pound-Drever-Hall locking technique (section 5.3), which keeps the optical pump cavity length in resonance with the pump wavelength. Therefore, any changes to the pump cavity optical length induced by moving the nonlinear crystal is compensated completely. However, this is achieved by changing the geometrical cavity length by moving a cavity mirror. As a consequence the optical cavity lengths of the e-wave and the o-wave cavities change, which results in a synchronized shift of both cavity detunings Δ_e and Δ_o. The change of the cavity detunings on laterally

moving the crystal is calculated in detail in section 5.6.4. The result is shown in Fig. 3.9 as the solid-line arrow. In this figure, the locking area is depicted for a quarter-wave plate angle of 6 deg, where the gray scales inside the locking area represent the intracavity pump photon number.

Tuning via the crystal temperature

The change of the refractive indices induced by a temperature change leads to a change of the optical cavity lengths of the three interacting waves. As before, with tuning via the lateral position of the crystal, the change of the pump optical cavity length is compensated completely by the Pound-Drever-Hall stabilization. As the derivatives of the pump and the o-wave refractive indices versus temperature are very similar, also the o-wave optical cavity length is almost compensated, but the change of the e-wave optical cavity length is about 10 times the change of the pump and the o-wave cavity length and is therefore not compensated. Absolute numbers are, again, calculated in section 5.6.4. The result of the calculations presented there is, that upon changing the crystal temperature the change of the o-wave detuning is only 0.2% of the change of the e-wave detuning, which results in an almost horizontal path within the plane spanned by the detunings, as is indicated by the dashed arrow in Fig. 3.9.

Tuning via the pump frequency

The changes of the cavity detunings as a function of the pump frequency detuning are similar to those induced by tuning via the crystal temperature. However, in practical situations the effect of changing the pump frequency is much smaller as compared to a change of the crystal temperature. In order to exploit tuning via the pump frequency for achieving results equivalent to temperature tuning, one had to tune the pump laser frequency over several tens of GHz, which is not practical due to mode hops of the pump laser. Therefore, for tuning the OPO into the locking range, we concentrate on the two possibilities named before, namely tuning via the crystal's lateral position and via the crystal temperature. In the experiment, the parameters crystal temperature and lateral position are adjusted alternately such that the OPO oscillates at minimum pump threshold, i.e. at maximum output power.

Estimation of the locking range

For an estimation of the experimentally observable locking range, we consider the OPO operating in the self-phase-locked state at minimum threshold. It was experimentally observed, that after operating in the self-phase-locked state for some time, the OPO leaves the self-phase-locked state, such that a beat note becomes measurable. Together with the observation, that the beat frequency, i.e. the frequency difference between the e- and the o-wave of the free-running OPO also slowly drifts with time, we assume that temperature drift is the main reason for the OPO to leave the locking range. In the following, we derive an estimate for the measurable locking range based on the assumption that the OPO leaves the self-phase-locked state due to a temperature drift.

For this estimation, we need to know two relations. Firstly, it is necessary to know, which values the detunings Δ_e and Δ_o acquire when the OPO drifts out of the locking range. And secondly, the resulting measurable beat frequency $\delta\nu_{beat}$ caused by the cavity detunings has to be known.

The starting point for our considerations is that the OPO operates in a self-phase-locked state, after the OPO output power has been optimized as described above. This corresponds to the cavity detunings being adjusted in a way that the OPO threshold is minimized, which corresponds to the dark gray area in Fig. 3.9 at approximately $\Delta_e = \Delta_o = 70$ MHz. The effect of a temperature drift is the same as that of tuning via the crystal temperature and is depicted by the dashed-line arrow in Fig. 3.9. We therefore simply consider a change of the cavity detunings Δ_e and Δ_o in the direction of the dashed arrow. Then the point of intersection of the arrow indicating the temperature drift in Fig. 3.9 with the boarder of the locking area is where the OPO leaves the locking range. From these crossing coordinates, one can retrieve the cavity detunings, at which the locking area is entered or left. These coordinates are here denoted by $\Delta_{e,lock}$ and $\Delta_{o,lock}$.

Figure 3.10 shows the outlines of the locking areas in the plane spanned by Δ_e and Δ_o for different QWP rotation angles, calculated for the experimental cavity decay rates ($\kappa_e = 114$ MHz, $\kappa_o = 117$ MHz). From the inner to the outer, the white traces give the contours of the locking area for $\vartheta = 0.25$, 0.5, 1, 2, 3, 4, 5, 6, 8, and 10 deg. The black arrow again indicates the direction of the changes of the cavity detuning induced by temperature drift. From Fig. 3.10 we obtain the coordinates $\Delta_{e,lock}$ and $\Delta_{o,lock}$ as a function of the QWP angle as the coordinates

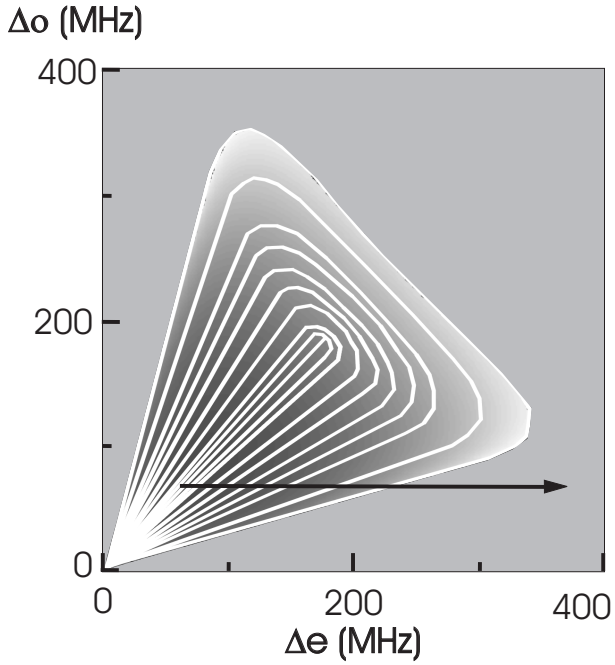

Figure 3.10: Outlines of the locking areas for different rotation angles of the QWP. From inner to outer, the QWP angles are 0.25, 0.5, 1, 2, 3, 4, 5, 6, 8, and 10 deg. The black arrow indicates the direction of temperature drift.

of the intersection of the temperature drift path (i.e. the black arrow) and the border of the locking range.

The second relation required for an understanding of the measurements is the correspondence of the cavity detunings to the measured beat frequency $\delta\nu_{beat}$. To obtain a relation for calculating the beat frequency, the situation at the edge of the locking area is depicted schematically in Fig. 3.11. Using the same notation as before, the e-wave frequencies, given by the upper axis, increase from left to right, while the o-wave frequencies, given by the lower axis, decrease from left to right. All e- and o-wave frequency-pairs allowed by energy conservation correspond to the intersection points of vertical lines with the axes. In Fig. 3.11b, the cold cavity mode of the e-wave is frequency-shifted to the right with respect to the first

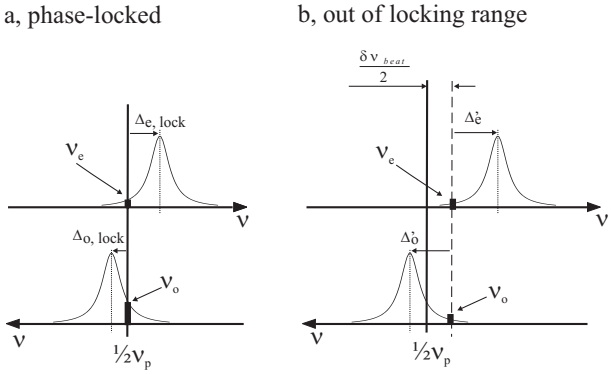

Figure 3.11: Schematic drawing of the cavity detunings when the OPO is temperature-drifting out of the locking area: a) the OPO is phase-locked, $\nu_e = \nu_o = \frac{1}{2}\nu_p$. b) the e-wave detuning is shifted further to the right, such that new e- and o-wave frequencies are more advantageous for the OPO threshold, indicated by the dashed vertical line.

case of phase-locked operation displayed in Fig. 3.11a, such that a new pair of e- and o-wave frequencies is more favorable regarding the OPO threshold. The OPO now oscillates at the e- and o-wave frequencies indicated by the dashed vertical line. The exact position of the dashed line in this notation is determined by the condition $\Delta'_e\kappa_o = \Delta'_o\kappa_e$ (Eq. 3.5), which defines the distance of the new frequencies to the nearest cavity modes, Δ'_e and Δ'_o. With this relation and with $\Delta'_e + \Delta'_o = \Delta_{e,lock} + \Delta_{o,lock}$, the new cavity detunings can be obtained:

$$\Delta'_e = \frac{\Delta_{e,lock} + \Delta_{o,lock}}{1 + \frac{\kappa_o}{\kappa_e}} \tag{3.27}$$

$$\text{and } \Delta'_o = \Delta'_e \frac{\kappa_o}{\kappa_e}$$

The beat frequency one would measure is then given by the difference between the new e-wave frequency and the o-wave frequency, which is twice the difference between either of the two waves and the exactly divided pump frequency:

$$\delta\nu_{beat} = 2|\nu_e - \nu_o| = 2|\frac{1}{2}\nu_p - \nu_e| = 2|\frac{1}{2}\nu_p - \nu_o|. \tag{3.28}$$

The beat frequency retrieved at the very edge of the locking range i.e., the smallest beat frequency that can be measured after the OPO has fallen out of the phase-locked state, $\delta\nu_{lock}$, is an important characteristic parameter of the by-two-divider: It is the full locking range of the divider $2\delta\nu_{lock}$. From Fig. 3.11 one can see, that at the edge of the locking range, the difference between the exactly divided pump frequency and the generated o-wave frequency equals the difference between the new detuning Δ'_o and $\Delta_{o,lock}$ or the equivalent relation for the e-wave detunings:

$$\delta\nu_{lock} = 2|\Delta'_o - \Delta_{o,lock}| = 2|\Delta'_e - \Delta_{e,lock}| \tag{3.29}$$

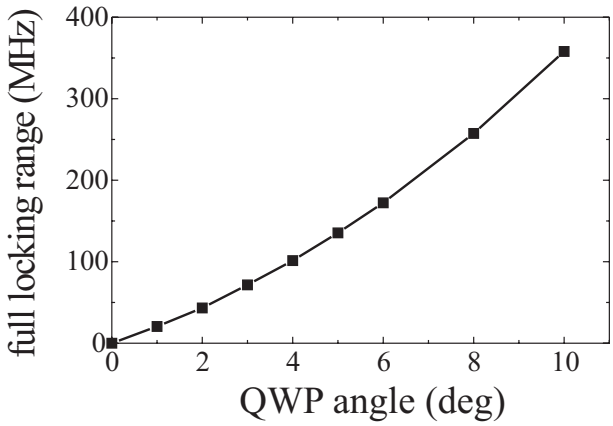

Figure 3.12: Calculated locking range for crystal temperature induced perturbations, as a function of the QWP rotation angle.

With the considerations described above, it is now possible to make an estimation for the locking range. The steps described above, i.e., calculating the locking area, retrieving the intersection coordinates, and determining the minimum measurable beat frequency, lead to an estimate of the locking range. Figure 3.12 shows the calculated full locking range (i.e. $2\delta\nu_{lock}$) as a function of the QWP rotation angle. One can see, that the locking range as derived from temperature drift increases with the QWP angle. The increase can be approximated with a quadratic function, as shown by the solid curve. For a quarter-wave plate angle of 6 deg,

we expect to measure a locking range of about 170 MHz. This calculated locking range will be compared with the experimental measurements in section 6.2.

3.7 Phase states and output wave powers

Up to now, the four linear coupled equations for the e-wave and the o-wave fields have been solved in steady-state, yielding a condition for self-phase-locked operation of the OPO divider. There are two solutions with different intracavity pump photon numbers, corresponding to two different pump powers at threshold. In the previous section, it has been shown that only the one with the lower pump threshold is stable. In this section, properties of the stable low-threshold state will be further investigated. Of special interest are the phases of the OPO subharmonic waves, because these are of great importance for characterizing the quality of the frequency by-two-divider. In a first step, expressions for the intracavity photon numbers of the subharmonic waves are derived. In a second step, the phases of the output waves are determined. Finally, we also derive an expression for the intracavity pump phase with respect to the phase of the input wave.

With the separation of the complex field amplitudes q_p, q_e, and q_o and the complex coupling parameter γ into real, positive amplitudes and real phases, and the pump rate F being analogously separated into the real, positive amplitude f and the phase β by $F = fe^{i\beta}$, the coupled field equations 3.1 can be separated into their real and imaginary parts. With the time derivatives set to zero, we obtain the following six equations:

$$0 = -\frac{1}{2}\kappa_p b_p - D b_e b_o \sin(\varphi_e + \varphi_o - \varphi_p) + f\cos(\varphi_p - \beta) \tag{3.30}$$

$$0 = -\frac{1}{2}\kappa_e b_e + D b_p b_o \sin(\varphi_e + \varphi_o - \varphi_p) + \gamma_0 b_o \cos(\varphi_e - \varphi_o - \theta)$$

$$0 = -\frac{1}{2}\kappa_o b_o + D b_p b_e \sin(\varphi_e + \varphi_o - \varphi_p) - \gamma_0 b_e \cos(\varphi_e - \varphi_o - \theta)$$

$$0 = D b_e b_o \cos(\varphi_e + \varphi_o - \varphi_p) - f\sin(\varphi_p - \beta)$$

$$0 = -\frac{1}{2}\Delta_e b_e + D b_p b_o \cos(\varphi_e + \varphi_o - \varphi_p) + \gamma_0 b_o \sin(\varphi_e - \varphi_o - \theta)$$

$$0 = -\frac{1}{2}\Delta_o b_o + D b_p b_o \cos(\varphi_e + \varphi_o - \varphi_p) + \gamma_0 b_e \sin(\varphi_e - \varphi_o - \theta)$$

First, by combining the fifth equation with the sixth, we find the relation

$$\frac{b_e}{b_o} = \sqrt{\frac{\Delta_o}{\Delta_e}}. \tag{3.31}$$

Using this relation and linear combinations of the Eqs. 3.30, we obtain the following expressions for the sum and the difference phases of the OPO's subharmonic waves:

$$\sin(\varphi_e + \varphi_o - \varphi_p) = \frac{1}{4Db_p}\left(\kappa_e\sqrt{\frac{\Delta_o}{\Delta_e}} + \kappa_o\sqrt{\frac{\Delta_e}{\Delta_o}}\right) \tag{3.32}$$

$$\cos(\varphi_e - \varphi_o - \theta) = \frac{1}{4\gamma_0}\left(\kappa_e\sqrt{\frac{\Delta_o}{\Delta_e}} - \kappa_o\sqrt{\frac{\Delta_e}{\Delta_o}}\right) \tag{3.33}$$

For given experimental parameters like, for example, the cavity losses, and for given cavity detunings, the phases of the OPO subharmonic fields can be determined with respect to the phase of the cavity internal pump field, φ_p. Later in this paragraph, we will also derive an expression for the cavity internal pump phase with respect to the external pump phase.

Note that, for a type-II phase-matched OPO without quarter-wave plate or with the plate adjusted to be neutral, i.e., $\vartheta_{QWP} = 0$ deg and hence $\gamma_0 = 0$, the sum of the subharmonic phases $\varphi_e + \varphi_o$ is well defined and follows the pump phase according to Eq. 3.32, while their difference $\varphi_e - \varphi_o$ is not defined [38]. In

consequence, trying to apply Eq. 3.33 does not return a result due to a division by zero. The phases themselves are free with respect to each other and undergo a phase-diffusion process.

Only if the OPO is self-phase-locked, the phase-diffusion process is suppressed, the phase difference is locked and follows the phase θ of the coupling parameter γ. Then the subharmonic phases are determined with respect to each other and therefore are determined as absolute numbers. In fact, from the phase sum in Eq. 3.32 being defined only modulo 2π, and as the phase difference does not change, if the two phases change by the same amount, we find that the subharmonic phases can assume one of two possible sets of subharmonic phases φ_e and φ_o, which are separated from each other by π. The existence of two phase eigenstates agrees with an earlier prediction, where an all-optical divider by n should possess n phase eigenstates [86].

Figure 3.13 shows the phase of the two subharmonic waves as a two-parameter plot in the plane spanned by the cavity detunings Δ_e and Δ_o. The e-wave phase is plotted in Fig. 3.13a, and the o-wave phase in Fig. 3.13b. The values displayed are calculated for an QWP angle of $\vartheta_{QWP} = 3$ deg using the Eqs. 3.32 and 3.33, and also the relation for the cavity internal pump phase, that will be derived later in this paragraph (Eqs. 3.36 and 3.37). Note, that the displayed e- and o-wave phases reflect only one of two possible cases. For a given set of cavity detunings, the phases would either assume the values given in Figs. 3.13, or both phases would be shifted with respect to those values by π.

Using linear combination of the upper three equations of 3.30 and using Eq. 3.31, one can derive the intracavity photon numbers of the e- and the o-wave. Per roundtrip, a certain percentage of the photons is coupled out through the cavity mirror, therefore the output power of the according wave is a direct measure of the intracavity photon number.

$$N_e = b_e^2 = \frac{4fb_p\cos(\varphi_p - \beta) - 2\kappa_p b_p^2}{\kappa_e + \kappa_o\frac{\Delta_e}{\Delta_o}} \tag{3.34}$$

$$N_o = b_o^2 = \frac{4fb_p\cos(\varphi_p - \beta) - 2\kappa_p b_p^2}{\kappa_o + \kappa_e\frac{\Delta_o}{\Delta_e}} \tag{3.35}$$

Considering the fact, that the OPO threshold can be lowered with respect to the non-locked state, depending on the cavity detunings, the question arises, whether also a higher output power can be expected from a self-phase-locked OPO.

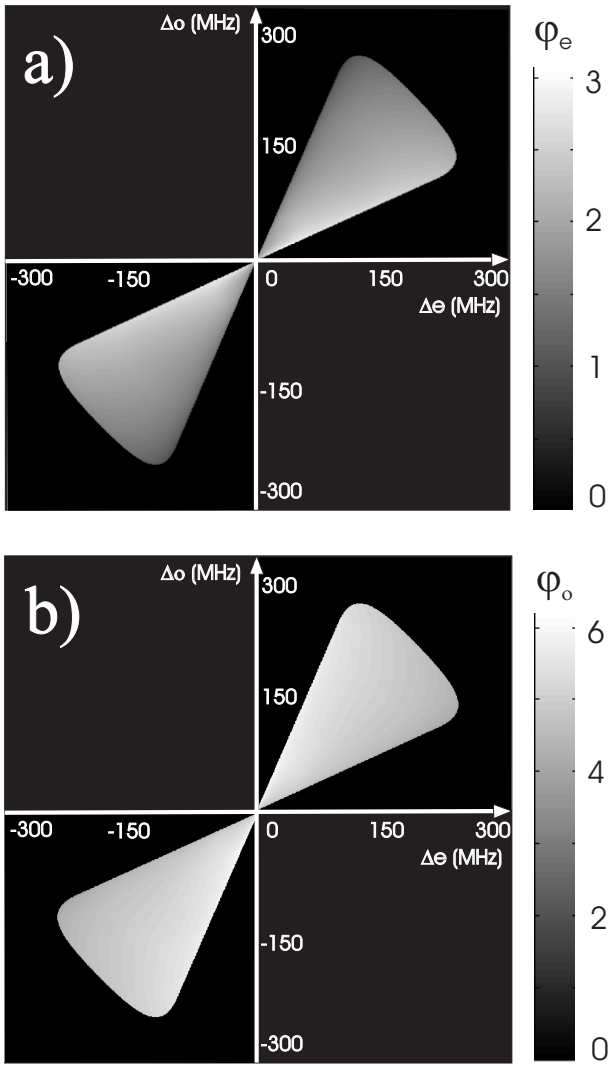

Figure 3.13: Phases of a) the e-wave and b) the o-wave in the self-phase-locked case. The phases are plotted in gray scales as a function of the cavity detunings and for a QWP angle of $\vartheta_{QWP} = 6$ deg.

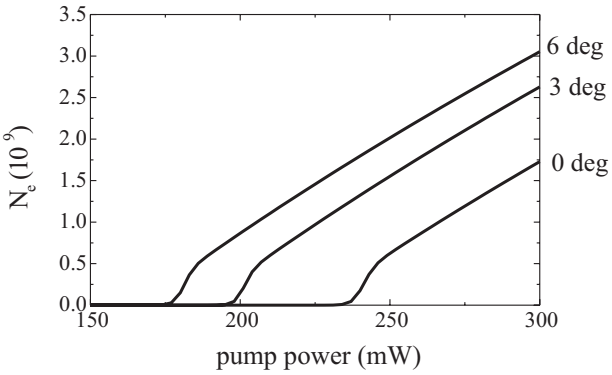

Figure 3.14: Intracavity photon number of the e-wave as a function of the external pump power, for quarter-wave plate rotation angles of $\vartheta_{QWP} = 6$ deg, 3 deg and 0 deg (from top to bottom). The photon numbers are calculated for cavity detunings of $\Delta_e = 50$ MHz and $\Delta_o = 51$ MHz, as they would be assumed also by the free-running OPO with cavity decay rates of $\kappa_e = 114$ MHz and $\kappa_o = 117$ MHz (see Eq. 3.5).

To answer this questions, the resonator-internal photon number of the e-wave has been calculated as a function of the external pump power for different quarter-wave plate rotation angles and for cavity detunings of $\Delta_e = 50$ MHz and $\Delta_o = 51$ MHz. Note that these cavity detunings would also be assumed by the free-running OPO with the cavity decay rates of $\kappa_e = 114$ MHz and $\kappa_o = 117$ MHz as present in our OPO (see Eq. 3.5). The result is displayed in Fig. 3.14. Shown are, from top to bottom and as a function of the external pump power, the resonator-internal e-wave photon numbers N_e for the quarter-wave plate rotated to $\vartheta_{QWP} = 6$ deg, to 3 deg, and to the neutral position at $\vartheta_{QWP} = 0$ deg. As one can see, the e-wave photon number and thus the output power of the OPO for a given external pump power above threshold indeed increases with the QWP rotation angle. Note, however, that the slope of the displayed curves is approximately constant, and that the increase in output power has its origin in the decreased threshold pump power.

In Fig. 3.15a, the intracavity photon number of the e-wave is displayed as a function of the cavity detunings for the constant external pump power of 300 mW. The according o-wave photon number is displayed in Fig. 3.15b. Both photon numbers are given for a QWP angle of 6 deg. As can be seen, the photon number

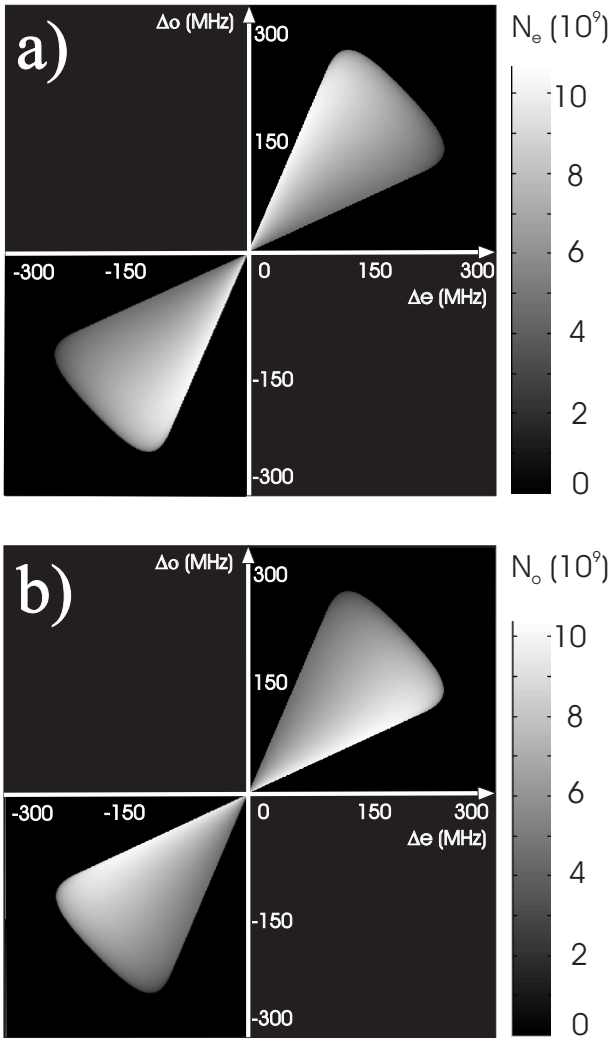

Figure 3.15: Intracavity photon number of a) the e-wave and b) the o-wave in the self-phase-locked case. The photon numbers are plotted in gray scales as a function of the cavity detunings and for a QWP angle of $\vartheta_{QWP} = 6$ deg.

of either of the waves decreases, when the according detuning increases.

Finally, the phase of the cavity internal pump field, φ_p can be determined. By summing up the squares of the first and the fourth Eqs. 3.30 we obtain

$$\cos(\varphi_p - \beta) = \frac{1}{f\kappa_p b_p}\left(f^2 + \frac{1}{4}\kappa_p^2 b_p^2 - D^2 b_e^2 b_o^2\right). \tag{3.36}$$

The last term, $D^2 b_e^2 b_o^2$ can be retrieved either from the Eqs. 3.34 and 3.35, which results in a quadratic equation of $\cos(\varphi_p - \beta)$, or by using the first and the fourth equation of 3.30, which yields

$$Db_e b_o - \frac{1}{2}\kappa_p b_p \sin(\varphi_e + \varphi_o - \varphi_p) = \sqrt{f^2 - \frac{1}{4}\kappa_p^2 b_p^2\left(1 - \sin^2(\varphi_e + \varphi_o - \varphi_p)\right)} \tag{3.37}$$

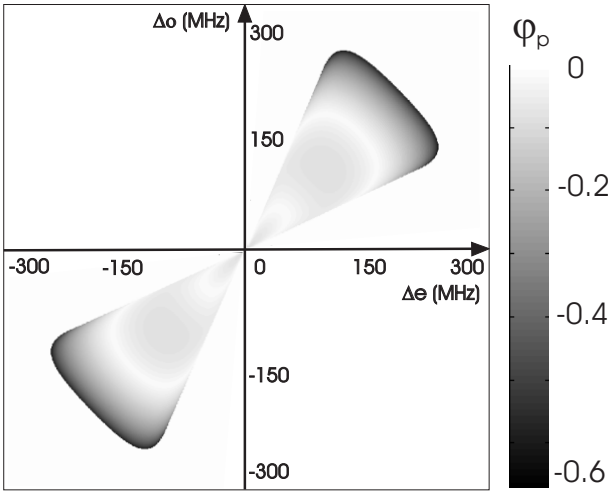

Figure 3.16: Phase of the intracavity pump field with respect to the external pump field phase, plotted in gray scales as a function of the cavity detunings and for a QWP angle of $\vartheta_{QWP} = 6$ deg.

By inserting Eq. 3.32 into Eq. 3.37 and further inserting the result into Eq. 3.36, finally one can determine the phase of the cavity internal pump field with respect to the external pump field. The result is depicted in Fig. 3.16 as a function of the cavity detunings, calculated for a QWP angle of 6 deg. Depending on the

cavity detunings, the cavity internal pump phase value acquires a value between $-\frac{\pi}{5}$ and zero with respect to the external pump field.

3.8 Frequency stability

In the previous sections, the coupled field equations have been solved in steady-state regime, yielding the condition for self-phase locking. The oscillation parameters of the self-phase-locked state, and in particular the phases of the subharmonic waves have been derived. In the following, we analytically derive the stability of frequency division, i.e., an expression for the residual time-averaged phase fluctuations. A similar expression has been derived and presented in our former work on a frequency-by-3 divider [65]. We also derive a proportionality factor, which allows to calculate the frequency instability of the frequency division by 2 from the measurement of the bandwidth of the beat signal between the two subharmonic waves (which is the bandwidth most easy to measure).

The precision of the frequency division is determined by a residual frequency instability, which could be caused as follows. In an experiment, the pump frequency ω_p and thus the exact one-half $\omega_p/2 = \Omega_e = \Omega_o$, is set by the pump laser. Nevertheless, as the OPO crystal's optical length is subject to a residual thermal drift, the cavity detunings Δ_e and Δ_o for the e- and the o-wave cavities, respectively, drift as well. Only the cavity detuning for the pump laser Δ_p remains zero, because the OPO cavity is locked to the pump laser wavelength via a Pound-Drever-Hall servo loop (see section 5.3). However this electronic servo loop possesses only a finite response time, which is in our experiments approximately 1.7 ms, given by the piezo-electric transducer. Acoustic perturbations with frequencies above 600 Hz may thus rapidly change the cavity length leading to small and random fluctuations of Δ_e and Δ_o as a function of time.

As the cavity detunings enter the eigenvalues φ_e and φ_o assumed by the divider in steady-state (see Eqs. 3.32 and 3.33 and compare Fig. 3.13), these eigenvalues are expected to drift and fluctuate as well. A temporal change of an eigenvalue $\varphi_x(t)$, however, corresponds via $d\varphi_x(t)/dt$ to a frequency deviation of the subharmonic frequencies from the exactly divided values. In our experiments, we indeed observed a slowly drifting frequency deviation (when the OPO was not self-phase-locked). The observations are described and quantified in section 6.3.2. In the following, we concentrate on this slow drift of the cavity detunings as the origin

of a residual frequency instability of the divider.

A measure for a residual frequency instability of the frequency divider is the full width at half maximum ($FWHM$) of the power spectrum [87] of the beat between one of the generated subharmonic frequencies and the exact one-half of the pump frequency, $FWHM(\nu_e - \frac{1}{2}\nu_p)$. First, we derive an expression for this deviation of the e-wave frequency of the exactly divided pump frequency by assuming that the cavity detunings Δ_e and Δ_o vary as functions of time as described:

$$\nu_e - \frac{1}{2}\nu_p = \frac{1}{2\pi}\frac{d}{dt}\left(\varphi_e - \frac{1}{2}\varphi_p\right). \tag{3.38}$$

For the term in brackets we can derive an expression by adding up Eqs. 3.32 and 3.33:

$$\varphi_e - \frac{1}{2}\varphi_p = \frac{1}{2}\theta + \frac{1}{2}f_1(\Delta_e, \Delta_o) + \frac{1}{2}f_2(\Delta_e, \Delta_o), \tag{3.39}$$

where $f_1(\Delta_e, \Delta_o)$ is defined as

$$f_1(\Delta_e, \Delta_o) := \varphi_e + \varphi_o - \varphi_p = \arcsin\left[\frac{1}{4Db_p}\left(\kappa_e\sqrt{\frac{\Delta_o}{\Delta_e}} + \kappa_o\sqrt{\frac{\Delta_e}{\Delta_o}}\right)\right], \tag{3.40}$$

and where $f_2(\Delta_e, \Delta_o)$ is defined as

$$f_2(\Delta_e, \Delta_o) := \varphi_e - \varphi_o - \theta = \arccos\left[\frac{1}{4\gamma_0}\left(\kappa_e\sqrt{\frac{\Delta_o}{\Delta_e}} - \kappa_o\sqrt{\frac{\Delta_e}{\Delta_o}}\right)\right]. \tag{3.41}$$

By inserting Eq. 3.39 into Eq. 3.38 and taking the time derivative, where we assume that θ is constant with respect to time, we find a beat frequency changing with time:

$$\nu_e - \frac{1}{2}\nu_p = \frac{1}{2\pi}\frac{d}{dt}\left(\varphi_e - \frac{1}{2}\varphi_p\right) = \frac{1}{4\pi}\frac{d}{dt}\left(f_1 + f_2\right), \tag{3.42}$$

where

$$\frac{d}{dt}\left(f_1 + f_2\right) = \frac{d\left(f_1 + f_2\right)}{d\Delta_e}\frac{d\Delta_e}{dt} + \frac{d\left(f_1 + f_2\right)}{d\Delta_o}\frac{d\Delta_o}{dt}. \tag{3.43}$$

In section 6.3.1, the different noise sources which lead to a broadening of the beat linewidth are discussed in more detail. Here, only the important results for calculating the frequency instabilities are summarized. A temperature drift

can be assumed as the major mechanism for a broadening of the beat linewidth, which enables the calculation of the link between the e- and the o-wave detunings. Using the Sellmeier coefficients for the refractive indices of lithium niobate [88], the changes of the crystal refractive indices with temperature for each of the three waves is calculated. Taking into account the cavity stabilization to the pump wavelength via the Pound-Drever-Hall stabilization, this yields as a result, that the e-wave detuning changes with temperature with a rate of 500 times of the rate of the o-wave detuning. This difference in rates can be directly transferred to the temporal derivatives: Assuming a temperature drift as the source of cavity length changes, a change of the e-wave detuning within a certain time period equals about 500 times the corresponding change of the o-wave detuning. This means, that the term $\frac{d\Delta_o}{dt}$ in the RHS of Eq. 3.42 is smaller than the term $\frac{d\Delta_e}{dt}$ by a factor of 500. Calculating the derivatives $\frac{d(f_1+f_2)}{d\Delta_e}$ and $\frac{d(f_1+f_2)}{d\Delta_o}$, on the other hand, yields that they are about equal. They differ considerably only at the edges of the locking area. Therefore we can neglect the second term in the RHS of Eq. 3.43 and consider only the first term. This corresponds to only considering the drift of the e-wave detuning and neglecting that of the o-wave detuning:

$$\frac{d}{dt}\left(f_1+f_2\right)=\frac{d\left(f_1+f_2\right)}{d\Delta_e}\frac{d\Delta_e}{dt}. \tag{3.44}$$

The spectral width of the beat $FWHM(\nu_e-\frac{1}{2}\nu_p)$ is given by the mean square value of the difference phase $\frac{1}{2\pi}\Psi_e(t):=\frac{1}{2\pi}\varphi_e(t)-\frac{1}{4\pi}\varphi_p(t)$ divided by the measurement time period τ [38]:

$$FWHM(\nu_e-\frac{1}{2}\nu_p)=\langle\left[\frac{1}{2\pi}\Psi_e(\tau)-\frac{1}{2\pi}\Psi_e(0)\right]^2\rangle\frac{1}{\tau}, \tag{3.45}$$

where the angular brackets denote the statistical mean value over many periods τ. Instead of $\langle\left[\frac{1}{2\pi}\Psi_e(\tau)-\frac{1}{2\pi}\Psi_e(0)\right]^2\rangle$ we can write

$$\langle\left[\frac{1}{4\pi}(f_1+f_2)(\Delta_e(\tau),\Delta_o(\tau))-\frac{1}{4\pi}(f_1+f_2)(\Delta_e(0),\Delta_o(0))\right]^2\rangle$$

(see Eq. 3.39), where for $(f_1+f_2)(\Delta_e,\Delta_o)$ we insert the RHS of Eq. 3.44 after carrying out an integration over time. The first factor on the RHS of Eq. 3.44 is constant with respect to time and can be extracted from the mean square values. We obtain:

$$FWHM(\nu_e - \frac{1}{2}\nu_p) = \frac{1}{16\pi^2}\left(\frac{d(f_1+f_2)}{d\Delta_e}\right)^2 \langle[\Delta_e(\tau) - \Delta_e(0)]^2\rangle \frac{1}{\tau}. \tag{3.46}$$

In the following, we use Eq. 3.46 to predict a quantitative value for the width of the beat between the generated e-wave and the desired wave with exactly one-half of the pump frequency, as would be expected for our experimental setup.

To calculate the width of the beat, we need to retrieve two numbers for the two factors on the RHS of Eq. 3.46. The first factor, $\left(\frac{d(f_1+f_2)}{d\Delta_e}\right)^2$, can be derived analytically from Eqs. 3.40 and 3.41. Therefore, the derivatives $(\frac{df_1}{d\Delta_e})$ and $(\frac{df_2}{d\Delta_e})$ are calculated separately:

$$\frac{df_1}{\Delta_e} = \frac{-1}{8Db_p\Delta_e} \cdot \frac{\kappa_e\sqrt{\frac{\Delta_o}{\Delta_e}} - \kappa_o\sqrt{\frac{\Delta_e}{\Delta_o}}}{\sqrt{1 - \left[\frac{1}{4Db_p}\left(\kappa_e\sqrt{\frac{\Delta_o}{\Delta_e}} + \kappa_o\sqrt{\frac{\Delta_e}{\Delta_o}}\right)\right]^2}}, \tag{3.47}$$

and

$$\frac{df_2}{\Delta_e} = \frac{1}{8\gamma_0\Delta_e} \cdot \frac{\kappa_e\sqrt{\frac{\Delta_o}{\Delta_e}} + \kappa_o\sqrt{\frac{\Delta_e}{\Delta_o}}}{\sqrt{1 - \left[\frac{1}{4\gamma_0}\left(\kappa_e\sqrt{\frac{\Delta_o}{\Delta_e}} - \kappa_o\sqrt{\frac{\Delta_e}{\Delta_o}}\right)\right]^2}}. \tag{3.48}$$

The two derivatives have been calculated as a function of the two cavity detunings Δ_e and Δ_o. As a result, it appears that both derivatives are small in the vicinity of the diagonal $\Delta_e = \frac{\kappa_e}{\kappa_o}\Delta_o$, i.e. in the center of the locking area and increase towards its edges. Figure 3.17 shows the two derivatives $\frac{df_1}{\Delta_e}$ and $\frac{df_2}{\Delta_e}$, calculated along a cross-cut through the locking area with constant o-wave detuning $\Delta_o = 100$ MHz for a number of different quarter-wave plate rotation angles ϑ_{QWP}. As can be seen from the Fig. 3.17, the derivative $\frac{df_1}{\Delta_e}$ shown in the graph on the left side, is smaller than the second derivative $\frac{df_2}{\Delta_e}$ shown on the right side by more than one order of magnitude over most of the locking area. Specifically, for all QWP rotation angles the first derivative is close to zero in the vicinity of the center of the locking area, where $\Delta_e \approx \frac{\kappa_e}{\kappa_o}\Delta_o$. As a value for the second derivative we retrieve $\frac{df_2}{\Delta_e} < 10^{-7}s$ from the graph on the right side of Fig. 3.17 for a QWP angle of $\vartheta_{QWP} = 3$ deg and in the vicinity of the center of the locking area. With this value, the first factor for the width of the beat $FWHM(\nu_e - \frac{1}{2}\nu_p)$as given by Eq. 3.46 reads:

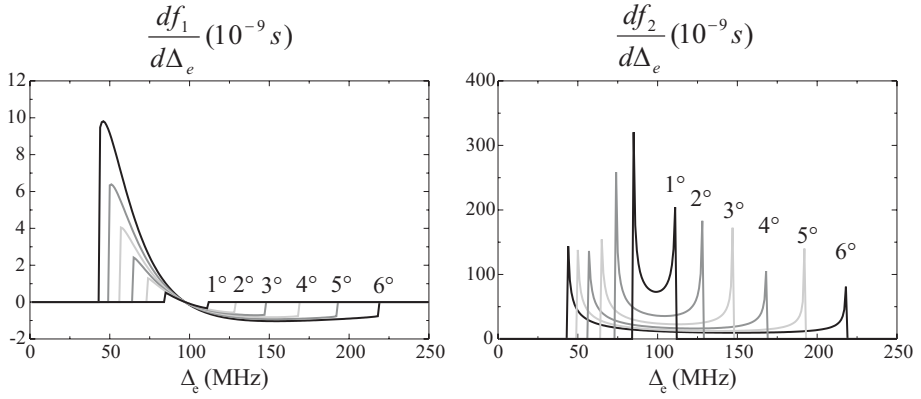

Figure 3.17: The derivatives $\frac{df_1}{\Delta_e}$ and $\frac{df_2}{\Delta_e}$ as a function of Δ_e, calculated along a cross-cut through the locking area with constant o-wave detuning $\Delta_o = 100$ MHz for different quarter-wave plate rotation angles ϑ_{QWP}= 1, 2, 3, 4, 5, and 6 deg.

$$\left(\frac{d(f_1+f_2)}{d\Delta_e}\right)^2 \approx \left(\frac{df_2}{d\Delta_e}\right)^2 \approx 1\cdot 10^{-14}s^2 \tag{3.49}$$

The second factor $\langle[\Delta_e(\tau)-\Delta_e(0)]^2\rangle\frac{1}{\tau}$ is retrieved from an experiment where the drift of the beat frequency between the two subharmonic waves was measured. The experiment will be presented in more detail in section 6.3.2. In a radio frequency (RF) measurement, a drift of the beat frequency of typically 360 kHz in a time period of $\tau = 10$ s was observed. As the beat frequency drift is caused mainly by a drift of the e-wave cavity detuning Δ_e, while the o-wave detuning Δ_o remains almost unchanged due to the cavity stabilization to the pump wavelength, we can assume an e-wave detuning of 360 kHz in 10 s, which corresponds to a value of $\langle[\Delta_e(\tau)-\Delta_e(0)]^2\rangle\frac{1}{\tau} = 1.3\cdot 10^{10}s^{-3}$ for the second factor of Eq. 3.46.

Using these values for the two factors on the RHS of Eq. 3.46, the spectral linewidth of the phase-locked OPO is calculated to be $FWHM(\nu_e - \frac{1}{2}\nu_p) = 0.8\cdot 10^{-6}Hz$. At an e-wave frequency of $\nu_e = 1.88\cdot 10^{14}$ Hz, this corresponds to a relative frequency instability of $FWHM(\nu_e - \frac{1}{2}\nu_p)/\nu_e = 4\cdot 10^{-21}$ for a measurement time of 10 s.

A direct measurement of this residual frequency instability would require to

first frequency-double the OPO's extraordinary polarized output wave and then superimpose it with the OPO's input pump frequency, to obtain a beat frequency in the RF range. In our experiment, however, we found it technically easier to perform a beat measurement in a different manner, i.e., by superimposing the two OPO output waves directly and to measure the beat frequency between them.

This measurement of $FWHM(\nu_e - \nu_o)$ (see section 6.3) compares the frequencies of the OPO output waves with each other, without taking into account the frequency of the OPO input wave. But as was shown above, the derived frequency stability of the divider depends mainly on the fluctuations of the phase difference $\varphi_e - \varphi_o$, which are described by the function $f_2(\Delta_e, \Delta_o)$ (see Eq. 3.40), while the fluctuations of the phase sum $\varphi_e + \varphi_o$, as calculated from $f_1(\Delta_e, \Delta_o)$ (Eq. 3.41) is smaller by more than one order of magnitude for all cases and by more than two orders of magnitude over most of the locking area and can be neglected. However, for a measurement of the fluctuations of the phase difference, a measurement of the beat bandwidth $FWHM(\nu_e - \nu_o)$ is fully sufficient. We should be able to derive a proportionality factor, with which the bandwidth of frequency division by 2, i.e., the fluctuations of the subharmonic e-wave frequency with respect to the exactly by 2 divided pump frequency, can be calculated from the beat bandwidth $FWHM(\nu_e - \nu_o)$ that is easier to measure. To calculate the corresponding proportionality factor, we use Eq. 3.41 to express the time dependence of the beat frequency $(\nu_e - \nu_o)$, i.e.,

$$\nu_e - \nu_o = \frac{1}{2\pi}\frac{d}{dt}(\varphi_e - \varphi_o) = \frac{1}{2\pi}\frac{d}{dt} f_2(\Delta_e, \Delta_o). \tag{3.50}$$

After carrying out the same steps as above we obtain the spectral bandwidth of this beat as

$$\begin{aligned} FWHM(\nu_e - \nu_o) &= \frac{1}{4\pi^2}\left(\frac{df_2}{d\Delta_e}\right)^2 \langle[\Delta_e(\tau) - \Delta_e(0)]^2\rangle \frac{1}{\tau} \\ &\approx 4FWHM(\nu_e - \frac{1}{2}\nu_p), \end{aligned} \tag{3.51}$$

readily giving the desired proportionality factor

$$\frac{FWHM(\nu_e - \nu_o)}{FWHM(\nu_e - \frac{1}{2}\nu_p)} \approx 4. \tag{3.52}$$

As a result of these calculations we expect for the by-2-divider OPO a spectral bandwidth of the beat frequency of $0.8 \cdot 10^{-6} Hz$, which means, that the OPO

should be able to divide the pump laser frequency by two with a fractional frequency instability of $4 \cdot 10^{-21}$. We have also found, that the divider's spectral bandwidth can be determined in good approximation by directly measuring the bandwidth of the beat signal between the two OPO subharmonic waves and dividing the obtained value by the proportionality factor 4.

3.9 Summary

Summarizing this chapter, self-injection locking of a type-II phase-matched, by-2-divider OPO has been investigated theoretically by solving the coupled field equations in steady-state regime. The steady-state values of the OPO in the phase-locked state have been calculated analytically under consideration of the experimental parameters such as the rotation of the cavity internal quarter-wave plate. In the self-phase-locked case, one obtains two different values for the pump power at threshold. For the first time, a stability analysis has been applied to these two solutions, which proves that the lower threshold state is stable, while the higher threshold state is not stable. Therefore, we expect that a high threshold state should never occur in the experiment. For the lower threshold state, a quantitative prediction of the expected measurable locking-range has been made for the (experimentally relevant) case that crystal temperature drift is the major mechanism for disturbing the self-phase-locked state. The locking range is predicted to be about 170 MHz for a quarter-wave plate rotation angle of 6 deg.

The investigation of the phases of the output waves revealed a two-fold symmetry in phase space, in agreement with earlier, general studies. Considering phase instabilities induced by crystal temperature drift as observed experimentally, the divider's fractional frequency stability is derived. The fractional frequency instability of the by-2-divider is predicted to be $4 \cdot 10^{-21}$. It is also found, that the spectral bandwidth of the divider can be determined in good approximation by directly measuring the bandwidth of the beat signal between the two OPO subharmonic waves and dividing the obtained value by the proportionality factor 4. The results obtained in this chapter will be compared with a numerical analysis presented in the next chapter, and with experimental studies in chapter 6.

Chapter 4

Numerical Evaluation

In this chapter, the properties of the self-injection-locked by-2-divider OPO are investigated, for the first time, by numerically solving the time-dependent coupled field equations with experimental parameters. Note that this is completely different to the analytical treatment presented in chapter 3, where the steady-state solutions of the coupled field equations were derived. The numerical analysis in this chapter is not only used to verify the steady-state results from the previous chapter, but also to investigate the dynamical behavior of the self-phase-locked divider. The result of this study are time evolution plots of the OPO amplitudes and phases, which illustrate the self-phase locking process, thus giving a much better insight than obtained with the analytical approach.

For a numerical investigation of the by-2-divider OPO, the time-dependent coupled field equations 3.1 are integrated numerically using a fourth-order Runge-Kutta-method [89], similar to our earlier calculations on all-optical by-three-division [77]. The calculations were carried out with the MATLAB® software packet [90] using the experimental parameters of the setup (see section 5.4). To understand and to be able to interpret the results of the numerical integration of the coupled field equations, we first present a typical example. Based on that, in section 4.1, the coupled field equations are integrated for specific cavity detunings Δ_e and Δ_o in order to verify the agreement with the analytical results obtained in chapter 3.

In Fig. 4.1, a typical example of the time evolution of the coupled fields is shown. In this example, a QWP angle of $\vartheta_{QWP} = 6$ deg and equal cavity detunings $\Delta_e = \Delta_o = 60$ MHz are chosen. Fig. 4.1a shows the amplitudes, and Fig. 4.1b the phases of the resonator-internal pump wave, the e-wave and the

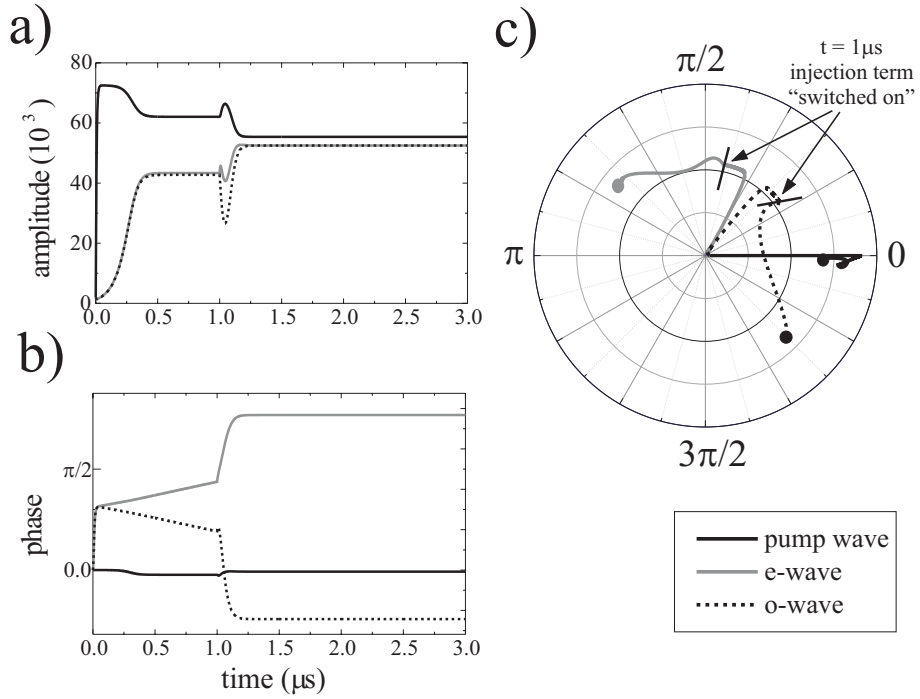

Figure 4.1: Time evolution of a) the amplitudes and b) the phases of the OPO fields for cavity detunings of $\Delta_e = \Delta_o = 60$ MHz. Solid black curve: pump wave, solid gray curve: e-wave, dashed black curve: o-wave. In c) the results are plotted together in a polar coordinate system, amplitudes as radius, phases as angle.

o-wave as a function of time. The pump wave data are displayed as solid black curve, the e-wave as solid gray curve and the o-wave as the dashed black curve. For a better visualization of the effect of phase locking, the OPO field equations are integrated by first turning off the effect of the quarter-wave plate (i.e., setting $\gamma = 0$ in Eqs. 3.1) for the first 1 μs. Thereafter, injection locking is "switched on", i.e. the coupled field equations are integrated by setting the phase locking terms to a nonzero value, which, in the case of Fig. 4.1 is $\gamma_0 = \sin(2 \cdot 6 \text{ deg}) \cdot \sqrt{\kappa_e \kappa_o} = 0.21 \cdot \sqrt{\kappa_e \kappa_o}$.

The effect of self-phase locking is clearly visible in Fig. 4.1. The oscillation of the three coupled fields starts at t = 0 from a low amplitude level. After about

0.5 μs, the amplitudes reach a steady state, while the phases of the e- and the o-wave diverge linearly as a function of time with equal speed but with opposite sign of the slope. In particular, the opposite-sign divergence shows that the sum of the two phases remains constant with respect to the resonator-internal pump phase. Note, that the data of the resonator-internal pump phase are with respect to the external pump field, and that the initial value of $\varphi_p = 0$ is the phase of the external pump field assumed for the numerical integration of the coupled field equations.

For the second part of the calculation, after 1 μs, the two subharmonic waves are injected into each other ($\gamma_0 = \sin(2 \cdot 6 \text{ deg}) \cdot \sqrt{\kappa_e \kappa_o}$). From Fig. 4.1b, one can see, that after 1 μs, the divergence of the phases first is accelerated and, after reaching a certain value, the divergence slows down and then stops. This process takes about 0.25 μs. The observed constancy of the phases with respect to the pump phase is a clear evidence of self-phase locking in the numerical model. This corresponds to the considerations in section 3.7, where the values of the OPO's subharmonic phases have been calculated explicitly. Note, that also the pump phase inside the OPO cavity is adjusted to a slightly different value with respect to the external pump phase.

One can see in Fig. 4.1a that, at the same time, the field amplitudes assume specific values, which are different from the ones before. Specifically, the values assumed by the e- and o-wave amplitudes are significantly higher than the former values, whereas the new value of the pump amplitudes is lower than the former, non-phase-locked steady-state value. The latter observation corresponds to and confirms the prediction of the analytical treatment, where it was found that the self-phase-locked divider OPO should have a lower oscillation threshold than the free-running OPO (compare section 3.4, Eq. 3.12, and Fig. 3.5)

The results of the two graphs of Fig. 4.1a and b are summarized as a polar diagram in Fig. 4.1c. Here, the complex amplitude of each of the three fields is displayed as radius and a corresponding phase angle, which results in three traces in Fig. 4.1c, that display the temporal evolution of the coupled fields. Upon startup of the OPO, the pump trace, the e-, and the o-wave traces emerge out of a location near the origin, because small field amplitudes were used as initial values for the calculation. Thereafter, the e- and the o-wave rotate, initially, with a constant angular velocity due to the constant non-zero detuning. The "turning-on" of the half-wave plate coupling between the two waves causes this rotation to

be modified at the positions of t = 1 μs as indicated by short solid lines. From thereon, the phases assume new and constant steady-states values at the positions indicated by dots. With a numerical calculation as the one presented, the effect of self-injection locking on the phases of the OPO subharmonic waves is demonstrated clearly.

4.1 Locking range

In the current section, the coupled field equations are integrated numerically for different cavity detunings Δ_e and Δ_o, such that the results can be compared with the analytical steady-state solution derived in the previous chapter. However, beyond this, we will show that the dynamics of self-injected OPOs can be very complex and shows a rich variety of scenarios.

Figure 4.2 shows another example of time evolution of the OPO's coupled fields with the detunings chosen such that the locking condition of Eq. 3.11 is fulfilled, so that self-phase locking should occur according to the analytical solution of the field equations. Here, the e-wave detuning is $\Delta_e = 60$ MHz, and the o-wave detuning is $\Delta_o = 30$ MHz. For this case we expect a self-phase-locked state with the field amplitudes of the e- and the o-wave having the relation $\frac{b_o}{b_e} = \sqrt{\frac{\Delta_e}{\Delta_o}} = \sqrt{2}$ (see Eq. 3.31). The time evolution of the divider's phases in Fig. 4.2b indeed shows evidence of the phases assuming certain values after the self-injection term is activated and from then remaining constant, which means that the OPO is self-phase-locked. The result of the corresponding time evolution of the amplitudes is shown in Fig. 4.2a. As the steady-state values we retrieve $b_o = 54638$ and $b_e = 38635$, which leads to $\frac{b_o}{b_e} = 1.4142\ldots \approx \sqrt{2}$, in excellent agreement with the analytical prediction.

As opposed to the previous example, self-phase locking is not expected to happen, if the detunings are chosen to be either $\frac{\Delta_e}{\Delta_o} < 0.43$ or $\frac{\Delta_e}{\Delta_o} > 2.19$, even if the detunings are small. To investigate the prototype behavior for such a case, the coupled field equations have been integrated for the cavity detunings $\Delta_e = 32$ MHz and $\Delta_o = 8$ MHz. With $\frac{\Delta_e}{\Delta_o} = 4 > 2.19$, this set of detunings is clearly outside the locking area, as depicted schematically in Fig. 3.3.

The result of the numerical evaluation is shown in Fig. 4.3. As before, the self-injection term of the two subharmonic waves is "switched on" after 1 μs. From Fig. 4.3a one can see that thereafter, the formerly steady subharmonic

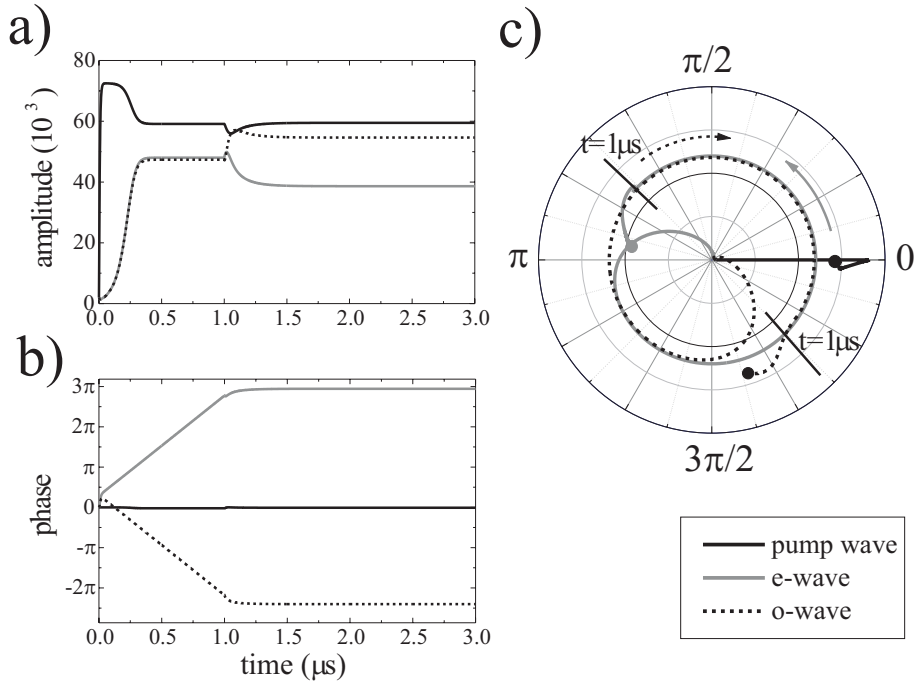

Figure 4.2: Time evolution of a) the amplitudes and b) the phases of the OPO fields for cavity detunings of $\Delta_e = 60$ MHz and $\Delta_o = 30$ MHz. Solid black curve: pump wave, solid gray curve: e-wave, dashed black curve: o-wave. In c) the results are plotted together in a polar coordinate system, amplitudes as radius, phases as angle.

amplitudes start oscillating. At the same time, the phases continue to diverge, where the continuous change of the phases's values contain a small fraction of an oscillation as well. The effect of the self-injection term can be seen nicely in the polar plot (Fig. 4.3c). The subharmonic waves' amplitudes first increase from their low (near zero) starting values to follow a clockwise (o-wave) and a counter-clockwise (e-wave) *circularly* rotating trace. After activating the self-injection term at t = 1 μs, the circular traces are altered into *elliptic* ones, while the direction of the rotations is maintained, as well as the average angular velocity i.e., the number of revolutions per time.

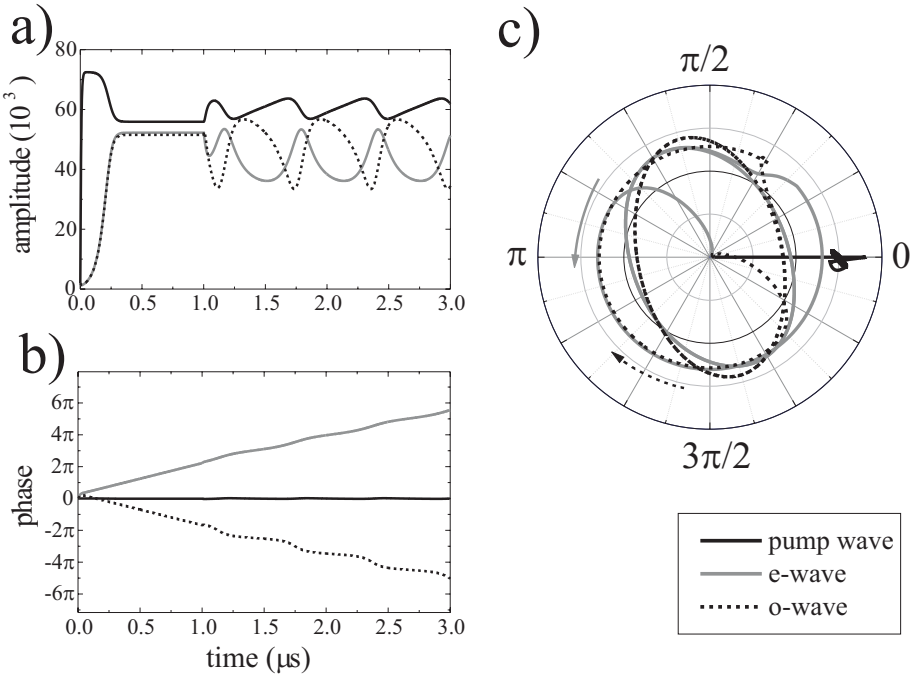

Figure 4.3: Time evolution of a) the amplitudes and b) the phases of the OPO fields for cavity detunings of $\Delta_e = 32$ MHz and $\Delta_o = 8$ MHz. c) results summarized in a polar coordinate system, amplitudes as radius, phases as angle. Solid black curve: pump wave, solid gray curve: e-wave, dashed black curve: o-wave.

The last prototype of self-injection dynamics is the case of detunings of opposite signs. According to the analytical solution and Eq. 3.11, there should be no locking for this case. As an example, the time evolution of the fields for Δ_e = 30 MHz and Δ_o = -30 MHz is shown in Fig. 4.4. As before, the subharmonic amplitudes start oscillating in absolute value after the self-injection term is activated at t = 1 μs, and the phases continue to diverge with an additional periodic modulation superimposed. Thus, indeed, there is no locking observable. As opposed to the case discussed before (with the two cavity detunings being of the same sign, but outside the locking area) the oscillations of the absolute values of the subharmonic amplitudes are perfectly mirrored. As opposed to this, such

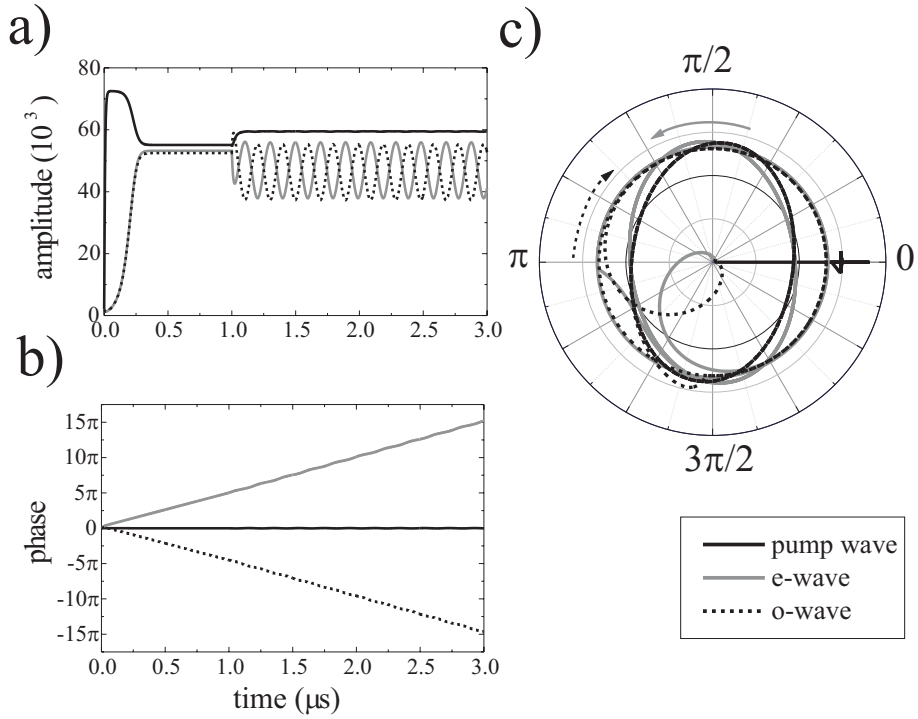

Figure 4.4: Time evolution of a) the amplitudes and b) the phases of the OPO fields for cavity detunings of $\Delta_e = 30$ MHz and $\Delta_o = -30$ MHz. c) results summarized in a polar coordinate system, amplitudes as radius, phases as angle. Solid black curve: pump wave, solid gray curve: e-wave, dashed black curve: o-wave.

behavior can never be observed for any pair of detunings having the same sign.

For spot checking the results at a large number of different detunings across the Δ_e-Δ_o-plane, the coupled fields of the OPO by-two-divider were integrated numerically in the same manner as for the examples discussed above. From these calculations we have found that the locking area has the same shape as depicted already in Fig. 3.6a, which is the locking area for the low threshold case. Our numerical calculation also confirms the shape of the "radial" border of the locking area of Fig. 3.6a: If the detunings are chosen to fulfill the locking condition of Eq. 3.11, but such that the threshold for OPO oscillation becomes too high to be

overcome with a pump power of 300 mW, the result of the numerical evaluation is that the e- and the o-wave amplitudes remain zero.

A final observation from the numerical calculation is the following: the steady-state values assumed by the three amplitudes and phases in the self-phase-locked operation agree well with the analytically predicted values (Eqs. 3.12, 3.34, 3.35, 3.36, 3.37 3.32, and 3.33). In summary, the numerical calculation agrees well with the analytical calculation, which indicates the reliability of our numerical approach.

4.2 The two threshold states

The possibility of numerically evaluating the OPO's coupled field equations enables a closer investigation of the high threshold states. Of particular interest is the question, whether we would be able to observe a stable solution for the OPO fields oscillating in the high-threshold state. By setting the initial values close to the analytical solutions for the high-threshold state, we can investigate not only whether there is a stable high-threshold solution in the numerical evaluation, but also whether there is any influence of an attractor observable, i.e., whether the OPO fields' amplitudes and phases do perform, for example, oscillations around the solution of the high-threshold state.

To follow this strategy, the coupled field equations are integrated numerically in two different ways: Firstly, the analytical solutions of the low-threshold state are used as the initial values of the pump, the e- and the o-wave amplitudes and phases, and secondly, the values of the high-threshold solution are used as the initial values. Such a solution consists of six numbers, namely the amplitudes and the phases of the three interacting fields: $\{b_p, b_e, b_o, \varphi_p, \varphi_e, \varphi_o\}$. To give a specific example, the initial values are calculated using the equations derived in chapter 3 for a quarter-wave plate rotation angle of $\vartheta_{QWP} = 6$ deg and cavity detunings of $\Delta_e = 50$ MHz and $\Delta_o = 45$ MHz. The actual values, which are derived for the two solutions and which are used as initial values for the numerical integration of the coupled field equations are listed in table 4.1. In this table, also the equations are noted, from which the respective numbers are obtained. Note, that the Eq. 3.12 for the pump field amplitude b_p yields two values due to the two possible signs of $\sqrt{\alpha}$, and that the equations derived thereafter subsequently also yield two numbers, because the pump field amplitude is a parameter to be inserted into each

of them.

	b_p	b_e	b_o	φ_p	φ_e	φ_o
Low	55215.7	51292.0	54066.5	0.00017	2.43693	−0.86579
High	71357.0	15100.4	15917.2	0.01310	2.77320	−0.52952
Equation	3.12	3.34	3.35	3.36, 3.37	3.32, 3.33	3.32, 3.33

Table 4.1: The solutions for the pump wave, the e- and the o-wave amplitudes and phases for the two threshold states, calculated for a quarter-wave plate rotation angle of $\vartheta_{QWP} = 6$ deg and for the cavity detunings $\Delta_e = 50$ MHz and $\Delta_o = 45$ MHz. These values are used as initial values for numerically integrating the coupled field equations.

Fig. 4.5a shows the amplitudes, and Fig. 4.5b the phases as a function of time for the case, that the OPO's coupled field equations are integrated starting from the low-threshold solution. As expected, the amplitudes and phases do not vary, but stay constant at the steady-state values of the stable solution. In contrast, when starting the integration from the high-threshold solutions, the amplitudes (Fig. 4.5c) as well as the phases (Fig. 4.5d) quickly (within the cavity lifetime of 0.2 μs) leave the high-threshold values and assume the low-threshold values, in full agreement with the prediction of the stability analysis of section 3.5. Note, that the process of assuming steady-state is strongly damped, as no oscillation can be observed. The same behavior has been found in numerous calculations in a wide range of values for Δ_e and Δ_o.

To conclude this section, the instability of the high-threshold state has been demonstrated also numerically. Here we have just given a single example, for the sake of specificity. The example shows that the high-threshold values are abandoned and the low-threshold values are assumed quickly in a strongly damped motion lacking any oscillatory behavior.

4.3 Behavior close to the steady-state solutions

From the observations presented in the previous section, the low-threshold steady-state solutions seem to be strongly attractive to the coupled field amplitudes and phases, such that they are assumed on a direct path in phase space. However, the question arises, how direct these paths are and, in general, what types of

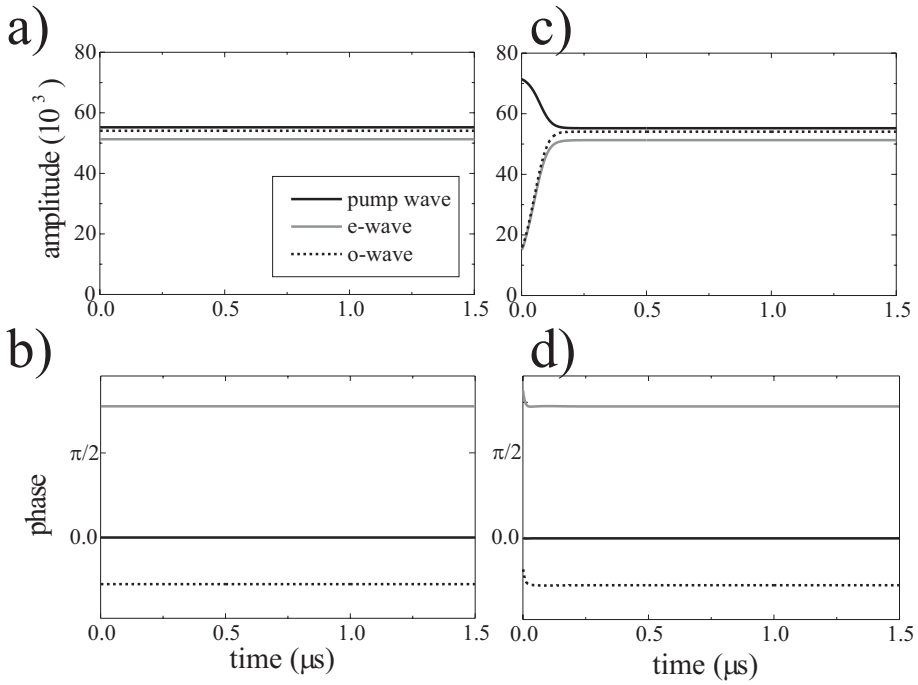

Figure 4.5: Time evolution of the coupled field equations. a) amplitudes and b) phases for the case, that the OPO fields are released in the low-threshold state. c) amplitudes and d) phases for the case, that the OPO fields are released with the analytical solutions of the high-threshold state as initial values. Calculation parameters: Quarter-wave plate angle of $\vartheta_{QWP} = 6$ deg, cavity detunings of $\Delta_e = 50$ MHz and $\Delta_o = 45$ MHz.

behavior OPO may exhibit around the analytical solutions. In particular, the OPO's intrinsic phase stability in the self phase locked state, in dependence of the operation parameters is of great interest. An important goal of these investigations is the identification of the optimum specifications of the OPO setup, in order to achieve a high stability of the divider in the experiment.

Therefore, we integrate the field equations in direct vicinity of the analytically determined stable (low threshold) steady-state solutions. For this, the initial values of the OPO fields are chosen to be almost equal to the steady-state values.

For these investigations, the notation of the stability analysis in section 3.5

is used again, by defining the amplitude and phase deviations $\delta b_x(t)$ and $\delta\varphi_x(t)$ as the difference between the actual values $b_x(t)$ and $\varphi_x(t)$ and the steady-state values:

$$\delta b_x(t) = b_x(t) - \overline{b_x} \tag{4.1}$$

$$\delta\varphi_x(t) = \varphi_x(t) - \overline{\varphi_x} \tag{4.2}$$

To recall the result of chapter 3, a complete solution for the OPO fields in steady-state consists of a set of six numbers $\{b_p, b_e, b_o, \varphi_p, \varphi_e, \varphi_o\}$. Therefore, for a given solution, the OPO fields can be elongated out of the steady-state in six directions (dimensions), by setting one or more of the six deviations $\{\delta b_p, \delta b_e, \delta b_o, \delta\varphi_p, \delta\varphi_e, \delta\varphi_o\}$ to a non-zero value. For each of the possible six independent deviations, the resulting dynamics of the six OPO variables, i.e., the three amplitudes and the three phases, can be studied. For brevity, in the following paragraphs, some representative calculations for three different possible OPO setups are presented and the results are compared.

4.3.1 OPO with a high-finesse cavity

One of the most desirable properties for an OPO is a low pump power at threshold. In the particular case of a by-2-divider OPO, a low threshold is imperative for OPO operation with the additional intracavity quarter-wave plate. As the first example for the investigation the stability characteristics, we assume that the OPO is designed for a low threshold having a high cavity finesse for all three interacting waves.

The general OPO setup is identical to the one introduced before (compare Fig. 3.1). In order to implement a high-finesse cavity with realistic parameters in the theoretical model, the cavity decay rates for the three OPO waves have to be determined for cavity mirrors, which are actually available in the experiment. Specifically, the pump input coupling mirror is chosen to allow 1% transmission of the pump wave and is highly reflective for the subharmonic waves, while the output coupling mirror is highly reflective for the pump radiation and transmits 1% of the subharmonic radiation. From these transmission values and from the given length and efficient nonlinearity of the PPLN crystal used in the OPO, the decay rates κ_p, κ_e, and κ_o, and the nonlinear coupling coefficient D can be calculated from the equations 3.2 and 3.4, respectively. In the example presented here, the

quarter-wave plate rotation angle is chosen to be $\vartheta_{QWP} = 9$ deg. Note, that a particular choice of the cavity detunings (here $\Delta_e = 150$ MHz and $\Delta_o = 110$ MHz), determines the actual steady-state fields of the self-phase-locked OPO, but has no effect on the OPO behavior in close vicinity of these steady-state values. The reason for this is, that in close vicinity of an equilibrium, the reaction of the three amplitudes and phases can in good approximation be described by a set of six linearized equations, which have been derived in the course of this work. These linearized equations, however, do not depend on the cavity detunings. This means, that the positions of the equilibria in phase-space do depend on the cavity detunings, but the movement of the fields' amplitudes and phases after a small elongation out of the equilibria do not. The operation parameters used for the following calculations are summarized in table 4.2.

κ_p	κ_e	κ_o	D	ϑ_{QWP}
23.5 MHz	39.6 MHz	38.8 MHz	438 Hz	9 deg

Table 4.2: Parameters used for the integration of the coupled field equations, as would be typical for an OPO with a high-finesse cavity.

Figure 4.6 shows one example of the divider's reaction on an elongation out of its steady state. In the case shown, the fields are located next to a low-threshold steady-state, such that initially only the e-wave is off its equilibrium value. Shown are the traces for twelve different initial values $\{0, \delta b_e, 0, 0, \delta\varphi_e, 0\}$, where the deviations of the e-wave amplitude and phase lie on a circle around the steady-state, such that $\left(\frac{\delta b_e}{10}\right)^2 + \left(\frac{\delta\varphi_e}{0.1rad}\right)^2 = 1$. In Fig. 4.6a the graph shows the reaction of the pump wave to these elongations of the e-wave, depicted as traces in the phase space of the pump wave. This means, that for each time within the considered time span after the elongation, the pump phase is displayed as a function of the pump amplitude, with respect to the steady-state values $\overline{b_p}$ and $\overline{\varphi_p}$ according to Eqs. 4.1 and 4.2. Analogously, Fig. 4.6b shows the reaction of the e-wave itself, and Fig. 4.6c shows the reaction of the o-wave.

One can see easily from Fig. 4.6, that the reaction of any of the three waves to the elongation of one wave is a confined oscillation around the steady-state value, which does not exceed a certain oscillation amplitude. A closer inspection

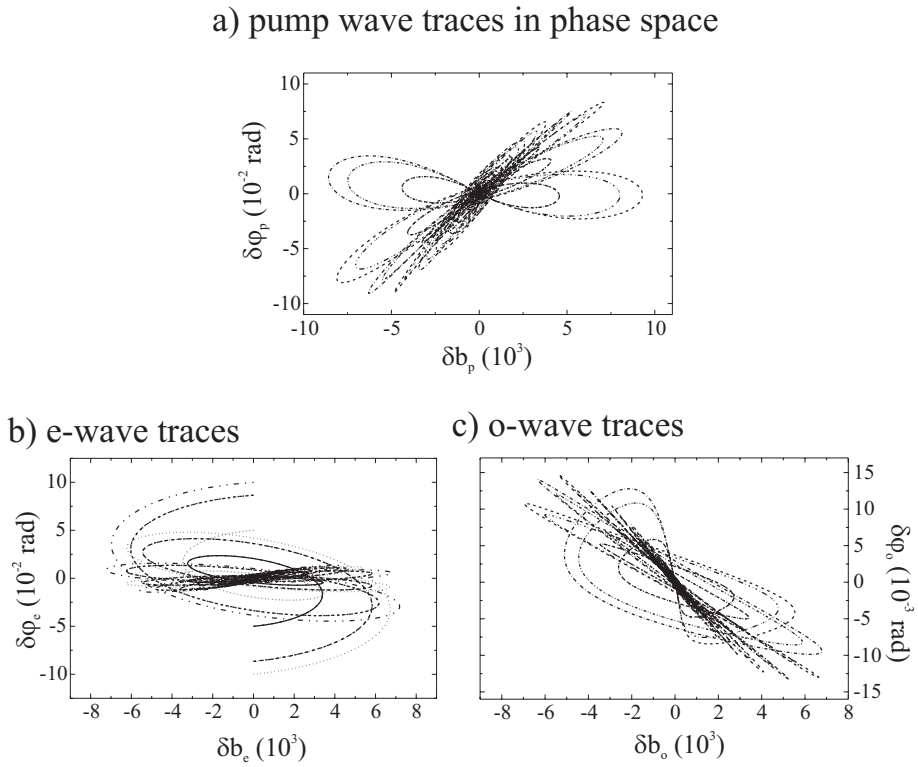

Figure 4.6: Time evolution of the divider's amplitudes and phases for small elongations of the e-wave out of its steady state, calculated assuming a high-finesse cavity. a) Upper graph: reaction of the pump wave to the elongation of the e-wave, plotted in the phase space of the pump wave i.e., variation of the pump amplitude δb_p as the x-axis, variation of the pump phase $\delta\varphi_p$ as the y-axis. b) Lower left: reaction of the e-wave, and c) lower right: reaction of the o-wave.

of Fig. 4.6 reveals, that the oscillation of the amplitudes of all three waves reaches values that are three orders of magnitude higher than the initial elongation of the e-wave amplitude, whereas the phase oscillations do not exceed the initial elongation of the e-wave phase (i.e. 0.1 rad). Therefore, one can conclude that the phase oscillations of the self-phase-locked by-two-divider are damped, while strong amplitude oscillations are induced.

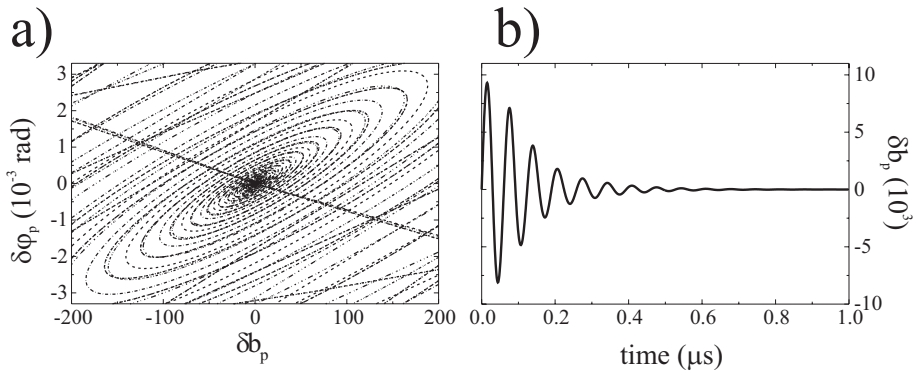

Figure 4.7: Time evolution of the pump wave after a small elongation of the e-wave. a) Magnification of graph a) of Fig. 4.6, showing the center of the oscillation of the pump wave amplitude and phase, b) pump wave amplitude as a function of time.

Figure 4.7a shows a magnification of the center of Fig. 4.6a, i.e. a magnification about the steady-state value of the pump wave in phase space. One can see that the pump wave amplitude and phase are both oscillating around the steady-state value, with a continuously decreasing oscillation amplitude. The resulting traces in phase space, which are displayed in Fig. 4.7a are thus spirals towards the center in clockwise direction. Figure 4.7b shows the amplitude of one of the pump wave traces as a function of time. From this figure one can see that the movement is indeed strongly oscillatory, but nevertheless damped. By fitting an exponential decay function to the envelope of the pump wave amplitude, we yield a characteristic time of $t_{exp} = 0.13$ μs, after which the pump wave amplitude is decreased to $\frac{1}{e}$ of its initial value.

The calculations presented here have treated the case, that only the amplitude and phase of the e-wave are elongated out of the equilibrium. Analogously, the pump wave or the o-wave amplitude and phase can also be subject to an elongation out of the steady-state values. In this case, the reactions of the three waves show a similar behavior as we observed with the elongation of the e-wave parameters. The amplitudes and phases of the three waves always return to the equilibrium, while they perform oscillations in the order $\approx 10^4$ and ≈ 0.1 rad for the amplitude

and phase, respectively.

Concluding this section, it has been observed that after elongation of the amplitude and phase of any one of the three interacting waves out of their steady-state values, these parameters show strong oscillations and a damped movement towards their equilibrium values, corresponding to one of the two low-threshold, self-phase-locked states of the by-2-divider.

However, the observed oscillatory behavior is not desirable for a frequency divider OPO, because it might reduce the divider's frequency stability. In order to reduce the oscillations, a higher damping is introduced into the system by increasing the cavity decay rates. In the following section the behavior of an OPO based on a cavity with a lower finesse is investigated.

4.3.2 OPO with a medium-finesse cavity

The second example considered here is an OPO with a cavity of lower finesse than the one described before. Again, transmission parameters for the cavity mirrors are used which were actually available in the experiment. The pump input coupling mirror (M1) is chosen to provide 6% transmission of the pump wave and is highly reflective for the subharmonic waves, while the output coupling mirror (M2) is highly reflective for the pump radiation and transmits 2% of the subharmonic radiation. Again, the parameters for numerically integrating the field equations are derived from Eqs. 3.2 and 3.4. The cavity detunings are chosen to be $\Delta_e = 150$ MHz and $\Delta_o = 110$ MHz. These detunings are within the locking area for the chosen quarter-wave plate rotation angle of $\vartheta_{QWP} = 9$ deg, which is the same as before. The operation parameters used for the calculations are summarized in table 4.3.

κ_p	κ_e	κ_o	D	ϑ_{QWP}
61.3 MHz	47.3 MHz	46.4 MHz	438 Hz	9 deg

Table 4.3: Parameters used for the integration of the coupled field equations, as typical for an OPO with a medium-finesse cavity.

With these parameters, the relaxation of the three waves after a small elongation of the e-wave from its steady-state values is calculated numerically. Figure

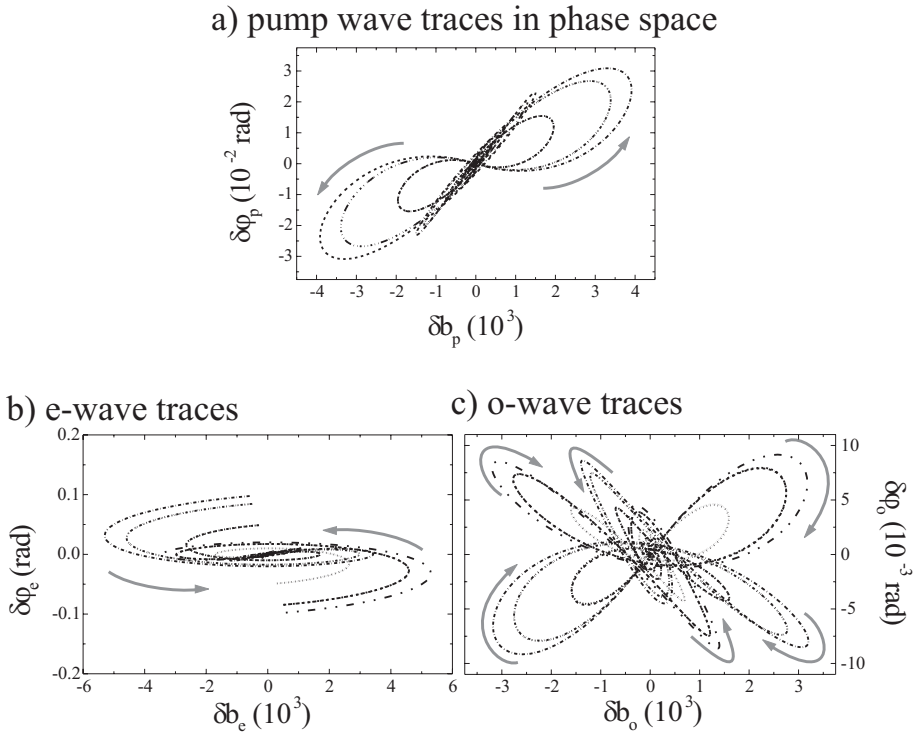

Figure 4.8: Time evolution of the divider's amplitudes and phases for small elongations of the e-wave out of its steady-state, calculated assuming a medium-finesse cavity. a) reaction of the pump wave to the elongation of the e-wave, plotted in the phase space of the pump wave, b) reaction of the e-wave, and c) reaction of the o-wave.

4.8a shows the reaction of the pump wave in its phase space, and analogously Figs. 4.8b and c display the reaction of the e-wave and the o-wave. In each graph, the direction, in which the respective wave travels through phase space, is indicated by gray arrows.

One can see easily from Fig. 4.8, that the reaction of any of the three waves to an initial elongation of the parameters of one of them is a confined oscillation about steady state, which does not exceed a certain oscillation amplitude. Note that traces in a phase space never cross: The apparent crossings in Fig. 4.8

arise from the fact, that the graphs actually are projections of the divider's six dimensional phase space onto two dimensions.

As in the example before, the oscillation of the amplitudes reach values higher than the initial elongation by three orders of magnitude, i.e., up to 10^4. The phase oscillations, however, are strongly damped and never reach values as high as the elongation itself, i.e., the phase elongation is always ≤ 0.1 rad.

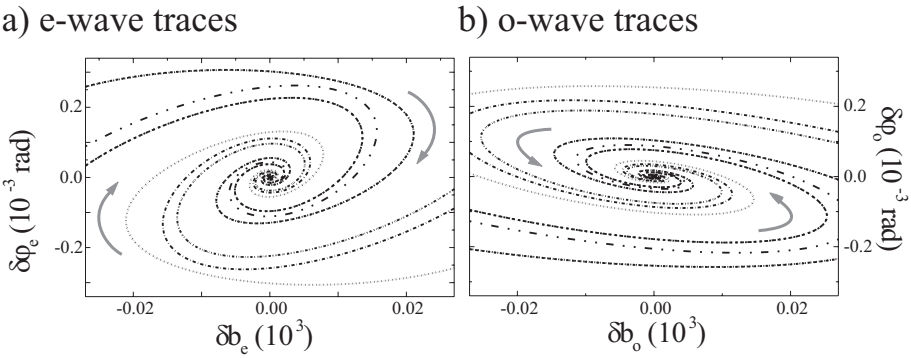

Figure 4.9: Magnification of the lower graphs of Fig. 4.8. a) center of the oscillation of the e-wave amplitude and phase, b) corresponding center of the o-wave oscillation.

A closer look of the center of either of the graphs in Fig. 4.8 shows that the coupled fields amplitudes and phases finally end up again in the steady-state values. This is shown in Fig. 4.9a, where the magnification of the e-wave's oscillation center is displayed, and in Fig. 4.9b, where the corresponding o-wave center is displayed. The direction of the traces with increasing time is indicated by arrows. Both waves head towards their steady-state centers in spirals. Note, that the e-wave traces performs a clockwise spiral, whereas the o-wave traces performs a counterclockwise spiral. This counterrotating behavior can be explained by combining two facts: firstly, the e- and o-wave phases are coupled due to their sum phase being determined by the approximately constant pump phase. Secondly, their amplitudes are coupled as well via the conversion process: if an e-wave photon is generated out of a pump photon, also an o-wave photon is generated. Therefore the absolute values of the subharmonic amplitudes are forced

to oscillate in phase, while the phases oscillate out of phase, which leads to the counterrotating movement of the two waves in their phase spaces.

In comparison to the high-finesse example investigated before in section 4.3.1, the oscillations predicted for medium finesse are much reduced. However, there are still oscillations observable, which might reduce the divider's phase stability. The partially successful reduction of the oscillations gives rise to the question, whether a further reduction of the OPO cavity finesse would also lead to a further diminishing of the oscillations. To follow that strategy of reducing the cavity finesse and eventually identify an optimum OPO cavity, in the following section an OPO with a cavity of still lower finesse is investigated regarding its behavior after a small elongation out of its phase-locked steady-state.

4.3.3 OPO setup with a low-finesse cavity

The low-finesse cavity is also based on the cavity mirrors used in the experiment. The pump input coupling mirror allows 15% transmission of the pump wave and is highly reflective for the subharmonic waves, while the output coupling mirror is highly reflective for the pump radiation and transmits 1% of the subharmonic radiation. The cavity decay rates κ_p, κ_e, and κ_o, and the nonlinear coupling coefficient D used for the numerical integration are derived from the experimental OPO operation characteristics (see section 5.4). Note, that the pump power at threshold is increased, such that with the cavity detunings used above, the OPO could not be operated above threshold. To reach threshold with the numerical calculations, this OPO is modeled with smaller cavity detunings, namely $\Delta_e = 50$ MHz and $\Delta_o = 18$ MHz. The quarter-wave plate rotation angle is maintained at $\vartheta_{QWP} = 9$ deg. The integration parameters are summarized in table 4.4.

κ_p	κ_e	κ_o	D	ϑ_{QWP}
350 MHz	114 MHz	117 MHz	1050 Hz	9 deg

Table 4.4: Parameters used for the integration of the coupled field equations as typical for an OPO with a low-finesse cavity.

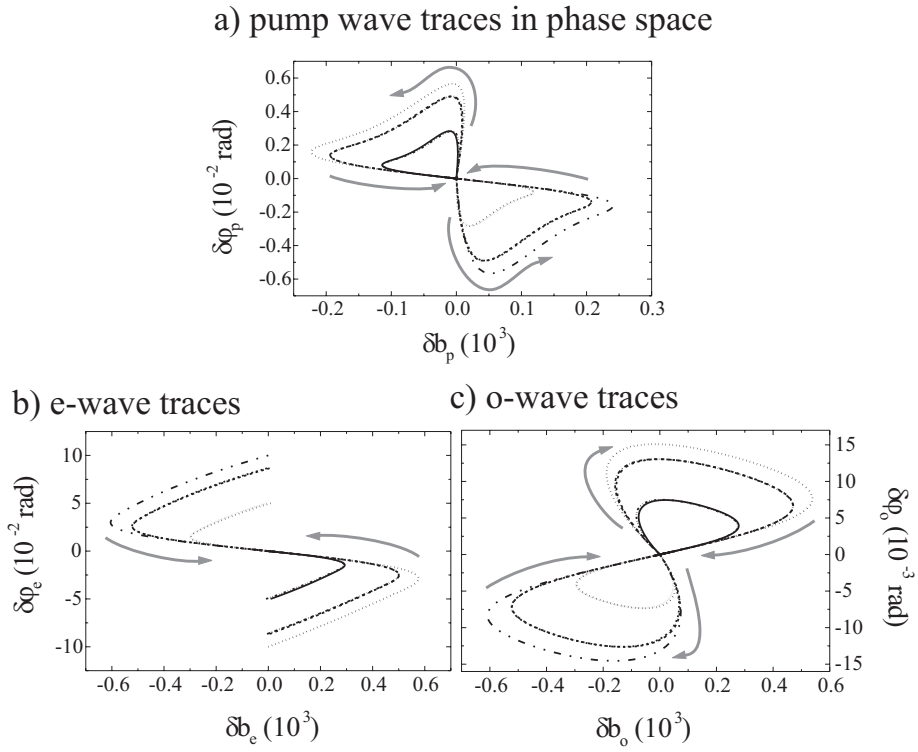

Figure 4.10: Time evolution of the divider's amplitudes and phases for small elongations of the e-wave out of its steady-state, calculated by assuming a low-finesse cavity. a) reaction of the pump wave to the elongation of the e-wave, plotted in the phase space of the pump wave, b) reaction of the e-wave, and c) reaction of the o-wave.

The reaction of the three waves to a small elongation of the e-wave out of its steady-state values are calculated as described before with these new parameters and the results are displayed in Fig. 4.10.

From Fig. 4.10b, which shows the e-wave reaction, one can see very clearly, that after elongation out of their steady-state values located in the origin of the phase space, the e-wave amplitude and phase strive back to these steady-state values. This is accompanied by reactions of the pump and of the o-wave, although whose initial values corresponded exactly to their steady-state values (The traces of the

pump and the o-wave are depicted in Figs. 4.10a and c, respectively). Note, that the elongation of each of the three amplitudes is less than 10% of the elongation they suffered in the case of a high-finesse cavity. From the graphs displayed in Fig. 4.10, it seems that each of the waves leaves their steady-state point and then strives back to that point in one wide arc. This process takes roughly 0.2 μs.

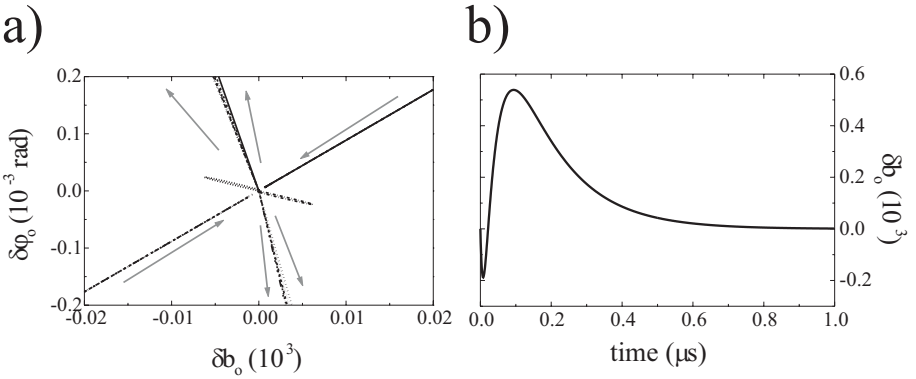

Figure 4.11: Time evolution of the o-wave after a small elongation of the e-wave. a) Magnification of graph c) of Fig. 4.10, showing the center of the oscillation of the o-wave amplitude and phase, b) o-wave amplitude as a function of time.

Figure 4.11a shows a magnification of the origin of Fig. 4.10c, i.e., around the steady state value of the o-wave in phase space. The direction of the traces is indicated by gray arrows. One can see that the traces leave the steady-state value on slightly different paths, according to the different directions of the e-wave elongation. However, all traces return to the steady-state on nearly the same path. Figure 4.11b shows the amplitude of one of the e-wave traces as a function of time. From this figure, one can see, that the movement is indeed strongly damped, such that no oscillation is observed, and the amplitude simply returns to the steady-state value in a curve that can be described by exponential decay. By fitting an exponential function to the amplitude for the time span after t = 0.2 μs, i.e., after the wide arc has been completed, we yield a characteristic time $t_{exp} = 0.14$ μs, after which the o-wave amplitude is decreased to $\frac{1}{e}$ of its value. The same behavior, including the exponential decay with a characteristic time of $t_{exp} = 0.14$ μs can be observed for the amplitudes and phases of all three waves.

In summary, the behavior of the interacting OPO waves has been investigated numerically in close vicinity of the steady-state solutions of the self-phase-locked by-2-divider OPO. Three typical cases that may be realized in an experiment (high, medium or lower finesse of the OPO cavity) have been analyzed. It is found, that a cavity with a relatively high finesse leads to temporary strong oscillations of the parameters of all three waves about their steady-state values in phase-space. In contrast to this, a relatively low finesse cavity ensures that the amplitude and phase of each of the OPO waves strives back to steady-state in a single, non-oscillating, strongly damped arc-shaped curve. In addition, the absolute value of the amplitude elongation of each of the three waves is reduced by more than 90% as compared to the case of a high-finesse cavity. The low-finesse case behavior promises a very high phase stability of the by-2-divider OPO. This is why for the experimental studies presented in chapter 6, the OPO setup with the lowest cavity finesse possible within the restrictions of the available pump power was used.

4.3.4 Small deviation from the high-threshold states

In view of the very stable behavior of the OPO with respect to thelow-threshold steady-state explored above, it is now particularly interesting to investigate a high-threshold solution for comparison. An analog time evolution calculation of the three coupled fields has been carried out with any of the OPO's waves slightly elongated out of the high-threshold steady-state values corresponding to the low-threshold example above. In Fig. 4.12, one representative example of the results is shown, namely the reaction of the e-wave to a small elongation of the e-wave from the high-threshold steady-state solution. For any small elongation, the OPO would leave the high-threshold solutions and assume the low-threshold steady-state values.

Figure 4.13 shows magnifications of two fragments of Fig. 4.12, in order to take a closer look at the behavior of the OPO fields around the analytical solutions. In Fig. 4.13a, the vicinity of the high-threshold solution is displayed, i.e. the starting point of the traces of Fig. 4.12. From this graph, one can see, that the traces strive away from the high-threshold solution on direct paths. This demonstrates clearly, that the high-threshold solution is not a quasi-stable or a locally, i.e., "weakly"-stable equilibrium, but that it is indeed an unstable solution, which has previously been mistaken as a stable operation point by others [73], [40].

In contrast, the magnification of the vicinity of the low-threshold solution dis-

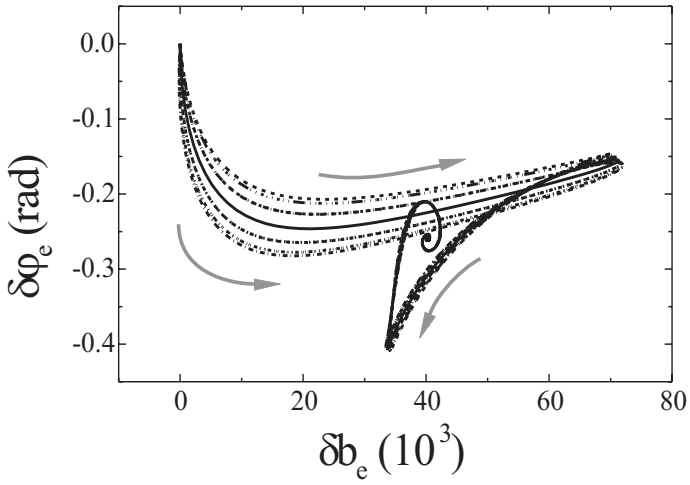

Figure 4.12: Time evolution of the e-wave amplitude and phase for small deviation of the o-wave out of the high-threshold steady-state values, plotted in the phase space of the e-wave. Out of the high-threshold steady-state, the amplitudes and phases of the coupled fields assume the low-threshold steady-state values.

played in Fig. 4.13b shows the same stable oscillation with damped amplitudes as was observed before in Fig. 4.9.

Summarizing this section, the vicinity of the low- and the high-threshold solutions have been numerically investigated by considering small deviations from the analytically calculated solutions. It has been shown, that after an elongation of amplitude or phase of any of the waves, the OPO reacts with oscillations around the low-threshold solution. By systematically investigating the behavior of the OPO waves in dependence of the cavity finesse after a small elongation out of steady-state, the optimum operation parameters for the by-2-divider are identified. It is found that the unwanted oscillations, which would negatively affect the quality of the phase-coherence, can be damped by introducing losses to the OPO cavity.

As opposed to this, if the OPO fields are released in close vicinity of the high-threshold solution, this solution is abandoned immediately and the low-threshold solution is assumed. This behavior is again in agreement with the stability analy-

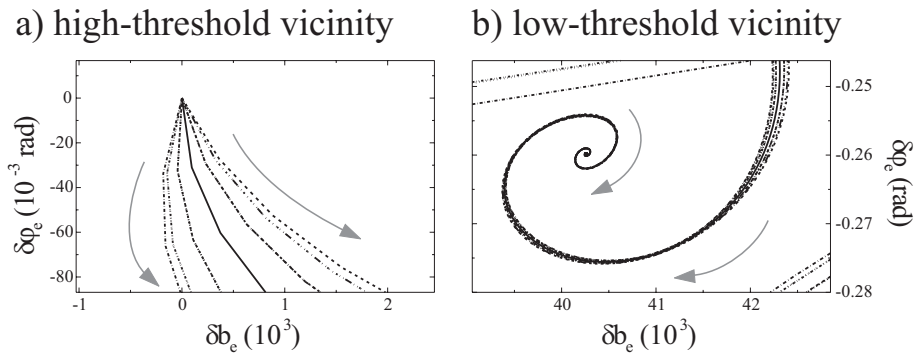

Figure 4.13: Magnifications of Fig. 4.12: a) Magnification of the vicinity of the high-threshold solution, and b) magnification of the vicinity of the low-threshold solution.

sis of section 3.5, which analytically lead to the conclusion that the high-threshold states for type-II phase-matched by-two-divider OPOs are not stable. In conclusion, one can expect a rich scenario of phase relaxation dynamics to be discovered in the experiment.

4.4 The two phase states

As a result of the analytical investigation in chapter 3, it was found that the self-phase-locked OPO can assume one of two phase-eigenstates. These two eigenstates have been found to be absolutely equivalent in steady-state, such that there is no parameter, which determines which one of the eigenstates is attained.

With the numerical integration of the time-dependent coupled field equations, the situation is different. Unlike the analytical calculations, the numerical model does not presume steady-state, such that the temporal development of any initial state can be investigated. In this section, this is used to answer the question of how the assumed eigenstate depends on the initial values used for the integration.

To investigate this dependence, the coupled field equations were integrated numerically while systematically changing several parameters. It was found that indeed two different phase states can appear as the result of the integration, and

that these phase states show a two-fold symmetry in phase space. As expected from the analytical calculations, it was also found that none of the external, i.e. experimentally adjustable, parameters, has any influence on which phase state would be assumed during the integration process.

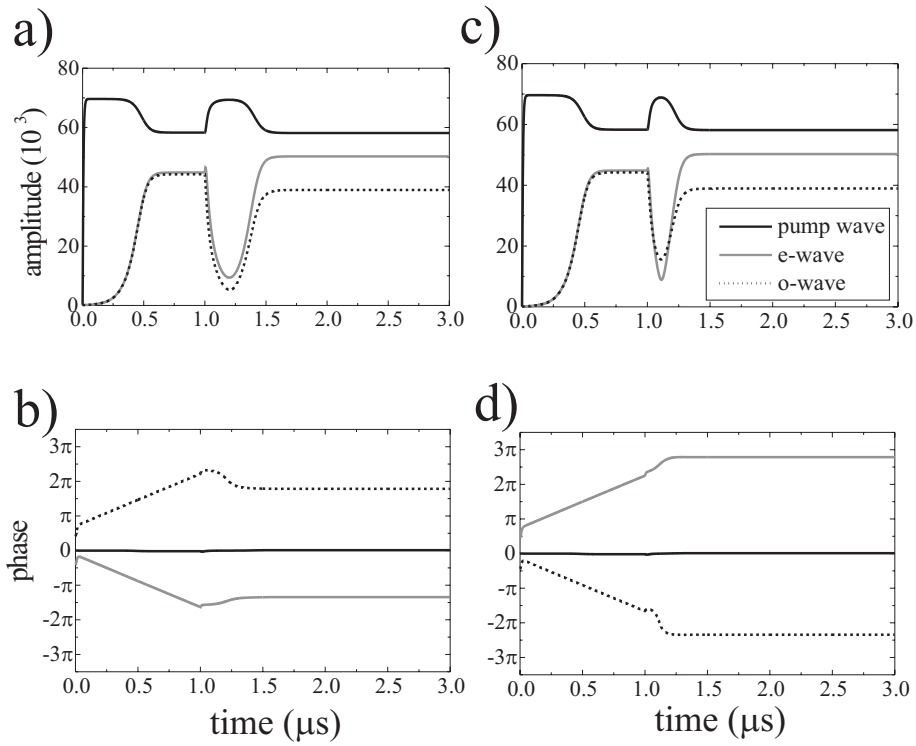

Figure 4.14: Time evolution of the coupled field equations for cavity detunings of Δ_e = 30 MHz and Δ_o = 50 MHz, where the self-injection term between the two waves is "switched on" at t = 1 μs. a) amplitudes and b) phases integrated with initial phases of φ_e^0 = -1.3 and φ_o^0 = 1.3 c) amplitudes and d) phases for the same parameters, but integrated with initial phases of φ_e^0 = -1.4 and φ_o^0 = 1.4.

The only integration parameters that have been found to have an influence on which phase state is assumed, are the initial values of the subharmonic phases. In Fig. 4.14, two examples are shown, which demonstrate this dependence. In both cases, the self-injection term is "switched on" after 1 μs, to make the effect of

self-injection visible. Both examples are generated by integrating the coupled field equations using the same parameters and the same cavity detunings $\Delta_e = 30$ MHz and $\Delta_o = 50$ MHz. Only the initial phases φ_e and φ_o are varied, while the other initial values are kept constant. The left graphs show the field amplitudes (Fig. 4.14a) and phases (Fig. 4.14b) for the case, that the field equations are integrated with the initial phases of φ_e^0 = -1.3 and φ_o^0 = 1.3. The subharmonic phases then assume values of $\overline{\varphi_{e,1}}$ = -4.22 and $\overline{\varphi_{o,1}}$ = 5.61 (see Fig 4.14b). The graphs 4.14 c and d are generated with the same parameters, but with slightly different initial phases φ_e^0 = -1.4 and φ_o^0 = 1.4. These different initial phases result in the phases assuming different steady-state values $\overline{\varphi_{e,2}}$ = -7.36 = $\overline{\varphi_{e,1}}$ - π, and $\overline{\varphi_{o,2}}$ = 8.75 = $\overline{\varphi_{o,1}}$ + π. Note, that the different phase states have no influence on the amplitudes of the self-phase-locked OPO, i.e., on the output power on the subharmonic waves (compare Figs. 4.14a and c). This demonstrates, that the initial values for the integration of the coupled field equations determine which phase eigenstate the OPO assumes.

For a more systematic approach, the coupled field equations are integrated 100 times, while all parameters are kept constant except for the phase difference $\varphi_e - \varphi_o$ of the initial values, which is varied in equidistant steps from 0 to 2π. The calculations have been carried out for a quarter-wave plate rotation angle of $\vartheta = 6$ deg and equal cavity detunings $\Delta_e = \Delta_o = 30$ MHz. The result is shown in Fig. 4.15a, where only the traces of the e-wave are plotted using polar coordinates, i.e., the amplitude b_e as radius and the phase φ_e as angle. Traces which end in the first phase state $\overline{\varphi_{e,1}} = 2.31$ are plotted black, those assuming the second state $\overline{\varphi_{e,2}} = 5.46$ gray. In Fig. 4.15a, one can see that all of the traces assume either the one or the other of the two steady-states on a direct path. Fig. 4.15b shows a magnification of the center of this polar plot, where the traces start with a low initial amplitude and with initial phases that cover the whole interval from 0 to 2π in 100 steps. The visible beginning of each of the 100 traces shows the respective initial phase φ_e for the integration of the coupled field equations. One can see, that the initial phase φ_e (and the o-wave phase φ_o, which is not shown here) strictly determines the steady-state that is assumed: the distribution of traces that belong to the first phase state (black) and those belonging to the other (gray), divide the polar plot into two perfectly symmetric halves, which proves the two-fold symmetry we were expecting to see. From this graph, it is evident that the phase state assumed by a self-phase-locked divider does directly

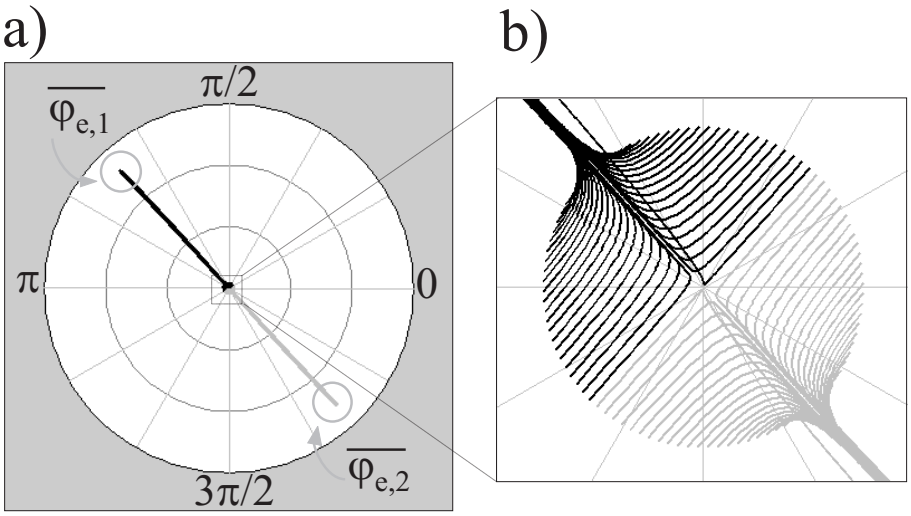

Figure 4.15: a) Traces of the e-wave for different initial values of the phase difference $\varphi_e - \varphi_o$, amplitudes as radius, phases as angle using polar coordinates. Traces ending in the fist phase eigenstate are plotted black, traces assuming the second phase eigenstate gray. b) Magnification of the center of the left graph. Calculation parameters: $\vartheta_{QWP} = 6$ deg, $\Delta_e = \Delta_o = 30$ MHz.

depend on the initial phases of the subharmonic waves.

The perfect two-fold symmetry in phase space displayed by the traces in Fig. 4.15 gives rise to the question, if there is always such a strict order observable. In the example given above, we have studied the behavior only for the case of equal detunings $\Delta_e = \Delta_o$. To investigate, if the two-fold symmetry is maintained for the case of asymmetric detunings, i.e., $\Delta_e \neq \Delta_o$, the same calculations are carried out for the *unequal* detunings $\Delta_e = 65.5$ MHz and $\Delta_o = 30$ MHz.

The result is displayed in Fig. 4.16. Again, the coupled field equations were integrated 100 times, while all parameters were kept constant except for the phase difference $\varphi_e - \varphi_o$, which is varied in equidistant steps from 0 to 2π. Except for the altered cavity detunings, $\Delta_e = 65.5$ MHz and $\Delta_o = 30$ MHz, the same parameters are used as before. The resulting traces of the e-wave with the amplitudes as radius and the phases as angle are shown in Fig. 4.16a. Traces ending in the first phase state $\overline{\varphi_{e,1}} = 0.12$ are plotted black, those assuming the second state $\overline{\varphi_{e,2}} = 3.26$

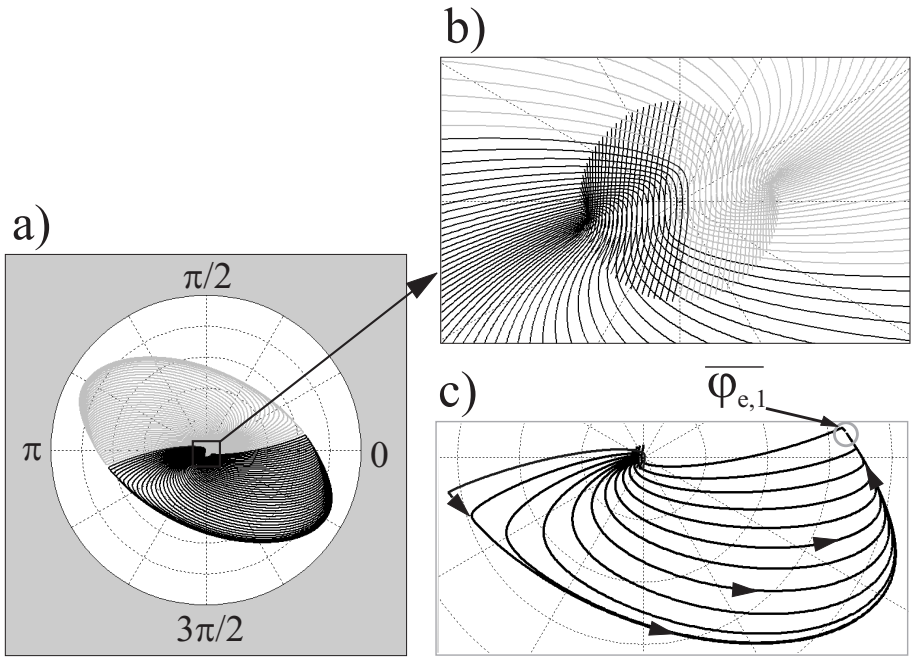

Figure 4.16: a) Traces of the e-wave for different initial values of the phase difference $\varphi_e - \varphi_o$, amplitudes as radius, phases as angle using polar coordinates. Traces ending in the first phase state are plotted black, traces assuming the second phase state gray. b) Magnification of the center of the upper graph, and c) Magnification of the phase space around the eigenstate the black traces assume. Parameters for the calculation: $\vartheta_{QWP} = 6$ deg, $\Delta_e = 65.5$ MHz, $\Delta_o = 30$ MHz.

gray.

From first glance at Fig. 4.16a, one can see that the eigenstates are not assumed via such straight paths as before. Instead, the traces describe a wide, curved arc, thereby evenly covering the phase space around the origin. Nevertheless, the twofold symmetry is maintained completely, as one can see from Fig. 4.16b, which shows a magnification around the center. Although the temporal development of the e-wave amplitudes and phases is more involved than in the example presented above (compare Fig. 4.15b), the division of the phase-space into two halves is clearly visible.

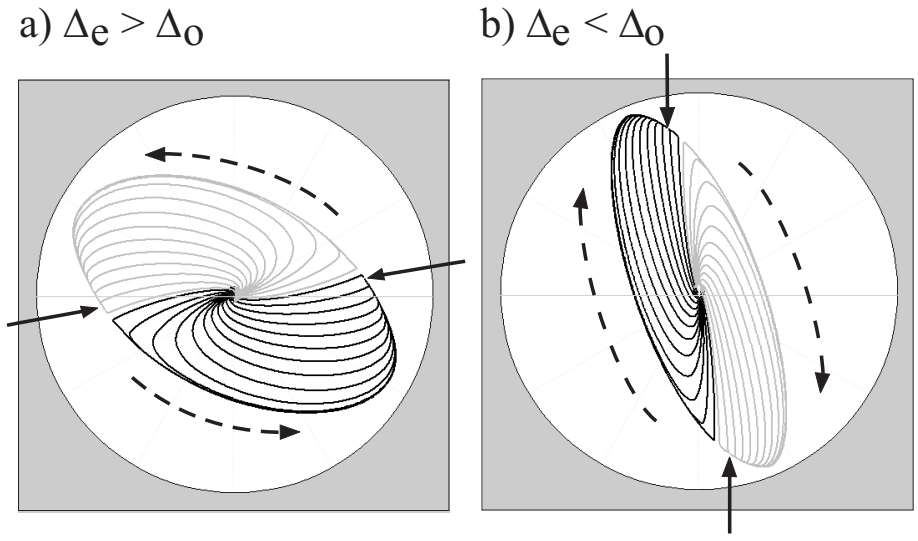

Figure 4.17: Traces of the e-wave for different initial values of the phase difference $\varphi_e - \varphi_o$ in polar coordinates. Calculation parameters for graph a): $\Delta_e = 65.5$ MHz, $\Delta_o = 30$ MHz, and for graph b): $\Delta_e = 30$ MHz, $\Delta_o = 69$ MHz. For both graphs $\vartheta_{QWP} = 6$ deg. Solid arrows show the location of the phase eigenstates, dashed arrows the direction of the traces' rotation.

Figure 4.16c shows a selection of the black traces assuming the first eigenstate $\overline{\varphi_{e,1}}$. From this graph one can see, that there is a strong preference for counter-clockwise rotation of the traces in phase space. The origin of this preference are the asymmetric cavity detunings, with $\Delta_e > \Delta_o$. To illustrate this dependence, in Fig. 4.17, where the e-wave traces are displayed in polar coordinates for two cases: in Fig. 4.17a for the case that $\Delta_e > \Delta_o$ ($\Delta_e = 65.5$ MHz and $\Delta_o = 30$ MHz), and in Fig. 4.17b for the opposite case, namely $\Delta_e < \Delta_o$ ($\Delta_e = 30$ MHz and $\Delta_o = 69$ MHz). In both graphs, the traces assuming the first of the two eigenstates are black, those assuming the second eigenstate are gray. The solid arrows indicate the location of the phase eigenstates. As one can see from Fig. 4.17a, the calculation for $\Delta_e > \Delta_o$ results in a prevailing counter-clockwise rotation of the phase of the e-wave. The direction of rotation is indicated by dashed arrows. In contrast, in Fig. 4.17b, which is calculated with $\Delta_e < \Delta_o$, the e-wave phase

rotates mainly clockwise to assume the phase eigenstate in that direction.

Regarding the experimental realization of a frequency-by-two divider, one could hardly have a method of deliberately setting the phases of the subharmonic waves to one or the other of the two possible steady-states. The reason for this is that a change of any experimentally accessible parameter does not create a preference for a certain state. As usually the OPO fields start from vacuum fluctuations, it must be considered to be completely determined by chance. Only by offering a certain phase to either one of the waves, i.e., by an additional injection seeding (using an external field with known phase), the self-phase-locked OPO could be forced to assume a pre-selected phase eigenstate.

4.5 Summary

In this chapter, for the first time a numerical integration of the coupled field equations of a by-2-divider OPO is presented. The solutions of the numerical calculations using experimental parameters show the expected phase-locking effect, in perfect agreement with the results obtained from the steady-state analysis in chapter 3: The locking area obtained numerically is identical to the one derived analytically. Within the locking range, the steady-state values derived numerically agree with the analytically found solutions in all cases and regarding any aspect.

By integrating the coupled field equations with their initial values set close to the analytical solutions, the instability of the high-threshold state is affirmed, whereas the low-threshold solutions are confirmed to be stable. A rich scenario of phase dynamics is revealed, which is still to be observed in the experiment. The qualitative observation of the OPO behavior around the stable low-threshold solutions reveals that relaxation oscillations of the OPO fields caused by small elongations from steady-state can be suppressed drastically by using an OPO cavity with a low finesse. This result is an important for the experimental realization of a frequency by-2-divider, because it enables to optimize the OPO design to achieve a maximum phase stability.

Finally, the numerical integration revealed the presence of two phase eigenstates, describing in which way they are assumed from different initial conditions. It is shown that the preference of the OPO for one or the other phase state depends only on the initial phases of the subharmonic waves, but not on any global experimental parameter. A systematic calculation of the assumed phase eigenstate

as a function of the initial subharmonic wave phases reveals a perfect two-fold symmetry in phase space.

Chapter 5

Experimental Setup and Characterization

In this chapter, the experimental setup for frequency division by two with a self-phase-locked optical parametric oscillator (OPO) is described. For the pump source a diode laser master-oscillator power-amplifier is used, which will be described in section 5.1. In section 5.2 the OPO setup with its nonlinear crystal and the linear two-mirror cavity is described, and section 5.3 deals with the cavity length stabilization, which enables continuous-wave operation of the OPO. In section 5.4 the operation characteristics of the OPO concerning the output power are presented. From these characteristics, the OPO parameters for the cavity losses and the nonlinear conversion efficiency are derived, which are used in chapters 3 and 4 to theoretically describe the OPO's locking behavior. Finally, in section 5.5 the coarse wavelength tuning via the crystal temperature is presented, and in 5.6 the fine wavelength tuning possibilities are investigated, in order to determine a strategy for tuning the OPO towards degeneracy.

5.1 The diode MOPA pump source

The basic requirements for a pump source for cw OPOs are a pump power considerably above the OPO threshold, and a high spectral and spatial beam quality. This is imperative for a high conversion efficiency of the pump source into the subharmonic waves, which is desirable for practical applications. The pump source for an

OPO that is to be used as a frequency by-two-divider should also be wavelength-flexible, such that this pump source can be locked to a selected frequency standard in the near infrared.

Single-stripe diode lasers provide readily excellent spectral and spatial beam quality combined with a high efficiency and compactness, which makes them ideal sources for small, portable systems. Today, diode lasers have become components widely used in everyday life like, for example, in CD players and fiber-optical networks. Although the usefulness of single-stripe diode lasers for nonlinear frequency conversion has been demonstrated [91], [68], their output powers of typically less than 100 mW are not sufficient in many cases. This problem can be solved by amplifying the diode laser power in a semiconductor amplifier, where the spectral and spatial beam characteristics of the single-stripe diode laser are maintained. With this method, up to several Watts of single-mode radiation in a near diffraction limited beam, tunable over a wavelength range of typically 20 nm can be generated, which has been proven to be suitable for nonlinear frequency conversion as well [92], [93], [94], [95], [96].

Besides diode lasers, diode-pumped solid state lasers (DPSSLs) are widely used in the field of nonlinear optics. DPSSLs can be made compact and efficient and, with respect to diode lasers, they provide even higher output powers. However, most DPSSLs, such as the commonly used Nd:YAG and Nd:YVO_4 lasers, operate at fixed wavelengths, and thus lack the wide range tunability of diode lasers. In general this means, that an OPO wavelength tuning via the pump wavelength is not possible, and the tuning is restricted to the other, usually slower methods, such as tuning via the temperature of the nonlinear crystal. In the present case, where the OPO shall be operated as a frequency divider, using a DPSSL as a pump laser means that it would only be possible to lock the pump laser to a rather limited number of atomic or molecular references, which happen to fall into the narrow operation bandwidth of these lasers. Therefore, a DPSSL cannot be considered a suitable pump source for our experiment.

An exception from the above are diode pumped fiber laser systems. These systems are now capable of generating output powers at the multi-Watt level, covering a considerable part of the NIR spectral region: Erbium-doped fiber lasers operate around 1.55 μm, and ytterbium-doped fiber lasers around 1.08 μm. Both types are tunable around their center frequencies by a few tens of nanometers. For example, an ytterbium-doped fiber laser has been demonstrated to cover the entire

wavelength range from 1032 to 1124 nm [97], with generating radiation suitable to pump an OPO [51].

However, diode lasers are by far more wavelength flexible, as they can be designed to emit throughout the whole visible spectral region, the near and mid infrared, and even up to the THz regime. Since a couple of years, blue diode lasers based on GaN and InGaN with an emission wavelength around 400 nm are commercially available, though at lower power [98], [99]. Tunable radiation at shorter wavelengths can be readily generated by frequency doubling of diode laser radiation [94] or by sum frequency generation of a tunable diode laser and a second laser [100]. Besides the commonly used GaInP diode laser, which emit around a wavelength of 670 nm, the visible and near infrared spectral range is covered by AlGaAs diode lasers, and InGaAs and InGaAsP diode lasers operate in the near infared region up to 1.7 μm. Laser radiation at longer infrared wavelength can be generated by lead-salt diode lasers, such as PbCdS lasers, which emit in the range from 2.8 to 4.2 μm, or PbSnTe and PbSnSe lasers, which are capable of generating laser radiation as far in the infrared as 32 μm [101]. Today, quantum cascade (QC) lasers can be designed to emit within most of the mid infrared and even considerable parts of the far infrared spectral region. Currently being not yet easy to handle due to their need for cooling and an often insufficient spectral beam quality, QC lasers might in future become powerful sources of IR radiation. So far, QC lasers have been reported with emission wavelengths as short as 3.4 μm [102] and very recently, the first THz QC was demonstrated, emitting at 85 μm [103]. In addition to their huge wavelength coverage, QC lasers offer a good spatial beam quality and continuous-wave radiation at output powers at the 100-mW level [104]. For a comprehensive review of recent developments of QC lasers see Ref. [105] and references therein.

The good spatial and spectral beam quality provided by diode lasers is not only a basic condition for an efficient nonlinear frequency conversion process, but is also required to lock the diode laser to an optical clock transition or another frequency standard. The possibility of stabilizing a diode laser to an atomic or molecular transition has been demonstrated for various absorption lines [106]. For example, commercially available diode lasers have been locked to the cesium D_2 line at 852 nm [107], to the cesium D_1 line at 894 nm [108], to a krypton line at 1534 nm [109], and to rubidium at 780 nm [110]. Frequency stabilization to a molecular transition has also been demonstrated using a QC laser [111]. With

suitable techniques, the frequency noise of diode lasers can be reduced resulting in a stability of the center frequency in the order of 10^{-12} and a spectral linewidth in the Hz-range can be achieved [112], [113].

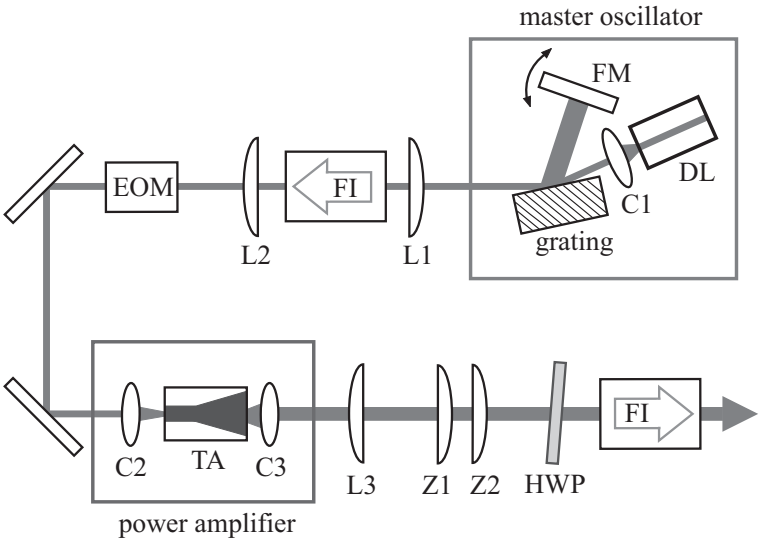

Figure 5.1: Setup of the diode MOPA system. The master oscillator is a single-stripe diode laser (DL) in an external cavity in Littman configuration. C1: collimating lens, FM: feedback mirror. FI: Faraday isolator, L1, L2: spherical lenses, EOM: electro-optic modulator. The power amplifier is a semiconductor tapered amplifier (TA). C2, C3: collimating lenses, L3, Z1 and Z2 are one spherical and two cylindrical lenses for shaping of the amplifier output beam. HWP: half-wave plate.

The pump laser used in this work is a diode laser master oscillator power amplifier (MOPA) system. The experimental setup of the pump source is shown schematically in Fig. 5.1. As the master oscillator we used a single-stripe diode laser with an external feedback cavity in Littman configuration [114], which consists of a grating and a feedback mirror. The collimated beam of the diode is diffracted from the grating (1800 lines/mm) in first order onto a highly reflecting plane mirror and fed back to the diode. The output beam is the zero-th order of diffraction, which is reflected from the grating under a grazing angle of about 80 deg. With this configuration, the linewidth of the diode laser is strongly re-

duced to the order of 100 kHz [115]. In addition, by tilting the feedback mirror the diode laser wavelength can be tuned via mode-hops within a range of about 25 nm around its center wavelength of 802 nm. With a precisely controlled alignment of the feedback mirror's pivot point, also a mode-hop free wavelength tuning can be achieved [116]. However, for the current work it was sufficient to adjust the wavelength coarsly from time to time, by tilting the feedback mirror, while the wavelength remained constant during the actual frequency locking experiments.

To inject the beam from the master-oscillator into the AlGaAs semiconductor power-amplifier, the beam is first focused through an optical isolator. This provides 60 dB suppression of the radiation emitted from the power-amplifier towards the master-oscillator, in order to prevent any influence on the spectral properties of the master-oscillator, or even destruction of the master-oscillator. Two collimating lenses are used at the anti-reflection coated input and output faces of the semiconductor amplifier. The amplifier (SDL 8630-E) has a 1-mm long waveguide section of 4 μm width, followed by a tapered geometry, where the stripe widens to 130 μm within 1 mm of length. The waveguide section serves as a spatial filter and as a pre-amplifier, in order to saturate the gain in the subsequent tapered section. The tapered guiding geometry guarantees that only the diffraction limited radiation of the waveguide is amplified. Due to the output facet being 100 times larger than the input facet, the intensity on the output facet and thus the risk of optical damage is reduced.

The injection current of up to 1 A and the temperature of the laser chip of 10 °C are controlled by a high-current diode laser driver (SDL 822). To compensate for astigmatism and ellipticity of the amplifier output beam, a beam correction optics is used, which consists of one spherical and to cylindrical lenses. Those three lenses form two independent telescopes in the planes parallel and perpendicular to the active layer of the amplifier. Behind the beam correction optics, an approximately round, near-diffraction limited beam of approximately 1 mm diameter is available. The amplifier beam is then sent through a second optical isolator, to suppress any influence by radiation reflected from the OPO pump input mirror. The pump power of the OPO can be varied by rotating the half-wave plate in front of the second isolator. At an injection current of 1 A and with about 15 mW injection power from the master-oscillator, up to 470 mW of amplified radiation at around 802 nm are measured directly at the output facet. This results in about 360 mW after the beam correction optics and the second isolator, which is available to

pump the OPO.

5.2 Experimental Setup of the OPO

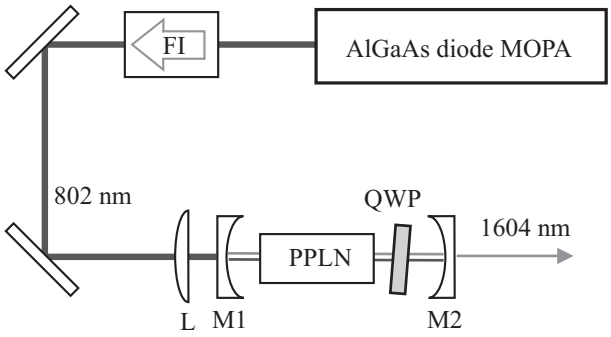

Figure 5.2: Experimental setup for frequency division by two of the pump frequency with a self-phase-locked OPO based on a PPLN crystal. FI: Faraday isolator, L: mode matching lens, M1: pump input coupling mirror, M2: output coupling mirror, QWP: quarter-wave plate.

Figure 5.2 shows the basic scheme of the OPO setup, which is similar to the one used by Mason and Wong in 1998 [73]. The frequency of 374 THz to be divided by 2 is provided by the 802 nm diode MOPA system described in section 5.1.

For frequency division, we use a triply-resonant two-mirror OPO, which is based on quasi-phase matching (QPM) in a periodically poled lithium niobate (PPLN) crystal. With a spherical lens of 100-mm focal length, the pump beam is spatially mode-matched to the fundamental mode of the linear two-mirror cavity.

A schematic drawing of the crystal is shown in Fig. 5.3. The 50-mm long crystal consists of PPLN, which carries a single poling period of $\Lambda = 10.1$ μm for type-II phase-matched generation of two subharmonic waves (at 1604 nm or 187 THz) near frequency degeneracy. The two faces with dimensions of 5 mm $\times$ 0.5 mm are polished with two wedges of approximately 0.25 deg, which add up to a total wedge of about 0.5 deg (poling and polishing by HC Photonics, Taiwan). This wedge in combination with changing the crystal temperature enables a continuous tuning of the OPO output wavelengths as described in section 5.6. The faces

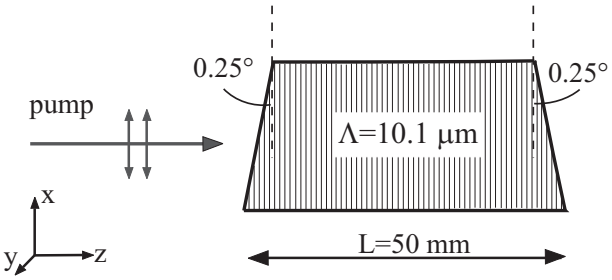

Figure 5.3: Schematic drawing of the 50-mm long, 0.5-mm thick and 5-mm wide crystal used for the by-two divider OPO. The coordinates are chosen such that the incident pump wave propagates along the z-axis, with the pump beam polarization being in x-direction. The crystal's c-axis is oriented along the y-axis, i.e., perpendicular to both the pump beam directions of propagation and polarization.

are anti-reflection-coated for the pump and the subharmonic wavelengths around 802 nm and 1604 nm, respectively, with a specified residual reflectivity of less than 1% (coating by Laseroptik GmbH, Garbsen, Germany). The crystal is mounted in a temperature-stabilized oven to control the phase-matching condition. Using a home-built electric temperature controller (Profile TED 200), the temperature is kept constant to a level of about 10 mK and can be set to temperatures of up to 200 °C.

The OPO cavity consists of two mirrors M1 and M2 with a radius of curvature (ROC) of 50 mm. The mirrors are placed in a distance of 120 mm, with the 50-mm crystal placed at the center of the cavity. The refractive indices are obtained from the Sellmeier coefficients [88] for a temperature of 203 °C, which is the temperature at which the OPO is expected to operate at frequency degeneracy. Details on the temperature dependence of the OPO subharmonic wavelengths are presented in section 5.5 later in this chapter. With this distance, with the refractive indices of the $LiNbO_3$ crystal of $n_p = 2.26$, $n_e = 2.14$, and $n_o = 2.21$, and with the physical crystal length, the free spectral ranges of the cavity can be calculated from Eq. 3.3 as $FSR_p = 820$ MHz, $FSR_e = 846$ MHz, and $FSR_o = 831$ MHz for the pump wave cavity, the e-wave, and the o-wave cavity, respectively. The confocal parameter inside the crystal b of the pump cavity is 38 mm, according to [117]

$$b = \sqrt{2 \cdot L_{eff}\,(2 \cdot ROC - L_{eff})}, \tag{5.1}$$

with the effective cavity length $L_{eff} = L_{cav} - L_{cr} + L_{cr}/n_p$ and the crystal length $L_{cr} = 50$ mm. This corresponds to a beam waist of $w_0 = 46$ μm for the fundamental cavity mode, which is given by [117]

$$w_0 = \sqrt{\frac{b\lambda_p}{2\pi n_p}}. \tag{5.2}$$

To enable optical parametric oscillation with a low threshold, the OPO cavity is chosen to provide enhancement of all three waves (triply resonant OPO, TRO). The pump input mirror M1 is highly reflective with R $>$ 99.98% for the subharmonic waves and has a transmission of 15% at the pump wavelength. The output mirror M2 is highly reflective with R $>$ 99.99% at the pump wavelength and provides an output coupling of each of the OPO output waves of 1%. The rear faces of all mirrors are anti-reflection coated for both wavelengths. The OPO output waves are collimated with a spherical lens of 100 mm focal length and the residual pump light is filtered using a mirror which is highly reflective at the pump wavelength (R $>$ 99.9%) and which transmits the subharmonic wavelengths (T $\approx$ 95%, mirror coating by Laseroptik GmbH, Garbsen, Germany).

A quarter-wave plate (QWP) placed in the OPO cavity serves for an adjustable amount of mutual injection of the two subharmonic waves. The QWP is anti-reflection-coated for the pump and the output wavelengths (true zero order wave plate with AR coating from Laser Components).

5.3 Cavity stabilization

For stable frequency division of the pump frequency, the OPO has to operate continuously and with low output power fluctuations. To achieve this, the cavity length is required to match the pump wavelength, such that pump light is coupled into the cavity continuously. Fluctuations of the cavity length, such as caused by acoustic perturbation or thermal drifts, would lead to a mismatch between the cavity resonance frequency and the external pump frequency, which would in turn lead to a fluctuating OPO threshold and fluctuating output power. In addition, if the cavity is resonant for one or both of the subharmonic waves as well, cavity length fluctuations also result in a fluctuation of the output wave frequencies and

even to mode-hops and cluster-hops, if the fluctuations exceed a certain amplitude (see section 5.6).

We found that, in our experiment, the cavity length is subject to fluctuations, which are mainly caused by thermally induced fluctuations of the refractive index of the crystal and the surrounding air, and by acoustically and thermally induced perturbations of the cavity mirror positions. These fluctuations usually are significant only for frequencies below 10 kHz. To suppress these fluctuations and achieve a stable output of an OPO with enhancement of the pump and the subharmonic waves, an active control of the cavity length is required, which provides a corresponding servo bandwidth [118].

For the described OPO setup, the cavity length is stabilized electronically to the pump wavelength. In principle, the same effect can be achieved by stabilizing the pump frequency to the cavity resonance, e.g. by modulating the diode laser current. One then could further increase the stability of the system by increasing the passive stability via, for example, a monolithic OPO setup [80]. However, as the goal of the described experiments is to divide an externally given reference frequency by two, we concentrate on stabilizing the cavity length to the pump wavelength. This means, that the detuning Δ_p between the incident pump frequency and the cavity resonance frequency is locked to zero, as was assumed for the theoretical considerations in chapters 3 and 4. With this pump detuning being zero, the OPO can be expected to operate at the lowest threshold and the highest output power, which is, however, still influenced by the double-resonance effect of simultaneous enhancement of the two subharmonic waves.

Several methods can be used to obtain the required electronic error signal to lock the pump cavity length to the pump laser wavelength. Ideally, this error signal should be proportional to the detuning of the cavity length from the pump wavelength like, for example, in fringe side locking [119], mode interference locking [120], spatial mode interference locking [121] or the Hänsch-Couillaud locking technique [122]. In this work, the Pound-Drever-Hall (PDH) technique is used [123], which utilizes the beat between the carrier wave and non-resonant phase modulation (PM) side-bands of the pump laser. The error signal is obtained by measuring the phase of the reflected carrier wave with respect to the phases of the side-bands. This error signal is amplified and used to control the OPO cavity length, such that an optimum input coupling of the pump wave into the cavity is achieved.

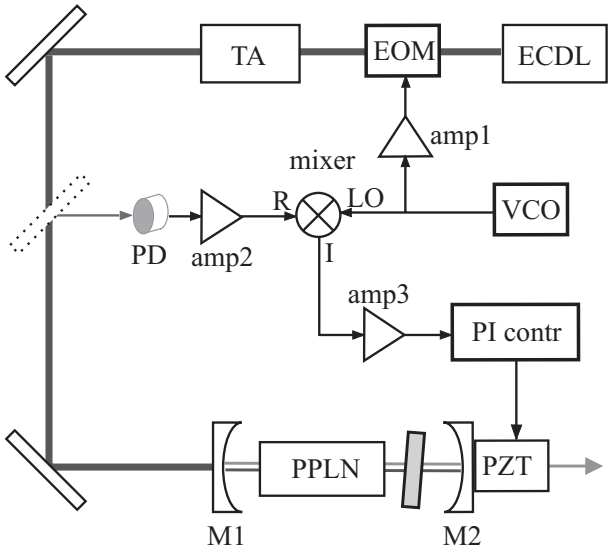

Figure 5.4: Pound-Drever-Hall stabilization scheme. ECDL: external cavity diode laser, EOM: electro-optic modulator, TA: tapered amplifier, PD: photodiode, amp1, amp2, amp3: amplifier, VCO: voltage controlled oscillator, PI contr: proportional integral controller, PZT: piezo transducer. For details see text.

Figure 5.4 shows the PDH stabilization scheme constructed and used to stabilize the OPO cavity length to the pump wavelength. To generate the required PM side-bands, an electro-optic modulator (EOM) is placed between the external cavity diode laser and the tapered amplifier. A Brewster-cut $LiNbO_3$ crystal is used which, combined with an inductivity, has a resonance frequency of about 110 MHz. The modulation frequency $\Omega = 110$ MHz is provided by a voltage controlled oscillator (VCO, Mini Circuits no. ZOS 150) and serves also as local oscillator (LO) for the mixer to obtain the error signal. To reach the RF power level required to drive the EOM, the VCO signal is amplified (Miteq AU 1310, 27 dB from 10 kHz to 500 MHz, amp1 in Fig. 5.4). If the carrier pump wavelength matches the cavity length and is therefore coupled into the cavity, the two side-bands are directly back-reflected from the input mirror, because the modulation bandwidth of $2\Omega = 220$ MHz is much larger than the cavity bandwidth for the pump wave, but also much smaller than the free spectral range. If the pump

wave is detuned from the cavity length by Δ_p, it is partly re-emitted from the cavity with a characteristic phase shift $\Delta\phi$, which is proportional to the detuning: $\Delta\phi = \Delta_p/FSR_p$. The phase-shift can be obtained by measuring the beat signal between the phase-shifted carrier wave and the unaltered PM side-bands. The phase of this beat signal changes with the cavity detuning [124]. In the described experiment, the beat signal is obtained by recording the reflected light with a fast photodiode (PD) and amplifying the signal (Miteq AU 1310, 27 dB from 10 kHz to 500 MHz , ampl2 in Fig. 5.4). By demodulating the beat signal with the LO frequency Ω using a mixer (Mini Circuits no. ZFM3), one obtains an error signal. After low-pass filtering and amplifying (home-built DC-amplifier amp3 with variable gain), the error signal is further processed by a proportional-integral controller to control the gain of the error signal (home-built controller PI contr in Fig. 5.4, see e.g. Ref. [125]). The servo loop is closed by feeding back the controller signal to the cavity by changing the cavity length via a piezo transducer (PZT), on which the output coupling mirror M2 is mounted.

With this PDH stabilization scheme, the cavity length of the OPO can be stabilized to the pump laser wavelength to provide continuous-wave output at stable output power levels. The bandwidth of this feedback system is limited by the bandwidth of the PZT to frequencies below approximately 600 Hz, which is sufficient for the experiments carried through in this work. Typically, the OPO equipped with the described PDH stabilization shows stable CW operation at optimum output power levels for several hours.

5.4 OPO operation characteristics and parameters

In this section, the OPO operation characteristics are described. In particular, the results obtained from these measurements are used to derive the parameters for the analytical and numerical calculations, which lead to a prediction of the locking behavior of the OPO.

As a first measurement, the OPO subharmonic power is determined for different input and output coupling mirror transmissions, for which we used a crystal temperature of 180 °C. To isolate the effect of the quarter-wave plate, the power characteristics are measured first without and then with the QWP, for different QWP angles.

The power of each of the subharmonic waves is measured behind the output coupling mirror M2 (see Fig. 5.2) as a function of pump power. For this, the OPO output beam is split up into the ordinary and the extraordinary polarized beam using a polarizing beam splitter, and the powers of the two subharmonic beams are measured with a wavelength-calibrated power meter (Newport 1815C).

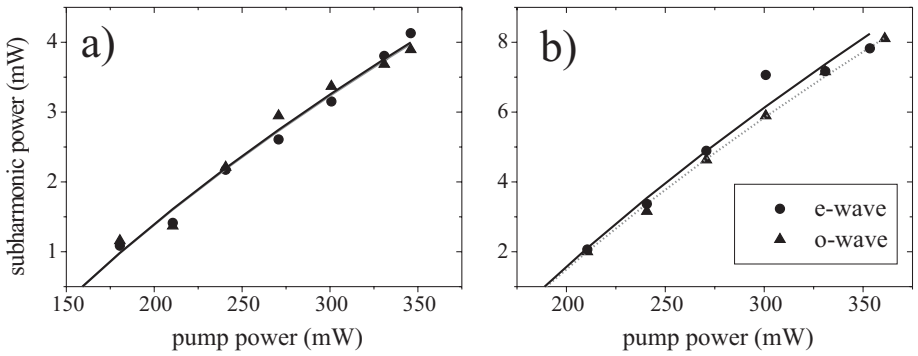

Figure 5.5: Power of the subharmonic waves as a function of the pump power with a, output coupling of 1% and b, of 2%. The measured values are given as symbols (o-wave power as triangles, e-wave power as circles), and the theoretical fit functions as curves (o-wave fit function given by the solid black curve, e-wave function by the dotted gray curve).

Figure 5.5 shows two examples of the measured output power as a function of pump power. The two measurements are performed with the same pump input coupling mirror of 15% transmission, but with different output coupling mirrors: Fig. 5.5a, with an output coupling of 1%, Fig. 5.5b, with output coupling of 2% for both, the e-wave and the o-wave. Each of the figures shows the measured data as symbols, the e-wave power values as circles, and the o-wave power values as triangles.

At pump powers higher than the threshold pump power, the e- and the o-wave powers increase with increasing pump power. With the 1%-output coupling mirror (see Fig. 5.5a), the threshold pump power is approximately 140 mW, and the maximum output power is about 4 mW for each of the subharmonic waves at the maximum pump power of 360 mW. In Fig. 5.5b (2% output coupling), the extrapolated threshold is higher (170 mW), but also the output power is higher

(8 mW for each of the subharmonic waves can be achieved). One can see, that the e-wave power slope is somewhat higher than the that of the o-wave power, which indicates that the losses on the o-wave are slightly higher.

In order to determine the parameters required for a theoretical description of the OPO's locking behavior, functions of the form $P_{e,o} = \eta_{e,o} \cdot \left(\sqrt{P_{th} P_p} - P_{th}\right)$ are fitted to the experimental values as described in Ref. [83]. Here, the slope efficiencies $\eta_{e,o}$ and the pump power threshold P_{th} are fitting parameters. For the given example, the fit-functions are given in Figs. 5.5a and b by the solid black curves (o-wave power) and by the dotted gray curves (e-wave power). The OPO parameters can now be determined in a manner similar to the one described in Ref. [65]. The power characteristics described above have been measured without the intracavity QWP in order to be able to observe the effect of the QWP separately, which will be done in the following.

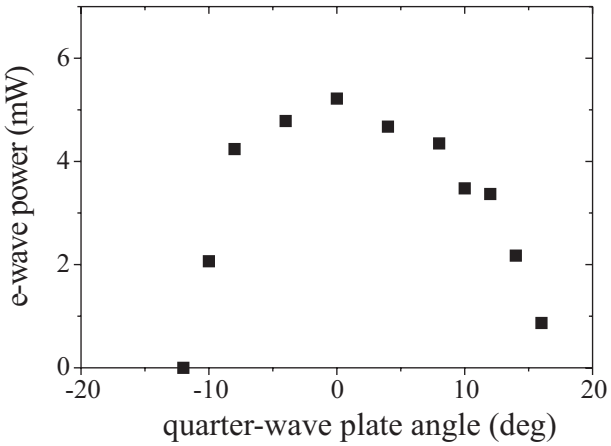

Figure 5.6: Measured e-wave power as a function of the QWP angle.

For an isolated determination of the effect of the QWP, the achievable e- and o-wave powers and the pump powers at threshold are measured for different QWP angles. As an example, Fig. 5.6 shows the measured e-wave power as a function of the QWP angle. These power values are measured with an output coupling mirror of 2% and the maximum available pump power of 360 mW. Without the QWP

being inserted in the cavity, the OPO emits 6.5 mW of e-wave power. From Fig. 5.6, one can see that with the QWP in the cavity, the OPO emits a maximum e-wave power of 5.2 mW at a QWP angle of 0 deg, and that the QWP can be rotated by more than 10 deg in both directions, before the output power decreases to zero. From this measurement and from the simultaneous recording of the pump power at threshold, it can be verified that the effect of the QWP on the pump wave can be assigned solely to an increase of the pump wave round-trip losses of 1.4% if the QWP angle is set to zero, and to a further increase of the pump losses by 0.25%/deg rotation angle of the QWP. The losses for the e- and the o-wave can be neglected.

single pass losses	
A_e	6.0%
A_o	6.3%
A_p (without QWP)	8.7%
A_p (with QWP)	10.1% + 0.25%/deg $\cdot \vartheta_{QWP}$
nonlinear coupling coefficient	
D	1050 Hz

Table 5.1: Experimental parameter values for the OPO setup.

Although the OPO can be operated with a rather large QWP rotation angle of more than 10 deg, in the experiment a QWP angle of only up to 6 deg was found to be practical, because the wavelength tuning range is strongly restricted at larger QWP angles, due to the increased pump losses and accordingly higher pump power at threshold. To compensate for the pump wave losses and to minimize the threshold, and in order to yield a maximum tuning range, a pump input coupling mirror with a higher transmission of 15% for the pump wave and an output coupling mirror with a lower transmission of 1% for the subharmonic waves were used for the main experiments. With these mirrors, the OPO generates two subharmonic waves of about 4 mW each, as displayed in Fig. 5.5a, and can be operated with a QWP rotation angle of up to 6 deg.

5.5 Coarse wavelength tuning via the crystal temperature

To characterize the coarse wavelength tuning properties of the cw OPO as a function of the crystal temperature, the output wavelengths are measured using an optical spectrum analyzer (ANDO AQ6315A), while the pump wavelength is kept constant at 801.8 nm. The temperature is varied step-wise, and the wavelengths are measured with a delay of several minutes, when a temperature equilibrium has been reached.

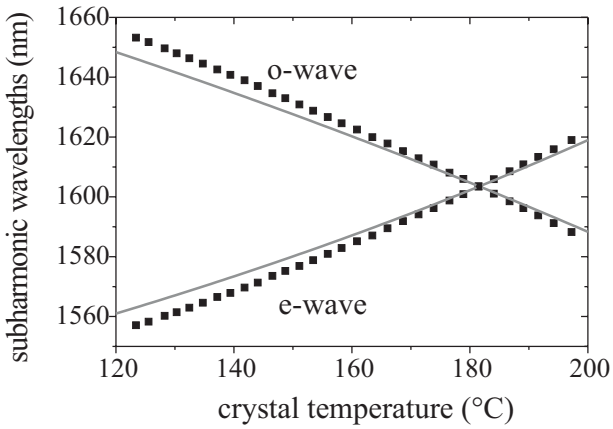

Figure 5.7: Subharmonic wavelengths as a function of the crystal temperature, measured values as symbols, theoretical tuning given by the gray curve.

Figure 5.7 shows the measured wavelength tuning as a function of the crystal temperature as squares. By changing the crystal temperature from 123 to 197 °C, a wavelength range of almost 100 nm around degeneracy, from 1557 to 1653 nm, is covered by the subharmonic waves. With increasing temperature, the wavelength of the ordinary polarized wave decreases, while the wavelength of the extraordinary wave increases. At a temperature of 181.5 °C, the wavelength curves intersect at two times the pump wavelength, i.e., at 1603.6 nm.

To calculate the theoretically expected OPO tuning behavior, we assume that the OPO oscillates at the wavelengths, for which the phase matching condition

is fulfilled, i.e. $\Delta k = 0$. For each temperature, the phase matching wavelengths are calculated using the Sellmeier coefficients given in Ref. [88]. The gray lines in Fig. 5.7 represent the e- and the o-wave wavelengths of the parametric gain maximum for each crystal temperature. Using a constant temperature offset of 23.9 °C as a fitting parameter, the calculations show reasonable agreement with the experimental data. The temperature offset and the somewhat slower change of the theoretically calculated wavelengths with the crystal temperature is due to slight errors in published Sellmeier coefficients, as was also found earlier by others and ourselves [68], [92].

Having characterized the temperature tuning behavior of the OPO, we have determined that the OPO oscillates close to degeneracy at a crystal temperature around 180 °C. However, the measurement presented above does not provide sufficient information to tune the OPO to its locking range in a deliberate manner. Particularly, the spectral resolution of 0.05 nm provided by the optical spectrum analyzer is too low to provide crucial information like the frequency difference between the two subharmonic waves on a MHz-scale or the occurrence of mode-hops. In order to be able to tune the OPO subharmonic wavelengths so close to each other, that self-phase locking can occur, one has to investigate the tuning behavior in more detail. In the last section of this chapter, the tuning properties of the OPO close to degeneracy are discussed on a MHz-scale. As the final goal of these considerations, a strategy will be developed which allows to tune the OPO to its self-phase locking range in a controlled manner.

5.6 Tuning the OPO towards degeneracy

5.6.1 Beat measurement setup

To observe the OPO's tuning behavior with an improved spectral resolution, a beat measurement is performed to determine the frequency difference between the two OPO output waves. The measurement setup is shown schematically in Fig. 5.8. The two subharmonic waves are projected onto a common polarization axis using a polarizer (Thorlabs LPIR050) set to 45 deg and then sent onto a fast photodiode (Atys No. 30617B, cutoff 3.5 GHz). The signal of the photodiode is split up into a low-frequency (DC, i.e. below ≈1 kHz) and a high-frequency (AC) component using a bias tee circuit. In this way, the DC optical power received on the photodiode can be monitored with an oscilloscope in order prevent saturation

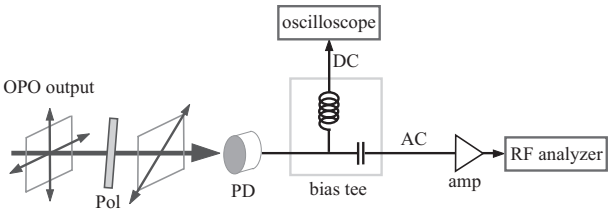

Figure 5.8: Experimental setup for the beat measurement. Pol: polarizer, PD: photodiode, amp: amplifier.

of the photodiode, while the AC component can be processed further for the beat measurement. The AC signal component is amplified (Mini Circuits amplifier ZKL 2R5, 30 dB from 10 MHz to 2.5 GHz) and the beat spectrum is measured using an RF spectrum analyzer (HP E4407B, 9 kHz to 26 GHz). The spectral range of the beat measurement is ultimately limited to below 2.5 GHz by the amplifier, and the resolution offered by the spectrum analyzer is specified to be 10 Hz. During the beat measurements, the OPO output wavelengths are monitored additionally on a larger scale with the optical spectrum analyzer (ANDO AQ6315A).

5.6.2 Observed beat frequency tuning

The OPO allows three methods of wavelength tuning: via the crystal temperature, via the pump wavelength, and via laterally shifting the crystal position, which changes the crystal length due to the crystal wedge. In the first experiments the OPO subharmonic wavelengths are tuned towards degeneracy by adjusting the crystal temperature, until we can observe the beat frequency of the two waves with the fast photodiode and the RF spectrum analyzer. By varying the lateral position of the crystal, the beat frequency can then be tuned continuously over a smaller range (approximately 40 MHz), after which a hop of the beat frequency follows.

Figure 5.9a shows an example of a beat spectrum. The beat frequencies are recorded with the RF analyzer set to max-hold-mode over a time span of a few seconds. During the measurement displayed in Fig. 5.9a, first a beat signal at frequency 1.54 GHz is generated. Upon changing the crystal position, the beat

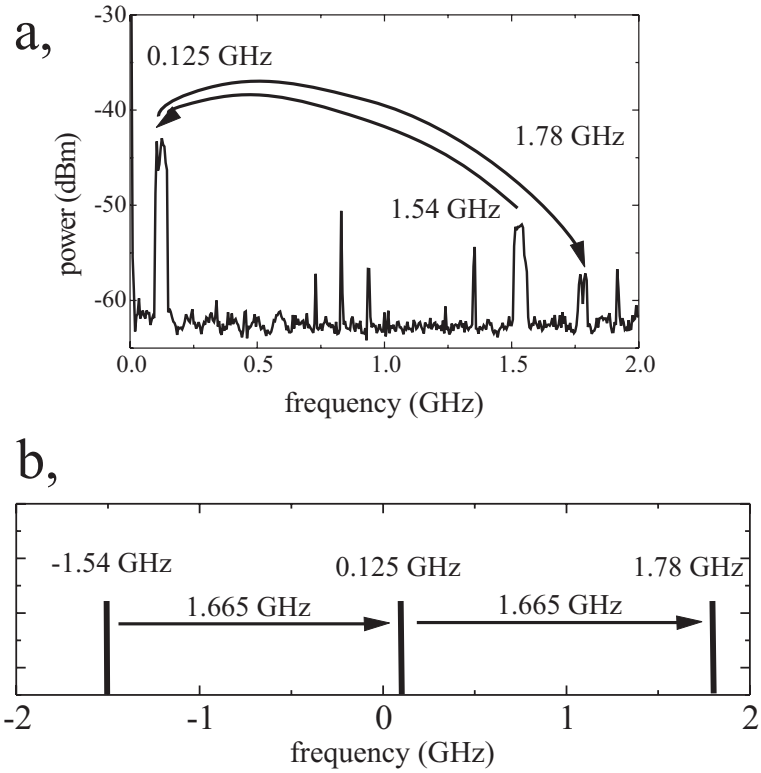

Figure 5.9: a) Beat signal as a function of beat frequency, recorded over a time span of a few seconds. The arrows indicate jumps of the beat signal from 1.54 GHz to 125 MHz, and then to a frequency of 1.78 GHz. The other, smaller peaks are picked up from surrounding laboratory equipment. b) Schematic drawing of a), unfolded to a two-sided spectrum.

signal jumps to a frequency of 125 MHz, and in the following jumps to 1.79 GHz.

Recalling that the beat power frequency spectrum shown in 5.9a is the projection of the two-sided amplitude spectrum onto the positive frequency axis, and after comparing several beat measurements recorded in the same manner, it can be concluded that the observed behavior corresponds to a pattern of 1.665-GHz jumps of the beat frequency. To illustrate this conclusion, the beat frequencies observed in Fig. 5.9a are denoted in a two-sided spectrum drawn schematically in

Fig. 5.9b. The first observed frequency at 1.54 GHz is denoted in the negative side at the spectrum, at $\nu_{beat} = \nu_e - \nu_o$ = -1.54 GHz. After adding a beat frequency jump of 1.665 GHz, the beat appears at a frequency of 125 MHz, and after the second beat jump of equal distance, at 1.78 GHz. All measurements performed can be explained by equidistant beat jumps in a similar manner. Finally, it should be noted, that the measurement presented in Fig. 5.9 demonstrates the impossibility to tune the OPO to exact frequency degeneracy by simply inducing discrete frequency hops.

In order to enter the range of near zero beat frequency, a better understanding of the tuning characteristic of the OPO was required, so that a reliable tuning strategy could be developed. In the following section, the effect of the different tuning methods will be explored, leading to an understanding of the observed tuning behavior. By combining the different methods appropriately, a strategy will be developed for tuning the OPO toward its self-phase locking range.

5.6.3 Determination of the beat frequency

The approach to investigate the tuning behavior of an OPO is to theoretically determine the position of the cavity modes of the e-wave and the o-wave cavity as a function of frequency, on a common frequency axis, where the origin is given by the exactly by-2 divided pump frequency. In the following paragraphs, this approach is described in detail.

In the experiment, the geometrical cavity length is stabilized to the pump wavelength using the Pound-Drever-Hall stabilization scheme (see section 5.3). For small changes of the optical cavity length of the pump wave, the stabilization would follow these changes, keeping the number of pump half-waves inside the cavity constant. Corresponding to the geometrical cavity length of about 120 mm and the pump wavelength of 802 nm, as used in the experiment, we estimate this number to be about N=455910. In order to be able to work with actual numbers, we now assume that this is the exact value for N. Corresponding to this N, the exact geometrical cavity length is

$$L_{geom} = N \cdot \frac{\lambda_p}{2} - L_{cr} \cdot (n_p - 1) \tag{5.3}$$

with the pump wavelength λ_p, the crystal length L_{cr} and the crystal temperature dependent refractive index n_p at the pump wavelength.

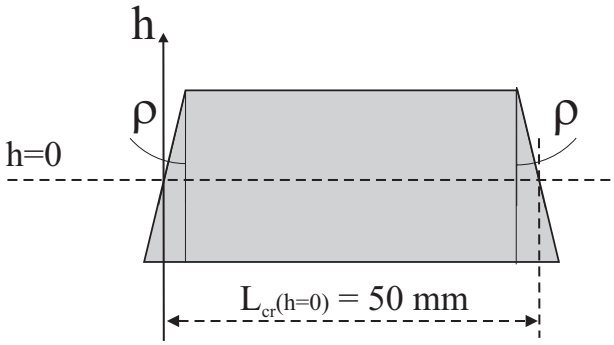

Figure 5.10: Schematic drawing of the wedged PPLN crystal. Each of the crystal faces is polished to form an angle of $\rho = 0.25°$ with the direction perpendicular to the beam propagation direction. Thus, he crystal length is a function of the crystal's lateral position h. At a crystal position of $h = 0$, the crystal length is 50 mm, where $h = 0$ is assumed to be in the center of the crystal.

The crystal length L_{cr} is a function of the lateral crystal position, due to the wedges on each side of the crystal. A schematic drawing of the wedged crystal is shown in Fig. 5.10. As a parameter for the crystal position we chose the height h, where $h = 0$ is in the center of the crystal. The crystal length at $h = 0$ is $L_{cr}\,(0)$ =50 mm. The wedge angles are specified by the manufacturer to be equal on both sides with $\rho = 15' = 0.25°$. Then, the crystal length as a function of the crystal height is:

$$L_{cr}(h) = L_{cr}(0) + 2h \cdot \tan\rho. \tag{5.4}$$

The optical cavity lengths for the e- and the o-wave are:

$$L_{opt,e,o} = L_{geom} + L_{cr} \cdot (n_{e,o} - 1)\,, \tag{5.5}$$

and the free spectral ranges for the two waves:

$$FSR_{e,o} = \frac{c}{2L_{opt,e,o}}. \tag{5.6}$$

Now the position of the cavity mode combs on the frequency axis needs to be specified. We define the exactly by 2 divided pump frequency $\nu_e^{(0)} = \nu_o^{(0)} = \frac{\nu_p}{2}$ as the zero frequency. The offset of the two combs, i.e., the distance between the

exactly divided pump frequency and the nearest cavity mode is then given by

$$\Delta_{e,o} = \left[\frac{\nu_p}{2FSR_{e,o}} - \text{ROUND}\left(\frac{\nu_p}{2FSR_{e,o}} \right) \right] \cdot FSR_{e,o}, \tag{5.7}$$

where the operator ROUND means rounding to the nearest integer. Having calculated the offset as well as the spacing of the e- and the o-wave cavity modes, the modes can be calculated on a frequency axis with respect to the exactly by two divided pump frequency.

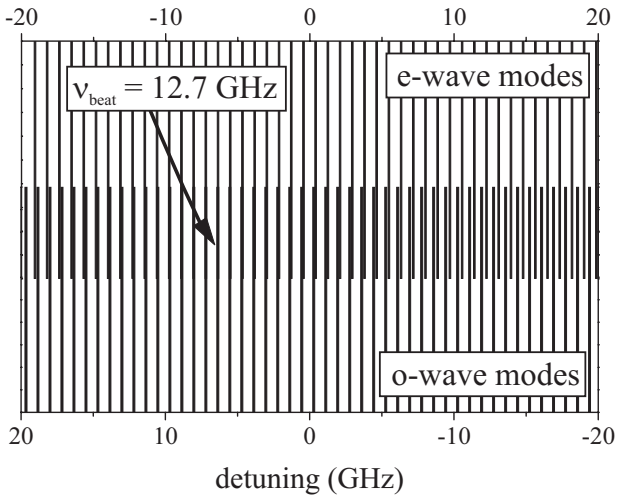

Figure 5.11: e-wave (upper part) and o-wave (lower part) cold cavity modes as a function of frequency detuning from the exactly by 2 divided pump frequency, calculated for a pump wavelength of $\lambda_p = 802$ nm, a crystal temperature of $T_{cr} = 203.2°\text{C}$, and a crystal height of $h = 0$. From left to right, the e-wave frequency increases, while the o-wave frequency decreases.

Figure 5.11 shows an example of e- and o-wave cavity mode combs calculated in the described way, for a crystal height of $h = 0$. In the lower part of Fig. 5.11, the e-wave cavity modes are displayed as a function of frequency detuning from the exactly divided pump frequency, and in the upper part the o-wave modes are displayed. Note, that the o-wave modes are displayed with decreasing frequency detuning. That means, that in Fig. 5.11, from left to right the e-wave frequency

increases, while the o-wave frequency decreases. The oscillation frequencies of the OPO are restricted by the condition $\nu_e + \nu_o = \nu_p$, which in Fig. 5.11 would be indicated by any vertical line which hits an e-wave mode as well as an o-wave mode (such as e.g. close to a detuning of -6.36 GHz. The correspondingly observed beat frequency for such a case would be about 12.7 GHz, indicated by the arrow. The precise e- and o-wave frequencies (for unequal losses) are determined by the condition $\frac{\Delta'_e}{\Delta'_o} = \frac{\kappa_e}{\kappa_o}$ (see Eq. 3.5), where Δ'_e and Δ'_o are the distances of the e- and the o-wave frequencies to the closest cavity modes.

By following the steps described in this section, we can now calculate the beat frequency between the e-wave and the o-wave for a given crystal height, temperature and pump wavelength. In the following section, the tuning behavior of the beat frequency will be explored.

5.6.4 Theoretical beat frequency tuning behavior

Tuning via the crystal vertical position

Upon changing the vertical position of the crystal while the PDH servo loop was turned off, the optical cavity lengths of the pump, e-wave and o-wave would change due to the wedged crystal. However, as the PDH servo loop is turned on during the OPO operation, the optical length of the pump cavity is stabilized to the pump wavelength by the Pound-Drever-Hall lock (section 5.3), such that the change is compensated completely by a corresponding movement of mirror M2. Thus the geometrical cavity length is changed by the difference in crystal length (given by Eq. 5.4) times the factor $(n_p - 1)$. The geometrical cavity length attained after a crystal shift can be calculated with Eq. 5.3. By then using Eq. 5.5, the new optical lengths of the e-wave and the o-wave cavities can be calculated. Following the steps described above, the beat frequency for each crystal position can be determined.

Figure 5.12 shows a calculation example of the beat frequency as a function of crystal position, for which we used a constant pump wavelength of $\lambda_p = 802$ nm and a constant crystal temperature of $T_{cr} = 203.2$ °C. It can be seen, that the beat frequency tunes in steps of 1.67 GHz, which occur after each 26 μm shifting the crystal. After each step, the beat tunes continuously over 36 MHz. Such a behavior was indeed observed in the experiment (see section 6.1), regarding the steps of 1.67 GHz as well as the continuous tuning range of 36 MHz.

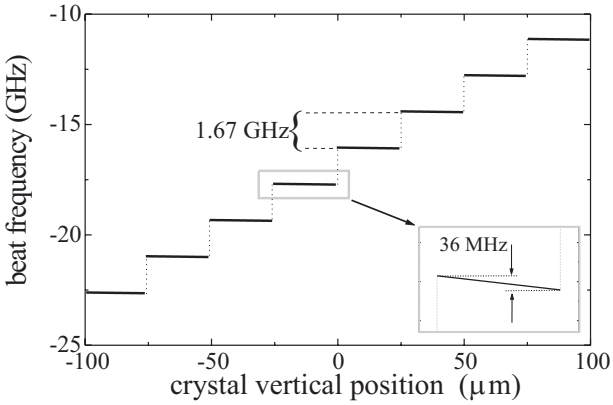

Figure 5.12: Tuning of the beat frequency via the crystal vertical position. The beat frequency tunes in steps of 1.67 GHz. Between the steps, the beat frequency can be tuned continuously over 36 MHz (see inset).

Note, that these considerations have been carried out with the assumption that the cavity length is stabilized to contain an even number of half-cycles (in the described case N = 455910) of the pump wavelength, which enables the beat frequency to attain certain equidistant values $f_0 + j \cdot$ 1.67 GHz, with a frequency offset f_0 and with j being an integer. If the cavity length was set to contain an odd number of half-cycles (e.g., N = 455909), the beat would then assume equidistant values exactly in between the former beat frequencies: $f_0 + \left(j + \frac{1}{2}\right) \cdot$ 1.67 GHz. In the experiment, this behavior was observed, as well. It was possible to "switch" between the two situations by briefly blocking the pump beam or by an acoustic perturbation of the optical table, thereby interrupting the Pound-Drever-Hall-stabilization. When the stabilization once more acquired a locking point, it could be either with an even or with an odd number of half-cycles in the cavity, leading to either the one or the other set of beat frequencies obtainable.

These calculations provide a comprehensive understanding of the experimentally observed tuning behavior. However, it seems impossible to deliberately tune to a near zero beat frequency with only shifting the crystal and re-lock the servo-loop.

Tuning via the crystal temperature

Upon changing the crystal temperature (and while the PDH servo loop was turned off), the optical cavity lengths change, because the refractive indices of the three interacting waves depend on temperature. This has two effects concerning the e-wave and o-wave frequencies: Firstly, the the cavity modes shift on the frequency axis. Secondly, the e-wave and o-wave frequencies with zero phase mismatch, $\Delta k = 0$, change, which corresponds to a shift of the parametric gain maximum on the frequency axis. The gain maximum is shifted by approximately 0.8 $\frac{nm}{K}$, while the full width at half maximum of the gain function (i.e. the parametric gain bandwidth) is about 1.5 nm. As will be shown in the next paragraphs, the changes required for a considerable tuning of the beat frequency are in the order of 10 mK. This temperature change would result in a shift of the parametric gain maximum of 0.008 nm (0.93 GHz at 1604 nm), which is only about one FSR of the cavity and much less than the parametric gain bandwidth. Therefore, the shift of the parametric gain maximum can be neglected, and we concentrate on the changes of the optical cavity lengths induced by a change of the crystal temperature.

When calculating the changes of the refractive indices induced by only a small change of the crystal temperature, only the first order derivatives $\frac{dn}{dT}$ need to be considered, where higher order derivatives can be neglected [126]. The refractive indices and their derivatives are calculated from the Sellmeier coefficients given in Ref. [88]. Around T = 203.2 °C, the pump wave refractive index changes with the rate $\frac{dn_p}{dT} = 4.5 \cdot 10^{-6} \frac{1}{K}$, and the o-wave refractive indices changes with a rate of the same order of magnitude, $\frac{dn_o}{dT} = 4.6 \cdot 10^{-6} \frac{1}{K}$. The e-wave refractive index, in contrast, changes with a ten-times higher rate: $\frac{dn_e}{dT} = 5.1 \cdot 10^{-5} \frac{1}{K}$. The change of the refractive indices induced by a temperature change would also lead to a change of the optical cavity length for the pump wave. However, as before, such a change is compensated completely by the Pound-Drever-Hall stabilization. As the derivatives of the pump and the o-wave refractive indices are very similar (less than a few percent difference), the o-wave optical cavity length is also almost compensated by the PDH servo. In contrast, the change of the e-wave optical cavity length is about 10-times the change of the pump and the o-wave optical cavity length thus tunes with temperature.

Using Eqs. 5.3 and 5.5, the changes to the geometrical cavity length, and to the optical cavity lengths of the e- and o-wave, and the resulting beat frequency can be calculated. Figure 5.13 shows the beat frequency tuning as a function of the

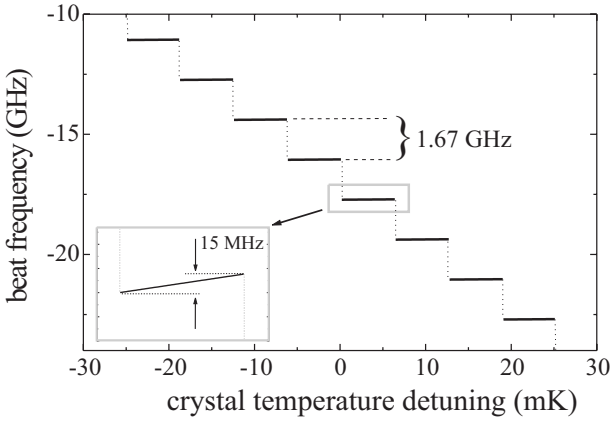

Figure 5.13: Tuning of the beat frequency via the crystal temperature. The beat frequency tunes in steps of 1.67 GHz and continuously over 15 MHz between the steps (see inset).

crystal temperature, as expected for a constant pump wavelength of $\lambda_p = 802$ nm and a constant crystal position of $h = 0$. With increasing crystal temperature, the beat frequency decreases in steps of 1.67 GHz per 6.3 mK. Between the steps, the beat frequency tunes continuously over 15 MHz.

Concluding this section, by changing the crystal temperature a step-wise tuning of the beat frequency should be achieved, similar to the tuning via the crystal's lateral position. Again, using only this single method of temperature tuning alone, a systematic tuning to approximately zero beat frequency can not be achieved.

Tuning via the pump frequency

A change of the pump frequency has several consequences: Firstly, with the pump frequency, also the target frequency of exactly half the pump frequency changes. This corresponds to a shift of the origin of the frequency axis by the amount of the pump frequency shift, while the e- and the o-wave cavity mode combs remain unaltered. However, the beat frequency involved with a certain pair of cavity modes now is calculated to be increased (or decreased) by the amount of the pump frequency shift. Secondly, as with temperature tuning, the maximum of the

parametric gain curve shifts, and as the last consequence, the refractive indices of the three interacting waves change.

Most important for a tuning of the beat frequency is the difference between the changes of the e- and the o-wave refractive indices, because this induces the required shift of the two cavity mode combs with respect to each other. Calculating the beat frequency as a function of the pump frequency detuning yields a similar step-wise tuning behavior as that induced by changing the crystal temperature. However, as a point of practical consideration, the pump frequency shift between two beat frequency jumps, i.e., between two steps requires a relatively large pump frequency tuning of 420 MHz, as compared to the relatively small crystal temperature change of 6 mK in Fig. 5.13. To make use of the former method, it would be necessary to change the pump laser frequency by several tens of GHz, which would result in a rather large and thus undesirable detuning of the parametric gain maximum.

Summarizing this section, all three investigated tuning methods, i.e., changing the crystal's lateral position, the crystal temperature, and changing the pump frequency, result in beat frequency tuning in steps of 1.67 GHz followed by continuous tuning over ranges in the order of tens of MHz between the steps. Deliberate tuning of the beat to and around zero frequency detuning is not likely to be achieved with any of the methods on its own. In order to identify a suitable tuning strategy, in the following section a combination of these tuning methods is investigated. Specifically, the tuning of the beat frequency by combining the tuning via changing the crystal's lateral position and the crystal temperature is considered. These two methods are chosen, because their effect and therefore their tuning range is larger as compared to tuning via the pump frequency. In addition, a frequency divider has to maintain a free choice of the frequency to be divided, such that it can be locked it to any particular frequency standard.

5.6.5 A strategy to tune the OPO towards degeneracy

Figure 5.14 shows the calculated beat frequency as a function of crystal position for a number of different crystal temperatures. This corresponds to the experimentally practical way to combine crystal temperature tuning with crystal position tuning. In the experiment, the crystal temperature is set to a certain value using the temperature controller (Profile TED200), and by changing the crystal position, the beat frequency is adjusted continuously within a certain range. Looking at

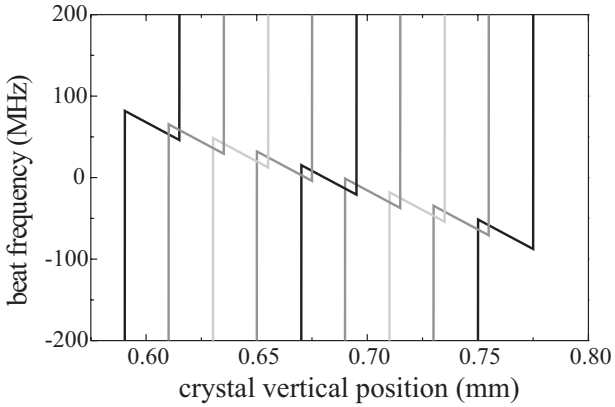

Figure 5.14: Tuning of the beat frequency with the combined methods of tuning via the crystal temperature and the crystal position. The beat frequency is shown as a function of the crystal vertical position for different crystal temperatures; from left to right: T=203.285 to T=203.325 °C in steps of 5 mK. The continuous tuning ranges of 36 MHz for each curve overlap, such that the beat signal can be tuned to any desired frequency.

Fig. 5.14, this means to chose one of the tuning curves for a certain crystal temperature. By adjusting the crystal position, the beat frequency then can be tuned continuously over about 36 MHz. As can be seen in Fig. 5.14, the continuous tuning ranges of the different curves overlap, if the temperature steps are chosen to be smaller than 10 mK. In the experiment, the temperature can indeed by adjusted in such fine steps, that a continuous tuning of the beat frequency is achieved.

The described method of combined temperature and position tuning seems to be a promising strategy to reliably control the subharmonic beat frequency produced by the OPO. The method predicts a change of the beat frequency of 3 MHz/mK. For a continuous tuning, the crystal position has to be adjusted by 4 μm/mK when changing the crystal temperature. These predictions are compared with the experimental observations in section 6.1 in the following chapter.

Summarizing this chapter, the experimental setup for phase-coherent frequency division by two with a cw OPO is described. As the pump source a diode master oscillator power amplifier is used, which generates up to 360 mW of 802-nm radiation of good spectral and spatial beam quality to pump the divider OPO.

The OPO is based on a periodically poled lithium niobate crystal in a linear two-mirror cavity. Continuous-wave output of the OPO is provided by using a Pound-Drever-Hall cavity stabilization scheme. This OPO generates more than 16 mW of subharmonic power in two perpendicularly polarized beams. To enable self-phase locking of the subharmonic beams, a polarization rotation of the two waves is provided by an intracavity quarter-wave plate. The subharmonic wavelengths of the OPO are tuned in a range of 100 nm around degeneracy at 1604 nm by changing the crystal temperature.

From the OPO's power characteristics, the operation parameters such as the losses for each of the three waves and the nonlinear coupling coefficient are determined. These parameters are of great importance for theoretically describing and predicting the locking behavior of the divider. The fine tuning properties of the OPO are investigated in detail to understand the experimental observations. As a result of the fine tuning analysis, a promising strategy to fine-tune the OPO towards and across its self-phase locking area is a combined temperature and position tuning of the OPO crystal. These considerations are a basic precondition to achieve self-phase locking and phase-coherent frequency division.

Chapter 6

Experimental Results

This chapter describes the experiments on all-optical, phase-coherent frequency division by 2 using a self-injection-locked continuous-wave optical parametric oscillator. Locking is achieved by setting the OPO output wavelengths to frequency degeneracy and by providing mutual injection of the two subharmonic waves with an intracavity quarter-wave plate. If the two waves are tuned closer to each other than a characteristic frequency difference, self-injection locking is expected to occur, in which case the subharmonic waves oscillates phase-coherently at exactly one-half of the pump frequency. The characteristic frequency difference, below which the OPO should be self-injection-locked, is called the locking range.

In section 6.1, the experimental tuning properties of the OPO close to frequency degeneracy are investigated and compared to the predicted tuning behavior as described in section 5.6.5. In section 6.2, self-phase locking of the OPO is presented. The locking range is measured as a function of the QWP rotation angle and the results are compared with the theoretical prediction derived in section 3.6. In section 6.3, for the first time, the frequency stability of a by-2-divider OPO is measured and the results are compared with the prediction derived in section 3.8. Finally, in section 6.4, a phase sensitive detector is used for the first quantitative phase measurement of an all-optical divider OPO.

6.1 Beat frequency tuning

In section 5.6.5, a strategy is described, which should enable a controlled tuning of the OPO subharmonic frequencies to the OPO's self-phase locking range, i.e., towards and across frequency degeneracy. The tuning method consists in changing the crystal temperature in small steps (in the order of 10 mK) and by simultaneously adjusting the lateral crystal position in a continuous way over 20 μm. A change of the beat frequency of 3 MHz/mK is predicted, and for a continuous tuning of the beat frequency, one predicts that the crystal position has to be adjusted by 4 μm/mK. For a given temperature, the continuous tuning range of the beat frequency should be 36 MHz. By changing the lateral crystal position at constant temperature, the beat frequency is expected to tune in steps of 1.67 GHz, assuming beat frequencies of one certain set $\nu_{beat} = f_0 + j \cdot 1.67$ GHz, with a frequency offset f_0 and with j being an integer. It is also expected, that it is possible to switch to a second set of equidistant beat frequencies exactly in between the former beat frequencies: $f_0 + \left(j + \frac{1}{2}\right) \cdot 1.67$ GHz by briefly interrupting the Pound-Drever-Hall lock for cavity length stabilization. These predicted tuning properties are compared with experimental observations in the following paragraphs.

To measure the beat frequency, the same setup is used as described in section 5.6.1 and shown in Fig. 5.8. The OPO subharmonic beams are projected onto a common polarization axis using a linear polarizer and then sent onto a fast photodiode. The photodiode signal is amplified and recorded using an RF spectrum analyzer. The cutoff frequency of the entire signal processing scheme is 2.5 GHz, limited by the amplifier.

To demonstrate the beat tuning behavior, the crystal temperature is changed in small steps, and the crystal lateral position is adjusted subsequently, while simultaneously the beat frequency from the OPO is monitored. Figure 6.1 shows the result of this tuning experiment. In Fig. 6.1a, the observed beat frequencies are displayed as a function of the crystal temperature. For each temperature, several beat frequencies can be generated by changing the crystal lateral position. As predicted, the beat frequency thereby jumps in steps of 1.67 GHz. By interrupting the Pound-Drever-Hall lock, e.g. by interrupting the pump beam, it is possible to switch between two sets of beat frequencies, i.e., to induce a smaller jump of the beat frequency of only 840 MHz. The two different sets of beat frequencies are indicated in Fig. 6.1a by filled and hollow symbols. As one can see from the gray lines, the beat frequencies indeed tune linearly with temperature, as predicted

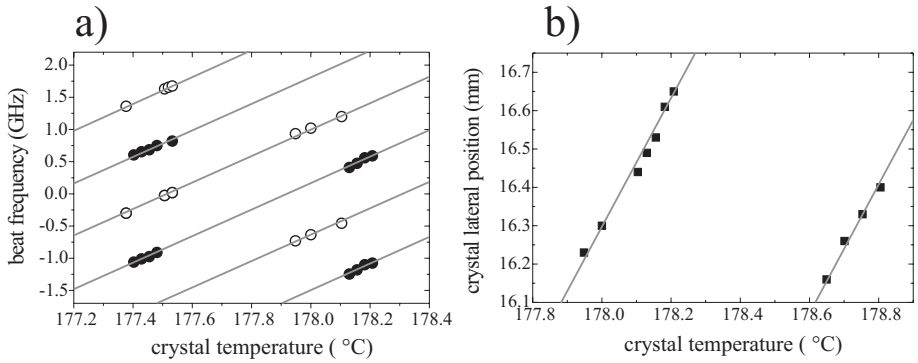

Figure 6.1: a) observed beat frequencies as a function of the crystal temperature. b) lateral crystal position corresponding to the measured beat frequencies as a function of crystal temperature.

from the calculations. The slope is 2.1 MHz/mK, which is in fairly good agreement with the predicted value of 3 MHz/mK. The deviation can be explained from small errors in the Sellmeier coefficients used for the calculations.

During the described measurement, the beat frequency is tuned in steps of 1.67 GHz via the lateral crystal position at a given crystal temperature. When the crystal position is adjusted such, that one specific beat frequency (around 600 MHz) is generated, the crystal lateral position is recorded as a function of the crystal temperature. This dependence is shown in Fig. 6.1b, where the lateral crystal position is plotted as a function of the crystal temperature. From the gray lines one can see that, in order to generate this specific beat frequency, the crystal has to be shifted by 1.6 μm/mK, which is less than half of the predicted shift of 4 μm/mK. However, this deviation can be readily explained by a deviation of the angles of the crystal wedges from the manufacturer's specifications (two wedges of 0.36 deg each instead of 0.25 deg).

Figure 6.2 shows an RF spectrum measured around a frequency of 140 MHz with the described setup. The black trace shows one single measurement, i.e., one scan of the RF analyzer over the chosen RF measurement interval (80 to 200 MHz). One can see one single peak at 143 MHz which is about 30 dB above the noise level. This peak is the beat signal of the e- and the o-wave, and its frequency is the

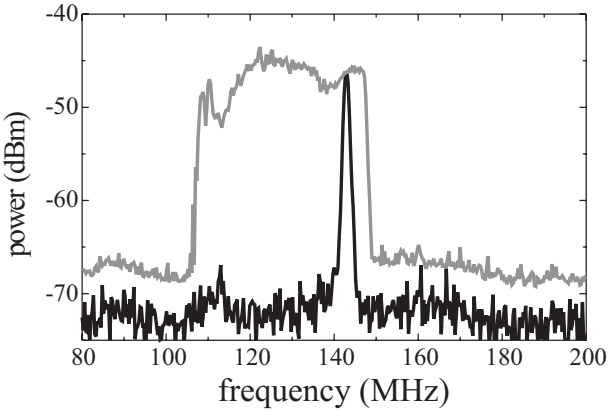

Figure 6.2: RF spectrum of the beat between the e- and the o-wave. Black trace: beat at $\nu_{beat} = 143$ MHz. Gray trace: Max-hold measurement indicating the continuous tuning range of the beat frequency of about 40 MHz, from approximately 108 MHz to 148 MHz.

difference between the e- and the o-wave frequency: $\nu_{beat} = |\nu_e - \nu_o| = 143$ MHz.

The gray trace in Fig. 6.2 is a max-hold trace recorded with a hold-time of several seconds. During the measurement displayed in Fig. 6.2, the crystal is laterally shifted by some ten μm. The approximately constant level of the max-hold trace shows that the crystal position tuning results in a continuous tuning of the beat frequency over 40 MHz. This continuous beat frequency tuning range is in good agreement with the theoretically predicted range of 36 MHz. A continuous beat frequency tuning over a larger range (> 400 MHz) can be achieved by changing the crystal temperature in small steps (< 10 mK) and by subsequently adjusting the lateral crystal position.

In summary, the experimentally observed fine tuning properties of the OPO subharmonic frequencies close to the exactly divided pump frequency are in good agreement with the theoretical predictions. With the proposed tuning method of combined crystal temperature changes and adjustment of the lateral crystal position, a continuous tuning of the beam frequency can be achieved. With this method, it should be possible to tune the OPO to frequency degeneracy and its self-phase locking range in a controlled manner.

6.2 Locking range measurement

In this section, measurements are presented on the OPO divider's locking range as a function of the rotation angle of the intracavity QWP. The tuning method used to continuously tune the beat frequency of the OPO subharmonic waves has been derived in section 5.6.5. In chapter 3, the properties of the OPO regarding self-injection locking have been investigated theoretically, from which we expect the locking range to increase with the QWP angle. For a QWP angle of 6 deg, the locking range is estimated to be about 170 MHz .

To measure the locking range, the same setup for measuring the beat signal of the OPO subharmonic is used as it is described in section 5.6.1. The OPO subharmonic frequencies are both tuned towards degeneracy by changing the crystal temperature, until a beat frequency is observed in the range of up to 2.5 GHz, which is limited by the RF amplifier used to amplify the photodiode signal. Thereafter, the beat frequency is tuned in mode-hops by changing the lateral crystal position, until the lowest possible beat frequency is observed in the range from 0 to 420 MHz (compare Fig. 5.12). The OPO then oscillates in the e- and o-wave cavity modes, which are closest to frequency degeneracy, and the actually measured beat frequency only depends on the cavity detunings Δ_e and Δ_o, i.e. the distance between the cold cavity modes and the exactly by-2 divided pump frequency.

As soon as the beat frequency is observed to be in the range from 0 to 420 MHz, the method of combined changing the crystal temperature and its lateral position is applied to continuously tune the beat frequency towards zero, where the beat signal is expected to vanish when optical self-phase locking occurs [76], [77]. Figure 6.3 shows two examples of the measured power of the RF beat as a function of the beat frequency, as recorded during a time interval of about 45 minutes, while varying the the crystal temperature from 178.68 °C at the left hand side of the graphs to 178.88 °C at the right hand side. During this measurement, the subharmonic wavelengths are monitored to remain at 1603.8 nm, within the 0.05 nm resolution limit of the optical spectrum analyzer used. The power of the beat signal is displayed by the black curves, and the gray curves give the background noise level, recorded with the photodiode blocked.

Note that the RF beat power measurement yields a one-sided spectrum of the beat signal containing only positive frequencies. Therefore in the shown example, the spectrum was in fact measured twice, namely first with the beat frequency *decreasing* from 200 MHz to zero (while *increasing* the crystal temperature from

178.68 to 178.78 °C), and then with the beat frequency *increasing* from zero to 200 MHz (while *still increasing* the temperature from 178.78 to 178.88 °C). From this observation, the two measurements can be assigned unambiguously to the two different sides of the beat amplitude spectrum. In Fig. 6.3, the two measurements are plotted as the two halves of a two-sided beat frequency spectrum, such that the crystal temperature increases from left to right.

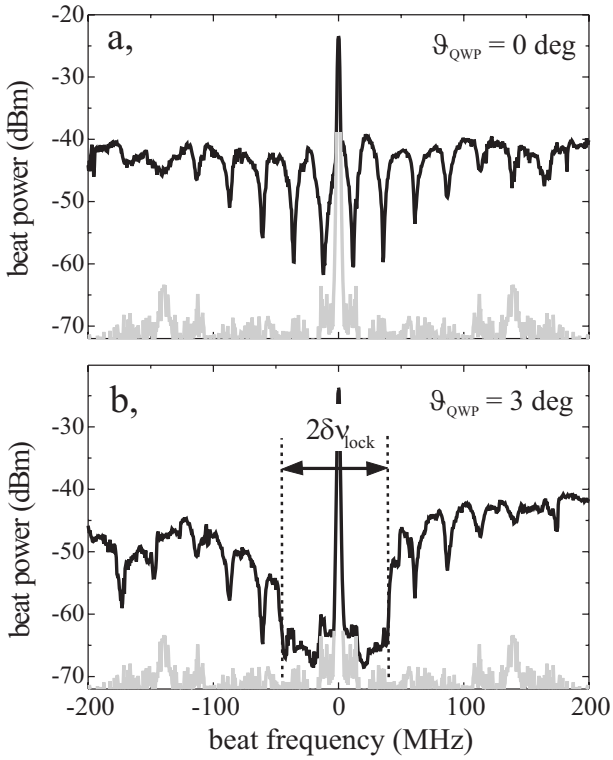

Figure 6.3: Measured beat frequency spectra for a) a quarter-wave plate angle of 0 deg and b) for a quarter-wave plate angle of 3 deg. The beat signal power is displayed by the black curves, and the gray curves are the background noise level, recorded with the photodiode blocked.

From the upper spectrum in Fig. 6.3a it can be seen that, with $\vartheta_{QWP} = 0$ deg, the beat signal was observable about 30 dB above the noise level at every fre-

quency within the 400-MHz tuning range. Particularly, with $\vartheta_{QWP} = 0$ deg, the OPO could be tuned smoothly through frequency degeneracy (i.e., through zero beat frequency), which proves the absence of self-phase locking. In contrast, with the QWP rotated to $\vartheta_{QWP} = 3$ deg (see Fig. 6.3b), the beat signal is strongly suppressed to the background noise level of -70 dB within a 80-MHz wide interval around zero beat frequency. The latter observation proves that the OPO is self-phase-locked within that interval. The OPO operates stably within this self-phase-locked regime for typically 15 minutes, before the subharmonic frequencies drift out of the locking range. The measured full range of beat suppression of 80 MHz corresponds to a full locking range of $2\delta\nu_{lock} = 80$ MHz, obtained with $\vartheta_{QWP} = 3$ deg.

In addition to these main features in Fig. 6.3a and 6.3b, namely the absence of self-injection locking, there are also a sharp central peak and a number of smaller peaks apparent. The central peak (at zero frequency) is caused by DC noise pickup, and is intrinsic to all RF measurements. We observed this peak independently of whether the OPO was turned on or off. The dips appearing with approximately regular spacing in both traces originate from a decrease of the OPO output power, as found from a simultaneous measurement of the OPO output power using a power meter (Newport 1815C). The spectral distance between the dips in the output power is not absolutely regularly, but increases slightly (from 24 to 27 MHz). The physical origin of the power dips in the OPO output is unclear so far.

The described measurement of the locking range has been repeated for different rotation angles of the QWP, i.e. for different strengths of injecting the e- and the o-waves. Figure 6.4 shows the measured full locking range as a function of the QWP angle as symbols. The experimental error in setting the QWP angle (shown as the horizontal, 2 deg wide error bars) is given by the small wave plate mount that was used, and by the limited space inside the OPO cavity. It can be seen that, increasing the QWP angle, the locking range increases steadily. The largest locking range measured is 160 MHz, achieved with a QWP angle of 6 deg. As described in section 5.4, the rotation of the QWP beyond 6 deg increases the pump losses and thus the OPO threshold, and therefore reduces the subharmonic frequency tuning range.

The experimental data in Fig. 6.4 is to be compared to the solid gray trace, which displays the theoretically expected locking range as calculated in section 3.6

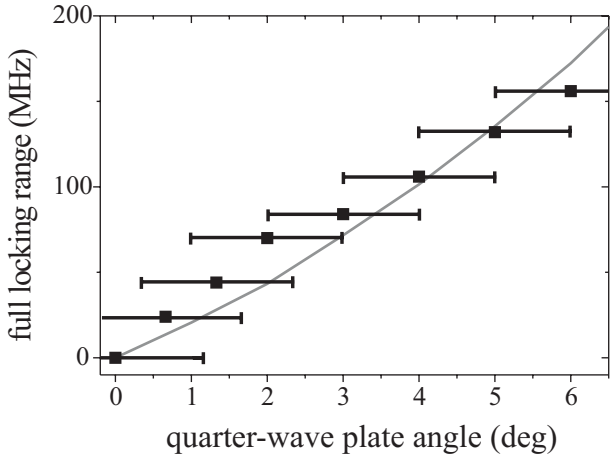

Figure 6.4: Measured full locking range as a function of the QWP rotation angle. The measured values are displayed as symbols, the error bars give the uncertainty for adjusting the QWP angle, and the solid curve shows the theoretically expected locking range as calculated in section 3.6.

and shown in Fig. 3.10. Within the experimental error, the measured values are in good agreement with the theoretically predicted locking range. For example, the locking range of 160 MHz measured for a QWP angle of 6 deg agrees well with the predicted locking range of 170 MHz. The predicted quadratic increase of the locking range with the QWP angle is consistent with the experimental data, but it can, however, not be affirmed from the measurements, due to the experimental error.

It should be noted here, that during several months of operating the by-2-divider OPO, during which it was tuned into and out of its locking range many times per day, there was always only a single pump power at threshold observed. This is in agreement with the prediction of our stability analysis, that there is only one single stable threshold state.

Summarizing this section, self-phase locking of the by-two divider OPO has been achieved. The OPO operates in the self-phase-locked regime for typically 15 minutes. In agreement with the stability analysis, there is only a single pump power at threshold observable. The locking range has been shown to increase with

the rotation angle of the intracavity QWP, in fairly good agreement with theory. A maximum locking range of 160 MHz has been measured for a QWP angle of 6 deg.

6.3 Frequency stability

In the previous section, experimental evidence on successful self-injection locking of the OPO has been presented, and thus successful all-optical frequency division. It has been shown, that within a certain range (the locking range), the beat signal between the OPO subharmonic waves vanishes. This means, that the beat frequency (the difference between the e-wave and the o-wave frequency) is zero within the RF spectrum analyzer resolution, given by the width of the central DC noise peak. In this section, the frequency stability of the self-phase-locked divider is investigated. This is a most important characteristic of the frequency divider, because it states the precision one can expect for the frequency-division process of the OPO pump frequency into the subharmonic frequencies.

The most obvious method for characterizing the frequency stability of the divider is to compare the input frequency with the output frequency, for example with an interference experiment. This, however, is not possible here, because the pump and the subharmonic frequencies are largely different, such that prior to superimposing the input and output, the output would have to be frequency doubled. This has two disadvantages: Firstly, doubling the frequency of one of the output waves would yield only very low powers (at the nanowatt level), which would result in a low signal-to-noise ratio. Secondly, in order to compare only the two desired waves, great efforts would have to be taken to filter out any residual pump light and light of the other subharmonic wave, so that sum frequency mixing of the two subharmonic waves in the doubling crystal is avoided.

We circumvented these problems by directly comparing the two subharmonic waves with each other, thus measuring the frequency deviations of these two waves with respect to each other. The OPO output waves are of sufficiently high power (more than 10 mW) to yield a very good signal-to-noise ratio in an interference experiment, and there are no other waves generated around 1.6 μm, which could add to the beat signal. In addition we have found from the analytical calculation of the frequency instability in section 3.8, that the divider's residual frequency instability can be calculated from the frequency instability of one subharmonic

wave with respect to the other subharmonic wave in good approximation.

In principle, there are two possibilities to measure the divider's residual frequency instability in a direct superposition of the e- and the o-wave. One method would be to count the zero-crossings of the beat signal amplitude in the time domain, which would yield the variance of the frequency as a function of time. However, upon time-averaging any temporal fluctuation would show up as a broadening of a beat signal [87]. Therefore measuring the linewidth of a beat signal in the frequency domain is also a possibility to determine a frequency stability. In the present work, we decided to use the latter method (beat linewidth measurement), because it is easier to implement.

In the following sections, first the noise sources leading to frequency instabilities are discussed on a qualitative basis, followed by the quantitative measurement of the drift of the beat frequency. These measurements yield the input values for the analytical derivation of the divider's frequency instability, which is presented in section 3.8. After explaining the measurement setup and discussing the resolution limiting factors, the measurement of the beat signal linewidth is presented, from which the divider's residual frequency instability is derived.

6.3.1 Noise sources

The most important source for instabilities of the by-2-divider process is the phase instability or phase noise intrinsically introduced by the OPO itself. This noise originates from the fact, that the subharmonic phases are not constant, but a function of the cavity detunings Δ_e and Δ_o even within the self-phase-locked regime of OPO operation (see Eq. 3.33). Residual instabilities could be caused as follows.

The cavity length of each of the three OPO waves is subject to temperature drift. As the pump cavity length changes due to a temperature change, for example, of the crystal, this length is maintained via the Pound-Drever-Hall loop (see section 5.3). However, the subharmonic cavity detunings Δ_e and Δ_o still may change, due to the different refractive indices and their different derivations with respect to temperature. In addition, the electronic servo loop for the pump cavity length possesses only finite response time, which is in our experiments approximately 1.7 ms. Acoustic perturbations with frequencies above 600 Hz may thus rapidly change the cavity length, leading to small and random fluctuations of the cavity detunings as a function of time.

As the detunings Δ_e and Δ_o both enter the eigenvalues assumed by the subharmonic phases (via Eqs. 3.32 and 3.33), these eigenvalues are expected to drift and fluctuate as well. However, such temporal change of the eigenvalues φ_e and φ_o corresponds, via $\omega_x = \frac{d\phi_x}{dt}$, to a frequency deviation of the subharmonic frequencies from the exactly by 2 divided pump frequency.

Note, that the effect of a temperature drift (i.e. the slow frequency part of the fluctuations) can in good approximation be described by a drift of the e-wave detuning Δ_e. A change of the pump cavity length via a change of the crystal refractive index at the pump wavelength, induced by a temperature at a rate of $\frac{dn_p}{dT} = 4.5 \cdot 10^{-6} \frac{1}{K}$ is cancelled by the electronic cavity length stabilization. The change of the o-wave cavity length at a very similar rate of $\frac{dn_o}{dT} = 4.6 \cdot 10^{-6} \frac{1}{K}$ is also almost completely cancelled, but the corresponding change of the e-wave cavity length possesses a ten-times higher rate, $\frac{dn_e}{dT} = 5.1 \cdot 10^{-5} \frac{1}{K}$, and is therefore not cancelled. From these numbers one can conclude, that a drift of the crystal temperature results mainly in a drift of the e-wave detuning Δ_e of about $\frac{d\Delta_e}{dT} = 2455$ MHz/K, while the corresponding change of the o-wave detuning is about $\frac{d\Delta_o}{dT} = 5$ MHz/K, which is about 0.2% of that of the e-wave detuning.

Drift and fluctuations of the pump frequency can have two different effects. Firstly, there is an effect due to the change of the optical cavity length, which is very similar to the effect due to temperature changes described above. The refractive index of the crystal for the pump wavelength changes with the pump frequency, and as a pump frequency change is accompanied by a change of the subharmonic frequencies by half the amount, the refractive indices for the subharmonic waves change as well. The ratio, in which the e- and the o-wave cavity detunings change due to the changes of the refractive indices, is about the same as with the changes due to the temperature drift, which means that again a change of the e-wave detuning Δ_e is the dominant effect. However, this effect is much smaller than the effect due to temperature changes. A grating-stabilized diode laser of the type used in the experiments, suffers a frequency drift of typically about 10 MHz per minute (as found in our former experiments). A change of the pump frequency by 10 MHz would have the same effect on the optical cavity length as a change of the temperature by 10 μK.

The second effect induced by a change of the pump frequency is more obvious. If the pump frequency changes by a certain amount, the subharmonic frequencies have to change by half the amount, to maintain exact frequency division by two.

Therefore, the eigenvalues, which the phases assume, change. This fact is taken into account by Eq. 3.32, which expresses that the sum of the subharmonic phases $\varphi_e + \varphi_o$ adiabatically follows the sum phase. From Eq. 3.32 in combination with Eq. 3.33 it follows, that each of the two subharmonic phases follows a change of the pump phase adiabatically by half the amount. Thus this effect does not add to the intrinsic noise sources of the divider. It could, however, lead to relaxation oscillations of the amplitudes and phases of the three waves (see section 4.3), until the phase of the cavity internal pump field is adjusted to a new external pump phase.

Additional instabilities of frequency division may be caused by power fluctuations of any of the three OPO waves. In section 4.3, it is shown that any small deviation of a field amplitude results in oscillations of the amplitudes and the phases of all three involved OPO fields. However, it is also shown, that the phase oscillation of the self-phase-locked by-two-divider are strongly damped. For example, if the pump wave amplitude is disturbed, the phases of the e- and the wave follow with a small delay of about 20 ns. After that, the phases return to equilibrium, while the elongation decreases exponentially. This should give rise to a particular time ($\approx$ 140 ns, see section 4.3.3), after which the phase deviation is reduced to $\frac{1}{e}$ of its value. In addition, power fluctuations of the cavity internal pump field are reduced by the Pound-Drever-Hall cavity stabilization to less than 1% RMS of residual fluctuations.

6.3.2 Beat frequency fluctuations

To enable an estimation of the frequency stability of the divider, the drift and faster fluctuations of the beat frequency are observed, while the OPO is not phase-locked. The measurement of the beat frequency drift of the free-running OPO allows a qualitative and quantitative description of fluctuations and drift of the cavity detunings, which have been used for the theoretical calculation of the divider frequency instability presented in section 3.8.

Figure 6.5 shows four examples of the measured beat drift. In each of the graphs, the beat frequency is displayed as a function of time. The gray line is a linear function fitted to the measurements to obtain an estimate for the linear drift. A number of similar measurements have been performed with different measurements periods τ between the individual measurement points. From all measurements, a mean value of 36 kHz/s is obtained for the linear drift.

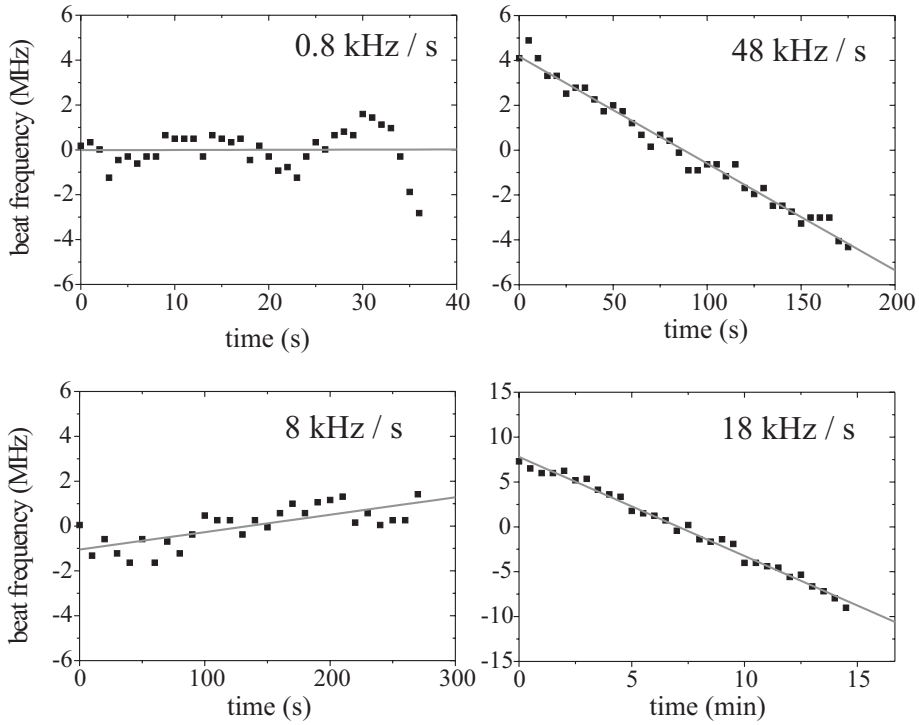

Figure 6.5: Slow drift of the beat frequency: Four examples of the beat frequency of the unlocked OPO measured as a function of time, displayed as symbols. The solid gray lines are linear fit functions to yield the mean drift, which is displayed by the number in the upper right corner of each graph.

In section 3.8, an expression for the stability of frequency division is derived. It is shown that the instability of the divider, i.e., the fluctuations of the subharmonic e-wave frequency ν_e with respect to the exactly divided pump frequency $\frac{1}{2}\nu_o$ are caused mainly by fluctuations of the phase difference of the subharmonics, $\varphi_e - \varphi_o$, while the fluctuations of the phase sum $\varphi_e + \varphi_o$ can be neglected. As only the phase sum and not the difference is influenced by the pump wave, the divider stability can be estimated in good approximation by measuring the fluctuations of the e-wave frequency with respect to the o-wave frequency. From the calculations presented in section 3.8, we obtained the result that the beat bandwidth to be

measured, $FWHM(\nu_e - \nu_o)$, is larger by a factor 4 than the beat bandwidth one would measure when comparing the subharmonic e-wave frequency directly to the exactly by-2 divided pump frequency, $FWHM(\nu_e - \frac{1}{2}\nu_p)$.

6.3.3 Measurement setup

In this section, the setup is described, that is used to measure the bandwidth of the beat signal between the two subharmonic waves, $FWHM(\nu_e - \nu_o)$. Next, the measurement itself is described and the resulting beat bandwidth is presented. The measured bandwidth is 4 times larger than the bandwidth of the deviation of the subharmonic e-wave frequency from the exactly divided pump frequency, which determines the residual frequency instability of the divider.

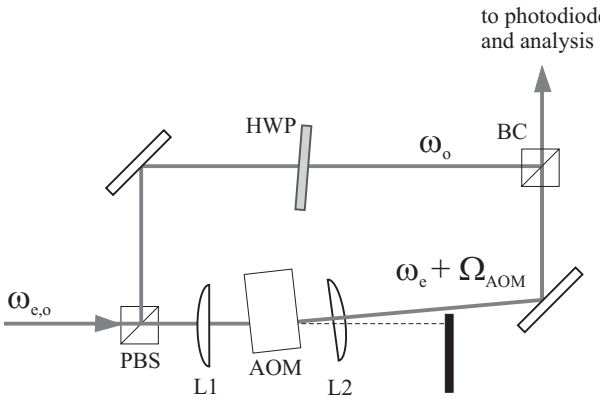

Figure 6.6: Setup used to shift the beat frequency out of the DC noise peak. PBS: polarizing beam splitter, AOM: acousto-optic modulator, L1 and L2: lenses used to focus through the AOM, HWP: half-wave plate, BC: beam combiner.

For measuring the bandwidth of the subharmonic beat signal, one has to consider that the average beat frequency is zero when the OPO is self-phase-locked. Thus the beat frequency would fall into the range of strong DC noise, making its detection rather difficult. To circumvent this problem, we shifted the beat frequency to a higher frequency using the setup shown in Fig. 6.6. After separating the e- and the o-wave using a polarizing beam splitter (PBS, Casix PBS0103, AR 1200-1550 nm), the e-wave is focused through an acousto-optic modulator (AOM,

Brimrose Corp. Model AMM-27-2, with driver model FFA-27-B1-F1) using two lenses (L1 and L2 in Fig. 6.6, each having a 80 mm focal length). Thereby the e-wave frequency is shifted by the AOM frequency of 27 MHz and diffracted under an angle of 8 mrad. The residual, non-shifted zero-order beam is blocked by a razor blade.

To superimpose the up-shifted e-wave with the non-shifted o-wave, the polarization of the o-wave is rotated by 90 deg using a half-wave plate (HWP). The beams are recombined with a beam combiner (BC, a 50% beam splitter cube CBS0105 from Casix) and interfere on a 3.5-GHz diode. The photodiode signal is sent through an RF-amplifier and to the RF-spectrum analyzer, the observation frequency range of which is around the AOM frequency of 27 MHz. The OPO subharmonic wavelengths are monitored parallel using the optical spectrum analyzer (ANDO AQ6315A) during the measurement, to be able to rule out that the OPO performs a spectral mode hop, which would bring the beat frequency out of the RF observation range and might be mistaken with a zero beat frequency.

The used setup should enable a measurement of the beat bandwidth, but, at the same time, it does add a number of extra sources for linewidth broadening, which have to be discussed before the results can be interpreted. Firstly, intensity fluctuations of the OPO subharmonic waves measured by the fast photodiode can lead to a broadening of the linewidth, since any amplitude modulation is related to a Fourier-frequency component added to the spectrum. However, as a result of the used Pound-Drever-Hall cavity stabilization, the output power of the divider OPO is fairly stable (residual pump power fluctuations $< 1\%$ RMS). Secondly, a residual frequency instability of the local quartz oscillator of the AOM may increase the measurable linewidth of the beat signal. The frequency stability of such a quartz oscillator is typically in the order of 10 Hz [125]. Finally, the minimum spectral resolution of the RF spectrum analyzer used is the upper limit for the accuracy of the linewidth measurement. For the used RF analyzer, this resolution is specified to be 10 Hz. In summary, the spectral resolution of the beat measurement can be composed from the linewidth broadening effects listed above. For our setup we expect that the 10-Hz spectral resolution of the RF spectrum analyzer or the 10-Hz stability of the AOM quartz oscillator will be the dominating contributions.

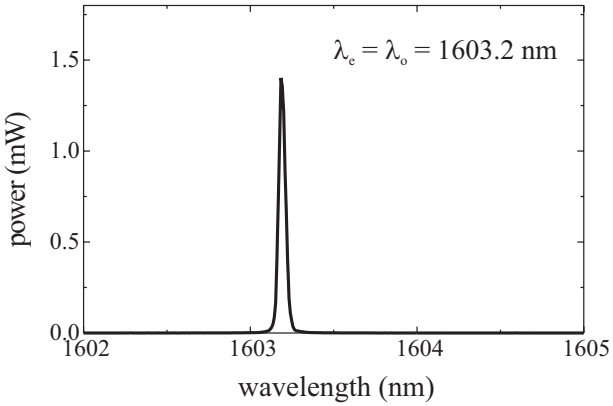

Figure 6.7: Spectrum of the OPO subharmonic wavelengths at frequency degeneracy on a large scale: $\lambda_e = \lambda_o = 1603.2$ nm

6.3.4 Frequency stability measurement

In the following, the measurement of the bandwidth of the beat frequency is presented. During this measurement, the crystal temperature is kept constant at 181.4 °C, and the subharmonic wavelengths are $\lambda_e = \lambda_o = 1603.2$ nm, as can be seen from the optical spectrum displayed in Fig. 6.7. The intracavity QWP was set to a rotation angle of $\vartheta_{QWP} = 3$ deg.

Figure 6.8 shows two examples of the measured spectra around the AOM frequency of 27 MHz for different observation spans. The measured spectra, displayed by the black traces in Figs. 6.8a and b are averaged over 20 sweeps, and the gray traces are the background spectra, recorded with the photodiode blocked. The main peak in the background spectra, which is actually rather weak (as it is typically 30 dB below the optical signal), is caused by RF-pickup from the AOM driver. The strong optical beat signal indicates that the two OPO subharmonic waves are phase-coherent (within the precision given by the narrow width of the optical beat signal).

Figure 6.8a shows the beat spectrum recorded over a span of 2 kHz. With the RF analyzer set to its highest resolution of nominally 10 Hz, the measurement time was 14 s (corresponding to 20 sweeps of 700 ms each). Fig. 6.8b) shows another

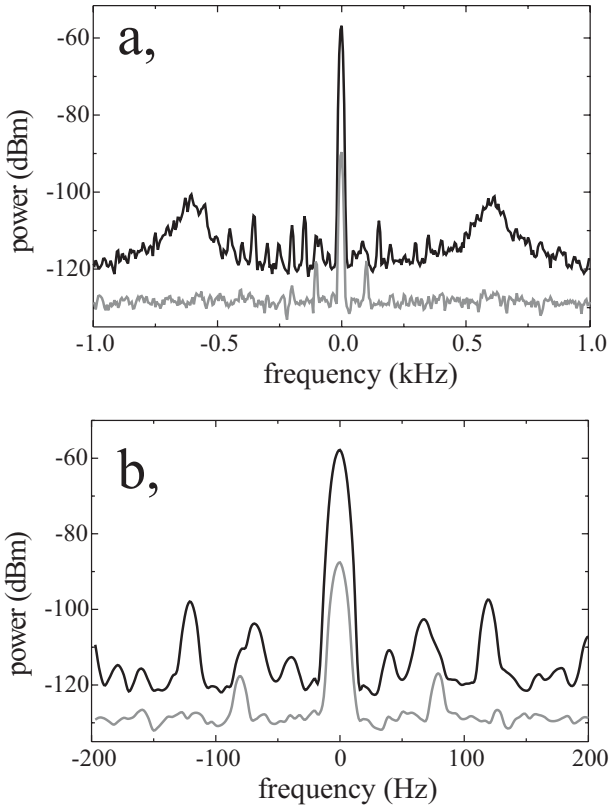

Figure 6.8: Spectra of the beat signal around the AOM frequency of 27 MHz. Black trace: beat spectra, averaged over 20 sweeps, gray trace: background signal.

beat spectrum recorded with a smaller span of 400 Hz and with a measurement time of 5 s (20 sweeps of 240 ms each). Measurements of the beat signal linewidth have been performed with measurement times between 200 ms and 14 s.

For an easier determination of the linewidth, the power of the beat signal is displayed as a function of its frequency on a linear scale in Fig. 6.9. This beat spectrum has been recorded over a span of 200 Hz and with a measurement time of 5 s (20 sweeps of 240 ms each). The full width at half maximum can be obtained from this measurement to be 11 Hz, which is limited by the resolution of the RF

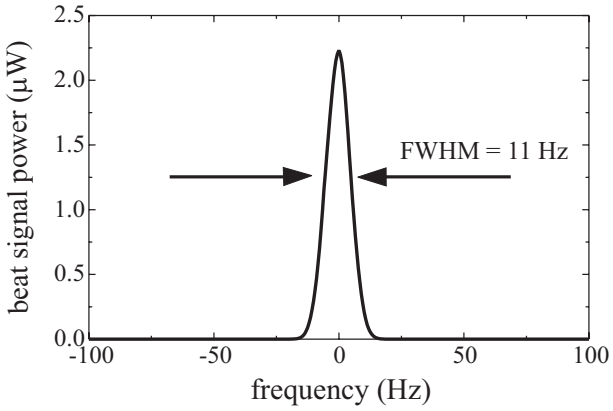

Figure 6.9: Spectrum of the beat signal around the AOM frequency at 27 MHz. The linewidth of the signal is 11 Hz (resolution limited).

analyzer used. We thus obtain a bandwidth of 11 Hz as an upper limit for the residual instability of the subharmonic frequencies with respect to each other. All measurements done with the RF analyzer set to the highest resolution bandwidth of 10 Hz yield the same full width at half maximum (FWHM) of the beat signal of 11 Hz. The background signal recorded with the photodiode blocked also yields a FWHM of 11 Hz (see the gray curve in Fig. 6.8 b), which indicates that the actual linewidth measurement is limited by the resolution bandwidth of the measurement equipment used.

According to the analytical calculation in section 3.8, this corresponds to a bandwidth of the e-wave fluctuations with respect to the exactly by two divided pump frequency of

$$FWHM(\nu_e - \frac{1}{2}\nu_p) \approx \frac{1}{4} FWHM(\nu_e - \nu_o) = 2.8Hz \tag{6.1}$$

for measurement times between 200 ms and 14 s. This value yields a residual fractional frequency instability $\frac{1}{\nu_e} FWHM(\nu_e - \frac{1}{2}\nu_p)$ of the by-2-divider OPO of $1.5 \cdot 10^{-14}$, which is resolution limited.

Besides the beat signal at 27 MHz, there are several several smaller peaks apparent in Figs. 6.8a and b. The broad sidebands in a distance of about 600 Hz

to the main peak in Fig. 6.8a are a often observed with phase locking experiments and are caused by the servo bandwidth of the OPO cavity length stabilization [127], [28], [128]. In Fig. 6.8b, a number of side peaks are apparent, which are caused by pickup of surrounding noise sources in the laboratory environment. An example is the peak at about 80 Hz, which is also visible in the background signal. However, as these peaks are below the beat signal by about 30 dB, they can be neglected when determining the beat bandwidth.

Summarizing this section, the residual frequency instability of the divider is determined for the first time in the frequency domain by measuring the bandwidth of the beat signal between the OPO subharmonic waves, which is shifted out of the DC noise peak to the frequency range around 27 MHz using an AOM. A linewidth of 11 Hz is obtained as an upper limit of the bandwidth. This corresponds to a bandwidth of 2.8 Hz of the subharmonic bandwidth with respect to exact division by 2, or to a fractional frequency instability of better than $1.5 \cdot 10^{-14}$ for measurement times between 200 ms and 14 s. Note, that the remaining instability is well comparable to the current primary standard for time measurements, as provided by the Cs atomic clock (with a relative instability of 10^{-15}).

6.4 Phase measurements

6.4.1 Measurement setup and working principle

To measure the phase relation of the OPO output waves, we use a polarization sensitive detector scheme, which has been introduced by Hänsch and Couillaud in 1980 [122], and the working principle of which can be described by the Jones-Matrix formalism of polarized light [129]. Originally, this detector is used to stabilize the frequency of a laser to a reference cavity. Here, however, we use such detection for the goal of retrieving the actual phase changes of the OPO waves.

The upper part of Fig. 6.10 shows the setup of the Hänsch-Couillaud-detector (HC-detector). The two OPO subharmonic waves pass a quarter-wave plate (QWP, Thorlabs WPQ501) which is set such that its fast axis forms an angle of 45 deg with either one of the OPO waves. After passing the QWP, the beam is split up by a polarizing beam splitter (PBS, Thorlabs PBS3). The two parts are detected by two fast Germanium-photodiodes (OEC GmbH, GM-3-HS, cut-off frequency 500 MHz) and electronically processed to yield both the sum and the difference of the measured photodiode signals.

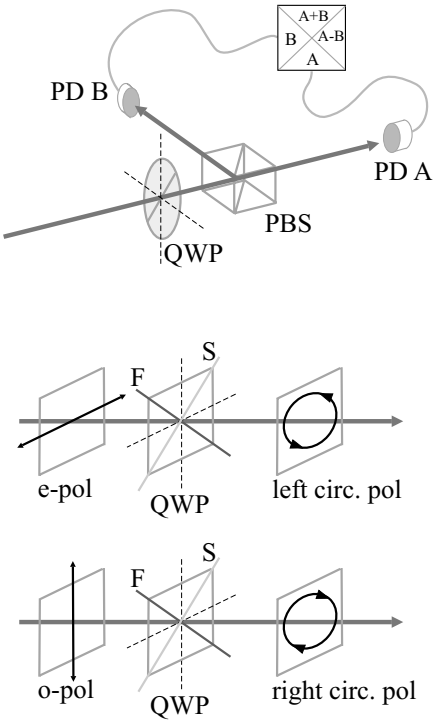

Figure 6.10: Setup of the Hänsch-Couillaud-detector (upper part) and the transformation of the polarization states (lower part). QWP: quarter-wave plate, fast axis set to form an angle of 45 deg with the polarization planes of both the e- and the o-wave; PBS: polarizing beam splitter; PD A and PD B: photodiodes. Lower part: A wave linear polarized in the e-wave plane is transformed into a left-circular polarized wave, and a wave linear polarized in the o-wave plane is transformed into a right-circular polarized wave. F: fast axis, S: slow axis of the QWP.

To understand the working principle of this detection and to be able to interpret the two electronic output signals, the transformations executed on the polarization

states of the e- and the o-wave are discussed in the following paragraphs. To follow the beam path as depicted in Fig. 6.10, we consider an arbitrarily polarized wave entering the HC-detector. Such a wave can be described as a superposition of two orthogonal polarizations, namely as a superposition of a wave being polarized in the plane of the e-wave and another wave being polarized in the plane of the o-wave.

This arbitrary polarized beam undergoes a polarization state transformation induced by the quarter-wave plate (QWP) with its fast axis set to 45 deg. Via the QWP, the wave which is linearly polarized in the extraordinary plane is transformed into a left circular polarized wave, and analogously, the wave linearly polarized in the ordinary plane is transformed into a right circular polarized wave. These polarization state transformations induced by the quarter-wave plate are depicted in the lower part of Fig. 6.10.

After the quarter-wave plate, the light is split up by the polarizing beam splitter into two linear polarized components, one being polarized in the ordinary, the other in the extraordinary plane. The component polarized in the ordinary plane is sent onto photodiode A, and the component polarized in extraordinary plane, is sent to photodiode B (PD A and PD B in Fig. 6.10). The signals of the two photodiodes are processed electronically to yield their sum and their difference.

The described steps have been carried out using the Jones-matrix formalism to calculate the difference signal we expect to measure with the Hänsch-Couillaud-detector. It has been found, that the difference signal varies as a cosine-function of the phase difference $\varphi_e - \varphi_o$. The amplitude of the signal is proportional to the geometrical average of the e- and the o-wave intensities, $\sqrt{b_e \cdot b_o}$. Therefore variations of the signal amplitude can be compensated for by dividing the difference signal by the sum signal. Note, that with the HC detector, it is not possible to distinguish the two phase eigenstates, as the phase difference $\varphi_e - \varphi_o$ determined by this detector is equal for both eigenstates. Note also, that the HC difference signal can be related unambiguously to a phase difference only modulo π. But as we are interested in the changes or drift of the phase difference, this is sufficient for our purpose.

The proper operation of our HC-detector was first tested by creating a wave with known polarization states. For this, one of the OPO subharmonic waves (with constant linear polarization) was filtered from the other and rotated by 45 deg with a half-wave plate. This beam was then split up by a polarizing beam splitter into

two beams with perpendicular polarization of approximately the same power, one being polarized in the extraordinary plane, the other one in the ordinary plane. The two beams were overlapped and then sent into the HC-detector. To introduce a phase shift between the waves, the path length of one of the waves (the one polarized in the extraordinary plane) was varied with a piezo transducer mounted behind a mirror, to which a triangular voltage was applied.

The cosine shape of the signal by introducing a linear change of the phase difference could be confirmed, as well as the fact that the amplitude of the difference signal divided by the sum signal remains constant, if the total power is changed. The constant proportion of the HC sum and difference signals provides a calibration factor of the HC-detector for conversion of the HC signal into the actual phase difference.

6.4.2 Measurement of a locked OPO's phase difference

With the described Hänsch-Couillaud-detector, it is possible to measure the phase difference of the OPO's subharmonic waves, $\varphi_e - \varphi_o$. When measuring the phases of the OPO subharmonic in the phase-locked state, we carefully checked that the OPO did not drift out of the locking range or mode-hopped to another subharmonic mode pair with its frequency difference above the cut-off frequency of the photodetectors used.

The subharmonic phases are measured as follows. Firstly, phase locking is achieved and verified by observing the beat signal at the AOM frequency with the RF analyzer, as described in the previous section 6.3. Thereafter, we use a flip-mirror (New Focus model no. 9891M), to direct the OPO output to the HC-detector setup. After having used the HC measurement for typically a few seconds, the beam is redirected to the RF analyzer to verify that the OPO is still self-phase-locked. Due to this procedure and our experience that the OPO is typically self-phase-locked for 15 minutes, we can safely assume that the OPO is indeed self-phase-locked during the entire HC-measurement.

Figure 6.11a shows an example of the HC difference signal measured as a function of time, where the quarter-wave plate is not yet inserted in the OPO cavity (and thus the OPO is not phase-locked). The frequency difference between the two subharmonic waves is well below the cutoff frequency of the HC detector photodiodes, as is confirmed by measuring the beat signal with the RF analyzer. As expected, the HC-signal displayed in Fig. 6.11a shows a cosine-function. From

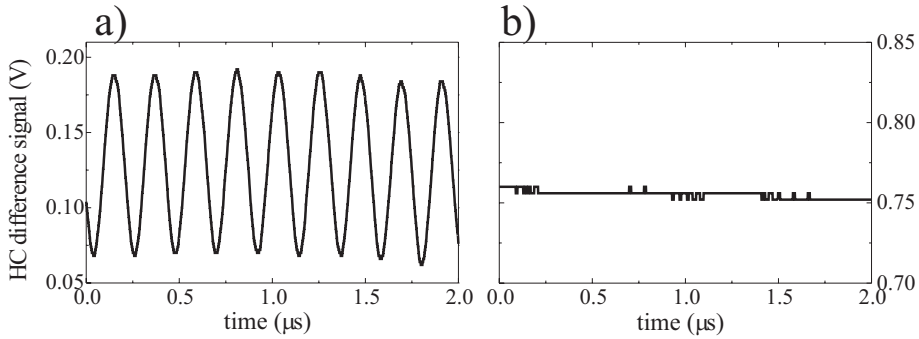

Figure 6.11: Measured HC difference signal as a function of time: a) while the OPO is not locked (without quarter-wave plate), and the beat frequency of the e- and the o-wave is about 4.5 MHz, and b) when the OPO is phase-locked.

the graph in Fig. 6.11a we obtain a period of the cosine-function of 0.2 μs, which corresponds to a beat frequency of $\nu_{beat} = |\nu_e - \nu_o| = 5$ MHz.

In contrast, Fig. 6.11b shows the signal of the HC detector as a function of time, when the OPO was phase-locked. The HC signal is constant in time, except for some steps in the trace, which are due to the limited resolution of the digital oscilloscope used for this measurement. This means, that the phase difference $\varphi_e - \varphi_o$ is stabilzed, the phases are locked with respect to each other, and residual fluctuations of the phase difference are suppressed. This is clear evidence, that the OPO is self-phase-locked and that the pump frequency is *phase-coherently* divided by 2 into the subharmonic frequency.

6.4.3 Phase stability

As demonstrated in the previous section, with the phase-sensitive Hänsch-Couillaud-detector, it is possible to directly measure the phase difference of the OPO subharmonic waves. Via $\omega = \frac{d\varphi}{dt}$, this should enable a measurement of the residual frequency instability of the divider with a considerably enhanced spectral resolution as compared to the measurement of the bandwidth of the beat signal described in section 6.3, where the resolution is ultimately limited by the spectral resolution of the RF analyzer (specified to be 10 Hz). With the HC technique, the

phase difference can be recorded directly as a function of time via, for example, an oscilloscope.

To measure the phase difference, the OPO output beams are measured using the Hänsch-Couillaud-detector as described in section 6.4.1 and shown in Fig. 6.10. After passing a quarter-wave plate (QWP, Thorlabs WPQ501) set to 45 deg, the beam is split up by a polarizing beam splitter (PBS2, Thorlabs model no. PBS3) and the two parts are detected by two Germanium-photodiodes (PD A and PD B, OEC GmbH, GM-3-HS). The photodiode signals are electronically processed to yield the sum and the difference of the measured signals, which are recorded as a function of time using an oscilloscope (Hameg 407-2). In order to obtain the phase difference of the subharmonic signals the HC-difference signal is scaled with the HC-sum signal (to compensate for power fluctuations) and with the calibration factor yielded from the initial test of the HC-detector. Calculating the arcus cosine of the resulting function gives then the phase difference of the subharmonic waves as a function of time.

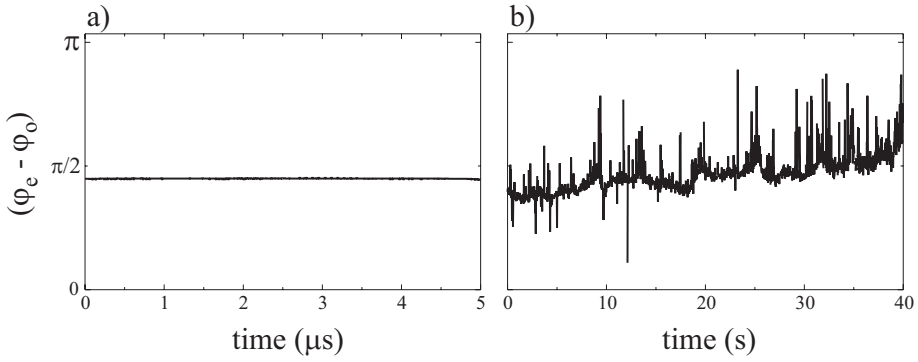

Figure 6.12: Measured subharmonic phase difference $\varphi_e - \varphi_o$ as a function of time. a) for a measurement time interval of 5 μs, and b) for a measurement time interval of 40 s.

In the experiment, the HC-signals were recorded for a number of different measurement intervals. During all of these measurements, the intracavity quarter-wave plate was set to 3 deg, and phase locking was verified by observing the beat frequency at the AOM frequency. Figure 6.12 shows two examples for a

measurement time interval of 5 μs (Fig. 6.12a) and for a measurement time interval of 40 s (Fig. 6.12b). From the first example shown in Fig. 6.12a, one can see, that the phase difference is highly stable over the measurement time of 5 μs. During this time, the phase difference stays within an interval of 0.02 rad.

In the second example shown in Fig. 6.12b, however, a measurable drift of the phase difference occurs. During this longer measurement interval of 40 s, the phase difference increases by about 0.71 rad. This corresponds to a temporal fluctuation of the phase difference $(\varphi_e - \varphi_o)$ which is as low as 0.018 rad/s or 2.8 mHz. Dividing this value by the frequency of the subharmonic waves, we obtain the residual frequency instability of the e-wave with respect to the o-wave and vice versa, which is $1.5 \cdot 10^{-17}$. Due to energy conservation the temporal change of the phases of the e-wave and the o-wave must be of the same absolute value, but of opposite sign with respect to the exactly by two divided pump frequency. Therefore, the residual phase fluctuation of the e-wave (or the o-wave) with respect to the target oscillation, namely the exactly by 2 divided pump wave, is then 1.4 mHz, which corresponds to a residual fractional frequency instability of by-2 division of $8 \cdot 10^{-18}$ for a measurement time of 40 s.

Note, that this very low instability is still higher than the theoretically derived possible fractional frequency instability based on the assumption by 3 orders of magnitude. This indicates, that the current stability measurement is probably limited by the stability of the measurement method, in particular of the electronic processing of the photodiode signal to yield the HC-sum and difference signals (electronic drifts of, for example, reference voltages).

Summarizing this section, the temporal fluctuation of the OPO's subharmonic phase difference has been measured as a function of time using the Hänsch-Couillaud detector. For a measurement time of 40 s, the residual phase fluctuation of the e-wave with respect to the exactly by 2 divided pump wave has been determined to be 1.4 mHz, which corresponds to an extraordinary low residual fractional frequency instability of by-2 division of $8 \cdot 10^{-18}$. Note, that this value is in the order of the high stability provided by modern atomic clocks in the visible spectral range.

6.4.4 The phase difference and power ratio of the subharmonic waves within the locking area

With the phase-sensitive Hänsch-Couillaud-detector it is possible to perform a stringent test of the theory derived in chapter 3. Specifically, this is done by changing the e- and o-wave detunings in a controlled manner, i.e., by taking a certain path over the e-o-plane or the locking area in Fig. 3.13, and by simultaneously measuring the phase difference $\varphi_e - \varphi_o$ as given by Eq. 3.33 and the power ratio of the two subharmonic waves.

Controlling the e- and o-wave cavity detunings

The most promising method for changing the e- and the o-wave detunings in a controlled manner is tuning via the crystal's lateral position. As compared to temperature tuning, changing the crystal position is faster, less influenced by drift, and therefore more reliable. Tuning via the pump frequency can also be considered, but the change in pump frequency required to tune the cavity detunings would be considerably too large in comparison with the mode-hop free tuning range of our diode laser. For these reasons, we choose to tune the e- and o-wave detunings via scanning the crystal position. To achieve this, the mount which supports the oven containing the crystal is equipped with a piezo actuator, as is described in more detail in the next section.

For a comparison of the measurements with theory, two relations have to be known. Firstly, it has to be determined, how the cavity detunings change when the lateral position of the crystal is scanned at a certain temperature. Secondly, the measurable quantities, i.e., the phase difference and the power ratio of the OPO subharmonic waves have to be calculated as a function of the cavity detunings determined before.

The cavity detunings Δ_e and Δ_o are calculated as a function of the crystal position using the expressions presented in section 5.6 with the corrected angles of the crystal's wedges (0.72 deg). The corrections are based on the observations presented in section 6.1.

The results of the expected position tuning are summarized in Fig. 6.13. In the plane spanned by the cavity detunings, the pathways along which the OPO is tuned by scanning the crystal position are given by the black lines. These are calculated for ten different crystal temperatures from 203.304 to 203.313 °C in 1-

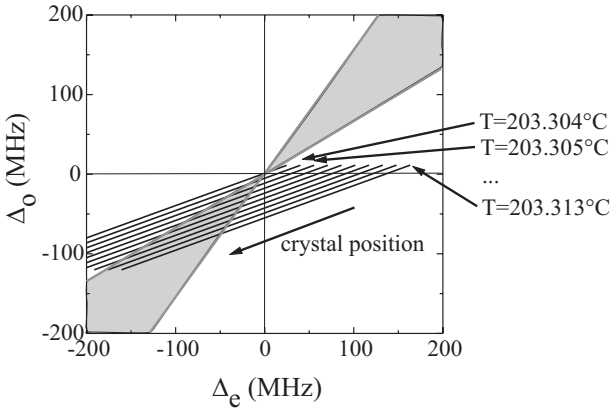

Figure 6.13: Possible pathways through the plane spanned by the e- and o-wave cavity detunings. The parallel black lines denote the paths along which the e- and o-wave detunings would tune by changing the crystal height for different crystal temperatures from 203.304 to 203.313 °C in 1-mK steps. The locking area for a quarter-wave plate angle of $\vartheta_{QWP} = 3$ deg is denoted by the gray area.

mK steps. The arrow indicates the tuning direction while increasing the position coordinate. The gray area indicates the locking area for a quarter-wave plate rotation angle of $\vartheta_{QWP} = 3$ deg. Figure 6.13 seems to imply, that the tuning path induced by changing the crystal position spans most of the locking area, such that a considerable part of the phase changes within the locking area should be observable. It can be expected, however, that only a limited portion of the locking area can be scanned, due to the occurrence of mode-hops (see section 5.6.4). In fact, the expected ranges over which the cavity detunings Δ_e and Δ_o can be changed continuously via the crystal position are 26 MHz and 10 MHz for the e-wave and the o-wave, respectively. To cover the entire locking area with such changes would be possible, in principle. In practice, however, this is difficult to realize in the present setup, because the temperature can be set only in steps of about 10 mK. Furthermore, while the OPO is self-phase-locked, there is no independent way to monitor the cavity detunings, which makes it impossible to select one particular path of those displayed in Fig. 6.13.

After having determined the path along which the e- and o-wave cavity detun-

ings change by scanning the crystal position, the phase difference $\varphi_e - \varphi_o$ and the power ratio of the subharmonic waves can be calculated along such a tuning path from Eq. 3.33. The power of either one of the subharmonic beams is given by the number of photons coupled out of the cavity per time unit times the photon energy. As the photon energy of the both subharmonic waves is the same, and the number of photons coupled out of the cavity is the respective intracavity photon number times the same output coupling factor, the external measurable power ratio equals the ratio of the intracavity photon numbers. The intracavity photon numbers can be calculated by raising the field amplitudes b_e and b_o to the square, which are given explicitly by Eqs. 3.34 and 3.35. However, to calculate the power ratio, Eq. 3.31 can be used, which after raising both sides to the square, yields

$$\frac{b_e^2}{b_o^2} = \frac{\Delta_o}{\Delta_e} \tag{6.2}$$

Figure 6.14 shows the expected, calculated phase difference of the e- and the o-wave with respect to each other (black traces) and the power ratio (gray traces), calculated as a function of the lateral position of the crystal. The traces are determined for five different examples with crystal temperatures ranging from 203.104 to 203.112 °C in steps of 2 mK. This corresponds to five of the tuning pathways displayed in Fig. 6.13. Note, that the shape of the traces does not change with temperature, but that they are stretched as the locking area broadens with increasing cavity detunings. Also, the power-ratio curves scale in the vertical direction, such that an absolute measurement of the power ratio is not required. In Fig. 6.14, the maximum continuous tuning range of the cavity mode detunings Δ_e and Δ_o of 26 MHz and 10 MHz, respectively, which can be expected by changing the lateral crystal position, correspond to a change of the lateral position of the crystal by 10.6 μm. In the lowest graph of Fig. 6.14 for a crystal temperature of 203.304 °C, it should be possible to scan the whole area without any mode-hop occurring. However, in the second lowest graph, for a crystal temperature of 203.306 °C, the width of the locking area is already five times the maximum range that can be scanned. The temperature can not be set with such a high accuracy, but we expect to experimentally catch at least a bigger portion of one of the phase and power traces in Fig. 6.14.

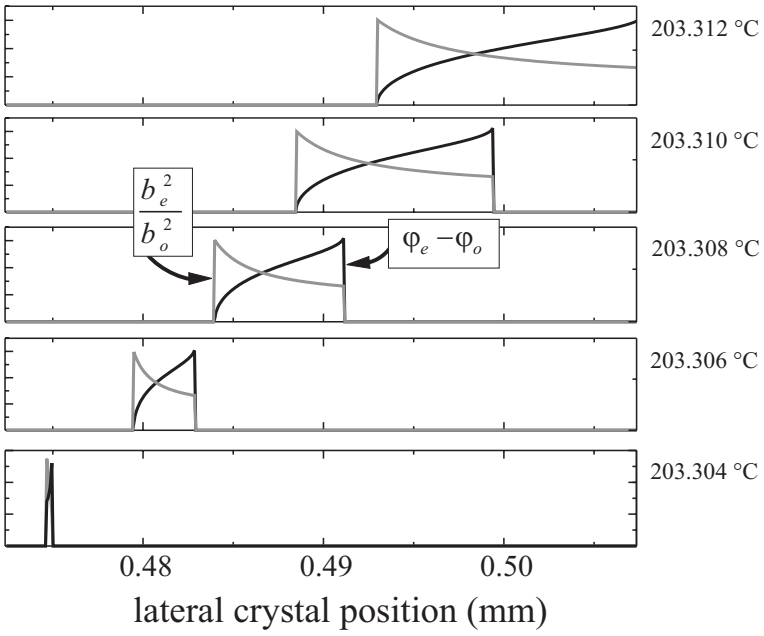

Figure 6.14: Phase difference $\varphi_e - \varphi_o$ (black traces) and power ratio b_e^2/b_o^2 (gray traces) of the OPO subharmonic waves calculated as a function of the lateral position of the crystal for different crystal temperatures from 203.304 to 203.312 °C in 2-mK steps.

Measurement setup

In order to be able to change the lateral position of the crystal in a way that its exact position can be determined at any time, the mount of the crystal oven is equipped with a piezo actuator (Piezomechanik GmbH, piezo stack 500/5/25, elongation of 25 μm per 500 V applied voltage). The crystal position is scanned by applying a triangular voltage, which is generated by a function generator (Voltcraft 7202 sweep/function generator) and amplified by a piezo-driver (Piezomechanik GmbH, SVR 500-3). The amplifier also supplies a monitor voltage, which is used to observe the applied voltage.

The setup used for simultaneously measuring the OPO's subharmonic phase difference and power ratio is shown in Fig. 6.15. Using a 50% beam splitter

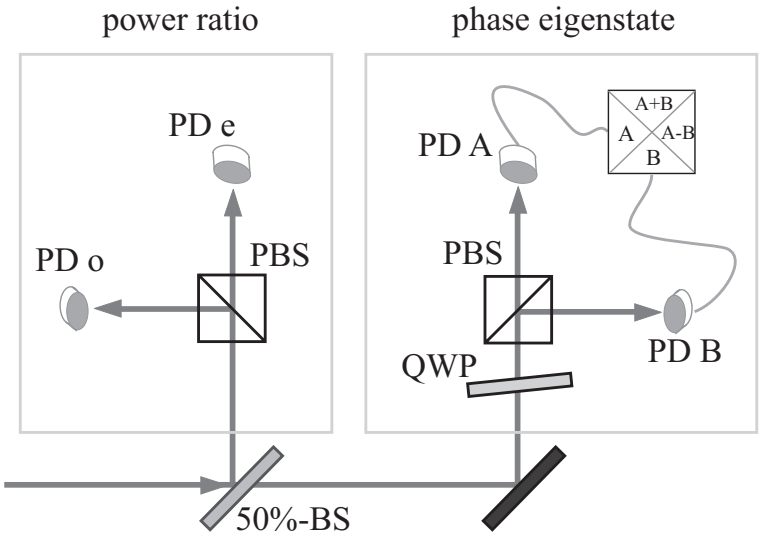

Figure 6.15: Setup for simultaneous measurement of the subharmonics phase difference and power ratio. The OPO output beam is split up using a 50%-beam splitter (50%-BS). Left part: setup for measurement of the power ratio. PBS1: polarizing beam splitter, PDe and PDo: photodiodes. Right part: HC-detector for measurement of the phase difference. QWP: quarter-wave plate, PBS2: polarizing beam splitter, PD A and PD B: photodiodes.

(Thorlabs BS012, 1100-1600 nm broadband beam splitter cube, 50%-BS in Fig. 6.15), the OPO subharmonic beams are split up into two parts. The beam splitter is chosen such that the two beams with different polarizations are split up with approximately the same ratio, in order minimize the error on the power ratio measurement. One part is used to measure the power ratio of the subharmonic beams. Therefore the extraordinary and the ordinary polarized parts are divided using a polarizing beam splitter (PBS1, Thorlabs model no. PBS3) and are measured with two Germanium-photodiodes (PDe for measurement of the e-wave power and PDo for the o-wave power, OEC GmbH, GM-5VHS-L). The right hand side of the setup shows the Hänsch-Couillaud-detector (HC-detector) used to measure the variation of the OPO's phase eigenstate, as discussed before in section 6.4.1 and shown in Fig. 6.10. After passing a quarter-wave plate (QWP, Thorlabs WPQ501) set to

45 deg, the second part of the beam is split up by a polarizing beam splitter (PBS2, Thorlabs model no. PBS3) and the two parts are detected by two Germanium-photodiodes (PD A and PD B, OEC GmbH, GM-3-HS). The photodiode signals are electronically processed to yield the sum and the difference of the measured signals.

The over-all efficiency, with which the power of the two subharmonic waves is measured, differs, due to the different transmission coefficients of the optical components for the two polarizations. The power ratio can thus not be determined absolutely, however, this is not required for comparison with theory.

In contrast, the phase difference measurement yields absolute values, after scaling the HC-difference signal with the sum signal to compensate for the power fluctuations and after scaling with the calibration factor obtained from the testing the detector as described in section 6.4.1. The only uncertainty left is a trivial phase offset between the measured values and the phase difference inside the OPO cavity, due to the different optical path lengths for the e- and the o-wave to the detector.

The described setup yields four signals, which are recorded in parallel using a data acquisition card (National instruments PCI 6013) and a PC: the voltage values of the two photodiodes PDe and PDo, and the sum and the difference signal generated by electronically processing the Hänsch-Couillaud-detector signals. As a fifth signal, the voltage applied to the piezo actuator to scan the crystal's lateral position is recorded as well.

Experimental Results

During the measurements presented in this section, the intracavity quarter-wave plate is set to 3 deg. The beat signal, which is observed on the RF analyzer, is tuned towards zero beat frequency, until the beat signal is detected at the AOM frequency, which means that the OPO is self-phase-locked.

To measure the OPO subharmonic phase difference and their power ratio, the lateral position of the crystal is scanned by applying a triangular voltage to the piezo actuator integrated in the crystal oven mount. To find a suitable range within which the crystal position is scanned, i.e. a suitable voltage span, the HC difference signal is observed using an oscilloscope. Figure 6.16 shows an example of such a measurement to illustrate the procedure. The difference signal of the HC-detector is shown as a function of time (black trace), while scanning the crystal

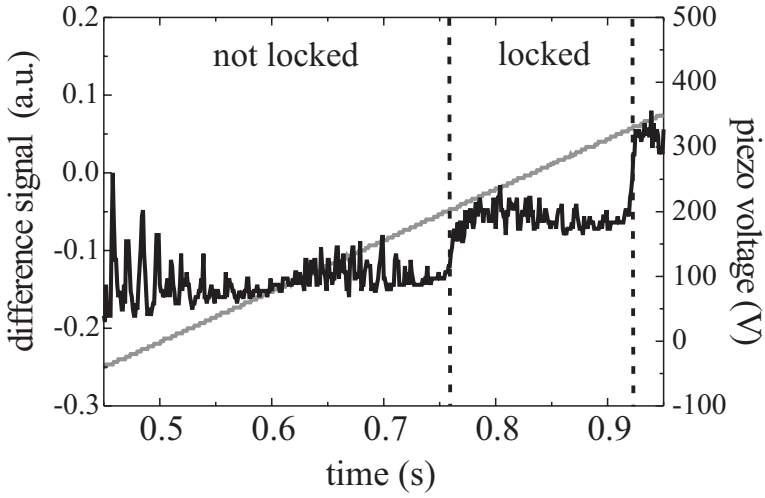

Figure 6.16: Difference signal of the HC-detector as a function of time, while the lateral position of the crystal is scanned with a triangular function. Black trace: HC difference signal, gray trace: voltage applied to the piezo actuator.

position according to the triangular function (gray trace). In this example, the crystal position is scanned over about 18 μm, which is more than the maximum scanning range possible without inducing a mode-hop of the OPO subharmonic waves. Such mode-hops were observed with the RF analyzer, which means that the OPO is phase-locked only during the time span indicated by the vertical dashed lines in Fig. 6.16. The events of the OPO entering and leaving the locking area can also be identified in the HC difference signal where discontinuities are observed at corresponding crystal positions (compare the intersection points of the dashed lines with the measured curve in Fig. 6.16). Note, that the HC difference signal shows rather large fluctuations within the locking area. These fluctuations are probably caused by the crystal position being scanned so fast, that the OPO subharmonic waves cannot follow adiabatically and exhibit relaxation oscillations around the steady-state solutions.

To avoid mode-hops during the measurement, the piezo voltage is reduced, until the OPO stays locked during the entire scan. This again is verified by observing the beat signal using the RF analyzer. Then the crystal height is changed rather slowly,

by about 5 μm/s, such that a steady state is maintained during the measurement and that the phases and the power values can follow the changing eigenstates. The signals of the photodiodes PDe and PDo, the HC sum and difference signal and the piezo voltage monitor signal are recorded with 2000 data points per second per channel.

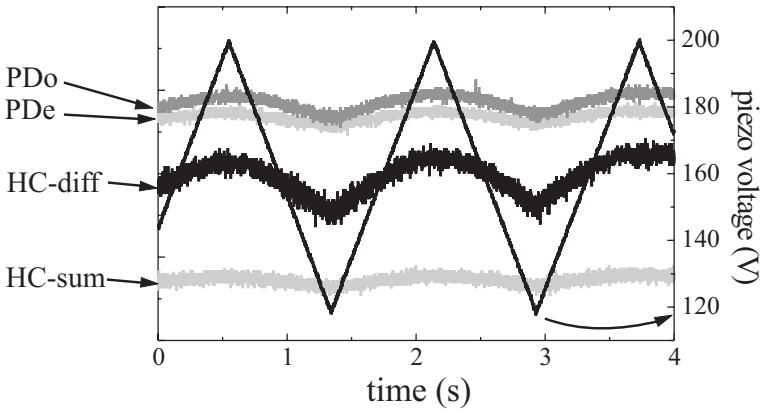

Figure 6.17: Signals obtained with the data acquisition card as a function of time, while the crystal height is scanned with a triangular function. The black triangular trace is the piezo voltage monitor signal, the other four traces are, from top to bottom: signal of photodiode PDo, signal of PDe, difference signal and sum signal of the HC-detector.

Figure 6.17 shows the result of a measurement. The monitor signal of the voltage applied to the piezo actuator is given by the black triangular function. The other traces in Fig. 6.17 are, from top to bottom, the signal of photodiode PDo for measurement of the o-wave power, the signal of photodiode PDe, the difference signal of the HC-detector and the corresponding sum signal.

For further evaluation, the shown measured signals are processed as follows. To remove the fast fluctuations on the signals, each of the traces is smoothed by averaging over 50 adjacent points, which corresponds to averaging over a time span of 25 ms. The photodiode signal PDe is divided by the signal PDo, which yields a trace proportional to the power ratio b_e^2/b_o^2. The HC-difference signal is scaled with the HC-sum signal to compensate for power fluctuations of both OPO

output beams and with the calibration factor yielded from the initial test of the HC-detector. Calculating the arcus cosine, the phase difference of the subharmonic waves is obtained. Finally, the applied voltage is converted into the crystal height scanned per time unit, using specified elongation of 25 μm per 500 V of the piezo actuator (Piezomechanik GmbH, piezo stack 500/5/25).

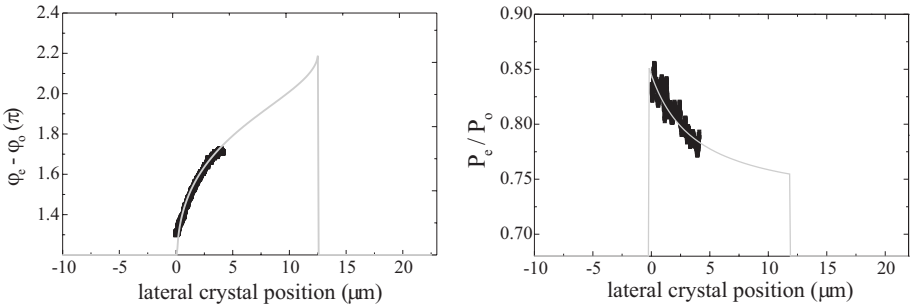

Figure 6.18: Left graph: phase difference and right graph: power ratio as a function of the lateral position of the crystal. Black trace: measured values, gray trace: theoretically calculated values.

The result is shown in Fig. 6.18. In the left graph, the measured phase difference $\varphi_e - \varphi_o$ is displayed as a function of the lateral crystal position by the black trace. The gray trace is the phase difference as calculated for a crystal temperature of T = 203.3108 °C. Note, that the only fit parameters used are a constant crystal temperature offset, a constant offset for the phase difference, and a constant offset for the lateral crystal position. The graph on the right hand side shows the power ratio as a function of the crystal position. Again the measured ratio is displayed by the black trace, and the gray trace gives the power ratio calculated for the same crystal temperature (T = 203.3108 °C) and using the same offset for the crystal position. As only the relative variation of the power ratio is measured, the calculated ratio has been scaled using a factor 9.

Note, that the part of the locking area which is covered by this measurement corresponds to a change of the e-wave detuning Δ_e of 24 MHz and a change of the o-wave detuning Δ_o of 9.6 MHz, which is also in agreement with the predicted values 26 MHz and 10 MHz, over which the cavity detunings Δ_e and Δ_o are expected to change without a mode-hop occurring. As mentioned before, scanning of the

crystal position over a wider range resulted in discontinuities in the traces (see Fig. 6.16), which indicates that the values of 24 MHz and 9.6 MHz indeed correspond to the widest scan of the cavity detunings within the locking area that is possible without mode-hops was scanned.

The experimentally observed subharmonic phase difference and the subharmonic power ratio are in full agreement with the theoretical prediction. The measured values of the largest continuous variation of the e- and o-wave detuning agree very well with theory. This proves the validity of the theory derived in chapter 3.

With the presented measurements, for the first time, it has become possible to monitor the e- and o-wave cavity mode detunings *without* the need of a beat measurement. At the same time, it has been demonstrated that these detunings can be fully controlled with respect to the exactly by-2 divided pump frequency via experimental system parameters. These experimental results demonstrate that two basic requirements for stable and reliable frequency division are fulfilled: firstly, via the measurement of the phase difference and power ratio, the cavity detunings can be determined. This means, that the position of the OPO within the locking area is known. Secondly, one can control the cavity mode detunings, which means that the position of the OPO within the locking area can be changed deliberately. Combined, this forms a valuable tool to steer the divider, such that the OPO can be kept in the self-phase-locked operation state, basically for an unlimited time.

In conclusion, we measured the phase difference and the power ratio of the self-phase-locked divider OPO as a function of the cavity detunings. The cavity detunings have been scanned in a controlled manner by using a piezo actuator to change the crystal's lateral position. Doing so, we have been able to scan an appreciable portion of the locking area, in full agreement with theory. The measured phase difference $\varphi_e - \varphi_o$ is also in excellent agreement with the predicted values. The power ratio has also been verified to show the predicted behavior. These measurements confirm the theory derived in chapter 3.

6.5 Summary

Summarizing this chapter, the first wavelength-tunable frequency-by-2-divider has been realized based on a self-phase-locked cw OPO. Self-phase-locked frequency division by 2 has been proven by measuring the suppression of the beat in a range

around zero beat frequency. Typically, the divider operates within the stable self-phase-locked state for 15 minutes. In agreement to the stability analysis, which predicts that there should be no high-threshold state observable in the experiment, we have observe only a single state of threshold pump power. The locking range has been measured to increase with the quarter-wave plate rotation angle, and to extend to 160 MHz at a QWP angle of 6 deg, in good agreement with the theoretical prediction of 170 deg.

For the first time, the frequency stability of the divider has been quantitatively determined by measuring the bandwidth of the beat signal between the OPO subharmonic waves. A linewidth of 11 Hz has been obtained as an upper limit of the bandwidth, which corresponds to a bandwidth of 2.8 Hz of the subharmonic bandwidth with respect to exact division by 2, or to a fractional frequency instability of better than $1.5 \cdot 10^{-14}$, which is resolution limited.

To achieve a much higher precision of the divider phase stability, a direct measurement of the phase difference of the two subharmonic waves was carried out by using a Hänsch-Couillaud-detector. This measurement yielded a residual fluctuation of the relative phase of the two subharmonic waves of 0.7 rad in 40 s. This corresponds to an extremely low residual fractional frequency instability of by-2 division of $8 \cdot 10^{-18}$.

Finally, the subharmonic phase difference and the power ratio of the self-phase-locked divider OPO have been measured as a function of the cavity detunings. The measured phase difference $\varphi_e - \varphi_o$ and power ratio are in excellent agreement with theory. For the first time, it has become possible to monitor and to fully control the e- and o-wave cavity mode detunings. This forms a valuable tool to steer the divider, such that the OPO can be kept in the self-phase-locked operation state, basically for an unlimited time.

Chapter 7

Summary

This thesis has investigated a new method, with which modern visible and near-infrared frequency standards can be transferred to longer, mid-infrared wavelengths so that their ultra-high frequency precision becomes available for metrological applications in this wavelength range. Specifically, the potential of a self-phase-locked cw OPO as a wavelength-flexible, phase-coherent frequency by-2-divider has been investigated theoretically and experimentally. This thesis could show that, based on a very versatile design, such an OPO can be realized to divide a given pump laser frequency by an exact factor of 2, with a precision that matches the highest precision currently available from atomic clocks operating in the visible and near-infrared.

Theoretical modelling

Theoretically, self-injection locking of a type-II phase-matched, by-2-divider OPO was investigated by solving the coupled field equations in steady-state regime. The steady-state values of the OPO parameters in the phase-locked state were calculated analytically, using the actual experimental parameters such as the cavity finesses and the rotation angle of the cavity internal quarter-wave plate. From the coupled field equations, the condition for occurrence of self-phase locking was derived. The dependence of the locking range, which is the minimum observable beat frequency of the subharmonic waves before self-phase locking, on different experimental parameters was investigated. By taking into account temperature drift as the major mechanism disturbing the self-phase-locked state, as observed

in the experiment, the locking range was calculated theoretically as a function of the rotation angle of the quarter-wave plate.

Previously it had been shown that in the self-phase-locked case there are two formal solutions of the coupled field equations, corresponding to two different values for the OPO pump power at threshold. In this work, the first mathematical stability analysis was applied to these solutions describing the by-2-divider. This stability analysis shows that only the solution corresponding to the lower threshold state is stable, whereas the one of the higher threshold state is unstable, which is in contrast to previous expectations. The stability analysis is confirmed by the experimental observation, that during the extended time periods over which our divider was being operated, always only one pump power at threshold was observed.

In order to obtain a theoretical prediction of fractional frequency stability, the dependence of the phases of the subharmonic waves on cavity mode parameters was studied. This revealed a two-fold symmetry in phase space, corresponding to two phase-eigenstates of the coupled field equations, in agreement with earlier studies. Considering phase instabilities induced by temperature drift, the theoretically possible fractional frequency stability of the divider was estimated to be as good as $4 \cdot 10^{-21}$. It was also found, that the spectral bandwidth of the divider can in good approximation be determined by directly measuring the bandwidth of the beat signal between the two OPO subharmonic waves and dividing the obtained value by a factor 4.

In order to extend the theoretical model of the frequency divider OPO from the described analytical description of the steady-state to a description of the dynamic properties, a numerical approach was used. Using experimental parameters, the coupled field equations were integrated numerically using a 4th order Runge-Kutta technique. Firstly, for comparison with the analytical model, the numerical steady-state solutions were determined. Both, the analytically and numerically derived steady-state values are in excellent agreement. In particular, for the self-phase-locked state, the numerical study confirms the existence of only a single stable threshold state, and the two-fold symmetry in phase space found already in the analytical study. Secondly, the numerical model was used to gain a deeper insight into the experimental relevance of the two phase eigenstates. It was found that the assumption of one or the other phase eigenstate does not depend on any experimental parameter, but only on the initial phases of the subharmonic waves.

In further numerical studies, a rich scenario of phase dynamics was discovered, which may certainly inspire and guide future experimental investigations.

Experimental results

The experimental setup of the phase-coherent frequency by-2 divider is based on a type-II phase-matched cw OPO that has an intracavity quarter-wave plate to enable self-injection locking of the two orthogonally polarized, frequency-degenerate subharmonic waves. In order to demonstrate the versatility of the frequency-divider concept, the types of components used in the OPO setup were chosen carefully to ensure full wavelength flexibility of the design.

Firstly, a wavelength-tunable pump source is used, which is in the present case a diode master-oscillator power-amplifier (MOPA) system. Diode lasers are available over a wide spectral range from the ultraviolet ($\lambda < 400$ nm emitted by GaN diode lasers) to the far infrared ($\lambda = 85$ μm from quantum cascade diode laser). In addition they provide the advantages of an excellent spectral and spatial beam quality, which offers the possibility to stabilize their oscillation frequency to, e.g. an optical clock transition. The diode MOPA used in this work generates up to 360 mW radiation around a wavelength of 802 nm in a single-frequency, near-diffraction limited beam.

The second choice taken to obtain wavelength flexibility is a nonlinear conversion process that is not restricted by the conditions of birefringent phase matching (BPM). Instead, the quasi-phase matching (QPM) method was used, because it allows one - as opposed to BPM - to phase-match in principle any three-wave mixing process within the entire transparency range of the crystal. For exploiting QPM in our experiment, a periodically poled lithium niobate (PPLN) crystal was chosen as the nonlinear medium, which is transparent over the wavelength range from 400 nm to 5 μm. Corresponding to our particular choice of the pump laser wavelength at around 800 nm, we used a PPLN crystal that was designed for OPO operation close to wavelengths of 1.6 μm, i.e. close to frequency degeneracy, where by-2 division of the pump laser frequency can be achieved.

In the experiment, self-phase-locked operation of the OPO at exactly one-half of the pump laser frequency is proven by measuring the suppression of the beat signal between the two subharmonic waves in a range around zero beat frequency. The locking range of the process was determined as a function of the coupling strength between the two subharmonic waves, as given by the rotation angle of

the intracavity quarter-wave plate. The results are in good agreement with theory, yielding a maximum locking range of 160 MHz at a quarter-wave angle of 6 deg, given by the pump power used.

Typically, the by-2-divider operates stably within the self-phase-locked state for 15 minutes, without any additional electronic stabilization of the phases of the subharmonic waves. In further theoretical and experimental investigations, the potential was explored of keeping the OPO for basically indefinite long time periods in the self-locked state. The phase difference and the power ratio of the self-phase-locked divider OPO are measured as a function of the detunings of the subharmonic cavity modes from the exact one-half of the pump laser frequency. The cavity detunings are scanned by changing the crystal's lateral position. A measurement of the phase difference $\varphi_e - \varphi_o$ and the power ratio of the two subharmonics as a function of the cavity detunings confirms the theoretical model of the divider developed in this thesis. These measurements demonstrate, that the parameters that determined the self-locking behavior of the divider can be controlled experimentally. Therefore, by using a conventional electronic controller it should become possible to keep the by-2-divider in the self-phase-locked state for practically unlimited periods of time.

Frequency stability measurements

For the first time, the frequency stability of a by-2-divider was determined experimentally, and it was done in two different ways. In the first experiment, the bandwidth of the beat signal between the OPO subharmonic waves was determined. The resolution-limited measurement yielded a linewidth of 11 Hz as an upper limit of the bandwidth of the beat signal, and thus a maximum bandwidth of 2.8 Hz of each of the subharmonics with respect to exact division by 2. This corresponds to a fractional frequency instability of better than $1.5 \cdot 10^{-14}$.

In the second experiment, the fluctuation of the relative phase of the two self-phase-locked subharmonic waves was monitored directly by using, for the first time, a Hänsch-Couillaud type phase-sensitive detection technique. In this experiment, a relative phase drift of only 0.07 rad in a time interval of 40 s was measurement. This corresponds to an extremely low residual fractional frequency instability of $8\dot{1}0^{-18}$. This excellent stability compares favorably with the best frequency stabilities currently achieved with optical frequency standards. This measurement thus proves that the OPO based by-2-divider should be capable of transferring modern

frequency standards to new wavelength ranges with maximum precision.

Conclusion

In conclusion, this work significantly contributes to the development of OPOs as stable, self-phase-locked all-optical frequency divider stages. In this work, the stable division of the output frequency from a diode laser was realized with an OPO device based on a modern quasi-phase-matching material. This demonstrates the full wavelength flexibility of the approach for future applications. Using the same basic design concept, the operation of future OPO frequency dividers can be extended to other wavelength ranges. For example, by using a different nonlinear material such as orientation patterned GaAs, it should be possible to cover the entire wavelength range from 0.9-17 μm [41] [42]. By exploiting quasi-phase matching in waveguides [43], the design of on-chip frequency divider stages seems well feasible. Due to their monolithic design, such on-chip devices should have an intrinsically high passive frequency stability. The high conversion efficiency typical for all OPOs should enable a cascading of self-phase-locked processes to achieve an all-optical frequency division also by higher integer numbers, such as 4 and 6. Divider stages like the one presented in this work may also be used to transfer any particular mode selected from a frequency stabilized optical frequency comb into the MIR. Future experiments might aim at an extension of the concept, for example from the all-optical division of a single frequency to the simultaneous division of several frequencies or even an entire comb.

The ultra-high stability of the self-phase-locked frequency by-2 divider together with the versatility of the concept due to its full wavelength flexibility, demonstrate the huge potential of such devices to become powerful tools for advanced precision metrology in the mid and far infrared.

Bibliography

[1] Bureau International des Poids et du Mesures, Organisation Intergouvernementale de la Convention du Mètre. The international system of units (SI). 7^{th} edition of the brochure, 1998. Electronic version available on http://www.bipm.fr.

[2] B.W. Petley. Time and frequency in fundamental metrology. *Proc. IEEE*, 79(7):1070–1076, July 1991.

[3] W. Lewandowski and C. Thomas. GPS time transfer. *Proc. IEEE*, 79(7):991–1000, July 1991.

[4] S.-C. Han, J.H. Kwon, and C. Jekeli. Accurate absolute GPS positioning through satellite clock error estimation. *J. Geodesy*, 75:33–43, 2001.

[5] O. Polat, H. Eyidogan, H. Haessler, A. Cisternas, and H. Philip. Analysis and interpretation of the aftershock sequence of the August 17, 1999, Izmit (Turkey) earthquake. *J. Seismol.*, 6(3):287–306, July 2002.

[6] A. Manake and M.N. Kulkarni. Study of the deformation of Koyna Dam using the Global Positioning System. *Surv. Rev.*, 36(285):497–507, July 2002.

[7] R.A. Bennett, B.P. Wernicke, N.A. Niemi, A.M. Friedrich, and J.L. Davis. Contemporary strain rates in the norhtern Basin and Range province from GPS data. *Tectonics*, 22(2):art. no. 1008, March 2003.

[8] J.H. Taylor, Jr. Millisecond pulsars: Nature's most stable clocks. *Proc. IEEE*, 79(7):1054–1062, July 1991.

[9] L.A. Rawley, J.H. Taylor, M.M. Davis, and D.W. Allan. *Science*, 238:761, 1987.

[10] P.J. Mohr and B.N. Taylor. CODATA recommended values of the fundamental physical constants: 1998. *Rev. Mod. Phys.*, 72(2):351–495, April 2000.

[11] R.F.C. Vessot, M.W. Levine, E.M. Mattison, E.L. Blomberg, T.E. Hoffman, G.U. Nystrom, B.F. Farrel, R. Decher, P.B. Eby, C.R. Baugher, J.W. Watts, D.L. Teuber, and F.D. Wills. Test of relativistic gravitation with a space-born hydrogen maser. *Phys. Rev. Lett.*, 45(26):2081–2085, December 1980.

[12] J.P. Turneaure, C.M. Will, B.F. Farrell, E.M. Mattison, and R.F.C. Vessot. Test of the principle of equivalence by a null gravitational red-shift experiment. *Phys. Rev. D*, 27(8):1705–1714, April 1983.

[13] T. Damour and J.H. Taylor. Strong-field tests of relativistic gravity and binary pulsars. *Phys. Rev. D*, 45(6):1840–1868, March 1992.

[14] A. Brillet and J.L. Hall. Improved laser test of the isotropy of space. *Phys. Rev. Lett.*, 42(9):549–552, February 1979.

[15] H. Müller, S. Herrmann, C. Braxmaier, S. Schiller, and A. Peters. Modern Michelson-Morley experiment using cryogenic optical resonators. *Phys. Rev. Lett.*, 91(2):Art. no. 020401, July 2003.

[16] D. Bear, R.E. Stoner, R.L. Walsworth, V.A. Kostelecky, and C.D. Lane. Limit on Lorentz and CPT violation of the neutron using a two-species noble-gas maser. *Phys. Rev. Lett.*, 85(24):5038–5041, December 2000.

[17] L.L. Lewis. An introduction to frequency standards. *Proc. IEEE*, 79(7):927–935, July 1991.

[18] A. Bauch and H.R. Telle. Frequency standards and frequency measurements. *Rep. Prog. Phys.*, 65:789–843, 2002.

[19] F.G. Major. *The quantum beat: the physical properties of atomic clocks.* Springer, New York, 1998.

[20] A.N. Luiten (ed.). *Frequency measurement and control - Advanced techniques and future trends.* Springer, Berlin, 2001.

[21] Th. Becker, J. v. Zanthier, A. Yu. Nevsky, Ch. Schedes, M.N Skvortsov, H. Walther, and E. Peik. High-resolution spectroscopy of a single In^+ ion: Progress towards an optical frequency standard. *Phys. Rev. A*, 63:art. no. 051802, 2001.

[22] R.J. Rafac, B.C. Young, J.A. Beall, W.M. Itano, D.J. Wineland, and J.C. Bergquist. Sub-dekahertz ultraviolet spectroscopy of $^{199}HG^+$. *Phys. Rev. Lett.*, 85(12):2462–2465, September 2000.

[23] C.W. Oates, E.A. Curtis, and L. Hollberg. Improved short-term stability of optical frequency standards: approaching 1 Hz in 1 s with the Ca standard at 657 nm. *Opt. Lett.*, 25(21):1603–1605, Novmeber 2000.

[24] Th. Udem, S.A. Diddams, K.R. Vogel, C.W. Oates, E.A. Curtis, W.D. Lee, W.M. Itano, R.E. Drullinger, J.C. Bergquist, and L. Hollberg. Absolute frequency measurements of the Hg^+ and Ca optical clock transitions with a femtosecond laser. *Phys. Rev. Lett.*, 86(22):4996–4999, May 2001.

[25] J. Stenger, C. Tamm, N. Haverkamp, S. Weyers, and H.R. Telle. Absolute frequency measurement of the 435.5-nm $^{171}Yb^+$-clock transition with a Kerr-lens mode-locked femtosecond laser. *Opt. Lett.*, 26(20):1589–1591, October 2001.

[26] C.O. Weiss. Frequency measurement chain to 30 THz using FIR Schottky diodes and a submillimeter backward wave oscillator. *Appl. Phys. B*, 34:63–67, 1984.

[27] H. Schnatz, B. Lipphardt, J. Helmcke, F. Riehle, and G. Zinner. First phase-coherent frequency measurement of visible radiation. *Phys. Rev. Lett.*, 76(1):18–21, January 1996.

[28] H.R. Telle, D. Meschede, and T.W. Hänsch. Realization of a new concept for visible frequency division: phase locking of harmonic and sum frequencies. *Opt. Lett.*, 15(10):532–534, May 90.

[29] N. C. Wong. Optical frequency counting from the UV to the near IR. *Opt. Lett.*, 17(16):1155–1157, August 1992.

[30] J. Reichert, R. Holzwarth, Th. Udem, and T.W. Hänsch. Measuring the frequency of light with mode-locked lasers. *Opt. Comm.*, 172:59–68, December 1999.

[31] A. V. Husakou and J. Hermann. Supercontinuum generation, four-wave mixing, and fission of higher-order solitons in photonic-crystal fibers. *J. Opt. Soc. Am. B*, 19(9):2171–2182, September 2002.

[32] J.K. Ranka, R.S. Windeler, and A.J. Stentz. Visible continuum generation in air-silica microstructure optical fibers with anomalous dispersion at 800 nm. *Opt. Lett.*, 25(1):25–27, January 2000.

[33] W.J. Wadsworth, J.C. Knight, A. Ortigosa-Blanch, J. Arriga, E. Silvestre, and P.St.J. Russel. Soliton effects in photonic crystal fibers at 850 nm. *El. Lett.*, 36(1):53–54, January 2000.

[34] Th. Udem, J. Reichert, R. Holzwarth, and T.W. Hänsch. Accurate measurement of large optical frequency differences with a mode-locked laser. *Opt. Lett.*, 24(13):881–883, July 1999.

[35] S.A. Diddams, Th. Udem, J.C. Bergquist, E.A. Curtis, R.E. Drullinger, L. Hollberg, W.M. Itano, W.D. Lee, C.W. Oates, K.R. Vogel, and D.J. Wineland. An optical clock based on a single trapped $^{199}Hg^{+}$ ion. *Science*, 293:825–828, August 2001.

[36] H. Figger, D. Meschede, and C. Zimmermann (Eds.). *Part I: Atomic and optical clocks*, chapter 1, pages 1–78. Springer-Verlag, Berlin Heidelberg New York, 2002.

[37] N. C. Wong. Optical frequency division using an optical parametric oscillator. *Opt. Lett.*, 15(20):1129–1131, October 1990.

[38] R. Graham and H. Haken. The quantum-fluctuations of the optical parametric oscillator. *Z. Phys.*, 210:276–302, 1968.

[39] A. E. Siegman. *Laser Injection Locking*, chapter 29, pages 1130–1170. In [69], 1986.

[40] C. Fabre, E.J. Mason, and N.C. Wong. Theoretical analysis of self-phase locking in a type II phase-matched optical parametric oscillator. *Opt. Comm.*, 170:299–307, 1999.

[41] T. Skauli, K. L. Vodopyanov, T. J. Pinguet, A. Schober, O. Levi, L. A. Eyres, M. M. Fejer, J. S. Harris, B. Gerard, L. Becouarn, E. Lallier, and G. Arisholm. Measurement of the nonlinear coefficient of orientation-patterned

GaAs and demonstration of highly efficient second-harmonic generation. *Opt. Lett.*, 27(8):628–630, April 2002.

[42] D. Zheng, L. A. Gordon, Y. S. Wu, R. S. Feigelson, M. M. Fejer, R. L. Byer, and K. L. Vodopyanov. 16-μm infrared generation by difference-frequency mixing in a diffusion-bonded-stacked GaAs. *Opt. Lett.*, 23(13):1010–1012, July 1998.

[43] G.Schreiber, H. Suche, Y. L. Lee, W. Grundktter, V. Quiring, R. Ricken, and W. Sohler. Efficient cascaded difference frequency conversion in periodically poled Ti:$LiNbO_3$ waveguides using pulsed and cw pumping. *Appl. Phys. B*, 73:501–504, 2001.

[44] J. A. Giordmaine and R. C. Miller. Tunable coherent parametric oscillation in $LiNbO_3$ at optical frequencies. *Phys. Rev. Lett.*, 14:973–976, 1965.

[45] W. R. Bosenberg, A. Drobshoff, and J. I. Alexander,L. E. Myers and R. L. Byer. 93% pump depletion, 3.5-W continuous-wave, singly resonant optical parametric oscillator. *Opt. Lett.*, 21:1336–1338, 1996.

[46] R. G. Smith, J. E. Geusic, H. J. Levinstein, J. J. Rubin, S. Singh, L. G. Van Uitert. Continuous Optical Parametric Oscillation in $Ba_2NaNb_5O_{15}$. *Appl. Phys. Lett.*, 12(9):308, 1968.

[47] R. L. Byer, M. K. Oshman, J. F. Young, S. E. Harris. Visible cw parametric oscillator. *Appl. Phys. Lett.*, 13:109, 1968.

[48] K. Burneika, M. Ignatavichyus, V. Kabelka, A. Piskarskas, A. Stabinis. Parametric light amplification and oscillation in KDP with mode-locked pump. *IEEE J. Quantum Electr.*, 8:574, 1972.

[49] T. Schröder, K.-J. Boller, A. Fix, R. Wallenstein. Spectral properties and numerical modelling of a critically phase-matched nanosecond LiB_3O_5 optical parametric oscillator. *Appl. Phys. B*, 58(5):425–438, 1994.

[50] K.L. Vodopyanov, F. Ganikhanov, J.P. Maffetone, I. Zwieback, and W. Ruderman. $ZnGeP_2$ optical parametric oscillator with 3.8-12.4 μm tunability. *Opt. Lett.*, 25(11):841–843, 2000.

[51] P. Groß, M.E. Klein, T. Walde, K.-J. Boller, M. Auerbach, P. Weßels, and C. Fallnich. Fiber-laser-pumped continuous-wave singly resonant optical parametric oscillator. *Opt. Lett.*, 27(6):418–420, March 2002.

[52] F. Kühnemann, K. Schneider, A. Hecker, A.A.E. Martis, W. Urban, S. Schiller, J. Mlynek. Photoacoustic trace-gas detection using a cw single-frequency parametric oscillator. *Appl. Phys. B*, 66:741–745, 1998.

[53] M. M. J. W. van Herpen, Shaocheng Li, S. E. Bisson, and F. J. M. Harren. Photoacoustic trace gas detection of ethane using a continuously tunable, continuous-wave optical parametric oscillator based on periodically poled lithium niobate. *Appl. Phys. Lett.*, 81(7):1157–1159, August 2002.

[54] S. T. Yang and S. P. Velsko. Frequency-agile kilohertz repetition-rate optical parametric oscillator based on periodically poled lithium niobate. *Opt. Lett.*, 24:133–135, 1999.

[55] G. Björk and Y. Yamamoto. Phase correlation in nondegenerate parametric oscillators and amplifiers: theory and applications. *Phys. Rev. A*, 37:1991, 1988.

[56] A. Heidmann, R. J. Horowicz, S. Reynaud, E. Giacobino, and C. Fabre. Observation of quantum noise reduction on twin laser beams. *Phys. Rev. Lett.*, 59:2555, 1987.

[57] N. C. Wong. Gravity-wave detection via an optical parametric oscillator. *Phys. Rev. A*, 45:3176, 1992.

[58] P. H. Souto Ribeiro, C. Schwob, A. Maitre and C. Fabre. Sub-shot-noise high-sensitivity spectroscopy with optical parametric oscillator twin beams. *Opt. Lett.*, 22:1893–1895, 1997.

[59] A. Yariv and P. Yeh. *Optical Waves in Crystals.* 1989.

[60] B. E. A. Saleh and M. C. Teich. *Fundamentals of Photonics.* Wiley series in pure and applied optics. John Wiley & Sons, Inc., New York, first edition, 1991. A Wiley-Interscience publication.

[61] H. Paul. *Nichtlineare Optik I/II.* Wissenschaftliche Taschenbücher, Bd. 99, Akademie-Verlag Berlin, 1 edition, 1973.

[62] L. E. Myers and W. R. Bosenberg. Periodically poled lithium niobate and quasi-phase-matched optical parametric oscillators. *IEEE J. Quantum Electron.*, 33:1663–1672, 1997.

[63] M. M. Fejer, G. A. Magel, D. H. Jundt, and R. L. Byer. Quasi-Phase-Matched Second Harmonic Generation: Tuning and Tolerances. *IEEE J. Quant. Elect.*, 28:2631–2653, 1992.

[64] K.-J. Boller, M. E. Klein, D.-H. Lee, P. Groß, H. Ridderbusch, M. A. Tremont, J.-P. Meyn, and R. Wallenstein. Diode-pumped optical parametric oscillators. *Conference on lasers and electro-optics Europe, conference digest (Optical Society of America, Washington, DC)*, page 13, 2000. invited paper no. CMD1.

[65] D.-H. Lee, M.E. Klein, J.-P. Meyn, R. Wallensten, P. Groß, and K.-J. Boller. Phase-coherent all-optical frequency division by three. *Phys. Rev. A*, 67:art. no. 013808, 2003.

[66] G. Imeshev, M. A: Arbore, M. M. Fejer, A. Galvanauskas, M. Fermann, and D. Harter. Ultrahort-pule second-harmonic generation with longitudinally nonuniform quasi-phase-matching gratings: pulse compression and shaping. *J. Opt. Soc. Am. B*, 17(2):304–317, February 2000.

[67] H. Ridderbusch, M. E. Klein, P. Groß, D.-H. Lee, J.-P. Meyn, R. Wallenstein, and K.-J. Boller. Electro-optic modification of second-harmonic phase-matching spectra in segmented periodically poled $LiNbO_3$. *J. Opt. Soc. Am B*, pages 280–288, 2002.

[68] P. Groß, M.E. Klein, H. Ridderbusch, D.-H. Lee, J.-P. Meyn, R. Wallenstein, and K.-J. Boller. Wide wavelength tuning of an optical parametric oscillator through electro-optic shaping of the gain spectrum. *Opt. Lett.*, 27(16):1433–1435, August 2002.

[69] A. E. Siegman. *Lasers*. University Science Books, Mill Valley, California, 1986.

[70] S.A. Diddams, D.J. Jones, J. Ye, S.T. Cundiff, J. Hall, J.K. Ranka, R.S. Windeler, R. Holzwarth, T. Udem, and T.W. Hänsch. Direct link between microwave and optical frequencies with a 300 THz femtosecond laser comb. *Phys. Rev. Lett.*, 84(22):5102–5105, May 2000.

[71] D. Lee, and N.C. Wong. Tunable optical frequency division using a phase-locked optical parametric oscillator. *Opt. Lett.*, 17(1):13–15, January 1992.

[72] A. Douillet, J.-J. Zondy, G. Santarelli, A. Makdissi, and A. Clairon. A phase-locked frequency divide-by-3 optical parametric oscillator. *IEEE Trans. Intrum. Meas.*, 50(2):548–551, April 2001.

[73] E. J. Mason and N. C. Wong. Observation of two distinct phase states in a self-phase-locked type II phase-matched optical parametric oscillator. *Opt. Lett.*, 23(22):1733–1735, November 1998.

[74] E. V. Kovalchuk, D. Dekorsy, A. I. Lvovsky, C. Braxmaier, J. Mlynek, A. Peters, and S. Schiller. High-resolution Doppler-free molecular spectroscopy with a continuous-wave optical parametric oscillator. *Opt. Lett.*, 26(18):1430–1432, September 2001.

[75] S. Slyusarev, T. Ikegami, and S. Ohshima. Phase-coherent optical frequency division by 3 of 532-nm laser light with a continuous-wave optical parametric oscillator. *Opt. Lett.*, 24(24):1856–1858, December 1999.

[76] D.-H. Lee, M.E. Klein, J.-P. Meyn, P. Groß, R. Wallenstein, and K.-J. Boller. Self-injection-locking of a CW-OPO by intracavity frequency-doubling the idler wave. *Opt. Expr.*, 5(5):114–119, August 1999.

[77] D.-H. Lee, M. E. Klein, J.-P. Meyn, P. Groß, S. Marzenell, R. Wallenstein, and K.-J. Boller. All-optical frequency-by-three division with a diode laser pumped CW-OPO using PPLN. *Proc. SPIE*, 3928:25–36, 2000.

[78] J.-J. Zondy, A. Douillet, A. Tallet, E. Ressayre, and M. Le Berre. Theory of self-phase-locked optical parametric oscillators. *Phsy. Rev. A*, 63:art. no. 023814, 2001.

[79] J.-J. Zondy. Stability of the self-phase-locked pump-enhanced singly resonant optical parametric oscillator. *Phys. Rev. A*, 67:art. no. 035801, 2003.

[80] C. D. Nabors, S. T. Yang, T. Day, and R. L. Byer. Coherence properties of a doubly resonant monolithic optical parametric oscillator. *J. Opt. Soc. Am. B*, 7(5):815–820, May 1990.

[81] P. Groß, K.-J. Boller, M.E. Klein, and D.-H. Lee. Frequency stability of a self-phase-locked degenerate continuous-wave optical parametric oscillator. *Conference on lasers and electro-optics, postdeadline papers book (Optical Society of America, Washington, DC)*, 2003. postdeadline paper no. CPDB1.

[82] W. Brunner and H. Paul. The optical parametric oscillator as a means for intracavity absorption spectroscopy. *Opt. Comm.*, 19(2):253–256, 1976.

[83] D.-H. Lee, M.E. Klein, and K.-J. Boller. Intensity noise of pump-enhanced continuous-wave optical parametric oscillators. *Appl. Phys. B*, 66:747–753, 1998.

[84] I. D. Huntley and R. M. Johnson. *Linear and nonlinear differential equations.* Ellis Horwood Series in Mathematics and its Applications. Ellis Horwood Limited, Market Cross House, Cooper Street, Chichester, West Sussex, PO19 1EB, England, 1983.

[85] M. Vidyasagar. *Nonlinear Systems Analysis.* Prentice Hall, Englewood Cliffs, New Yersey 07632, 2nd edition, 1993.

[86] K. P. Chung and A. Marcano O. Phase stabilization of optical subharmonic signals. *J. Opt. Soc. Am. B*, 5(12):2524–2529, December 1988.

[87] J. Rutman. Characterization of phase and frequency instabilities in precision frequency sources: fifteen years of progress. *Proc. IEEE*, 66(9):1048–1075, September 1978.

[88] G.J. Edwards and M. Lawrence. A temperture-dependend dispersion equation for congruently grown lithium niobate. *Opt. and Quant. El.*, 16:373–375, 1984.

[89] A. L. Garcia. *Numerical Methods for Physics*, chapter 3, pages 67–105. Prentice Hall, Inc., Upper Saddle River, New Jersey 07458, 2nd edition, 2000.

[90] MATLAB® is a registered trademark of The Math Works, Inc.

[91] M. Scheidt, B. Beier, R. Knappe, K.-J. Boller, and R. Wallenstein. Diode-laser-pumped continuous-wave KTP optical parametric oscillator. *J. Opt. Soc. Am. B*, 12(11):2087–2094, November 1995.

[92] M.E. Klein, D.-H. Lee, J.-P. Meyn, K.-J. Boller, and R. Wallenstein. Singly resonant continuous-wave optical parametric oscillator pumped by a diode laser. *Opt. Lett.*, 24(16):1142–1145, August 1999.

[93] M.E. Klein, D.-H. Lee, J.-P. Meyn, B. Beier, K.-J. Boller, and R. Wallenstein. Diode-pumped continuous-wave widely tunable optical parametric oscillator based on periodically poled lithium niobate. *Opt. Lett.*, 23(11):831–833, June 1998.

[94] B. Beier, D. Woll, M. Scheidt, K.-J. Boller, and R. Wallenstein. Second harmonic generation of the output of an AlGaAs diode oscillator amplifier system in critically phase matched LiB_3O_5 and β-BaB_2O_4. *Appl. Phys. Lett.*, 71:315–317, July 1997.

[95] M. Scheidt, B. Beier, K.-J. Boller, and R. Wallenstein. Frequency-stable operation of a diode-pumped continuous-wave $RbTiOAsO_4$ optical parametric oscillator. *Opt. Lett.*, 22(17):1287–1289, September 1997.

[96] D. Woll, B. Beier, K.-J. Boller, R. Wallenstein, M. Hagberg, and S. O'Brien. 1 W of blue 465-nm radiation generated by frequency doubling of the output of a high-power diode laser in critically phase-matched LiB_3O_5. *Opt. Lett.*, 24(10):691–693, May 1999.

[97] M. Auerbach, P. Adel, D. Wandt, C. Fallnich, S. Unger, S. Jetschke, and H.-R. Müller. 10 W widely tunable narrow linewidth double-clad fiber ring laser. *Opt. Expr.*, 10(2):139–144, January 2002.

[98] S. Nakamura nad G. Fasol. *The blue laser diode.* Springer-Verlag, Heidelberg, 1997.

[99] S. Nakamura. The roles of structural imperfections in InGaN-based blue light-emitting diodes and laser diodes. *Science*, 281:956–961, August 1998.

[100] J. Alnis, U. Gustafsson, G. Somesfalean, and S. Svanberg. Sum-frequency generation with a blue diode laser for mercury spectroscopy at 254 nm. *Appl. Phys. Lett.*, 76(10):1234–1236, March 2000.

[101] F.K. Kneubuehl and M.W. Sigrist. *Laser.* Teubner, Stuttgart, Germany, 4th edition, 1995.

[102] J. Faist, F. Capasso, D.L. Sivco, A.L. Hutchinson, S.N.G. Chu, and A.Y. Cho. Short wavelength ($\lambda \approx 3.4$ μm) quantum cascade laser based on strained compensated InGaAs/AlInAs. *Appl. Phys. Lett.*, 72:680–682, 1998.

[103] R. Köhler, A. Tredicucci, F. Beltram, H.E. Beere, E.H. Linfield, A.G. Davies, and D.A. Ritchie. Low-threshold quantum-cascade lasers at 3.5 THz ($\lambda =$ 85 μm). *Opt. Lett.*, 28(10):810–812, May 2003.

[104] C. Gmachl, F. Capasso, A. Tredicucci, D.L. Sivco, J.N. Baillargeon, A.L. Hutchinson, and A.Y.Cho. High-power, continuous-wave, current-tunable, single-mode quantum-cascade distributed-feedback lasers at $\lambda \cong 5.2$ and $\lambda \cong$ 7.95 μm. *Opt. Lett.*, 25(4):230–232, February 2000.

[105] F. Capasso, R. Paiella, R. Martini, R. Colombelli, C. Gmachl, T.L. Myers, M.S. Taubman, R.M. Williams, C.G. Bethea, K. Unterrainer, H.Y. Hwang, D.L. Sivco, A.Y. Cho, A.M. Sergent, H.C. Liu, and E. A. Whittaker. Quantum cascade lasers: Ultrahigh-speed operation, optical wireless communication, narrow linewidth, and far-infrared emission. *IEEE J. Quant. El.*, 38(6):511–532, June 2002.

[106] T. Ikegami, S. Sudo, and Y. Sakai. *Frequency stabilization of semiconductor laser diodes*. Artech House, Boston, 1995.

[107] N. Beverini, E. Maccioni, P. Marsili, A. Ruffini, and F. Sorrentino. Frequency stabilization of a diode laser on the Cs D_2 resonance line by the Zeeman effect in a vapor cell. *Appl. Phys. B*, 73:133–138, 2001.

[108] D. Cassettari, E. Arimondo, and P. Verkerk. External-cavity broad-area laser diode operating on the D_1 line of cesium. *Opt. Lett.*, 23(14):1135–1137, July 1998.

[109] Y.C. Chung and C.B. Roxlo. Frequency-locking of a 1.5 μm DFB laser to an atomic krypton line using optogalvanic effect. *El. Lett.*, 24(16):1048–1049, August 1988.

[110] M. Merimaa, T. Lindvall, I. Tittonen, and E. Ikonen. All-optical atomic clock based on coherent population trapping in ^{8}5Rb. *J. Opt. Soc. Am. B*, 20(2):273–279, February 2003.

[111] R.M. Williams, J.F. Kelly, J.S. Hartman, S.W. Sharpe, M.S. Taubman, J.L. Hall, F. Capasso, C. Gmachl, D.L. Sivco, J.N. Baillargeon, and A.Y. Cho. Kilohertz linewidth from frequency-stabilized mid-infrared quantum cascade lasers. *Opt. Lett.*, 24(24):1844–1846, December 1999.

[112] M. Ohtsu. *Highly coherent semiconductor lasers.* Artech House, Boston, 1992.

[113] Y. Shevy and H. Deng. Frequency-stable and ultranarrow-linewidth semiconductor laser locked directly to an atomic-cesium transition. *Opt. Lett.*, 23(6):472–474, March 1998.

[114] K. Liu and M.G. Littman. Novel geometry for single-mode scanning of tunable lasers. *Opt. Lett.*, 6(3):117–119, March 1981.

[115] K.C. Harvey and C.J. Myatt. External-cavity diode laser using a grazing-incidence diffraction grating. *Opt. Lett.*, 16(12):910–912, June 1991.

[116] D. Wandt, M. Laschek, K. Przyklenk, A. Tünnermann, and H. Welling. External cavity laser diode with 40 nm continuous tuning range around 825 nm. *Opt. Comm.*, 130:81–84, September 1996.

[117] H. Kogelnik and T. Li. Laser beams and resonators. *Appl. Opt.*, 5:1550–1567, October 1966.

[118] A.J. Henderson, M.J. Padgett, F.G. Colville, J. Zhang, and M.H. Dunn. Doubly-resonant optical parametric oscillators: tuning behavior and stability requirements. *Opt. Comm.*, 119:256–264, August 1995.

[119] R.L. Barger, M.S. Sorem, J.L. Hall. Frequency stabilization of a CW dye laser. *Appl. Phys. Lett.*, 22(11):573–577, June 1973.

[120] C.E. Wieman and S.L. Gilbert. Laser-frequency stabilization using mode interference from a reflecting reference interferometer. *Opt. Lett.*, 7(10):480–482, October 1982.

[121] D.A. Shaddock, M. B. Gray, and D.E. McClelland. Frequency locking a laser to an optical cavity by use of spatial mode interference. *Opt. Lett.*, 24(21):1499–1501, November 1999.

[122] T. W. Hänsch and B. Couillaud. Laser frequency stabilization by polarization spectroscopy of a reflecting reference cavity. *Opt. Comm.*, 35(3):441–444, December 1980.

[123] R.W.P. Drever, J.L. Hall, F.V. Kowalski, J. Hough, G.M. Ford, A.J. Munley, and H. Ward. Laser phase and frequency stabilization using an optical resonator. *Appl. Phys. B*, 31:97–105, 1983.

[124] G.C. Bjorklund, M.D. Levenson, W. Lenth, and C. Ortiz. Frequency modulation (FM) spectroscopy. *Appl. Phys. B*, 32:145–152, 1983.

[125] U. Tietze and Ch. Schenk. *Halbleiter-Schaltungstechnik*. Springer-Verlag, Berlin, Germany, 5th edition, 1980.

[126] R. L. Eckardt, C. D. Nabors, W. J. Kozlovsky, and R. L. Byer. Optical parametric oscillator frequency tuning and control. *J. Opt. Soc. Am. B*, 8(3):646–667, March 1991.

[127] L.R. Brothers, D. Lee, and N.C. Wong. Terahertz optical frequency comb generation and phase locking of an optical parametric oscillator at 665 GHz. *Opt. Lett.*, 19(4):245–247, February 1994.

[128] D.W. Sprehn, C.L. Rettig, and N.C. Luhmann, Jr. Phase locking and frequency locking of a 140 GHz klystron and a 280 GHz carcinotron. *Rev. Sci. Intrum.*, 63(10):4685–4687, October 1992.

[129] B. E. A. Saleh and M. C. Teich. *Fundamentals of Photonics*, chapter 6, pages 193–237. In *Wiley series in pure and applied optics* [60], first edition, 1991. A Wiley-Interscience publication.

Acknowledgements

I would like to thank all those friends, colleagues and relatives, who supported me during these years and contributed directly or indirectly to this work.

First of all, I am very grateful for the hearty welcome that I received by the members of the Laser Physics and Nonlinear Optics group at the university of Twente, when I moved to Enschede in autumn 2000. Since then, working in this group has always been very interesting and exciting, and it has also been great fun, due to the diversity of the work and of the characters in this group.

This positive experience was of course initiated by my promoter Prof. Dr. Klaus-Jochen Boller, whom I want to thank for the opportunity to continue my PhD work in the Netherlands. Without his perpetual interest in discussing all theoretical and practical aspects that emerged in the course of my work, a successful completion of my thesis would have been impossible. His sharp eye for the basic aspects of all the theories and experiments involved, and his great teaching skills were of considerable help for gaining a good understanding of the subject.

Many thanks to Dr. Herman Offerhaus and Dr. Marvin Klein, for carefully and in part "last-minute" reading of the manuscript and for finding all the scientific and linguistic mistakes and for helpful suggestions. Thanks also to Aart Schoonderbeek for his indispensable help with the Dutch abstract!

For daily physical discussions and close cooperation in the lab I owe thanks to the people of the OPO sub-group: Dr. Marvin Klein, Dr. Herman Offerhaus, Tom Walde, Balaji Adhimoolam, and Dr. Ian Lindsay.

The international PhD-student community has been indispensable for me due to the continuously good atmosphere they spread throughout the group. Therefore, thank you, Balaji Adhimoolam, Dennis Deriga, Liviu Prodan, Isabel de la Fuente Valentin, Denny Mathew, Iuri Volokhin, Anton Azarov, Lars Casper, Aart Schoonderbeek, Dr. Sergei Starostin, Daniele Marinazzo, and Anjali Shah.

Many thanks to Dr. Peter van der Slot, for volunteering to take a new student in his office, for giving me a good start in the solid-state laser lab, and for eventual preparing of a grande cuisine.

Thanks also to Jeroen Wieland and Claudia Ruygrok for many a lunch in the mensa, TN cantine, and vrijhof, and for beer brewing sessions, and for looking after my pets, respectively.

I also would like to thank all the other colleagues of the Laser Physics group and NCLR b.v. (in arbitrary order: Dr. Bert Bastiaens, Dr. Fred van Goor, Twan Bouman, Dr. Jeroen Verschuur, Ab Nieuwenhuis, Jacob Couperus, Huub van Heel, Dr. Yuri Udalov, Leon Raanhuis, Dr. Piet Peters, Simone ter Hedde-Sloot, Dr. Ramon Hofstra, Dr. Cees Biesheuvel, Arco Krijgsman, Dr. Sergej Mitko, Otto van Donselaar, Dr. Arsen Khachatrayan, Gerard Oude Meijers, Henk Prins), who were always willing to discuss physics and technical problems, and the technicians and computer experts who were always helpful in solving hardware and software problems.

Many, many thanks I want to express to my "old" colleagues from Kaiserslautern. I am indebted to Prof. Dr. R. Wallenstein for providing excellent conditions in his research group during the first year of my PhD studies, and, by sponsoring some valuable equipment, also in the last three years. Since I am bound to the group in friendship. Amongst them, I would like to thank Dr. Dong-Hoon Lee, for continuous and interested discussions not only on OPO dividers. Thanks to Dr. Jan-Peter Meyn, who designed and manufactured most of the PPLN crystals I used during my thesis. Prof. Dr. Beigang, Dr. Andrew Robertson, Dr. Dirk Woll, Dr. Gregor Anstett, Dr. Ralf Knappe, Dr. Jürgen Bartschke, Heiko Ridderbusch, Marc Tremont, Dr. Johannes L'Huillier, Dr. Thorsten Andres, Sascha Zelt, Dr. Volker Wesemann, Dr. Gunter Bitz, Claus Seibert, and many others are to be thanked not only for their cooperation in the physics lab, but also for their competition on the indiaca, volleyball, football and barbecue ground.

The last and most emphasized position in this acknowledgement is reserved for my parents, my brother, and my grand-ma, who enabled and encouraged my studies of physics.

Thank you all!